Uniwersytet im. Adama Mickiewicza w Poznaniu
Wydział Chemii

ROZPRAWA DOKTORSKA

Mgr Marcin Runowski

Synteza, modyfikacja powierzchni i charakterystyka fizykochemiczna wielofunkcyjnych nanomateriałów luminescencyjnych zawierających jony pierwiastków ziem rzadkich

Synthesis, surface modification and physicochemical characteristics of multifunctional, luminescent nanomaterials containing rare earth ions

w formie spójnego tematycznie cyklu artykułów opublikowanych w czasopismach naukowych

Promotor: prof. dr hab. Stefan Lis
Promotor pomocniczy: dr Tomasz Grzyb

Poznań 2016

Podziękowania

Dla prof. dr. hab. Stefana Lisa za nieocenione wsparcie naukowe, wielką życzliwość, liczne dyskusje dotyczące problemów badawczych oraz rady udzielone w trakcie pisania pracy

Dla dr. Tomasza Grzyba za pomoc w rozwiązywaniu problemów naukowych, liczne dyskusje, otwartość oraz wsparcie w prowadzeniu prac badawczych

Dla koleżanek i kolegów z laboratorium, za pomoc i wsparcie, prowadzenie dyskusji naukowych, cierpliwość i zawsze pozytywne nastawienie.

Mojej żonie Marcie i Rodzicom za nieocenione wsparcie na każdym kroku mojego rozwoju naukowego, ogromną cierpliwość i wyrozumiałość.

Ministerstwu Nauki i Szkolnictwa Wyższego za dofinansowanie projektu badawczego „Synteza i charakterystyka fizykochemiczna nanomateriałów domieszkowanych jonami lantanowców, charakteryzujących się strukturą typu rdzeń-powłoka (ang. core/shell)”, w ramach programu „Diamentowy Grant” (UMO-9114/DIA/2012/41)

Fundacji na rzecz Nauki Polskiej za wsparcie finansowe w postaci stypendium naukowego START, dla wybitnych młodych uczonych na początku kariery naukowej posiadających udokumentowane osiągnięcia w swojej dziedzinie badań

Spis treści

Cel pracy

Celem naukowym rozprawy doktorskiej było otrzymanie, modyfikacja powierzchni i zbadanie właściwości fizykochemicznych wielofunkcyjnych nanomateriałów luminescencyjnych opartych o jony pierwiastków ziem rzadkich. Badania oparte były o materiały złożone z nieorganicznych, nanokrystalicznych fluorków, fosforanów i wanadanów domieszkowanych jonami lantanowców, Ln^{3+}. Struktury tych związków powinny charakteryzować się wydajną wielokolorową luminescencją, której barwę można modulować w zależności od zastosowanych jonów domieszki, parametrów syntezy oraz obróbki poreakcyjnej zsyntetyzowanych układów. Istotny wpływ na morfologię, strukturę, charakter powierzchni oraz właściwości spektroskopowe powstałych nanoluminoforów mogą mieć użyte podczas reakcji związki organiczne o charakterze anty-aglomerantów i surfaktantów zmniejszających napięcie powierzchniowe układu. Przeprowadzona funkcjonalizacja otrzymanych nanostruktur, powinna doprowadzić do powstania wielofunkcyjnych nanomateriałów wykazujących przestrajalną luminescencję, mających organicznie sfunkcjonalizowaną reaktywną powierzchnię, wykazujących jednocześnie właściwości magnetyczno-luminescencyjne oraz aktywność biologiczną. Większość takich zaawansowanych, funkcjonalnych nanomateriałów złożona jest z nanostruktur typu rdzeń/powłoka (*core/shell*). W pracy zostaną przedstawione metody syntezy otrzymanych nanomateriałów oraz ich szczegółowa charakterystyka fizykochemiczna. Ponadto, przedstawione zostaną wyniki badań nad wpływem otrzymanych nanomateriałów na wybrane linie komórkowe, co związane jest z oceną ich cytotoksyczności jako potencjalnych nanomateriałów biokompatybilnych.

Streszczenie rozprawy doktorskiej

Nanomateriały złożone są z bardzo małych cząstek o wielkości, z reguły nieprzekraczającej 100 nm. Takie nanocząstki często wykazują zmienione właściwości fizykochemiczne w porównaniu do ich makroskopowych odpowiedników. Nanostruktury charakteryzują się dużą wartością stosunku liczby atomów powierzchniowych i przypowierzchniowych do tych znajdujących się wewnątrz danej cząstki (duży stosunek powierzchni do objętości). Efekt ten wyraża się zmianą otoczenia koordynacyjnego powierzchniowych atomów/jonów w stosunku do tych znajdujących się wewnątrz nanocząstki. Z powodu licznych defektów punktowych (elektronowych i atomowych) oraz powierzchniowych (np. dyslokacji) istnieje znaczna ilość niewysyconych miejsc koordynacyjnych na powierzchni takich układów, co skutkuje zmianą właściwości spektroskopowych takiego nanomateriału. Efekt ten występuje na przykład w nanocząstkach nieorganicznych fluorków domieszkowanych jonami lantanowców. Może się on też ujawniać w zmianie charakteru widma, tj. kształtu i intensywności niektórych pasm oraz w pojawieniu się drugiej składowej emisyjnego czasu życia podczas analizy zaniku luminescencji.

Nanostruktury typu rdzeń/powłoka (*core/shell*) złożone są z co najmniej dwóch różnych faz, mianowicie rdzenia otoczonego zewnętrzną warstwą powłoki. Struktury te wykazują jednocześnie właściwości rdzenia oraz powłoki (lub powłok), co wpływa na ich unikatową wielofunkcyjność. Dzięki temu można połączyć na przykład w jednym materiale właściwości magnetyczne rdzenia z luminescencyjnymi powłoki, otrzymując dwufunkcyjny materiał luminescencyjno-magnetyczny. Ponadto, dzięki zastosowaniu odpowiedniej powłoki można zabezpieczyć rdzeń przed niekorzystnym wpływem otoczenia zewnętrznego oraz zmienić właściwości powierzchniowe rdzenia. Zmiana taka może korzystnie wpłynąć na zwiększoną stabilność koloidów tworzonych przez dany układ, ładunek powierzchniowy, powinowactwo chemiczne, luminescencję oraz cytotoksyczność nanomateriałów.

Dzięki unikatowym właściwościom jonów lantanowców, nanomateriały zawierające jony Ln^{3+} mogą wykazywać intensywną, wielokolorową luminescencję, będąca wynikiem przejść 4f-4f elektronowych. Ich właściwości luminescencyjne

charakteryzują się obecnością wąskich pasm absorpcyjnych i emisyjnych, długimi (rzędu mikro- do milisekund) czasami życia luminescencji, stabilnością świecenia, trwałością termiczną i fotochemiczną oraz podatnością na przestrajanie barwy luminescencji.

Celem naukowym rozprawy doktorskiej było otrzymanie, modyfikacją powierzchni oraz zbadanie właściwości fizykochemicznych wielofunkcyjnych nanomateriałów luminescencyjnych opartych o jony pierwiastków ziem rzadkich.

Pierwszym etapem badań była synteza nanokrystalicznych fluorków, fosforanów i wanadanów pierwiastków ziem rzadkich (RE), domieszkowanych odpowiednimi jonami lantanowców (Ln^{3+}), tj. $REF_3:Ln^{3+}$; $GdVO_4:Ln^{3+}$; Sr_2REF_7, $REF_3:Ln^{3+}$ (RE = La, Ce, Gd; Ln = Sm, Eu, Tb). Nanomateriały otrzymane zostały różnymi metodami tzw. „mokrej chemii" z wykorzystaniem strategii syntezy typu „*bottom-up"*, tj. współstrącanie (*coprecipitation*), metody micelarne, synteza w warunkach hydrotermalnych oraz w mikroemulsji. Otrzymane produkty wykazywały intensywną, wielokolorową luminescencję, zależną od użytego jonu aktywatora. Istotny wpływ na właściwości otrzymanych nanoluminoforów miało również użycie, podczas syntezy, organicznych anty-aglomerantów i surfaktantów. Część zsyntetyzowanych produktów poddawano po syntezie obróbce hydrotermalnej lub organicznej modyfikacji powierzchni (nanomateriały hybrydowe). Dzięki temu, odpowiednio zmodyfikowane nanomateriały wykazywały efekt przestrajalnej wielobarwnej luminescencji, tj. $CeF_3:Gd^{3+}$, Sm^{3+}; $LaPO_4:Ln^{3+}$/organic (Ln = Eu, Tb). Właściwości fizykochemiczne otrzymanych luminoforów zostały szczegółowo zbadane metodami proszkowej dyfrakcji rentgenowskiej (XRD), transmisyjnej mikroskopii elektronowej (TEM), spektroskopii w podczerwieni (FT-IR) oraz spektrofluorymetrii.

W kolejnym etapie wyselekcjonowano nanocząstki charakteryzujące się monodyspersyjnością, najbardziej intensywną luminescencją w zakresie widzialnym oraz największą stabilnością formowanych koloidów. Tak wybrane struktury poddano modyfikacji powierzchni na drodze hydrolizy i ko-kondensacji odpowiednich pochodnych silanowych (TEOS, APTES, EDATAS), wykorzystując zmodyfikowaną metodę Stöbera. W wyniku tego otrzymano nanostruktury typu rdzeń/powłoka (*core/shell*), sfunkcjonalizowane powierzchniowo grupami aminowymi lub karboksylowymi, tj. $LnF_3/SiO_2/NH_2$/organic, $LaPO_4:Tb^{3+}/SiO_2/NH_2$, Fe_3O_4/SiO_2/COOH.

Modyfikacja powierzchni wpłynęła znacząco na zmianę właściwości fizykochemicznych i biologicznych otrzymanych produktów, w porównaniu do

niepokrytych nanocząstek. Zmianie uległy właściwości spektroskopowe, morfologiczne, wielkość powierzchni właściwej, ładunek powierzchniowy (zeta potencjał) oraz aktywność biologiczna (cytotoksyczność) zsyntetyzowanych nanomateriałów.

Wybrane nanoluminofory oparte o domieszkowane fluorki lub wanadany lantanowców użyto do dalszej syntezy złożonych nanostruktur luminescencyjno-magnetycznych typu core/shell, tj. $Fe_3O_4/SiO_2/COOH/GdVO_4:Eu^{3+}$; $Fe_3O_4/SiO_2/NH_2/PAA/CeF_3$: 10% Gd^{3+}, 10% Tb^{3+}; LaF_3: 10% Ce^{3+}, 30% Gd^{3+}, 1% Eu^{3+}. Otrzymane wielofunkcyjne nanomateriały wykazywały jednocześnie intensywną zieloną lub czerwoną luminescencję (charakterystyczną dla jonów Tb^{3+} lub Eu^{3+}) pod wpływem promieniowania UV oraz odpowiedź na przyłożone pole magnetyczne.

Właściwości otrzymywanych nanomateriałów zostały zbadane przy użyciu metod spektrofluorymetrii, dyfraktometrii proszkowej (XRD), spektroskopii w podczerwieni (FT-IR), mikroskopii elektronowej (TEM, HR-TEM, SEM, STEM), analizy składu pierwiastkowego (EDX, ICP-OES, analiza elementarna), badań powierzchni właściwej, analizy wielkości cząstek i zeta potencjału (DLS, ELS), testów umożliwiających ocenę ich cytotoksyczności i innych technik badawczych.

Zsyntetyzowane nanomateriały o wielofunkcjonalnych właściwościach mogą zostać potencjalnie zastosowane jako nowoczesne środki kontrastowe, nośniki leków, środki daktyloskopijne, bio-sensory, znaczniki luminescencyjne czy nowe wydajne źródła światła.

Abstract of doctoral dissertation

Nanomaterials are composed of very small particles, usually smaller than 100 nm. Such nanoparticles often exhibit altered physicochemical properties in comparison with their bulk analogues. Nanostructures have a high ratio of surface and near surface atoms/ions to the ones situated inside of a given particle (large surface-to-volume ratio). This effect can be manifested in the altered coordination environment of such surface and near surface atoms/ions. Because of numerous structural defects, nanoparticles have significant number of unsaturated coordination sites, situated on their surface, what causes changes of spectroscopic properties of such nanomaterial. The mentioned effect can be observed, for example, in the case of nanocrystalline, inorganic fluorides doped with lanthanide ions. It can be manifested as altered shape and intensity of the bands in the emission spectrum and as an occurrence of second lifetime component.

Core/shell type nanostructures are composed of at least two different phases, namely of the core surrounded/coated by the external layer of the shell. Such structures reveal simultaneously properties of the core and the shell (or shells), what is a reason of their unique multifunctionality. Thanks to the mentioned features, the magnetic properties of the core can be combined with luminescence properties of the shell, in a single nanomaterial, resulting in a formation of bifunctional luminescent-magnetic nanomaterial. Moreover, due to the use of appropriate shell, the core can be protected from damaging impact of external environment, as well as to change surface characteristics of the core. Such alternation can influence stability of the colloids formed, surface charge, chemical affinity, luminescence and cytotoxicity of the modified nanomaterial.

Thanks to the unique properties of lanthanide ions, Ln^{3+}, the nanomaterials containing such ions, can exhibit intense, multicolour luminescence, as a results of 4f-4f electronic transitions. Their luminescence properties are featured with the presence of narrow absorption and emission bands, long radiative lifetimes in the range of micro- to milliseconds, stability of emission, thermal and photochemical stability, as well as their ability to tune the colour of luminescence.

The scientific aim of the doctoral dissertation was preparation, surface modification and investigation of physicochemical properties of the multifunctional, luminescent nanomaterials, based on the rare earth ions (RE).

The first part of the research was the synthesis of nanocrystalline rare earths fluorides, phosphates and vanadates, doped with appropriate lanthanide ions, i.e. $REF_3:Ln^{3+}$; $GdVO_4:Ln^{3+}$; Sr_2REF_7, $REF_3:Ln^{3+}$ (RE = La, Ce, Gd; Ln = Sm, Eu, Tb). The nanomaterials were prepare by various "wet chemistry" methods, using the "bottom-up" approach, i.e. coprecipitation, normal micelle method, synthesis under hydrothermal conditions and synthesis in microemulsion system. The products obtained exhibited intense, multicolour luminescence, dependent on the activator Ln^{3+} ion used. The use of anti-agglomeration agents and surfactants during the synthesis process, significantly influenced properties of the nanoluminophores obtained. After the synthesis, part of the synthesized products was hydrothermally post-treated or organically surface modified (hybrid nanomaterials). Due to these modifications, the nanomaterials exhibited tuneable multicolour luminescence phenomenon, i.e. $CeF_3:Gd^{3+}$, Sm^{3+}; $LaPO_4:Ln^{3+}$/organic (Ln = Eu, Tb). The physicochemical properties of the nanoluminophores obtained were examined by the means of powder X-ray diffraction (XRD), transmission electron microscopy (TEM), infrared spectroscopy (FT-IR) and spectrofluorometry.

The next step of the studies was related to the selection of monodisperse nanoparticles, exhibiting most intense luminescence in a visible range and good stability of the colloids formed. The selected structures were surface modified by hydrolysis and co-condensation of appropriate silane derivatives (TEOS, APTES, EDATAS), via a modified Stöber method. The performed modifications resulted in the formation of core/shell type nanostructures, whose surface was functionalized with amino or carboxyl groups, i.e. $LnF_3/SiO_2/NH_2$/organic, $LaPO_4:Tb^{3+}/SiO_2/NH_2$, $Fe_3O_4/SiO_2/COOH$.

The performed surface modification influenced on physicochemical and biological properties of the products obtained, in comparison with uncoated nanoparticles. Those alternations concerned favourably spectroscopic properties, morphology, specific surface area, surface charge (zeta-potential) and biological activity (cytotoxicity) of the nanomaterials synthesized.

The selected nanoluminophores based on the doped lanthanide fluorides and vanadates, were used further in the synthesis of complex, core/shell type luminescent-

magnetic nanostructures, i.e. $Fe_3O_4/SiO_2/COOH/GdVO_4:Eu^{3+}$; LaF_3: 10% Ce^{3+}, 30% Gd^{3+}, 1% Eu^{3+}; $Fe_3O_4/SiO_2/NH_2/PAA/CeF_3$: 10% Gd^{3+}, 10% Tb^{3+}. The as-prepared multifunctional nanomaterials, simultaneously exhibited red or green luminescence (characteristic for Eu^{3+} or Tb^{3+} ions, respectively) under UV light irradiation and a response to the applied magnetic field.

The properties of the nanomaterials synthesized were investigated by the use of following methods: spectrofluorometry, XRD, FT-IR spectroscopy, electron microscopy (TEM, HR-TEM, SEM, STEM), elemental composition analyses (EDX, ICP-OES, elemental analysis), surface area measurements, analysis of hydrodynamic size distribution and zeta-potential of the particles (DLS, ELS), SRB tests for cytotoxicity evaluation and other analytic techniques.

The multifunctional nanomaterials obtained can be potentially applied as advanced contrast agents, drug-carriers, fingerprint powders in dactyloscopy, bio-sensors, luminescence tracers or novel and efficient light sources.

Życiorys naukowy

Mgr Marcin Runowski
Data i miejsce urodzenia: 30.06.1989, Poznań
Adres: ul. Osiedlowa 34 - Jerzykowo 62-007
Telefon: 691 963 225 Email: runowski@amu.edu.pl, runowski.marcin@gmail.com

Wykształcenie

Studia doktoranckie, Wydział Chemii, UAM Poznań	2012-
Magister Chemii, specjalność: chemia materiałowa, Wydział Chemii, UAM Poznań	2011-2012
Licencjat Chemii, specjalność: synteza i analiza chemiczna, Wydział Chemii, UAM Poznań	2008-2011
III LO w Poznaniu, profil: biol-chem	2005-2008

Praktyki, staże, kursy

- Miesięczna (01-25.07 2008) oraz półtoramiesięczna (11.08-17.09 2010) **- praktyki zagraniczne**, które odbyłem dwukrotnie w okresie letnich wakacji, **w Szwajcarii na** Wydziale Chemii **Uniwersytetu w Genewie**. W grupie prof. Alana F. Williamsa brałem udział w projekcie badawczym dotyczącym syntezy i analizy (charakterystyka fizykochemiczna wraz z badaniami spektroskopowymi – NMR, FT-IR, MS) pochodnych benzimidazolu, ograno-żeli, czynników wiążących fosforany i tematyką z nimi związaną. Rezultatem tej pracy badawczej jest publikacja w czasopismie naukowym New Journal of Chemistry.
- **Staż naukowy w ramach stypendium START** (01.07.2015-04.10.2015) w grupie badawczej Profesora Michaela Giersiga - Freie Universität Berlin, FB Physik, Inst. f. Experimentalphysik, Institute of Nano-architectures for Energy Conversion, Helmholtz-Zentrum Berlin für Materialien und Energie. Podczas wyjazdu studyjnego nauczyłem się: syntezy i modyfikacji powierzchni zaawansowanych, funkcjonalnych nanomateriałów o złożonej, wielowarstwowej strukturze; syntezy nowych luminescencyjnych, magnetycznych i luminescencyjno-magnetycznych nanomateriałów oraz nanostruktur typu core/shell; badać właściwości fizykochemiczne otrzymanych nanomateriałów przy użyciu mikroskopu elektronowego. Staż w grupie Profesora Michaela Giersiga znacząco poszerzył moje horyzonty badawcze i umożliwnił mi uzyskanie nowej wiedzy w zakresie nanotechnologii.
- **Zaawansowany kurs nanotechnologii,** 10-23.07.2011 Praga, Czechy (Czech Technical university in Prague) **– „***Nanosized particles as building blocks for creation of nanostructures"* - Erasmus Intensive Programme. Koordynatorami kursu były uczelnie z Polski, Czech i Niemiec. Z końcowego egzaminu uzyskałem ocenę bardzo dobry, co jest równoważne 5 punktom ECTS które zostały mi przyznane.
- **Zaawansowany kurs „PLASMAG"** (Plasmonic and Magnetic Nanomaterials), 30.06.-13.07.2013 Poznań – *Erasmus Intensive Programme* - Koordynatorami kursu były uczelnie z Polski i Niemiec. Z końcowego egzaminu uzyskałem ocenę bardzo dobry, co jest równoważne 6 punktom ECTS które zostały mi przyznane.

Udział w grantach badawczych

- Kierownik projektów: „**Diamentowy Grant**" - UMO-9114/DIA/2012/41 (MNiSW - 2012-2015); grant „**Preludium**" - UMO-2015/17/N/ST5/01947 (NCN - 2016-2019)
- Wykonawca projektów: grant „Ventures" - 2009-4/2 (FNP - 2009-2011); „Sonata" - UMO-2011/03/D/ST5/05701 (NCN - 2012 – 2016); „Harmonia" - UMO-2012/06/M/ST5/00325 (NCN - 2013 – 2015)

Osiągnięcia i nagrody

- Współautor **19 publikacji** naukowych
- Współautor **70 komunikatów** naukowych
- Współautor **zgłoszenia patentowego**
- I miejsce – **Złoty Medal Chemii**, w ogólnopolskim konkursie na najlepszą pracę licencjacką/inżynierską wykonaną w roku akademickim 2010/2011, organizowanym przez Instytut Chemii Fizycznej Polskiej Akademii Nauk (IChF PAN).
- Laureat programu „**Diamentowy Grant**" (2012)
- Wyróżnienie Polskiego Towarzystwa Chemicznego - PTChem - do **Nagrody im. Janiny Janikowej** na najlepszą pracę magisterską zrealizowaną w roku 2012
- I miejsce w konkursie na najlepszą pracę magisterską realizowaną w roku akademickim 2011/2012 na Wydziale Chemii UAM w Poznaniu
- Nagroda zespołowa III stopnia Rektora UAM za osiągnięcia w pracy naukowej (2014)
- Nagroda zespołowa II stopnia Rektora UAM za osiągnięcia w pracy naukowej (2015)
- **Stypendium Ministra Nauki i Szkolnictwa Wyższego dla doktorantów** za wybitne osiągnięcia w roku akademickim 2015/2016
- **Stypendium START 2015 i 2016 dla wybitnych młodych uczonych** na początku kariery naukowej posiadających udokumentowane osiągnięcia w swojej dziedzinie badań
- Stypendium Funduszu im. Rodziny Kulczyków dla najlepszych doktorantów (2014/2015)
- Stypendium naukowe Miasta Poznania dla młodych badaczy z poznańskiego świata nauki (2014)
- Stypendium Fundacji UAM dla doktorantów UAM (2014/2015)
- Stypendia naukowe dla najlepszych doktorantów, stypendia projakościowe i doktoranckie w latach 2012-2015
- Stypendium rektora I stopnia dla najlepszych studentów (2011-2012)
- Stypendium naukowe za bardzo dobre wyniki w nauce (2010-2011)
- Nagroda za działalność społeczną i organizacyjną w ramach Naukowego Koła Chemików, na Wydziale Chemii UAM (2012)
- I miejsce za najlepszy poster naukowy, z badań własnych, w kategorii chemia materiałów, podczas 55 Zjazdu Naukowego Polskiego Towarzystwa Chemicznego i Stowarzyszenia Inżynierów i Techników Przemysłu Chemicznego (PTCHEM), 16-20.09.2012, Białystok.
- II miejsce/nagroda w konkursie na najlepszy poster podczas międzynarodowej konferencji pt. „4th Summer Symposium on Nanomaterials and their application to Biology and Medicine" (15-18.06.2014 Poznań)
- Wyróżnienie za najlepszy poster podczas konferencji środowiskowej „Wielkopolskie Centrum Zaawansowanych Technologii Materiały i Biomateriały", 28-29.11.2011, Poznań.
- I miejsce w kategorii prezentacja z badań własnych podczas XXXV Ogólnopolskiej Szkoły Chemii, 9-13.11.2011, Karpicko.
- I miejsce w konkursie na najlepsze wystąpienie ustne podczas X Ogólnopolskiego Sympozjum NKCh, 22-25.03.2012, Jeziory.
- II miejsce w konkursie na najlepsze wystąpienie ustne podczas VIII Ogólnopolskiego Sympozjum NKCh, 21-24.10.2010, Jeziory.
- III miejsce w konkursie na najlepsze wystąpienie ustne podczas VII Ogólnopolskiego Sympozjum NKCh, 25-28.03.2010, Jeziory.
- III miejsce w konkursie na najlepsze wystąpienie ustne podczas VI Ogólnopolskiego Sympozjum NKCh, 15-18.10.2009, Jeziory.
- Wyróżnienie w konkursie na najlepszą prezentację ustną podczas międzynarodowej konferencji naukowej pt. „Chemistry, Environment and Nanotechnology" (CEN), 15-17.04.2015, Gdańsk

Lista publikacji

Publikacje wchodzące w skład rozprawy doktorskiej

1. Marcin Runowski, Stefan Lis, Synthesis of lanthanide doped CeF_3:Gd^{3+}, Sm^{3+} nanoparticles, exhibiting altered luminescence after hydrothermal post-treatment, **Journal of Alloys and Compounds**, 661, **2016**, 182-189 (IF = 2.999; punkty MNiSW = 35)

2. Marcin Runowski, Stefan Lis, Preparation and photophysical properties of luminescent nanoparticles based on lanthanide doped fluorides (LaF_3:Ce^{3+}, Gd^{3+}, Eu^{3+}), obtained in the presence of different surfactants, **Journal of Alloys and Compounds**, 597, **2014**, 63–71 (IF = 2.999; punkty MNiSW = 35)

3. Marcin Runowski, Sangeetha Balabhadra, Stefan Lis, Nanosized complex fluorides based on Eu^{3+} doped Sr_2LnF_7 (Ln = La, Gd), **Journal of Rare Earths**, 32, **2014**, 242–247 (IF = 1.261; punkty MNiSW = 25)

4. Marcin Runowski, Anna Ekner-Grzyb, Lucyna Mrówczyńska, Sangeetha Balabhadra, Tomasz Grzyb, Jan Paczesny, Anna Zep, Stefan Lis, Synthesis and Organic Surface Modification of Luminescent, Lanthanide-Doped Core/Shell Nanomaterials (LnF_3@SiO_2@NH_2@Organic Acid) for Potential Bioapplications: Spectroscopic, Structural, and in Vitro Cytotoxicity Evaluation, **Langmuir**, 30, **2014**, 9533–9543 (IF = 4.457; punkty MNiSW = 35)

5. Marcin Runowski, Tomasz Grzyb, Anna Zep, Paulina Krzyczkowska, Ewa Gorecka, Michael Giersig, Stefan Lis, Eu^{3+} and Tb^{3+} doped $LaPO_4$ nanorods, modified with luminescent organic compound, exhibiting tunable multicolour emission, **RSC Advances**, 4, **2014**, 46305-46312 (IF = 3.840; punkty MNiSW = 35)

6. Marcin Runowski, Krystyna Dąbrowska, Tomasz Grzyb, Paulina Miernikiewicz, Stefan Lis, Core/shell-type nanorods of Tb^{3+}-doped $LaPO_4$, modified with amine groups, revealing reduced cytotoxicity, **Journal of Nanoparticle Research**, 15, **2013**, 2068–2083 (IF = 2.184; punkty MNiSW = 30)

7. Marcin Runowski, Stefan Lis, Synthesis, surface modification/decoration of luminescent–magnetic core/shell nanomaterials, based on the lanthanide doped fluorides (Fe_3O_4/SiO_2/NH_2/PAA/LnF_3), **Journal of Luminescence**, 170, **2016**, 484-490 (IF = 2.719; punkty MNiSW = 35)

8. Agata Szczeszak, Anna Ekner-Grzyb, Marcin Runowski, Lucyna Mrówczyńska, Tomasz Grzyb, Stefan Lis, Synthesis, photophysical analysis, and in vitro cytotoxicity assessment of the multifunctional (magnetic and luminescent) core@shell nanomaterial based on lanthanide-doped orthovanadates, **Journal of Nanoparticle Research**, 17, **2015**, 143–153 (IF = 2.184; punkty MNiSW = 30)

Pozostałe publikacje

9. Tomasz Grzyb, Lucyna Mrówczyńska, Agata Szczeszak, Zbigniew Śniadecki, Marcin Runowski, Bogdan Idzikowski, Stefan Lis, Synthesis, characterization and cytotoxicity in human erythrocytes of multifunctional, magnetic and luminescent nanocrystalline rare earth fluorides, **Journal of Nanoparticle Research**, 17, **2015**, 399-416 (IF = 2.184; punkty MNiSW = 30)

10. Konrad Kubasiewicz, Marcin Runowski, Stefan Lis, Agata Szczeszak, Synthesis, structural and spectroscopic studies on $GdBO_3$:Yb^{3+}/Tb^{3+}@SiO_2 core-shell nanostructures, **Journal of Rare Earths**, 33, **2015**, 1148-1154 (IF = 1.261; punkty MNiSW = 25)

11. Andrii Shyichuk, Marcin Runowski, Stefan Lis, Jakub Kaczkowski, Andrzej Jezierski, Semiempirical and DFT computations of the influence of Tb(III) dopant on unit cell dimensions of cerium(III) fluoride, **Journal of Computational Chemistry**, 36, **2015**, 193-199 (IF = 3.589; punkty MNiSW = 35)

12. Tomasz Grzyb, Marcin Runowski, Stefan Lis, Facile synthesis, structural and spectroscopic properties of GdF_3:Ce^{3+}, Ln^{3+}(Ln^{3+} = Sm^{3+}, Eu^{3+}, Tb^{3+}, Dy^{3+}) nanocrystals with bright multicolor luminescence, **Journal of Luminescence**, 154, **2014**, 479–486 (IF = 2.719; punkty MNiSW = 35)
13. Tomasz Grzyb, Marcin Runowski, Krystyna Dąbrowska, Michael Giersig, Stefan Lis, Structural, spectroscopic and cytotoxicity studies of TbF_3@CeF_3 and TbF_3@CeF_3@SiO_2 nanocrystals, **Journal of Nanoparticle Research**, 15, **2013**, 1958–1972 (IF = 2.184; punkty MNiSW = 30)

14. Tomasz Grzyb, Marcin Runowski, Agata Szczeszak, Stefan Lis, Structural, morphological and spectroscopic properties of Eu^{3+} doped rare earth fluorides synthesized by hydrothermal

method, **Journal of Solid State Chemistry**, 200, **2013**, 76–83 (IF = 2.133; punkty MNiSW = 30)

15. Marcin Runowski, Tomasz Grzyb, Stefan Lis, Magnetic and luminescent hybrid nanomaterial based on Fe_3O_4 nanocrystals and $GdPO_4$:Eu^{3+} nanoneedles, **Journal of Nanoparticle Research**, 14, **2012**, 1188-1195 (IF = 2.184; punkty MNiSW = 30)

16. Tomasz Grzyb, Marcin Runowski, Agata Szczeszak, Stefan Lis, Influence of the matrix on the luminescent and structural properties of glycerin capped, Tb^{3+} doped fluoride nanocrystals, **Journal of Physical Chemistry C**, 116, **2012**, 17188−17196 (IF = 4.772; punkty MNiSW = 35)

17. Unusual solidification and phosphate binding to benzimidazole cations in the presence of water - Sarah E. Clifford, Marcin Runowski, Nalini Parthasarathy, Céline Besnard, Xavier Melich and Alan F. Williams - **New Journal of Chemistry**, 36, **2012**, 823–829 (IF = 3.086; punkty MNiSW = 30)

18. Marcin Runowski, Tomasz Grzyb, Stefan Lis, Bifunctional luminescent and magnetic core/shell type nanostructures Fe_3O_4@CeF_3:Tb^{3+}/SiO_2, **Journal of Rare Earths**, 29, **2011**, 1117-1122 (IF = 1.261; punkty MNiSW = 25)

Prace przeglądowe

19. Marcin Runowski, Nanotechnology – nanomaterials, nanoparticles and multifunctional core/shell type nanostructures (Nanotechnologia – nanomateriały, nanocząstki i wielofunkcyjne nanostruktury typu rdzeń/powłoka), **Chemik**, 68, **2014**, 766-775 (punkty MNiSW = 8)

Zgłoszenia patentowe

Tytuł wynalazku: "Sposób otrzymywania submikrokrystalicznego fluorku itrowo-potasowego KY_3F_{10}", autorzy: Marcin Runowski, Tomasz Grzyb. Stefan Lis, Szymon Goderski, Numer zgłoszenia: P.414738, znak: WP150/130/1/15, data zgłoszenia: 2015-11-10

Udział w konferencjach naukowych

*Najważniejsze komunikaty przedstawione na konferencjach naukowych (**łącznie: 70**)*

1. 16-19.03.2016 **Kiel, Niemcy - 18th JCF – Fruhjahrssymposium –** M. Runowski, S. Goderski, N. Stopikowska, S. Lis - Preparation of luminescent-plasmonic core/shell nanomaterials based on lanthanide and gold nanoparticles **(poster)**

2. 26-28.10.2015 **Wrocław – 4th International Conference on RARE EARTH MATERIALS (REMAT)** M. Runowski, S. Goderski, S. Lis - Synthesis of rare earth fluorides as active components of luminescent nanomaterials - ISBN: 978-83-940861-1-4 **(poster)**

3. 23-25.04.2015 **Thiruvananthapuram, Kerala, Indie – International Conference on Science, Technology and Applications of Rare Earths – ICSTAR 2015** – M. Runowski, S. Lis - Synthesis and surface modification of hybrid, luminescent nanoparticles, based on lanthanide doped fluorides - $LnF_3:X^{3+}$ (X = Sm, Eu, Tb; Ln = La, Ce, Gd) **(wystąpienie ustne)**

4. 15-17.04.2015 **Gdańsk – International Science Conference – Chemistry, Environment and Nanotechnology (CEN)** – M. Runowski, A. Zep, A. Ekner-Grzyb, T. Grzyb, S. Lis - Preparation and surface modification of multifunctional core/shell nanomaterials, doped with Ln^{3+} ions - photophysical and biological studies **(wystąpienie ustne)**

5. 25-28.03.2015 Münster, Niemcy - 17th JCF – Fruhjahrssymposium – M. Runowski, A. Zep, T. Grzyb, S. Lis - Synthesis, surface modification and photophysical studies of multifunctional, hybrid and core/shell nanomaterials **(poster)**

6. 07-08.11.2014 **Poznań – II International Scientific Conference OXYGENALIA 2014** – M. Runowski, T. Grzyb, S. Lis – Preparation of Luminescent Nanomaterials in Aqueous medium - ISBN: 978-83-7597-246-7 **(poster)**

7. 13-18.07.2014 **Wrocław – 17th International Conference on Luminescence and Optical Spectroscopy of Condensed Matter** – M. Runowski, K. Gogolewski, S. Lis – Luminescent nanomaterials based on lanthanide doped inorganic fluorides – $LnF_3:X^{3+}$ (Ln = La, Ce, Gd, Y; X = Pr, Sm, Eu) - ISBN: 978-83-60043-14-1 **(poster)**

8. 15-18.06.2014 **Poznań - 4th Summer Symposium on Nanomaterials and their application to Biology and Medicine** – M. Runowski, K. Dąbrowska, T. Grzyb, S. Lis - Preparation of luminescent core/shell type nanomaterials doped with lanthanide ions and examination of their cytotoxicity **(poster)**

9. 26-29.03.2014 **Jena, Niemcy - 16th JCF – Fruhjahrssymposium** – M. Runowski, K. Dąbrowska, A.

Zep, T. Grzyb, K. Kubasiewicz, K. Gogolewski, S. Lis – Synthesis and characterization of multifunctional luminescent nanomaterials doped with lanthanide ions – surface modification and cytotoxicity evaluation **(poster)**

10. 16-20.09.2013 **Siedlce – 56 Zjazd Naukowy Polskiego Towarzystwa Chemicznego i Stowarzyszenia Inżynierów i Techników Przemysłu Chemicznego (PTChem)** – M. Runowski, S. Balabhadra, A. Zep, T. Grzyb, K. Kubasiewicz, Stefan Lis – Synteza nieorganiczno-organicznych nanomateriałów domieszkowanych jonami lantanowców, oraz modyfikacja ich powierzchni – ISBN: 978-83-60988-15-2 **(poster)**

11. 26-28.04.2013 **Wrocław – International Conference on RARE EARTH MATERIALS (REMAT)** - M. Runowski, S. Balabhadra, S. Lis – Nanosized complex fluorides based on Eu^{3+} doped $LnSr_2F_7$ (Ln = La,Gd) **(poster)**

12. 16-20.09.2012 **Białystok – 55 PTCHEM i SITPCHEM – Zjazd Naukowy Polskiego Towarzystwa Chemicznego i Stowarzyszenia Inżynierów i Techników Przemysłu Chemicznego** – M. Runowski, T. Grzyb, K. Kubasiewicz, M. Węcławiak, S. Lis – Nanomateriały typu core/shell oparte o jony lantanowców – ISBN: 978-83-60988-12-1 **(poster)**

13. 20-24.06.2012 Poznań – **2nd Summer Symposium on Nanomaterials and their Application to Biology and Medicine** - M. Runowski, T. Grzyb, K. Kubasiewicz, S. Lis – Core/Shell type nanomaterials based on lanthanide ions **(poster)**

14. 18-21.03.**2012 Rostock, Niemcy - 14th JCF – Fruhjahrssymposium** - M. Runowski, T. Grzyb, S. Lis – Rare-earth doped nanophosphors – fabrication, physicochemical studies and applications **(poster)**

15. 18-19.11.2011 **Warszawa – (International) Marie Skłodowska-Curie Symposium on the Foundations of Physical Chemistry** - M. Runowski, T. Grzyb, S. Lis – Core/shell type nanostructures, as multifunctional nanocomposite compounds exhibiting luminescent and magnetic properties **(poster)**

16. 13-15.06.2011 **Wrocław – The Second International Conference on RARE EARTH MATERIALS (REMAT)** - M. Runowski, T. Grzyb, S. Lis – Synthesis and characterisation of core/shell type nanostructures, as multifunctional nanocomposite compounds exhibiting luminescent and magnetic properties **(poster)**

17. 23-26.03.2011 **Erlangen, Niemcy - 13th JCF – Fruhjahrssymposium** – M. Runowski, T. Grzyb, S. Lis –Synthesis and Characterisation of Core/Shell nanostructures, as Multifunctional Nanocomposite Compounds which can exhibit Luminescent and Magnetic Behaviour, Based on Spectroscopic Properties of Rare Earths Ions **(poster)**

Wstęp teoretyczny

Nanomateriały

Nanomateriał jest produktem złożonym z małych cząstek (nanocząstek), w których przynajmniej jeden wymiar jest mniejszy niż 100 nm. Dzięki małemu rozmiarowi, nanocząstki mogą tworzyć stabilne roztwory koloidalne, co jest szczególnie ważne w przypadku zastosowań medycznych takich jak obrazowanie luminescencyjne lub magnetyczne, oraz metod znakowania w kryminalistyce, biodetekcji czy w inżynierii materiałów [1–5]. Wiele nanomateriałów wykazuje zmienione właściwości fizykochemiczne w porównaniu do ich makroskopowych odpowiedników [6–8]. Zmiany te wynikają z ograniczenia kwantowego elektronów w małych nanocząstkach oraz często ze zwiększonego stosunku atomów/jonów powierzchniowych i przypowierzchniowych do tych znajdujących się wewnątrz danej cząstki (duży stosunek powierzchni do objętości). Następstwem tego jest bardzo duża powierzchnia właściwa nanomateriałów, co skutkuje zwiększeniem się ilości niewysyconych miejsc koordynacyjnych, defektów oraz naprężeń sieci krystalicznej. Dlatego też atomy i jony powierzchniowe usytuowane są w innym otoczeniu koordynacyjnym, co implikuje zmianę właściwości fizykochemicznych wielu nanomateriałów. Przykłady takich odmiennych właściwości mogą być następujące: zmienione właściwości spektroskopowe, temperatura topnienia, gęstość, rozpuszczalność, właściwości elektryczne i mechaniczne (sprężystość, tarcie, ciągliwość), zmienione napięcie powierzchniowe, inna odpowiedź na przyłożone pole magnetyczne, zmiany struktury, zwiększona aktywność katalityczna oraz cytotoksyczność (zmiany właściwości biologicznych) [8–16].

Efekty w nanoskali

Do efektów występujących w nanomateriałach, zależnych od rozmiaru cząstek można zaliczyć: ograniczenie kwantowe w półprzewodnikowych kropkach kwantowych (zmiana barwy emisji) [17], superparamagnetyzm w nanocząstkach ferro- i ferrimagnetycznych [18], dwuwykładniczy zanik luminescencji [19], oraz efekty plazmoniczne w nanocząstkach metali (zmiana barwy materiału) [20].

Ograniczenie kwantowe

Efektem występującym w nanoskali jest ograniczenie kwantowe elektronów (*quantum confinement*) występujące najczęściej w półprzewodnikach, z reguły wówczas, gdy rozmiar cząstek jest mniejszy od 10 nm, co zależy od wielkości promienia Bohra ekscytonu w danym materiale [21,22]. Nanostruktury półprzewodnikowe, w których obserwuje się to zjawisko, ograniczone w jednym wymiarze nazywane są „studniami kwantowymi" (*quantum wells*) [23], ograniczone w dwóch wymiarach to „druty kwantowe" (*quantum wires*) [24], natomiast ograniczone w trzech wymiarach to „kropki kwantowe" (*quantum dots*) [25,26]. Przykładem wspomnianego zjawiska jest wielokolorowa luminescencja kropek kwantowych. W wyniku naświetlenia promieniowaniem UV o określonej długości fali, następuje emisja w zakresie widzialnym, zależnym od rozmiaru nanocząstek tworzących dany produkt. Efekt ten jest związany ze zwiększaniem się przerwy wzbronionej w danym materiale, wraz ze zmniejszaniem się rozmiaru tworzących go cząstek. W wyniku tego mniejsze nanocząstki półprzewodnikowe, np. CdSe, CdS czy ZnO mogą wykazywać pod wpływem promieniowania UV luminescencję przesuniętą w stronę koloru niebieskiego, natomiast większe w stronę koloru czerwonego [17,27].

Plazmony powierzchniowe

Następnym przykładem zjawisk, które mogą być obserwowane w nanomateriałach jest zmiana barwy nanocząstek metali szlachetnych np. złota i srebra, które wraz ze zmniejszaniem się ich rozmiaru wykazują odmienną barwę, poczynając od niebieskiej (większe cząstki) a na czerwonej kończąc (mniejsze cząstki). Zmiana koloru takich metalicznych nanocząstek jest spowodowana rezonansową absorpcją promieniowania przez kolektywnie oscylujące powierzchniowe elektrony walencyjne, zwane plazmonami powierzchniowymi (*surface plasmons*). Skutkuje to różnicową absorpcją światła widzialnego, zależną od wielkości cząstek. Efekt ten jest silnie zależny od morfologii cząstek i pojawia się z reguły gdy ich rozmiar jest mniejszy od 150 nm [20,28]. Jeżeli jednak nanocząstki będą za małe lub zbyt duże wówczas mogą wykazywać absorpcję odpowiednio jedynie w ultrafioletowej lub podczerwonej części zakresu spektralnego, w wyniku czego stają się bezbarwne, a utworzony z nich koloid może być przeźroczysty.

Superparamagnetyzm

Superparamagnetyzm jest formą magnetyzmu występującą w materiałach ferromagnetycznych i ferrimagnetycznych, w przypadku, gdy rozmiar tworzących je cząstek zostanie zmniejszony do nanoskali, z reguły do około kilkunastu lub kilkudziesięciu nanometrów. Krytyczny rozmiar warunkujący pojawienie superparamagnetyzmu zależy od rodzaju materiału, a dokładnie od wartości jego anizotropii magnetycznej, która z kolei zależny od składu chemicznego, struktury krystalicznej i morfologii produktu. Materiały superparamagnetyczne nie wykazują zjawiska remanencji (pomagnetyzacji która pozostaje po odjęciu zewnętrznego pola magnetycznego), a ich koercja jest zerowa, czyli wartość pola magnetycznego potrzebna do całkowitego zredukowania pozostałej magnetyzacji. Skutkuje to powstaniem „granicy superparamagnetycznej". Po wyłączeniu pola magnetyczne działającego na taki materiał, tworzące go nanocząstki tracą magnetyzację z powodu uśrednienia się ich momentów magnetycznych (każde ziarno składa się w takim przypadku tylko z jednej domeny magnetycznej) spowodowanego energią cieplną [18,29]. Dobrym przykładem mogą być nanocząstki magnetytu - Fe_3O_4, które stają się superparamagnetyczne po osiągnięciu rozmiarów mniejszych niż ≈ 12 nm. Warto dodać, że wspomniana „granica superparamagnetyczna" determinuje również maksymalną pojemność nośników danych opartych o pamięci magnetyczne.

Toksyczność nanocząstek

Obecnie kluczowym problemem jest kwestia toksyczności nanocząstek. Ze względu na fakt, że nanomateriały charakteryzują się często odmiennymi właściwościami w porównaniu do ich makroskopowych odpowiedników, wpływa to również na ich właściwości biologiczne. Niestety, zmiana właściwości biologicznych nanomateriałów jest często niepożądana w przypadku zastosowań medycznych, z powodu częstej wysokiej cytotoksyczności małych nanocząstek. Materiały zazwyczaj obojętne dla organizmów żywych, mogą wykazywać znaczny wzrost cytotoksyczności, gdy zmniejszony zostanie rozmiar tworzących je cząstek do skali nanometrycznej [15,16]. Toksyczność ta może być na przykład spowodowana zwiększonym uwalnianiem się jonów metali ciężkich z powierzchni nanocząstek, co obserwuje się w przypadku kropek kwantowych takich jak CdSe, CdTe czy PbS [30,31]. Cytotoksyczność nanomateriałów może być również związana z porowatością nanocząstek, ich tendencją do aglomeracji, zwiększonym

powinowactwem chemicznym do różnych struktur biologicznych oraz zwiększoną reaktywnością chemiczną ich powierzchni [32,33]. Ważną rolę odgrywają też czynniki fizyczne i mechaniczne, tj. rozmiar porównywalny lub mniejszy od struktur biologicznych. Nanocząstki mogą tworzyć stabilne zawiesiny w powietrzu, przez co tworzą się szkodliwe pyły, które inhalowane przez ludzi, mogą powodować pylicę oraz raka płuc [34,35]. Ze względu na bardzo mały rozmiar, niektóre nanocząstki mogą zostać wchłonięte na drodze endocytozy przez komórki organizmów żywych oraz kumulować się w wyniku przyłączania się do białek, błon komórkowych i innych struktur biologicznych [33]. Procesy te mogą powodować uszkodzenia komórek i tkanek wskutek zwiększonego poziomu stresu oksydacyjnego, blokowania kanałów jonowych lub mechanicznego uszkodzenie błony komórkowej i innych organelli [36,37]. Czynniki takie mogą także zaburzać proliferację komórek, w wyniku czego następuje ich obumieranie lub niekontrolowany wzrost, prowadzący do powstawania zmian nowotworowych [38].

Nanomateriały funkcjonalne

Nanomateriały hybrydowe złożone są z nanometrycznej części nieorganicznej połączonej z odpowiednią fazą organiczną. **Nanokompozyty** są to materiały stałe zawierające dwie lub więcej faz, w których przynajmniej jedna faza ma wymiary nanometryczne lub uporządkowaną w nanoskali strukturę (np. materiały nanoporowate). **Nanostruktury typu rdzeń/powłoka (ang. *core/shell*)** złożone są z nanometrycznego rdzenia pokrytego odpowiednią nanopowłoką (ochronną lub funkcjonalną), co czyni je materiałami wielofunkcyjnymi, wykazującymi jednocześnie właściwości charakterystyczne dla rdzenia i powłoki. Jednoczesna obecność wielu pożądanych właściwości fizykochemicznych i biologicznych powoduje, że wymienione nanostruktury stanowią nową klasę materiałów wielofunkcjonalnych i biomateriałów, które mogą znacząco wpłynąć na rozwój inżynierii materiałów, nanomedycyny i nanotechnologii [39][40][41].

Nanostruktury typu core/shell

Nanostruktury typu rdzeń/powłoka (*core/shell*) złożone są z co najmniej dwóch różnych faz o odmiennym składzie chemicznym lub o innej strukturze krystalicznej. Dzięki ich specyficznej budowie materiały takie są wielofunkcyjne, gdyż wykazują

jednocześnie właściwości rdzenia i powłoki. Rys. 1 przedstawia schemat budowy nanostruktur typu core/shell.

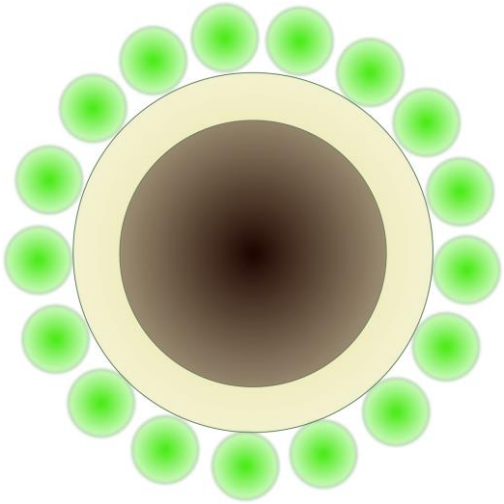

Rys. 1 Schemat budowy nanostruktur typu core/shell.

Środek danej struktury stanowi zwykle nieorganiczny nanordzeń pokryty jedną lub wieloma powłokami o odmiennych właściwościach chemicznych i/lub fizycznych. W zależności od pożądanego zastosowania finalnego produktu, rdzeń taki może być oparty o nanocząstki magnetyczne, np. Fe_3O_4 (magnetyt), wykazywać właściwości luminescencyjne, jak np. półprzewodnikowe kropki kwantowe typu ZnO, CdSe [42,43] czy nanokrystaliczne luminofory domieszkowane jonami Ln^{3+}, np. $CeF_3:Ln^{3+}$, $LaF_3:Ln^{3+}$, $LaPO_4:Ln^{3+}$, $GdVO_4:Ln^{3+}$ (Ln = Sm, Eu, Tb, Yb, Er) [19,44–46], lub też wykazywać inne pożądane właściwości. Natomiast powłoka, może być: polimerem organicznym [47,48]; obojętnym chemicznie, amorficznym związkiem nieorganicznym jak np. TiO_2 czy SiO_2 [44,45,49]; lub też składać się z nanokryształów luminescencyjnych [50–52].

Właściwości magnetyczne nanomateriałów z reguły bazują na użyciu nanokrystalicznych ferromagnetyków lub ferrimagnetyków [53]. Nanostruktury typu core/shell mające rdzeń magnetyczny jak np. Fe_3O_4/SiO_2 mogą zostać wykorzystane jako związki oczyszczające wodę i inne media zawierające jony metali ciężkich takich jak Cd^{2+}, Hg^{2+} czy Pb^{2+} [54]. Usunięcie ich jest możliwe dzięki znacznemu powinowactwu odpowiednio sfunkcjonalizowanej powłoki do jonów metali ciężkich. Poprzez odpowiednie manipulowanie polem magnetycznym, nanocząstki o właściwie zmodyfikowanej powierzchni mogą wiązać się do błony komórkowej bakterii i wirusów lub przyłączać się do wybranych komórek w organizmie, które zostały chorobowo

zmienione [55]. Następnie możliwe jest usunięcie takich połączeń z danego organizmu lub selektywne zniszczenie niepożądanych komórek (hipertermia). Małe superparamagnetyczne nanocząstki magnetytu stosowane są również jako środki kontrastowe w obrazowaniu rezonansu magnetycznego, MRI (*Magnetic Resonance Imaging*) [56].

Właściwości kontrastowe i stabilność nanostruktur typu rdzeń/powłoka mogą dodatkowo zostać zwiększone, poprzez odpowiednią modyfikację powierzchni, tj. pokrycie ich odpowiednią powłoką ochronną i/lub funkcjonalną. Przy zastosowaniu powłoki luminescencyjnej, możliwe jest uzyskanie wielofunkcyjnych nanomateriałów luminescencyjno-magnetycznych. Materiały takie można potencjalnie zastosować w multimodalnym obrazowaniu struktur biologicznych, tj. komórek i tkanek.

Metody otrzymywania nanostruktur typu core/shell

Istnieje wiele metod otrzymywania nanostruktur typu core/shell. Najczęściej stosowane polegają na wytrącaniu pożądanego związku o charakterze powłoki na powierzchni rdzenia, pokryciu rdzenia cząsteczkami modyfikatora organicznego w roztworze na drodze oddziaływań elektrostatycznych lub kowalencyjnych, utlenianiu lub redukcji powierzchni, etc. Często stosowane są również metody typu zol-żel, takie jak metoda Stöbera [57]. Metoda ta polega na hydrolizie odpowiednich pochodnych silanowych, które są prekursorami powłoki i ich późniejszej kondensacji na powierzchni rdzenia, który został uprzednio odpowiednio zdyspergowany w roztworze reakcyjnym, z reguły przy użyciu ultradźwięków.

Właściwości nanopowłoki i modyfikacja powierzchni

Ze względu na fakt, że małe nanocząstki mają duży stosunek powierzchni do objętości, są zatem bardzo wrażliwe na działanie czynników agresywnych, zmianę pH, procesy redox oraz inny wpływ środowiska zewnętrznego. Stąd też, aby uniknąć rozkładu danego produktu lub utraty jego właściwości fizykochemicznych, pokrywa się go zewnętrzną powłoką ochronną, co powoduje utworzenie się omawianych nanostruktur typu core/shell [58,59]. Powłoka ta może być obojętna lub aktywna w stosunku do określonych ugrupowań chemicznych, jak również może zostać zmodyfikowana w pożądany sposób, który zależy od późniejszych zastosowań. Często prowadzi się modyfikacje powłok poprzez sprzęganie ich z innymi biologicznie czynnymi molekułami organicznymi o

charakterze linkerów, antygenów i innych struktur organicznych, dla zaawansowanych aplikacji biologicznych [47,60]. Modyfikacja może zachodzić wskutek utworzenia się trwałego wiązania kowalencyjnego, np. $-Si-(CH_2)_3-NH_2$ [44,61], oddziaływań elektrostatycznych lub sił Van der Waalsa [62]. Tak sfunkcjonalizowane nanostruktury typu core/shell mogą wykazywać selektywne powinowactwo do określonych ugrupowań chemicznych i miejsc aktywnych w komórce, dzięki czemu możliwe jest zastosowanie ich w nowoczesnych terapiach celowanych, jako nośniki leków lub biomarkery [63]. Następstwem modyfikacji powierzchni może być również zmiana właściwości biologicznych danych nanocząstek, np. zmniejszenie się ich cytotoksyczności [44,64].

Znane są również nanostruktury typu yolk/shell, które są podobne do struktur typu core/shell. Takie struktury charakteryzują się tzw. „pustym rdzeniem". Można je otrzymać już w czasie syntezy lub też w wyniku odpowiedniej modyfikacji po syntezie. Takie nanostruktury typu yolk/shell mogą potencjalnie znaleźć zastosowanie jako nowoczesne, bardzo wydajne i selektywne nośniki leków w terapiach celowanych (lek jest zamknięty w pustym rdzeniu i uwalniany selektywnie dopiero w pożądanym miejscu).

Reasumując, zaawansowane nanostruktury typu rdzeń/powłoka - core/shell są nową klasą materiałów kompozytowych o unikatowych właściwościach. Ich wielofunkcyjność wynika z połączenia w jednym materiale właściwości rdzenia i powłoki. Takie wielofunkcyjne nanomateriały mogą na przykład jednocześnie wykazywać wielobarwną i/lub przestrajalną luminescencję oraz właściwości magnetyczne (odpowiedź na przyłożone zewnętrzne pole magnetyczne). Nanomateriały typu core/shell, dzięki swej wielofunkcyjności i biokompatybilności mogą zostać potencjalnie wykorzystane do obrazowania multimodalnego i detekcji rozmaitych struktur nieorganicznych i organicznych oraz ich jednoczesnej separacji magnetycznej. Dzięki wspomnianym właściwościom, materiały te mają liczne możliwości aplikacyjne i mogą zostać wykorzystane w wielu dziedzinach nauki i przemysłu, np. w medycynie, biologii, inżynierii materiałów, nanobioinżynierii, kryminalistyce oraz w przemyśle materiałów funkcjonalnych i materiałów codziennego użytku.

Metody syntezy nanomateriałów

Istnieją dwie odmienne strategie otrzymywania nanomateriałów, a mianowicie typu „top-down" i „bottom-up" [10,65]. Metody typu top-down polegają na rozdrabnianiu materiałów litych do nanocząstek (np. rozdrabnianie w młynach kulowych i litografia). Są stosowane w przemyśle, jednak często dostarczają produktów o zdefektowanych, polidyspersyjnych cząstkach. Metody typu bottom-up polegają na tworzeniu się klasterów z pojedynczych atomów/jonów i ich kontrolowanym wzroście do nanocząstek. Polegają one na otrzymywaniu nanomateriałów na drodze syntezy chemicznej, jak również dzięki wykorzystaniu odpowiednich procesów fizycznych. Do metod typu „bottom-up" można zaliczyć: współstrącanie nanocząstek w roztworach, nanoszenie prekursorów/produktów warstwa po warstwie (technika Langmuira-Blodgetta), powierzchniowa wymiana redox, napylanie w próżni, metody kondensacji w fazie ciekłej lub gazowej, rozkład prekursorów organicznych, synteza w warunkach hydrotermalnych, hydroliza reagentów i ich późniejsza kondensacja, itp. Metodami tymi można otrzymać zaawansowane, monodyspersyjne nanostruktury (np. typu rdzeń/powłoka, nanokompozyty i materiały hybrydowe), o dużym stopniu krystaliczności i odpowiednio zmodyfikowanej powierzchni. Poniżej przedstawiono schemat syntezy nanocząstek metodami „top-down" i „bottom-up" (Rys. 2).

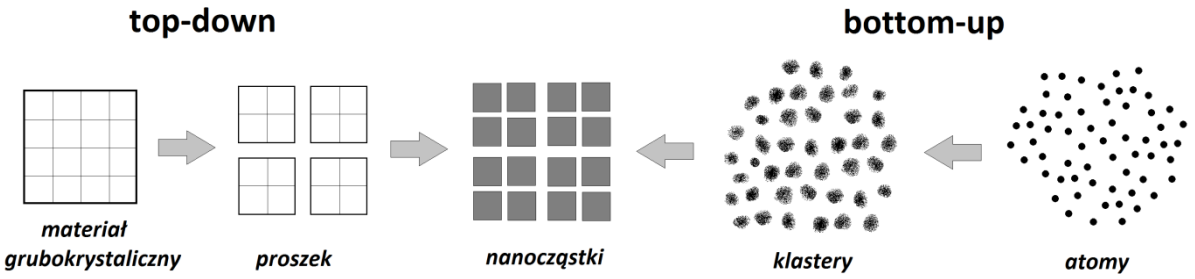

Rys. 2 Schemat syntezy nanocząstek metodami typu „top-down" i „bottom-up".

Metody analizy właściwości nanomateriałów

Właściwości nanomateriałów mogą być badane przy użyciu następujących metod:

- *Dyfrakcja promieniowania rentgenowskiego (XRD)* – identyfikacja struktury produktu, wyznaczenie parametrów komórki elementarnej, określenie stopnia krystaliczności produktu oraz oszacowanie wielkości krystalitów na podstawie równania Scherrer'a;
- *Transmisyjna i skaningowa mikroskopia elektronowa (TEM i SEM)* – obrazowanie struktury, morfologii oraz rozmiaru cząstek, wraz z określeniem stopnia ich jednorodności, agregacji i aglomeracji;
- *Analiza rozpraszania promieniowania rentgenowskiego (EDX) oraz spektroskopia strat energii elektronów (EELS)* – analiza, mapowanie składu i rozmieszczenia pierwiastków w strukturze materiału;
- *Analiza elementarna* – określenie składu pierwiastkowego próbki;
- *Spektrofluorometria* – pomiary widm emisji/wzbudzenia, krzywych zaniku luminescencji, obliczenie emisyjnych czasów życia, wyznaczenie wydajności kwantowej luminescencji;
- *Spektroskopia w podczerwieni (FT-IR)* – analiza struktury i składu produktów, detekcja organicznych modyfikatorów powierzchni nanocząstek;
- *Spektroskopia UV-Vis* – pomiar widm absorpcji koloidalnych nanocząstek;
- Dynamiczne i elektroforetyczne rozpraszanie światła (DLS i ELS) – określenie rozkładu wielkości cząstek koloidalnych na podstawie pomiarów ich wielkości hydrodynamicznych; pomiary uśrednionego ładunku powierzchniowego cząstek, tj. zeta-potencjału;
- *Powierzchniowo wzmocniona Spektroskopia Ramana (SERS)* – analiza struktury wybranych związków organicznych zaadsorbowanych na powierzchni nanomateriałów luminescencyjno-plazmonicznych;
- *Pomiary właściwości powierzchniowych* – analiza wielkości powierzchni właściwej i porowatości materiałów.

Luminescencja

Promieniowanie elektromagnetyczne może oddziaływać z materią na wiele sposobów. Do najbardziej znanych należy absorpcja i rozpraszanie światła. Rozpraszanie światła, możemy z kolei podzielić na elastyczne, tzw. rozpraszanie Rayleigha oraz nieelastyczne, tzw. rozpraszanie Ramana. Zjawiska absorpcji światła oraz następującej po nim relaksacji promienistej, zostaną szerzej omówione w tej pracy. Według rozkładu Boltzmanna większość elektronów w związkach chemicznych znajduje się w stanie podstawowym, zatem proces absorpcji może być opisany jako wzbudzenie elektronu ze stanu podstawowego (o mniejszej energii) do stanu wzbudzonego (o większej energii). Elektron może powrócić do swojego stanu podstawowego na drodze wielu różnych mechanizmów. Relaksacja bezpromienista (wygaszanie fononowe elektronu, tj. na drodze drgań cieplnych sieci krystalicznej) jest najbardziej powszechnym i jednocześnie niepożądanym procesem wygaszania luminescencji. Innymi procesami bezpromienistymi są przejście międzysystemowe, ISC (*Inter System Crossing*), przeniesienie ładunku, CT (*Charge Transfer*) oraz przeniesienie energii, ET (*Energy Transfer*). Relaksacja promienista, tj. luminescencja zachodzi na drodze powrotu elektronu ze stanu wzbudzonego do jego stanu podstawowego, czemu towarzyszy emisja fotonów (emisja światła). Jeśli wspomniany proces zachodzi bez zmiany multipletowości układu, to taki proces nazywamy fluorescencją. Natomiast, gdy następuje zmiana multipletowości, proces ten nazywamy fosforescencją. Z punktu widzenia reguł wyboru, fluorescencja jest procesem dozwolonym, gdyż zachodzi bez zmiany spinowego momentu pędu elektronu. Natomiast fosforescencja jest procesem wzbronionym, któremu towarzyszy zmiana spinowego momentu pędu elektronu. Skutkiem tego, związki wykazujące fluorescencję odznaczają się z reguły bardzo krótkimi czasami życia stanów wzbudzonych, rzędu nanosekund. Natomiast, układy wykazujące fosforescencję wykazują z reguły długie czasy życia stanów wzbudzonych, przeważnie w zakresie mikrosekund lub milisekund, a w przypadku niektórych układów sekund, minut a nawet godzin.

Właściwości luminescencyjne jonów Ln^{3+}

W przypadku układów gdzie aktywatorem jest jon lantanowca, proces emisji promienistej nazywamy ogólnie luminescencją, gdyż związany jest z przejściami elektronu pomiędzy wyższymi stanami wzbudzonymi, poziomami energetycznymi o różnej

multipletowości (termy elektronowe). W układach opartych o luminescencję jonów lantanowców, absorpcja jak i emisja promieniowania elektromagnetycznego związana jest głównie z przejściami elektronowymi w obrębie wewnętrznej podpowłoki 4f. Przejścia takie nazywane są przejściami typu 4f-4f. Elektrony znajdujące się na podpowłoce 4f są ekranowane (chronione) od zewnętrznego otoczenia przez elektrony podpowłok 5s i 5p. W wyniku wspomnianego ekranowania, pasma na widmach absorpcyjnych i emisyjnych związków zawierających jony lantanowców (Ln^{3+}) są z reguły wąskie i o dyskretnej strukturze. Energia poziomów energetycznych 4f jest tylko w bardzo niewielkim stopniu zależna od otoczenia koordynacyjnego jonu Ln^{3+}, tj. ligandów, przeciwjonów i innych cząsteczek obecnych w sferze koordynacyjnej. Ze względu na obecność wielu elektronów 4f, struktura poziomów energetycznych jonów Ln^{3+} jest bardzo skomplikowana, a podstawowe poziomy energetyczne są rozszczepione, tworząc liczne nowe termy elektronowe. Istnieją trzy główne czynniki mające wpływ na rozszczepienie poziomów energetycznych jonów Ln^{3+}, tj. odpychanie elektronowe > sprzężenie spinowo-orbitalne > wpływ pola krystalicznego (uszeregowane zgodnie z malejącym wpływem na poziomy energetyczne jonów Ln^{3+}). Jak widać odpychanie elektronowe ma największy wpływ na omawiane rozszczepienie, natomiast wpływ pola krystalicznego (ligandów) jest minimalny, co związane jest ze wspomnianym wcześniej ekranowaniem elektronów 4f. Odwrotnie jest w przypadku pierwiastków bloku d, gdzie na energię poziomów energetycznych elektronów 3d, 4d i 5d dominujący wpływ ma zewnętrze pole krystaliczne, otoczenie koordynacyjne (efekt ekranowania jest w ich przypadku minimalny).

Przejścia 4f-4f w jonach Ln^{3+} są wzbronione przez reguły wyboru i charakteryzują się małym molowy współczynnikiem absorpcji, skutkuje to więc niską wydajnością generowanej w ten sposób luminescencji. Aby zwiększyć efektywność luminescencji układów opartych o jony Ln^{3+}, stosuje się w nich efekty umożliwiające przeniesienie energii i przeniesienie ładunku. Przeniesienie energii może zachodzić w związkach kompleksowych, których ligandy charakteryzują się obecnością wzbudzonych stanów trypletowych o wyższej energii niż najniżej położone stany wzbudzone skompleksowanych jonów Ln^{3+}. Przeniesienie energii może zachodzi również pomiędzy dwoma jonami Ln^{3+}, np. w układzie $Ce^{3+}\rightarrow Tb^{3+}$, gdzie jon Ce^{3+} efektywnie absorbuje energię wzbudzenia w zakresie UV (≈ 250 nm), któremu towarzyszy dozwolone przejście elektronowe typu f-d [66]. Następnie, energia jest przekazywana do jonu aktywatora luminescencji, tj. jonu Tb^{3+} i emitowana w formie światła zielonego [67]. Podobna sytuacja ma miejsce w przypadku pary jonów $Gd^{3+}\rightarrow Eu^{3+}$, gdzie energia przekazywana

jest od jonu Gd^{3+} do jonu Eu^{3+} i emitowana w formie światła czerwonego [67,68]. Należy pamiętać, iż aby opisywane zjawisko przeniesienia energii było efektywne i zachodziło z dużą wydajnością, całki nakładania donora i akceptora musza się wzajemnie pokrywać, natomiast przerwa energetyczna pomiędzy stanami wzbudzonymi poszczególnych jonów musi być niewielka. Zjawisko przeniesienia ładunku można obserwować na przykład w tlenkach i nieorganicznych solach kwasów tlenowych domieszkowanych jonami lantanowców, np. $Y_2O_3:Eu^{3+}$, $LaPO_4:Eu^{3+}$ czy $GdVO_4:Eu^{3+}$ [41,51]. W tego typu układach występuje możliwość przeniesienia ładunku (elektronu) od anionu tlenkowego do jonu Eu^{3+}, skutkujące efektywną luminescencją takich układów [69].

W przypadku lantanowców, luminescencja zachodzi z reguły w układach domieszkowanych trójdodatnimi jonami Ln^{3+}, takimi jak Pr^{3+}, Sm^{3+}, Eu^{3+}, Tb^{3+}, Dy^{3+}, Ho^{3+} , Er^{3+} i Tm^{3+}. Jednak również niektóre jony dwudodatnie takie jak Sm^{2+} czy Eu^{2+} wykazują po wzbudzeniu emisję w zakresie widzialnym.

Charakter przejść elektronowych w jonach Ln^{3+}

Za luminescencję jonów lantanowców odpowiadają głównie przejścia elektronowe typu dipola magnetycznego oraz dipola elektrycznego. Przejścia dipola magnetycznego są nieczułe na zmianę symetrii lokalnego otoczenia koordynacyjnego danego jonu. Przykładem tego może być zielona luminescencja jonu Tb^{3+} związana głównie z przejściami $^5D_4 \rightarrow {}^7F_J$ (J = 6 – 3) [66]. Natomiast przejścia dipola elektrycznego są wrażliwe na zmianę symetrii lokalnego otoczenia koordynacyjnego danego jonu. Dobrym przykładem występowania tego typu przejść jest jon Eu^{3+}, wykorzystywany jako sonda strukturalna w różnych układach, ze względu na bardzo zbliżoną wielkość jego promienia jonowego oraz podobieństwo we właściwościach chemicznych do jonów Ca^{2+} i Mg^{2+}, co ma kluczowe znaczenia w wielu bioaplikacjach [70,71]. Czerwono-pomarańczowa luminescencja jonu Eu^{3+} związana jest głównie z występowaniem przejść $^5D_0 \rightarrow {}^7F_0$ (przejście pseudo-kwadrupola elektrycznego); $^5D_0 \rightarrow {}^7F_1$, $^5D_0 \rightarrow {}^7F_3$ (przejścia dipola magnetycznego); $^5D_0 \rightarrow {}^7F_2$, $^5D_0 \rightarrow {}^7F_4$ (przejścia dipola elektrycznego) [72]. W badaniach zmian symetrii lokalnego otoczenia koordynacyjnego w układach zawierających jon Eu^{3+}, porównuje się stosunek zintegrowanej intensywności pasma związanego z przejściem nadczułym $^5D_0 \rightarrow {}^7F_2$ (*hypersensitive transition*; przejście bardzo czułe na symetrię), do intensywności pasma związanego z przejściem $^5D_0 \rightarrow {}^7F_1$ (przejście nieczułe na symetrię). Wartość ta zwana jest parametrem asymetrii. Układy (kompleksy, niektóre sole nieorganiczne i organiczne) wykazujące dużą intensywność pasma związanego z

przejściem $^5D_0 \rightarrow {}^7F_2$ jonu Eu^{3+}, odznaczają się niską symetrią lokalnego otoczenia koordynacyjnego. Warto nadmienić, iż w jonie Eu^{3+} można obserwować przejście 0-0, czyli wspomniane przejście $^5D_0 \rightarrow {}^7F_0$ [70]. Takiego przejścia nie obserwuje się w przypadku innych jonów, gdyż jest ono wysoce wzbronione przez reguły wyboru. W jonie Eu^{3+} przejście to staje się częściowo dozwolone w układach niecentrosymetrycznych, z powodu silnego sprzężenia spinowo-orbitalnego. Dekonwolucja tego pasma pozwala na określenie liczby różnych otoczeń koordynacyjnych jonu Eu^{3+} występujących w danym układzie. Możliwe jest to dzięki temu, iż liczba pasm powstałych po dekonwolucji jest związana z ilością form specjacyjnych jonu Eu^{3+} [73].

Nanomateriały luminescencyjne domieszkowane jonami lantanowców (Ln^{3+})

Jak już wcześniej wspomniano, luminescencja jest emisją światła powstałą w wyniku wzbudzenia elektronów danego materiału promieniowaniem o odpowiedniej długości fali (UV, Vis, IR) i ich późniejszą relaksacją promienistą do stanów podstawowych. Nanostruktury wykazujące intensywną luminescencję są szeroko badane ze względu na ich obiecujące możliwości zastosowań w wielu dziedzinach nauki i przemysłu. W przeszłości używano głównie luminoforów organicznych, które wykazują dużą wartość molowego współczynnika absorpcji. Jednakże, takie luminofory organiczne mają wiele wad, tj. ulegają fotodegradacji, wykazując obniżenie intensywności luminescencji w czasie świecenia, niewielkie przesunięcie Stokesa oraz bardzo krótkie radiacyjne czasy życia. Krótkie czasy życia luminescencji (rzędu nanosekund) są niepożądane w przypadku zastosowania luminoforów w technikach bioobrazowania, gdyż ich sygnał może być łatwo zakłócony fluorescencją tła struktur biologicznych. Dlatego też obserwuje się ostatnio zwiększone zainteresowanie półprzewodnikowymi kropkami kwantowymi. Nanostrukturalne kropki kwantowe są odporne na fotodegradację i wysokie temperatury oraz mogą wykazywać intensywną luminescencję charakteryzującą się znacznymi przesunięciami Stokesa i wąskimi pasmami emisyjnymi. Niestety, okazało się, że takie bardzo małe (z reguły ≤ 10 nm) cząstki oparte o jony metali ciężkich są często toksyczne w stosunku do organizmów żywych [30,31].

Optymalną grupą luminoforów wydają się być nieorganiczne, trudno rozpuszczalne sole pierwiastków ziem rzadkich, takie jak: fluorki, tlenofluorki, fosforany, wanadany, borany, etc. Pierwiastki ziem rzadkich mogą występować zarówno jako jony matrycy i domieszki w takich strukturach. Związki te mogą być względnie łatwo zsyntetyzowane w

nanoskali i domieszkowane pożądanymi jonami Ln^{3+}, zyskując wówczas miano nanoluminoforów. Tego typu luminescencyjne nanomateriały domieszkowane jonami Ln^{3+} charakteryzują się wielobarwną emisją (zależną od jonu aktywatora, np. Tb^{3+} - zielony, Eu^{3+} - czerwony), długimi czasami świecenia (rządu milisekund), dużymi przesunięciami Stokesa, wąskimi pasmami emisyjnymi, dużą odpornością fotochemiczną i termiczną, wysoką stabilnością tworzonych koloidów wodnych oraz niską cytotoksycznością [66,71,72,74,75], dzięki czemu mogą być potencjalnie zastosowane w rozmaitych aplikacjach biologicznych. Luminofory oparte o jony pierwiastków ziem rzadkich wykorzystywane są w wyświetlaczach plazmowych [76], systemach detekcyjnych [77], optoelektronice [78], biomarkerach [79], technikach oświetleniowych [76], znakowaniu luminescencyjnym [80] oraz jako luminescencyjne rdzenie w nanostrukturach typu rdzeń/powłoka [19,44].

Nanocząstki oparte o jony Ln^{3+} mogą wykazywać efekty nano-rozmiarowe, np. dwuwykładniczy zanik luminescencji, zmienioną intensywność emisji i wydajność kwantową, przestrajalny kolor emisji, etc. [81] Wiele nanomateriałów domieszkowanych jonami Ln^{3+} wykazuje skrócony czas życia luminescencji związany z jonami powierzchniowymi (zwiększone wygaszanie przez cząsteczki wody i powierzchniowe związki organiczne), co może powodować obserwowany, wspomniany uprzednio dwuwykładniczy zanik ich emisji. Efekty te można często zaobserwować w nanokrystalicznych fluorkach i fosforanach lantanowców. Zaletami obu tego rodzaju struktur jest duża łatwość otrzymania ich w formie bardzo małych sferycznych nanocząstek (fluorki) i wydłużonych nanodrutów, nanopręt̨ów lub nanoigieł (fosforany). Struktury te są stabilne i odporne na działanie czynników zewnętrznych, jak również wykazują intensywną luminescencję po domieszkowaniu odpowiednim jonem Ln^{3+}. Cechą charakterystyczną fluorków lantanowców jest niska energia fononów ich sieci krystalicznej (≈ 350-400 cm^{-1}) [82], dzięki czemu drgania termiczne sieci krystalicznej tylko w niewielkim stopniu wpływają na obniżenie intensywności luminescencji, na drodze wygaszania bezpromienistego. Fosforany natomiast mogą odznaczać się dużym stosunkiem długości do szerokości (*high aspect ratio*), z powodu swojej podłużnej morfologii, co może mieć wpływ na ich właściwości luminescencyjne, elektryczne, magnetyczne oraz aktywność biologiczną.

Metody syntezy nanomateriałów użyte w pracy doktorskiej

- **Współstrącanie** (*coprecipitation*) – polegające na stopniowym mieszaniu (wkraplanie) dwóch lub więcej roztworów zawierających odpowiednie kationy (np. La^{3+}, Gd^{3+}, Eu^{3+}) i aniony (np. PO_4^{3-}, F^-), po czym następuje wytrącenie produktu z roztworu.

- **Metody micelarne** - polegają na wykorzystaniu w syntezie nanomateriałów jonowych albo niejonowych surfaktantów lub innych związków organicznych o budowie amfifilowej, pozwalających na kontrolowany wzrost nanocząstek. Dodając wybranych surfaktantów do roztworu podczas syntezy, można wpływać na strukturę, morfologię i stopień aglomeracji cząstek.

- **Metoda hydrotermalna** – poddanie warunkom hydrotermalnym, tj. wysokiej temperaturze (150-300^oC) i podwyższonemu ciśnieniu (10-100 bar) wcześniej otrzymanego produktu lub krystalizacja *in-situ* nanokryształów. Metoda zapewnia wysoką krystaliczność produktów, co skutkuje intensywną emisją powstałych nanoluminoforów.

- **Synteza w mikroemulsji** – jest metodą polegającą na zmieszaniu, w odpowiednich proporcjach molowych fazy organicznej, wodnej, surfaktantu i ko-surfaktantu, zapewnia to odpowiednie wzajemne wymieszanie tych układów. W porównaniu do zwykłej emulsji, mikroemulsja jest termodynamicznie stabilna i pozwala na otrzymanie monodyspersyjnych nanocząstek. Synteza nanocząstek odbywa się tu w powstałych tzw. „nanoreaktorach" micelarnych, które przez ograniczony rozmiar zapobiegają nadmiernemu wzrostowi nanocząstek, zapewniając jednocześnie ich monodyspersyjność.

- **Metoda Stöbera –** polega na hydrolizie i późniejszej kondensacji pochodnych silanowych w środowisku wodno-etanolowym, co prowadzi do utworzenia się cząstek krzemionki [57]. W reakcji tej tetraetoksysilan (TEOS) jest źródłem krzemionki. Podczas, gdy dodatki innych pochodnych silanowych takich jak 3-aminopropylotrietoksysilan (APTES), N-(trimethoxysilylpropyl)ethylenediamine triacetic acid (EDATAS) lub na przykład 3-mercaptopropylotrimetoksysilan (MPTMS) skutkują wprowadzeniem do struktury krzemionki odpowiednio grup aminowych $–NH_2$, karboksylowych -COOH lub tiolowych –SH. Jeśli w roztworze dodatkowo obecne są cząstki stałe (np. nanocząstki lantanowców), to możliwe jest utworzenie na ich powierzchni nanopowłoki krzemionkowej, co prowadzi do powstania nanostruktur typu core/shell.

Najważniejsze metody charakterystyki nanomateriałów użyte w pracy doktorskiej

Dyfraktometria proszkowa - XRD (X-Ray Diffraction)

Metoda ta polega na dyfrakcji wiązki promieni rentgenowskich na płaszczyznach sieciowych badanych substancji krystalicznych. W wyniku tego procesu uzyskujemy zbiór refleksów (pików), przedstawiany w formie wykresu (dyfraktogramu) zależności intensywności od kąta odbłysku 2Θ. Dzięki temu możliwe jest zidentyfikowanie struktury otrzymanego związku poprzez porównanie otrzymanego dyfraktogramu z odpowiednim wzorcem z bazy danych. Intensywność poszczególnych refleksów jest związana ze stopniem krystaliczności produktu oraz, niekiedy, preferowanym kierunkiem wzrostu krystalitów. W przypadku materiałów domieszkowanych jonami o promieniach mniejszych lub większych od promieni jonów matrycy, obserwuje się przesunięcie refleksów w stronę większych lub mniejszych wartości kąta 2Θ. Zależność ta umożliwia obliczenie parametrów komórki elementarnej analizowanej struktury. W przypadku substancji nanokrystalicznych, obserwuje się również znaczące poszerzenie refleksów, wynikające z ograniczonej liczby płaszczyzn sieciowych w kryształach, na których odbywa się dyfrakcja wiązki promieni rentgenowskich. Dzięki temu zjawisku, można oszacować średnią wielkość krystalitów tworzących dany produkt, korzystając z równania Scherrer'a [83]. Wiarygodne wartości uzyskuje się dla cząstek mniejszych niż 100 nm. Równanie to przyjmuje postać:

$$D = \frac{k\,\lambda}{\cos\theta\sqrt{\beta^2 - \beta'^2}}$$

D – uśredniony rozmiar krystalitów

K – współczynnik kształtu (≈ 0.9 dla cząstek sferycznych)

λ – długość fali promieniowania

θ – kąt odbłysku

β – szerokość refleksu w połowie jego wysokości

β' – efekt aparaturowy

Transmisyjna mikroskopia elektronowa – TEM (Transmission Electron microscopy)

Technika ta służy do obrazowani struktury i morfologii oraz wyznaczenia rozmiaru cząstek. Pozwala również na określenie stopnia jednorodności, agregacji i aglomeracji cząstek. Zasada działania tej techniki polega na wykorzystaniu działa elektronowego będącego rurą próżniową, gdzie na skutek podwyższonej temperatury (termoemisja) lub przyłożonego wysokiego napięcia elektrycznego (emisja polowa) następuje emisja wysokoenergetycznych elektronów z katody. Elektrony stanowiące wiązkę charakteryzują się taką samą energią (zwykle rzędu 80-300 keV) oraz muszą być odpowiednio kolimowane i ogniskowane w celu uzyskania obrazu dobrej jakości i zaobserwowania ultrastruktury badanego materiału. W celu zobrazowania danego nanomateriału, przygotowuje się jego rozcieńczony roztwór koloidalny, zwykle przy użyciu ultradźwięków, a następnie nanosi na bardzo cienką siateczkę miedzianą, wzmocnioną folią formwarową i napyloną amorficznym węglem. Podczas pomiarów elektrony padające na próbkę ulegają w większości rozproszeniu (ciemne punkty obrazu) natomiast część z nich przechodzi przez próbkę i trafia do detektora (jasne obszary). Elektrony ulegają rozproszeniu na atomach badanego preparatu, tym silniej im większa jest liczba atomowa danego pierwiastka. Stąd też, w przypadku obrazowania w jasnym polu, metale ciężkie są widoczne jako ciemne punkty/obszary i dają większy kontrast w porównaniu do pierwiastków o małej liczbie atomowej. Efekt ten jest szeroko wykorzystywany w przypadku badania nanostruktur typu rdzeń/powłoka (core/shell), złożonych na przykład z magnetycznego lub luminescencyjnego rdzenia (o dużej liczbie atomowej) pokrytego powłoka krzemionkową (o małej liczbie atomowej). W takim przypadku rdzeń jest widoczny na obrazie mikroskopowym jako ciemny obszar otoczony dużo jaśniejszą powłoką. Wykorzystując efekt dyfrakcji elektronów na kolumnach atomów badanego nanomateriału, możemy bezpośrednio określić jego strukturę i wyznaczyć parametry sieci krystalicznej. Ponadto, przy wykorzystaniu odpowiedniego detektora, można uzyskać widmo emisji promieniowania rentgenowskiego – EDX (energy dispersive X-ray analysis), charakterystycznego dla pierwiastków tworzących próbkę. Pozwala to na wykonanie analizy jakościowej jak i przybliżonej analizy ilościowej badanego nanomateriału.

Spektroskopia w podczerwieni – FT-IR (Fourier Transform Infrared Spectroscopy)

Metoda ta pozwala na analizę struktury substancji organicznych i nieorganicznych, poprzez detekcję charakterystycznych grup funkcyjnych. Polega ona na absorpcji promieniowania podczerwonego przez badane związki chemiczne, co jest przedstawiane w formie wykresu (widma IR) zależności intensywności transmitancji/absorbancji analitu od liczby falowej (odwrotność długości fali), wyrażanej w cm^{-1}. Absorpcja promieniowania zachodzi w zakresie częstotliwości charakterystycznym dla danego typu grup funkcyjnych i dla określonego związku chemicznego, dzięki zjawisku oscylacji (drgań) różnych cząsteczek. Skutkiem tego na widmie IR możemy obserwować drgania oscylacyjne (rozciągające i zginające) od ugrupowań chemicznych znajdujących się w badanej próbce. Pomiary można prowadzić w trybie transmisyjnym lub odbiciowym. Spektroskopia w podczerwieni jest bardzo użyteczna metodą badawczą w analizie nanomateriałów, pozwalając w łatwy i szybki sposób potwierdzić obecność pożądanych struktur/ugrupowań chemicznych. Ponadto, w przypadku nanocząstek modyfikowanych powierzchniowo, metoda ta pozwala na wykrycie cząsteczek związków organicznych zaadsorbowanych na powierzchni takich nanocząstek. W przypadku materiałów nanoporowatych można również potwierdzić obecność substancji zaabsorbowanej w porach badanego nanomateriału.

Spektroskopia luminescencyjna

Metoda ta polega na badaniu emisji promieniowania elektromagnetycznego (światła) przez badane substancje. Emisja ta następuje na skutek wzbudzenia badanej substancji promieniowaniem o wyższej energii, mniejszej długości fali niż promieniowanie emitowane przez próbkę, jest to tzw. emisja stokesowska. W przypadku niektórych układów (głównie materiałów domieszkowanych jonami lantanowców, tj. Yb^{3+}/Er^{3+}, Ho^{3+}, Tm^{3+}) można obserwować emisję antystokesowską, tzw. up-konwersję (konwersję energii w górę), polegającą na emisji fotonów o wyższej energii niż promieniowanie wzbudzające. W obu przypadkach emisja może zachodzić w zakresie ultrafioletowym (UV), widzialnym (Vis) i podczerwonym (IR). W przypadku klasycznej luminescencji, do wzbudzania próbki używa się przeważnie światła UV, natomiast w przypadku up-konwersji światła NIR (bliska podczerwień; z reguły ≈ 980 nm). Emisja promieniowania jest wynikiem wzbudzenia elektronów próbki do stanów wzbudzonych i ich późniejszej relaksacji

promienistej do stanów podstawowych. Światło emitowane ma energię równą przerwie energetycznej pomiędzy wzbudzonym poziomem emisyjnym a poziomem podstawowym. Spektroskopia luminescencyjna może służyć do detekcji w próbce określonych grup funkcyjnych, związków kompleksowych i jonów wykazujących emisję światła w wyniku wzbudzenia promieniowaniem o charakterystycznej dla danej substancji długości fali. W badaniach spektroskopowych wykonuje się głównie pomiary widm emisji i wzbudzenia luminescencji związane z zakresem spektralnym, w którym badana substancja absorbuje i emituje promieniowanie. Istotne informacje dotyczące kinetyki procesów promienistych zachodzących w układzie, dają pomiary krzywych zaniku luminescencji, na podstawie których możliwe jest wyznaczenie emisyjnych czasów życia badanych substancji. Na podstawie analizy stosunku fotonów emitowanych do zaabsorbowanych przez próbkę można wyznaczyć wydajność kwantową luminescencji, będącą miarą ilościową efektywności tego procesu. Wydajność kwantowa może być absolutna, określona poprzez zliczenie liczby fotonów zaabsorbowanych i wyemitowanych lub względna, wyznaczona na podstawie porównania z odpowiednim wzorcem. Istotną kwestią jest także określenie koordynatów chromatyczności danego luminoforu na podstawie zarejestrowanych widm emisji i naniesienie ich na odpowiedni diagram barw. W wyniku tego możliwe jest liczbowe porównanie kolorów emisji różnych próbek, co jest szczególnie istotne w przypadku dyskutowania efektu przestrajalnej luminescencji, czyli zmiany jej koloru w wyniku modyfikacji badanej próbki lub zmiany parametrów pomiarowych.

W przypadku nanomateriałów, szczególnie użytecznymi parametrami spektroskopii luminescencyjnej są analiza krzywych zaniku luminescencji i wyznaczanie wartości emisyjnych czasów życia. Pomiary takie mogą dawać informację na temat wpływu jonów powierzchniowych i przypowierzchniowych na właściwości spektroskopowe luminoforów oraz ich stosunku do jonów znajdujących się wewnątrz danej struktury. Jony powierzchniowe znajdują się w innym otoczeniu koordynacyjnym niż jony wewnątrz cząstki, co może skutkować pojawieniem się drugiej składowej emisyjnego czasu życia, widocznej w profilu krzywej zaniku luminescencji. Efekt ten jest szczególnie intensywny w przypadku małych (kilka-kilkanaście nm) nanocząstek, mających duży stosunek powierzchni do objętości.

Literatura

[1] C. Bouzigues, T. Gacoin, A. Alexandrou, Biological applications of rare-earth based nanoparticles., ACS Nano. 5 (2011) 8488–505. doi:10.1021/nn202378b.

[2] X. Xue, F. Wang, X. Liu, Emerging functional nanomaterials for therapeutics, J. Mater. Chem. 21 (2011) 13107–13127. doi:10.1039/c1jm11401h.

[3] S. Zeng, D. Baillargeat, H.-P. Ho, K.-T. Yong, Nanomaterials enhanced surface plasmon resonance for biological and chemical sensing applications, Chem. Soc. Rev. 43 (2014) 3426–3452. doi:10.1039/c3cs60479a.

[4] S. Ranjan, M.K.G. Jayakumar, Y. Zhang, Luminescent lanthanide nanomaterials: an emerging tool for theranostic applications, Nanomedicine. 10 (2015) 1477–1491. doi:10.2217/nnm.14.229.

[5] W.A. Pisarski, J. Pisarska, R. Lisiecki, Ł. Grobelny, G. Dominiak-Dzik, W. Ryba-Romanowski, Erbium-doped oxide and oxyhalide lead borate glasses for near-infrared broadband optical amplifiers, Chem. Phys. Lett. 472 (2009) 217–219. doi:10.1016/j.cplett.2009.03.018.

[6] M. Bayer, P. Hawrylak, K. Hinzer, S. Fafard, M. Korkusinski, Z.R. Wasilewski, et al., Coupling and entangling of quantum states in quantum dot molecules., Science, 291 (2001) 451–453. doi:10.1126/science.291.5503.451.

[7] V. Skumryev, S. Stoyanov, Y. Zhang, G. Hadjipanayis, D. Givord, J. Nogués, Beating the superparamagnetic limit with exchange bias., Nature. 423 (2003) 850–853. doi:10.1038/nature01687.

[8] K. Ostrikov, E.C. Neyts, M. Meyyappan, Plasma nanoscience: from nano-solids in plasmas to nano-plasmas in solids, Adv. Phys. 62 (2013) 113–224. doi:10.1080/00018732.2013.808047.

[9] J.C. Love, L.A. Estroff, J.K. Kriebel, R.G. Nuzzo, G.M. Whitesides, Self-assembled monolayers of thiolates on metals as a form of nanotechnology., Chem. Rev. 105 (2005) 1103–1169. doi:10.1021/cr0300789.

[10] M. Kelsal, R. W.; Hamley, I. W.; Geoghegan, ed., Nanotechnologie, PWN, Warszawa, 2008.

[11] S. Polizzi, M. Battagliarin, M. Bettinelli, A. Speghini, G. Fagherazzi, Investigation on lanthanide-doped Y_2O_3 nanopowders obtained by wet chemical synthesis, J. Mater. Chem. 12 (2002) 742–747. doi:10.1039/b106240a.

[12] Xavier Batlle and Amílcar Labarta, X. Batlle, A. Labarta, Finite-size effects in fine

particles: magnetic and transport properties, J. Phys. D Appl. Phys. 35 (2002) R15–R42. doi:http://dx.doi.org/10.1088/0022-3727/35/6/201.

[13] Y. Liang, Y. Li, H. Wang, J. Zhou, J. Wang, T. Regier, et al., Co_3O_4 nanocrystals on graphene as a synergistic catalyst for oxygen reduction reaction, Nat. Mater. 10 (2011) 780–786. doi:10.1038/nmat3087.

[14] D. Astruc, F. Lu, J.R. Aranzaes, Nanoparticles as recyclable catalysts: the frontier between homogeneous and heterogeneous catalysis., Angew. Chem. Int. Ed. 44 (2005) 7852–7872. doi:10.1002/anie.200500766.

[15] M.V.D.Z. Park, A.M. Neigh, J.P. Vermeulen, L.J.J. de la Fonteyne, H.W. Verharen, J.J. Briedé, et al., The effect of particle size on the cytotoxicity, inflammation, developmental toxicity and genotoxicity of silver nanoparticles., Biomaterials. 32 (2011) 9810–9817. doi:10.1016/j.biomaterials.2011.08.085.

[16] S.A. Love, M.A. Maurer-Jones, J.W. Thompson, Y.-S. Lin, C.L. Haynes, Assessing nanoparticle toxicity., Annu. Rev. Anal. Chem. 5 (2012) 181–205. doi:10.1146/annurev-anchem-062011-143134.

[17] H.A. Weller H., Schmidt H.M., Koch U., Fojtik A., Onset of Light Absoption as a Function of Size of Extremely Small CdS Particles, Chem.Phys.Letters. 124 (1986) 557–560.

[18] V. Skumryev, S. Stoyanov, Y. Zhang, G. Hadjipanayis, D. Givord, J. Nogués, Beating the superparamagnetic limit with exchange bias., Nature. 423 (2003) 850–853. doi:10.1038/nature01687.

[19] M. Runowski, A. Ekner-Grzyb, L. Mrówczyńska, S. Balabhadra, T. Grzyb, J. Paczesny, et al., Synthesis and Organic Surface Modification of Luminescent, Lanthanide-Doped Core/Shell Nanomaterials (LnF_3@SiO_2@NH_2@Organic Acid) for Potential Bioapplications: Spectroscopic, Structural, and in Vitro Cytotoxicity Evaluation., Langmuir. 30 (2014) 9533–9543. doi:10.1021/la501107a.

[20] W.L. Barnes, A. Dereux, T.W. Ebbesen, Surface plasmon subwavelength optics., Nature. 424 (2003) 824–830. doi:10.1038/nature01937.

[21] Z. Tang, N. a Kotov, M. Giersig, Spontaneous organization of single CdTe nanoparticles into luminescent nanowires., Science. 297 (2002) 237–240. doi:10.1126/science.1072086.

[22] H. Chander, Development of nanophosphors—A review, Mater. Sci. Eng. R Rep. 49 (2005) 113–155. doi:10.1016/j.mser.2005.06.001.

[23] L. Yang, J. Motohisa, J. Takeda, K. Tomioka, T. Fukui, Size-dependent

photoluminescence of hexagonal nanopillars with single InGaAs/GaAs quantum wells fabricated by selective-area metal organic vapor phase epitaxy, Appl. Phys. Lett. 89 (2006) 203110. doi:10.1063/1.2372710.

[24] H. Yu, J. Li, R.A. Loomis, L.-W. Wang, W.E. Buhro, Two- versus three-dimensional quantum confinement in indium phosphide wires and dots., Nat. Mater. 2 (2003) 517–20. doi:10.1038/nmat942.

[25] A.P. Alivisatos, Semiconductor Clusters, Nanocrystals, and Quantum Dots, Science, 271 (1996) 933–937. doi:10.1126/science.271.5251.933.

[26] K. Tvrdy, P. V Kamat, Substrate driven photochemistry of CdSe quantum dot films: charge injection and irreversible transformations on oxide surfaces., J. Phys. Chem. A. 113 (2009) 3765–3772. doi:10.1021/jp808562x.

[27] A. Fojtik, Quantum state of small semiconductor clusters - "exciton", radiation chemistry of "Q-state" particles, Int. J. Radiat. Appl. Instrum. C Radiat. Phys. Chem. 28 (1986) 463 – 465.

[28] S. Link, M.A. El-Sayed, Spectral Properties and Relaxation Dynamics of Surface Plasmon Electronic Oscillations in Gold and Silver Nanodots and Nanorods, J. Phys. Chem. B. 103 (1999) 8410–8426. doi:10.1021/jp9917648.

[29] S. Laurent, D. Forge, M. Port, A. Roch, C. Robic, L. Vander Elst, et al., Magnetic iron oxide nanoparticles: synthesis, stabilization, vectorization, physicochemical characterizations, and biological applications., Chem. Rev. 108 (2008) 2064–2110. doi:10.1021/cr068445e.

[30] F. Gagné, D. Maysinger, C. André, C. Blaise, Cytotoxicity of aged cadmium-telluride quantum dots to rainbow trout hepatocytes, Nanotoxicology. 2 (2008) 113–120. doi:10.1080/17435390802245708.

[31] C. Kirchner, T. Liedl, S. Kudera, T. Pellegrino, A. Muñoz Javier, H.E. Gaub, et al., Cytotoxicity of colloidal CdSe and CdSe/ZnS nanoparticles., Nano Lett. 5 (2005) 331–338. doi:10.1021/nl047996m.

[32] M.-A. Shahbazi, M. Hamidi, E.M. Mäkilä, H. Zhang, P. V Almeida, M. Kaasalainen, et al., The mechanisms of surface chemistry effects of mesoporous silicon nanoparticles on immunotoxicity and biocompatibility., Biomaterials. 34 (2013) 7776–7789. doi:10.1016/j.biomaterials.2013.06.052.

[33] Y. Zhao, X. Sun, G. Zhang, B.G. Trewyn, I.I. Slowing, V.S.-Y. Lin, Interaction of mesoporous silica nanoparticles with human red blood cell membranes: size and surface effects., ACS Nano. 5 (2011) 1366–1375. doi:10.1021/nn103077k.

[34] P.J.A. Borm, W. Kreyling, Toxicological Hazards of Inhaled Nanoparticles—Potential Implications for Drug Delivery, J. Nanosci. Nanotech. 4 (2004) 521–531. doi:10.1166/jnn.2004.081.

[35] M. Geiser, W.G. Kreyling, Deposition and biokinetics of inhaled nanoparticles., Part. Fibre Toxicol. 7 (2010) 2. doi:10.1186/1743-8977-7-2.

[36] E. Fröhlich, Cellular Targets and Mechanisms in the Cytotoxic Action of Non-biodegradable Engineered Nanoparticles, Curr. Drug Metab. 14 (2013) 976–988.

[37] A. Stoccoro, H.L. Karlsson, F. Coppedè, L. Migliore, Epigenetic effects of nano-sized materials, Toxicology. 313 (2013) 3–14. doi:10.1016/j.tox.2012.12.002.

[38] X. Yang, J. Liu, H. He, L. Zhou, C. Gong, X. Wang, et al., SiO2 nanoparticles induce cytotoxicity and protein expression alteration in HaCaT cells., Part Fibre Toxicol. 7 (2010) 1–12. doi:10.1186/1743-8977-7-1.

[39] S.A. Corr, Y.P. Rakovich, Y.K. Gun'ko, Multifunctional Magnetic-fluorescent Nanocomposites for Biomedical Applications, Nanoscale Res. Lett. 3 (2008) 87–104. doi:10.1007/s11671-008-9122-8.

[40] S.T. Selvan, T.T.Y. Tan, D.K. Yi, N.R. Jana, Functional and Multifunctional Nanoparticles for Bioimaging and Biosensing., Langmuir. 26 (2009) 11631–11641. doi:10.1021/la903512m.

[41] M. Runowski, T. Grzyb, A. Zep, P. Krzyczkowska, E. Gorecka, M. Giersig, et al., Eu^{3+} and Tb^{3+} doped $LaPO_4$ nanorods, modified with luminescent organic compound, exhibiting tunable multicolour emission, RSC Adv. 4 (2014) 46305–46312. doi:10.1039/C4RA06168C.

[42] S. Hsu, Y.Y. Lin, S. Huang, K.W. Lem, D.H. Nguyen, D.S. Lee, Synthesis of water-dispersible zinc oxide quantum dots with antibacterial activity and low cytotoxicity for cell labeling., Nanotechnology. 24 (2013) 475102–475112. doi:10.1088/0957-4484/24/47/475102.

[43] Y. Tang, S. Han, H. Liu, X. Chen, L. Huang, X. Li, et al., The role of surface chemistry in determining in vivo biodistribution and toxicity of CdSe/ZnS core-shell quantum dots., Biomaterials. 34 (2013) 8741–55. doi:10.1016/j.biomaterials.2013.07.087.

[44] M. Runowski, K. Dąbrowska, T. Grzyb, P. Miernikiewicz, S. Lis, Core/shell-type nanorods of Tb^{3+}-doped $LaPO_4$, modified with amine groups, revealing reduced cytotoxicity, J. Nanopart. Res. 15 (2013) 2068–2083. doi:10.1007/s11051-013-2068-5.

[45] T. Grzyb, M. Runowski, K. Dąbrowska, M. Giersig, S. Lis, Structural, spectroscopic and cytotoxicity studies of TbF_3@CeF_3 and TbF_3@CeF_3@SiO_2 nanocrystals, J. Nanopart. Res. 15 (2013) 1958–1972. doi:10.1007/s11051-013-1958-x.

[46] P. Yuan, Y.H. Lee, M.K. Gnanasammandhan, Z. Guan, Y. Zhang, Q.-H. Xu, Plasmon enhanced upconversion luminescence of $NaYF_4$:Yb,Er@SiO_2@Ag core–shell nanocomposites for cell imaging, Nanoscale. 4 (2012) 5132–5137. doi:10.1039/c2nr31241g.

[47] Z.S. Haidar, Bio-Inspired/-Functional Colloidal Core-Shell Polymeric-Based NanoSystems: Technology Promise in Tissue Engineering, Bioimaging and NanoMedicine, Polymers (Basel). 2 (2010) 323–352. doi:10.3390/polym2030323.

[48] R.A. Ramli, W.A. Laftah, S. Hashim, Core–shell polymers: a review, RSC Adv. 3 (2013) 15543–15565. doi:10.1039/c3ra41296b.

[49] S.C. Pang, S.Y. Kho, S.F. Chin, Fabrication of Magnetite/Silica/Titania Core-Shell Nanoparticles, J. Nanomater. 2012 (2012) 1–6. doi:10.1155/2012/427310.

[50] M. Runowski, T. Grzyb, S. Lis, Magnetic and luminescent hybrid nanomaterial based on Fe_3O_4 nanocrystals and $GdPO_4$:Eu^{3+} nanoneedles, J. Nanopart. Res. 14 (2012) 1188–1195. doi:10.1007/s11051-012-1188-7.

[51] A. Szczeszak, A. Ekner-Grzyb, M. Runowski, L. Mrówczyńska, T. Grzyb, S. Lis, Synthesis, photophysical analysis, and in vitro cytotoxicity assessment of the multifunctional (magnetic and luminescent) core@shell nanomaterial based on lanthanide-doped orthovanadates, J. Nanopart. Res. 17 (2015) 143–153. doi:10.1007/s11051-015-2950-4.

[52] M. Runowski, S. Lis, Synthesis, surface modification/decoration of luminescent–magnetic core/shell nanomaterials, based on the lanthanide doped fluorides (Fe_3O_4/SiO_2/NH_2/PAA/LnF_3), J. Lumin. 170 (2016) 484–490. doi:10.1016/j.jlumin.2015.05.037.

[53] Y. Jun, J. Choi, J. Cheon, Heterostructured magnetic nanoparticles: their versatility and high performance capabilities., ChemComm. 28 (2007) 1203–1214. doi:10.1039/b614735f.

[54] J. Wang, S. Zheng, Y. Shao, J. Liu, Z. Xu, D. Zhu, Amino-functionalized Fe_3O_4@SiO_2 core-shell magnetic nanomaterial as a novel adsorbent for aqueous heavy metals removal., J. Colloid Interface Sci. 349 (2010) 293–299. doi:10.1016/j.jcis.2010.05.010.

[55] H. Xu, Z.P. Aguilar, L. Yang, M. Kuang, H. Duan, Y. Xiong, et al., Antibody

conjugated magnetic iron oxide nanoparticles for cancer cell separation in fresh whole blood., Biomaterials. 32 (2011) 9758–9765. doi:10.1016/j.biomaterials.2011.08.076.

[56] C. Billotey, C. Wilhelm, M. Devaud, J.C. Bacri, J. Bittoun, F. Gazeau, Cell internalization of anionic maghemite nanoparticles: quantitative effect on magnetic resonance imaging., Magn. Reson. Med. 49 (2003) 646–654.

[57] W. Stöber, Controlled growth of monodisperse silica spheres in the micron size range, J. Colloid Interface Sci. 26 (1968) 62–69. doi:10.1016/0021-9797(68)90272-5.

[58] J.-N. Park, P. Zhang, Y.-S. Hu, E.W. McFarland, Synthesis and characterization of sintering-resistant silica-encapsulated Fe_3O_4 magnetic nanoparticles active for oxidation and chemical looping combustion., Nanotechnology. 21 (2010) 225708–225716. doi:10.1088/0957-4484/21/22/225708.

[59] M. Runowski, T. Grzyb, S. Lis, Bifunctional luminescent and magnetic core/shell type nanostructures Fe_3O_4@CeF_3:Tb^{3+}/SiO_2, J. Rare Earths. 29 (2011) 1117–1122. doi:10.1016/S1002-0721(10)60609-6.

[60] C.W. Warren, P.D. Chan, Bio-applications of Nanoparticles, Springer S, New York, 2009.

[61] M.R. Mello, D. Phanon, G.Q. Silveira, P.L. Llewellyn, C.M. Ronconi, Amine-modified MCM-41 mesoporous silica for carbon dioxide capture, Microporous Mesoporous Mater. 143 (2011) 174–179. doi:10.1016/j.micromeso.2011.02.022.

[62] P.K. Jal, S. Patel, B.K. Mishra, Chemical modification of silica surface by immobilization of functional groups for extractive concentration of metal ions., Talanta. 62 (2004) 1005–1028. doi:10.1016/j.talanta.2003.10.028.

[63] P. Yang, Z. Quan, Z. Hou, C. Li, X. Kang, Z. Cheng, et al., A magnetic, luminescent and mesoporous core-shell structured composite material as drug carrier., Biomaterials. 30 (2009) 4786–4795. doi:10.1016/j.biomaterials.2009.05.038.

[64] H. Nabeshi, T. Yoshikawa, A. Arimori, T. Yoshida, S. Tochigi, T. Hirai, et al., Effect of surface properties of silica nanoparticles on their cytotoxicity and cellular distribution in murine macrophages., Nanoscale Res. Lett. 6 (2011) 93–98. doi:10.1186/1556-276X-6-93.

[65] W. Lu, C.M. Lieber, Nanoelectronics from the bottom up., Nat. Mater. 6 (2007) 841–850. doi:10.1038/nmat2028.

[66] T. Grzyb, M. Runowski, A. Szczeszak, S. Lis, Influence of Matrix on the

Luminescent and Structural Properties of Glycerine-Capped, Tb^{3+}-Doped Fluoride Nanocrystals, J. Phys. Chem. C. 116 (2012) 17188−17196. doi:10.1021/jp3010579.

[67] T. Grzyb, M. Runowski, S. Lis, Facile synthesis, structural and spectroscopic properties of GdF_3:Ce^{3+}, Ln^{3+} (Ln^{3+}=Sm^{3+}, Eu^{3+}, Tb^{3+}, Dy^{3+}) nanocrystals with bright multicolor luminescence, J. Lumin. 154 (2014) 479–486. doi:10.1016/j.jlumin.2014.05.020.

[68] M. Runowski, S. Lis, Preparation and photophysical properties of luminescent nanoparticles based on lanthanide doped fluorides (LaF_3:Ce^{3+}, Gd^{3+}, Eu^{3+}), obtained in the presence of different surfactants, J. Alloy. Comp. 597 (2014) 63–71. doi:10.1016/j.jallcom.2014.01.209.

[69] E. Zych, D. Hreniak, W. Strek, Spectroscopic Properties of Lu_2O_3/Eu^{3+} Nanocrystalline Powders and Sintered Ceramics, J. Phys. Chem. B. 106 (2002) 3805–3812. doi:10.1021/jp012468+.

[70] K. Binnemans, C. Görller-Walrand, Application of Eu^{3+} ion for site symmetry determination, J. Rare Earths. 14 (1996) 173–180.

[71] S. Lis, Luminescence spectroscopy of lanthanide(III) ions in solution, J. Alloy. Compd. 341 (2002) 45–50. doi:10.1016/S0925-8388(02)00055-5.

[72] B.G. Wybourne, L. Smentek, Optical spectroscopy of lanthanides, CRC Press, New York, 2007.

[73] R. Pązik, K. Zawisza, A. Watras, K. Maleszka-Bagińska, P. Boutinaud, R. Mahiou, et al., Temperature induced emission quenching processes in Eu^{3+}-doped $La_2CaB_{10}O_{19}$, J. Mater. Chem. 22 (2012) 22651. doi:10.1039/c2jm34687g.

[74] M. Runowski, S. Balabhadra, S. Lis, Nanosized complex fluorides based on Eu^{3+} doped Sr_2LnF_7 (Ln=La, Gd), J. Rare Earths. 32 (2014) 242–247. doi:10.1016/S1002-0721(14)60058-2.

[75] T. Grzyb, L. Mrówczyńska, A. Szczeszak, Z. Śniadecki, M. Runowski, B. Idzikowski, et al., Synthesis, characterization, and cytotoxicity in human erythrocytes of multifunctional, magnetic, and luminescent nanocrystalline rare earth fluorides, J. Nanopart. Res. 17 (2015) 399–416. doi:10.1007/s11051-015-3191-2.

[76] R.S. Yadav, V.K. Shukla, P. Mishra, S.K. Pandey, K. Kumar, V. Baranwal, et al., Enhanced blue luminescence in $BaMgAl_{10}O_{17}$:Eu, Er, Nd nanophosphor for PDPs and Mercury free fluorescent lamps, J. Alloy. Comp. 547 (2013) 1–4. doi:10.1016/j.jallcom.2012.08.107.

[77] G. Wang, Q. Peng, Y. Li, Lanthanide-doped nanocrystals: synthesis, optical-magnetic properties, and applications., Acc. Chem. Res. 44 (2011) 322–332. doi:10.1021/ar100129p.

[78] D. Zhang, C. Chen, F. Wang, D.M. Zhang, Optical gain and upconversion luminescence in LaF_3: Er, Yb nanoparticles-doped organic–inorganic hybrid materials waveguide amplifier, Appl. Phys. B. 98 (2009) 791–795. doi:10.1007/s00340-009-3851-y.

[79] Y. Liu, D. Tu, H. Zhu, X. Chen, Lanthanide-doped luminescent nanoprobes: controlled synthesis, optical spectroscopy, and bioapplications., Chem. Soc. Rev. 42 (2013) 6924–6958. doi:10.1039/c3cs60060b.

[80] P. Kulpinski, M. Namyslak, T. Grzyb, S. Lis, Luminescent cellulose fibers activated by Eu^{3+}-doped nanoparticles, Cellulose. 19 (2012) 1271–1278. doi:10.1007/s10570-012-9709-1.

[81] M. Runowski, S. Lis, Synthesis of lanthanide doped CeF_3:Gd^{3+}, Sm^{3+} nanoparticles, exhibiting altered luminescence after hydrothermal post-treatment, J. Alloy. Compd. 661 (2016) 182–189. doi:10.1016/j.jallcom.2015.11.182.

[82] H. Moos, Spectroscopic relaxation processes of rare earth ions in crystals, J. Lumin. 1-2 (1970) 106–121.

[83] J.I. Langford, a. J.C. Wilson, Scherrer after sixty years: A survey and some new results in the determination of crystallite size, J. Appl. Crystallogr. 11 (1978) 102–113. doi:10.1107/S0021889878012844.

Część eksperymentalna

Synteza nanoluminoforów opartych o jony pierwiastków ziem rzadkich

Luminofory oparte o jony Sm^{3+} są kilkadziesiąt razy tańsze w produkcji od analogicznych układów domieszkowanych np. jonami Eu^{3+}, co znacząco zwiększa ich potencjalne możliwości aplikacyjne. Problemem badawczym, jaki podjąłem w pracy pt. *„Synthesis of lanthanide doped CeF_3:Gd^{3+}, Sm^{3+} nanoparticles, exhibiting altered luminescence after hydrothermal post-treatment”* było otrzymanie efektywnych i relatywnie tanich w wytworzeniu nanoluminoforów domieszkowanych jonami Sm^{3+}. W wyniku prowadzonych badań zsyntetyzowano nanomateriały oparte o fluorki domieszkowane jonami samaru (III), tj. CeF_3:Gd^{3+}, Sm^{3+}. Związki te otrzymano metodą współstrąceniową w obecności EDTA, kwasu cytrynowego lub bez użycia modyfikatorów organicznych, co potwierdzono metodami dyfraktometrii proszkowej (XRD), transmisyjnej mikroskopii elektronowej (TEM) i spektroskopii w podczerwieni widma (FR-IR). Następnie, wybrane układy wykazujące najintensywniejszą luminescencję poddano warunkom hydrotermalnym co spowodowało nieoczekiwaną zmianę barwy luminescencji (przestrojenie koloru) z różowej na pomarańczową. Dzięki zastosowaniu spektroskopii luminescencyjnej, zarejestrowano widma wzbudzenia i emisji oraz krzywe zaniku luminescencji dla otrzymanych produktów, a następnie wyznaczono dla nich czasy życia i wydajności kwantowe luminescencji. Na podstawie uzyskanych danych spektroskopowych i strukturalnych ustalono, iż powodem zmiany koloru emisji był wzrost stopnia krystaliczności i rozmiaru cząstek poddanych warunkom hydrotermalnym (40 atm, 180^oC). Dzięki temu znacząco zwiększyła się wydajność przeniesienia energii z jonów Ce^{3+} poprzez Gd^{3+} do Sm^{3+} (zmniejszyła się niepożądana emisja Ce^{3+} w zakresie ultrafioletu (UV) i barwy niebieskiej). Dodatkowo nastąpił znaczący wzrost całkowitej intensywności emisji w zakresie widzialnym (pomarańczowa luminescencja). Zaobserwowano także istotny wpływ użytych surfaktantów na strukturę, morfologię i stopień aglomeracji otrzymanych nanostruktur. Aby potwierdzić skład pierwiastkowy otrzymanych nanoluminoforów zastosowano metodę dyspersji energii promieniowania rentgenowskiego (EDX). Natomiast

w celu ustalenia stosunku fazy nieorganicznej do organicznej (cząsteczki modyfikatorów organicznych osadzone na powierzchni nanostruktur) w otrzymanych produktach, wykonano analizę termograwimetryczną.

Wkład własny w powstanie pracy: koncepcja badań, wykonanie syntezy i zbadanie właściwości fizykochemicznych otrzymanych produktów. Analiza uzyskanych wyników, opracowanie danych i zredagowanie publikacji.

Journal of Alloys and Compounds 661 (2016) 182–189

Contents lists available at ScienceDirect

Journal of Alloys and Compounds

journal homepage: http://www.elsevier.com/locate/jalcom

Synthesis of lanthanide doped CeF_3:Gd^{3+}, Sm^{3+} nanoparticles, exhibiting altered luminescence after hydrothermal post-treatment

Marcin Runowski, Stefan Lis*

Adam Mickiewicz University, Faculty of Chemistry, Department of Rare Earths, Umultowska 89b, 61-614 Poznań, Poland

ARTICLE INFO

Article history:
Received 14 May 2015
Received in revised form
5 November 2015
Accepted 23 November 2015
Available online 27 November 2015

Keywords:
Tuneable emission
Lanthanide fluorides
Samarium (III) ions
Energy transfer
Coprecipitation synthesis
Luminescent nanoparticles

ABSTRACT

The series of nanocrystalline (≈5–10 nm), lanthanide doped fluorides – CeF_3:Gd^{3+}, Sm^{3+} were prepared by a simple coprecipitation method. The as-prepared nanoparticles were hydrothermally treated, which resulted in increased crystallinity and size of the nanocrystals formed (≈50–100 nm). The precipitated products (before the hydrothermal treatment) exhibited pink luminescence. The hydrothermal post-treatment of the colloidal nanomaterials caused alteration of their luminescence, namely the emission was tuned from pink to orange. This was because of the increased energy transfer from Ce^{3+} and Gd^{3+} ions to the Sm^{3+} ion (luminescence activator), in larger and better crystallized nanoparticles. The products obtained in the presence of EDTA and citric acid revealed altered morphology, being more homogeneous and monodisperse, as well. The structural and morphological properties of the nanomaterials synthesized were determined by powder X-ray diffraction (XRD), transmission electron microscopy (TEM) and infrared spectroscopy (FT-IR). Elemental analysis, thermogravimetric–differential thermal analysis (TG–DTA) and energy dispersive X-ray analysis (EDX) confirmed the nanomaterials composition. The luminescence properties of the products were studied based on the recorded excitation/emission spectra and emission–decay curves. Radiative lifetimes and luminescence quantum yields were also determined.

1. Introduction

In the last few years much attention has been paid to the investigation of luminescent inorganic nanomaterials [1–4]. Such materials are usually composed of inorganic semiconductors (e.g. CdSe, ZnO quantum dots) or lanthanide (Ln^{3+}) doped nanoparticles [5–10]. In contrast to organic compounds, they are photostable and resistant to oxidation and high temperatures. Due to their small size and multicolour emission of such nanostructures, they can be potentially used for bioapplications as biomarkers, contrast agents, drug carriers, etc. However, Ln^{3+} doped nanomaterials reveal generally much longer luminescence lifetime (several milliseconds) [11–14], and lower toxicity in comparison to the most of quantum dots consisting of heavy metal ions [2,15–18]. Because of the above-mentioned benefits, lanthanide based nanoparticles are very desirable for various bioapplications [19,20].

Inorganic, crystalline compounds doped with appropriate Ln^{3+} ions can reveal luminescence in the ultraviolet (UV), visible or infrared (IR) ranges upon excitation with UV (energy down-conversion) or IR (energy up-conversion) light [21–23]. In the case of the UV excited systems, the most intense luminescences are usually exhibited by Eu^{3+} (red emission) and Tb^{3+} ions (green emission), because of their large band gaps between emitting and ground levels [21]. Sm^{3+} and Dy^{3+} ions have smaller band gaps, however they are large enough to achieve intense coloured luminescence after UV light irradiation [21]. Moreover, samarium (metal or oxide) is much less expensive (about 50 times) than europium or terbium, which is a crucial issue in industrial applications (e.g. new light sources, luminescent tracers).

Direct excitation of Ln^{3+} activator ions e.g. Sm^{3+}, Eu^{3+}, Tb^{3+}, Er^{3+} results in their inefficient luminescence because the internal 4f–4f transitions occurring in these ions, are forbidden by the selection rules [24,25]. That is why, the energy transfer (ET) and/or charge transfer (CT) phenomena are employed to enhance the emission of the products by the use of indirect excitation [23,26–28]. The energy donor – sensitizer (light harvesting species) can be organic ligands in the case of organic complexes and other Ln^{3+} ions (Ce^{3+}, Gd^{3+}, Yb^{3+}) in inorganic compounds [23,27–29].

* Corresponding author.
E-mail address: blis@amu.edu.pl (S. Lis).

http://dx.doi.org/10.1016/j.jallcom.2015.11.182
0925-8388/

Nanocrystalline, inorganic fluorides based on Ln^{3+} ions have been intensively investigated as promising luminescent materials over the last few years [11,22,30–33]. They can be easily obtained as fine nanoparticles, doped with the desired activator ions. The matrices based on LnF_3 or their complex analogues have very small phonon energies of their crystal lattices, e.g. 350 cm^{-1} in the case of the LaF_3 [34]. This internal feature is a trigger of low non-radiative relaxation of the Ln^{3+} excited states, which results in a relatively high values of the luminescence quantum yield (QY) and intense multicolour emission of such structures [35,36]. Moreover, low-cytotoxicity, photostability, long emission lifetimes and easily modified surfaces of the Ln^{3+} doped fluorides, make them very useful nanomaterials for various applications, such as luminescent tracers, biomarkers, drug carriers, tuneable light sources or active components of advanced hybrid nanomaterials [2,15,20,32,37–39].

Here we report, the synthetic procedure and photophysical characterization of the luminescent, nanocrystalline fluorides, based on a CeF_3 matrix doped with Gd^{3+} and Sm^{3+} ions. The nanoparticles were obtained via a coprecipitation method, and subsequently subjected to a hydrothermal post-treatment, leading to the luminescence tuning (pink → orange emission). The synthesis of the products was performed in pure water and in the presence of EDTA or citric acid acting as surfactants, which resulted in a different morphology of the nanoparticles formed.

2. Experimental section

2.1. Materials

Gd_2O_3, and Sm_2O_3 (Stanford Materials, 99.99%) were separately dissolved in concentrated HNO_3 (POCh S.A., ultra-pure) in order to obtain $Gd(NO_3)_3$ and $Sm(NO_3)_3$ aqueous solutions. $CeCl_3 \cdot 7H_2O$ (99.9%) was purchased from Sigma Aldrich. NH_4F (ACS grade, ≥98%), ethylenediaminetetraacetic acid – EDTA (pure p.a., >98%) and citric acid (hydrate, pure p.a., >99.5%) were purchased from POCh S.A. Double distilled water was used for all experiments.

2.2. Synthesis

The syntheses were carried out to produce 0.75 g of the product. A typical synthesis procedure was performed as follows. NH_4F (50% excess) was dissolved in 25 mL of water (solution A). An aqueous solution B was prepared that contained $Ln(NO_3)_3$ and $CeCl_3$ which were mixed at the desired molar ratio (0.01 $Sm(NO_3)_3$, 0.15 $Gd(NO_3)_3$ and 0.84 $CeCl_3$ mol%), and diluted with water to make 100 mL. In the case of the products obtained in the presence of EDTA and citric acid, 0.5 wt.% of the desired polycarboxylic acid was additionally dissolved in solutions A and B. The pH of the systems was adjusted to ≈7, by the use of an aqueous NaOH solution. Solution B was added dropwise to solution A, resulting in the precipitation of the lanthanide doped fluorides (LnF_3). The reaction was performed at 343 K, with continuous stirring. The addition was completed in 0.5 h. Afterward the as-prepared products were divided into two parts. Half of the product was purified by centrifugation and washed several times with water. After this the product was dried overnight in the oven (at 358 K). The rest of the colloidal precipitate was transferred into a Teflon vessel and hydrothermally treated for 2 h, at 453 K/40 bar (microwave autoclave – ERTEC, Magnum II, 600 W). When the reaction was finished, the product obtained under hydrothermal conditions was purified by centrifugation and dried in the oven, as well. Fig. 1 presents the scheme of the coprecipitation process and subsequent hydrothermal treatment of the nanoparticles synthesized (recrystallization and growth of the nanocrystals).

2.3. Characterization

Powder XRD were collected using a Bruker AXS D8 Advance diffractometer in the Bragg–Brentano geometry, employing CuKα_1 radiation (λ = 1.5406 Å) in the 6°–60° 2θ range, at a resolution of 0.05°/step. The average grains sizes were estimated based on the experimental patterns and Scherrer's equation [40]:

$$D = \frac{k\lambda}{\cos\theta\sqrt{\beta^2 - \beta'^2}}$$

Where D is the grain size, k is the shape factor, which is ≈ 0.9 for spherical objects, λ is the radiation wavelength, θ is the angle of diffraction, β is the Full Width at Half Maximum (FWHM) and β' is the apparatus effect. TEM images were measured with a Transmission Electron Microscope JEM 1200 EXII, JEOL (80 kV). The elemental analyses of the nanomaterials were performed with an Elementar Analyser Vario EL III. The TG–DTA analyses were carried out with Setaram Setsys 1200 device, with a heating rate of 5 °C/min, in air. The EDX spectra were recorded using a Scanning Electron Microscope FEI Quanta 250 FEG, with EDAX detector. The excitation/emission spectra and luminescence decay profiles were recorded using a Hitachi F-7000 spectrofluorometer, at ambient conditions. The spectra were measured at a resolution of 0.2 nm and corrected for the instrument response. The absolute luminescence quantum yields (QY) of the products synthesized were determined based on the method described by Wrighton et al. [41] and successfully applied by others [32,42]. The diffuse reflectance of the sample relative to a nonabsorbing standard (La_2O_3) was measured, at the excitation and emission wavelengths of the sample, under the same conditions. The luminescence QY obtained is a ratio of the emitted photons to the difference in the diffuse reflected photons by the measured sample and the non-absorbing standard. The absolute luminescence QY (φ) of the nanomaterials was calculated based on the equation:

$$\varphi = \frac{E}{(R - R')}$$

where E is the integrated luminescence intensity of the product, R is the integrated diffuse reflectance intensity of the non-absorbing standard and R′ is the integrated diffuse reflectance intensity of the measured products. The data were recorded at excitation wavelength = 254 nm. IR spectra were recorded with a FT-IR spectrophotometer, JASCO 4200. The spectra were measured in the transmission mode, at a resolution of 4 cm^{-1}. Before the measurements, the products were mixed with KBr, ground and pressed into pellets.

3. Results and discussion

The aim of this work was to obtain new lanthanide based nanomaterials, exhibiting intense luminescence in the visible range. Samarium ions (Sm^{3+}) were selected as luminescence activators, and Ce^{3+} and Gd^{3+} ions were used as luminescence sensitizers (light harvesting ions). We focused on the Sm^{3+} ions mainly because of their low price (low-cost phosphors), desired emission range (pink–orange), intensive luminescence and the relatively scarce literature data concerning Sm^{3+} doped nanophosphors [21,43]. It is worth noting, that Sm^{3+} based compounds (salts, oxides and other precursors) are much less expensive (by tens of times) in comparison to the commonly used Eu^{3+} and Tb^{3+} ions.

The series of CeF_3 nanoparticles co-doped with Gd^{3+} and Sm^{3+} ions were synthesized via a co-precipitation method. On the basis of a comparison of the integral emission intensity of the products

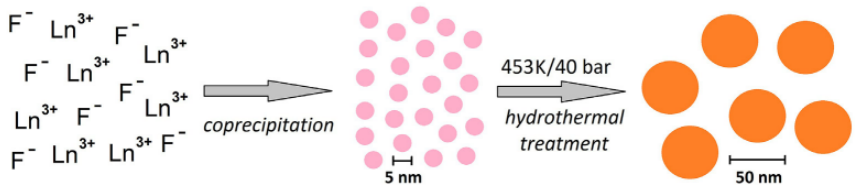

Fig. 1. Synthesis scheme of CeF_3:Gd^{3+}, Sm^{3+} nanoparticles.

synthesized, the optimal concentration of dopants was found to be 15% for Gd^{3+} and 1% for Sm^{3+} ions (CeF_3:Gd^{3+} 15%, Sm^{3+} 1%). This concentration provided the most intensive luminescence of the products (pink emission of the Sm^{3+} ions). The XRD data, excitation/emission spectra, luminescence decay curves and the comparisons of the total luminescence intensities of the variously doped CeF_3:Gd^{3+} X% (X = 5–50%), Sm^{3+} X% (X = 0.5–10%) products are presented and discussed in Supporting Information (Figs. S1–S9).

3.1. Structure and morphology

The series of six compounds composed of CeF_3:Gd^{3+} 15%, Sm^{3+} 1% were synthesized as nanocrystalline white powders exhibiting bright pink–orange luminescence. Three of them were obtained via the co-precipitation method (one in pure water - surfactant-free system, and two in the presence of surfactants, i.e. EDTA and citric acid). The other three materials were obtained by the hydrothermal treatment of the compounds previously synthesized by the co-precipitation method.

All of the products fitted well the reference pattern of hexagonal CeF_3 (P3c1 space group, ref. 086–0967) from the ICDD (Inorganic Crystal Diffraction Data) database, which confirms the successful substitution of the Ce^{3+} (host ions) by the Gd^{3+} and Sm^{3+} (dopants ions). The obtained experimental diffraction patterns (Fig. 2) revealed significant broadening of reflexes caused by the small size of the crystals forming the given product. This phenomenon is well-known for the compounds composed of crystalline nanoparticles. On the basis on the Scherrer equation, the average crystal sizes of the obtained CeF_3:Gd^{3+} 15%, Sm^{3+} 1% nanomaterials were estimated, and shown in Fig. 2. The particles of the hydrothermally treated products (22–41 nm) were significantly larger in comparison to the untreated products – the as-prepared from the co-precipitation synthesis (7–11 nm). Moreover, the nanoparticles synthesized in the presence of EDTA and citric acid were smaller than the ones obtained in the surfactant-free systems, both in the case of the as-prepared (20–30% decrease) and hydrothermally treated products (35–45% decrease). This fact confirmed the impact of the organic compounds used on the structure and morphology of the final nanomaterials.

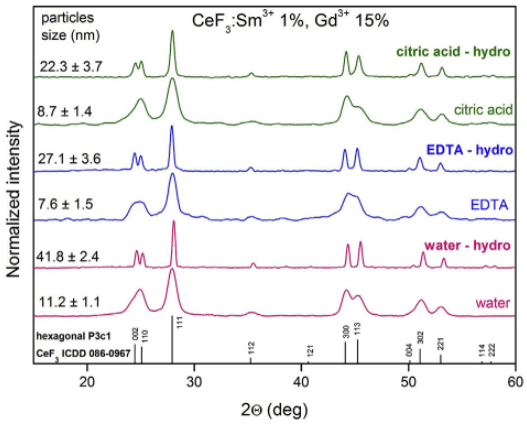

Fig. 2. XRD patterns of CeF_3:Gd^{3+} 15%, Sm^{3+} 1% nanocrystals.

TEM images of the synthesized CeF_3:Gd^{3+} 15%, Sm^{3+} 1% nanostructures are presented in Fig. 3. The first image (a) depicts the compound obtained in water, whereas the second one (b) shows the same product but post-synthesis treated under hydrothermal conditions. It is clearly seen that the first product consists of small (8–13 nm), very agglomerated nanoparticles, whereas the hydrothermally treated one is composed of much larger (20–150 nm) nanocrystallites with a broad size/shape distribution. The product obtained in the presence of EDTA (c) is composed of much less agglomerated, small (4–6 nm) nanoparticles forming individual nanoclusters with a size in the range of 30–60 nm. When this product (prepared in the presence of EDTA) was subjected for post-synthesis treatment under hydrothermal conditions, its particles transformed into larger (20–50 nm), well-crystallized nanospheres (d). A similar situation took place in the case of the product precipitated in the presence of citric acid (e), composed of small (7–12 nm) nanoparticles, which after hydrothermal treatment recrystallized into larger (15–35 nm) ones (f). Summing up, the hydrothermal treatment of the products resulted in a recrystallization of the precipitated nanoparticles into larger and better crystallized ones, with a lower level of agglomeration, as well. The syntheses performed in the presence of surfactants provided a smaller size and higher monodispersity of the final nanoparticles.

In order to determine the amount of organic modifiers in the nanomaterials synthesized, the elemental analysis of CeF_3:Gd^{3+} 15%, Sm^{3+} 1% (LnF_3) obtained in pure water and in the presence of citric acid or EDTA (via co-precipitation method) was performed. For LnF_3 (water), the content of N, C, H was 0.080, 0.140 and 0.428 (wt. %), respectively. For LnF_3 (EDTA), the content of N, C, H was 1.022, 3.141 and 0.751 (wt. %), respectively, whereas for LnF_3 (citric acid), the content of N, C, H was 0.255, 0.782 and 0.497 (wt. %), respectively. On the basis of the data collected, the molar concentration of the organic compounds bound to the nanoparticles surface was determined as 0.2617 mmol (7.65 wt. %) and 0.1086 mmol (2.09 wt. %) per one gram of LnF_3 obtained in the presence of EDTA and citric acid, respectively. The excessive amount of hydrogen and nitrogen in their structures was related to the adsorbed water molecules and bound NH_4^+/NO_3^- species. The small amount of carbon detected in the LnF_3 (water) product, was probably related to the organic impurities and adsorbed CO_2 molecules.

TG–DTA analyses were performed to examine the stability of the organic modifiers and composition of the products obtained. The obtained data agree with the elemental analysis results, and they are presented in supporting information (Fig. S11).

The EDX spectra of the nanomaterials obtained are presented in

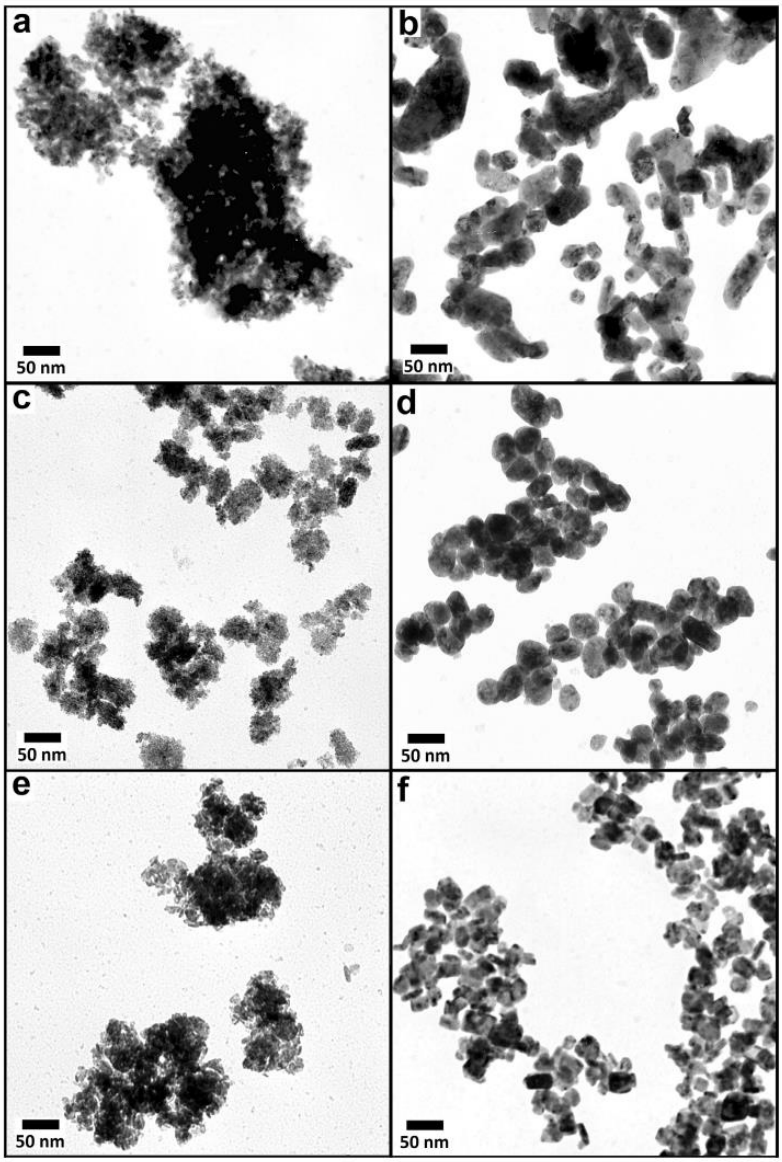

Fig. 3. TEM images of CeF_3:Gd^{3+} 15%, Sm^{3+} 1% nanocrystals, synthesized in the surfactant-free system (a, b), in the presence of EDTA (c, d) and citric acid (e, f); coprecipitated (a, c, e) and hydrothermally post-treated (b, d, f) products.

Fig. S12. The performed measurements confirm the desired composition of the lanthanide fluoride nanoparticles, and reveal the same ratio of metal ions in the products synthesized.

FT-IR spectra of the nanomaterials synthesized are shown in Fig. 4. All of the spectra reveal the intense and broad band around 3450 cm^{-1}, related to the O–H stretching (ν) vibrations and around 1640 cm^{-1} related to the O–H deformation (σ) vibrations of the adsorbed H_2O molecules. The very intense bands centered at 390 cm^{-1} corresponding to the Ln-F vibrations can be observed in all spectra, as well [44–46]. In the case of the products synthesized in the presence of EDTA and citric acid, two other bands corresponding to the asymmetric (≈1590 cm^{-1}) and symmetric (≈1400 cm^{-1}) ν vibrations of -COO^- groups can also be observed. The intensity of these bands decreased after hydrothermal treatment of the products, probably because of the decomposition of organic compounds followed by their removal from the surface. Moreover, in the spectrum of the EDTA modified product subjected to hydrothermal treatment (EDTA – hydro), a new band around 1500 cm^{-1} appears. This band suggests a change in the coordination mode of the carboxylic group to the Ln^{3+} ions, in the hydrothermally treated nanomaterial. The presence of the above-mentioned bands (≈1400–1590 cm^{-1}, νCOO^-) confirms the deprotonated character of the carboxylic groups originating from EDTA and citric acid, as well as their interaction with the surface of

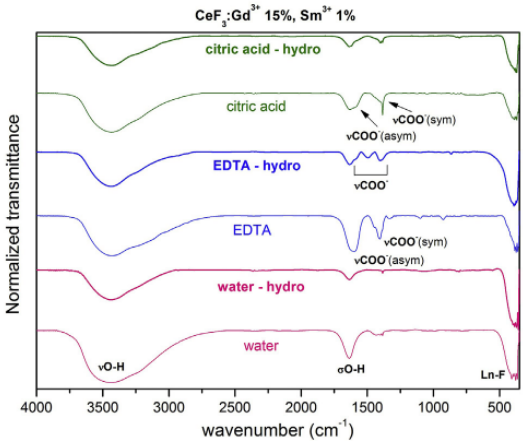

Fig. 4. FT-IR spectra of CeF_3:Gd^{3+} 15%, Sm^{3+} 1% synthesized in the presence of EDTA and citric acid.

the nanoparticles.

3.2. Luminescence properties

The products obtained exhibited intense bright emission due to the efficient ET from Ce^{3+} (sensitizer) via Gd^{3+} (energy mediator) to Sm^{3+} ions (luminescence activator). The Gd^{3+} ions acted as energy mediators, which decrease the band gap between the lowest excited states of Ce^{3+} and Gd^{3+} ions (see ET scheme in Fig. 5), making the ET and Sm^{3+} emission more efficient. As mentioned previously, CeF_3:Gd^{3+} 15%, Sm^{3+} 1% was selected as an optimal product exhibiting the most intense emission. The higher concentration of dopants resulted in lower emission intensity because of the occurrence of luminescence concentration quenching (see Fig. S9).

The luminescence properties of the CeF_3:Gd^{3+} 15%, Sm^{3+} 1% nanophosphors obtained in pure water and in the presence of surfactants, before and after the hydrothermal treatment (HT) are presented in Figs. 6–10. All of the spectra were recorded in ambient conditions, at 293 K.

The excitation spectra of the products measured at λ_{em} = 596 nm (centre of the most intense emission band originating from the $^4G_{5/2} \rightarrow {}^6H_{7/2}$ transition in Sm^{3+} ion), are presented in Fig. 6. Almost all of the spectra in Fig. 6 were normalized to the intensity of the most intense band, which was the $4f^1 \rightarrow 4f\,5\,d^1$ ET transition of Ce^{3+}. The exception was the spectrum of the product precipitated in the presence of EDTA. This spectrum was normalized to the $^4H_{5/2} \rightarrow {}^4G_{7/2}$ transition of Sm^{3+} (4f–4f transition). That product exhibited the lowest total luminescence in the visible range. However, after HT, the ET and luminescence intensity became much greater. In the range of 300–450 nm the low intensity and narrow bands corresponding to the forbidden $4f^5$–$4f^5$ intrinsic transitions in the Sm^{3+} ion can be observed in the presented spectra. All of the spectra reveal a very broad and intense band ranging from 200 to 300 nm, corresponding to the allowed 4f → 5d electric dipole transition in Ce^{3+} ion, related to ET to the Gd^{3+} and Sm^{3+} ions. After HT these bands became narrower and much more intense (in the normalized spectra of the HT products the 4f–4f transitions of the Sm^{3+} ion are hardly observed, because of much higher intensity of the 4f → 5d transition). The reason for this observation is probably related to the enhanced crystallinity of the products, resulting in a better embedding of the dopants into the crystal structure and a more uniform coordination environment for the ions. At 310 nm the low intensity band corresponding to the $^8S_{7/2} \rightarrow {}^6P_J$ transition in the Gd^{3+} ion (ET to Sm^{3+}) was observed, as well. It is worth noting that, the $^8S_{7/2} \rightarrow {}^6I_J$ transition in Gd^{3+} ion, which should be situated around 272 nm, was not observed in the spectra, because it overlapped with the broad 4f → 5d transition of the Ce^{3+} ion [21,32].

The emission spectra of the nanomaterials obtained are shown in Fig. 7. All of the spectra were recorded at λ_{ex} = 254 nm (centre of the broad band in the excitation spectra, corresponding to the Ce^{3+} 4f → 5d transition). In order to compare the shape of the different nanophosphors spectra, they were normalized to the intensity of the $^6P_J \rightarrow {}^8S_{7/2}$ transition in the Gd^{3+} ion (for the 270–450 nm

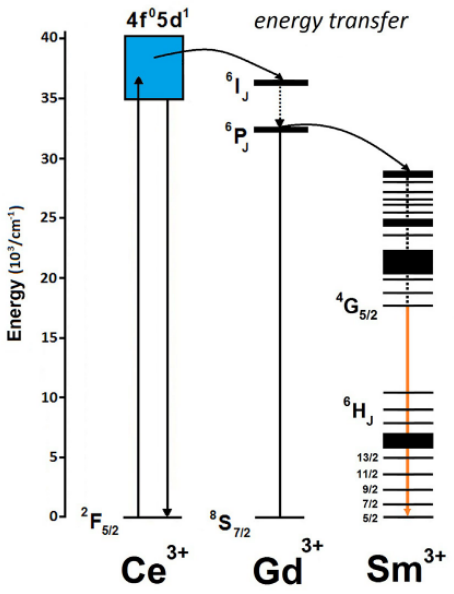

Fig. 5. Scheme of energy transfer within CeF_3:Gd^{3+} 15%, Sm^{3+} 1% system.

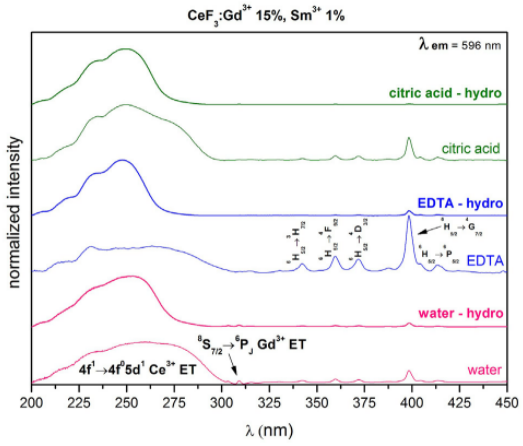

Fig. 6. Excitation spectra of CeF_3:Gd^{3+} 15%, Sm^{3+} 1% (λ_{em} = 596).

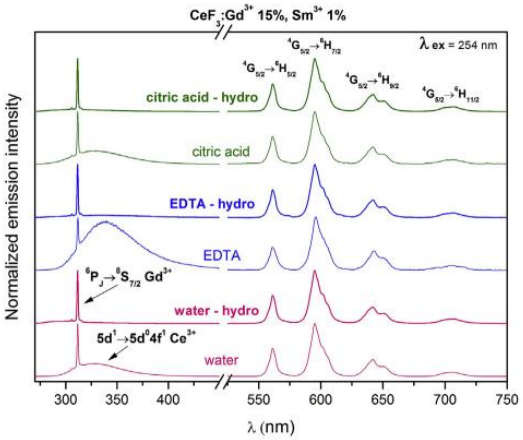

Fig. 7. Emission spectra of CeF_3:Gd^{3+} 15%, Sm^{3+} 1% (λ_{ex} = 254).

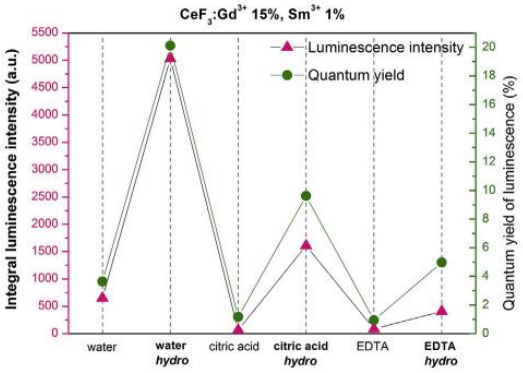

Fig. 9. Comparison of total luminescence intensity and quantum yield of the coprecipitated and HT CeF_3:Gd^{3+} 15%, Sm^{3+} 1% products (λ_{ex} = 254).

spectral region) and to the $^4G_{5/2} \rightarrow {}^6H_{7/2}$ transition in the Sm^{3+} ion (in the 500–750 nm spectral region). The intensity ratio of the bands corresponding to the transitions in the Sm^{3+} ion ($^4G_{5/2} \rightarrow {}^6H_J$) in a visible part of the spectra is generally the same in the presented series of the products. This is because the compounds synthesized are composed of the same hexagonal fluoride with a fixed elemental composition. The most significant differences in the shape of the spectra can be observed in their UV-blue region. The nanoparticles coprecipitated in pure water and in the presence of surfactants exhibit very intense UV-blue luminescence, in contrast to the HT ones. It is related to the emission of Ce^{3+} (broad band ≈ 330–340 nm) and Gd^{3+} (narrow band ≈ 310 nm) ions. The broad, allowed band of Ce^{3+} almost disappeared after HT. This phenomenon can be explained as much more efficient ET from the Ce^{3+} ion to the Gd^{3+} and Sm^{3+} ions in the larger nanoparticles having a higher level of crystallinity and well-defined crystal structure. The observed sharp/narrow emission band of the Gd^{3+} ion in case of the HT samples became less intense in comparison to the precipitated ones (non-HT). The nanomaterials synthesized in the presence of EDTA exhibited much weaker emission in the visible range (500–750 nm) in comparison to UV-blue emission. This is better shown in Fig. S10, which presents the emission spectra normalized only to the intensity of the $^6P_J \rightarrow {}^8S_{7/2}$ transition in the Gd^{3+} ion (the most intense band).

Fig. 8 presents a chromaticity diagram (CIE 1964 10 deg observer) and photographs of the nanophosphors obtained, taken in a daylight (a, b) and under UV light irradiation (c–h). It is clearly seen that if the coprecipitated products were subjected for the hydrothermal post-treatment, their emission was shifted from the blue–pink region to the orange region. Such luminescence tuning/

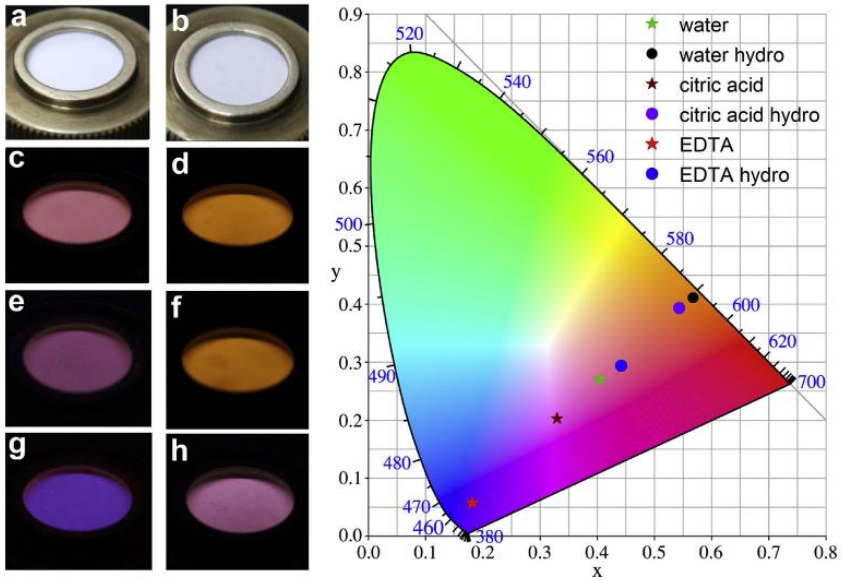

Fig. 8. Chromaticity diagram and photographs taken in a day light (a, b) and under UV light (c–h; λ_{ex} = 254 nm) of CeF_3:Gd^{3+} 15%, Sm^{3+} 1%, coprecipitated (a, c, e, g) and HT (b, d, f, h), obtained in pure water (a–d), in the presence of citric acid (e, f) and EDTA (g, h).

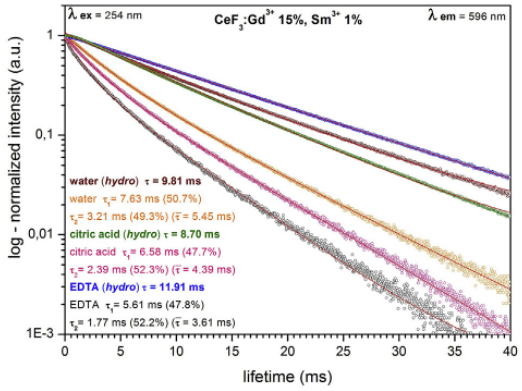

Fig. 10. Luminescence decay curves of CeF_3:Gd^{3+} 15%, Sm^{3+} 1% (λ_{ex} = 254 nm; λ_{em} = 596 nm).

alteration of the nanomaterials synthesized is related mainly to the crystallinity level of the products, their morphology and grain size.

Fig. 9 shows comparisons of the total luminescence intensities and absolute quantum yields of luminescence of the nanophosphors synthesized, measured for the visible range (Sm^{3+} emission), at λ_{ex} = 254 nm. It is clearly seen that the HT products exhibit several times higher intensity and QY of luminescence (up to ≈ 20%), than the precipitated ones (non-HT). This is because of their better crystallinity and bigger size of the nanoparticles, which results in improved ET and decreased amount of crystal defects (diminished quenching of the luminescence). The nanoparticles obtained in the presence of citric acid and EDTA revealed lower intensity and QY of luminescence in comparison to the products synthesized without surfactants. This phenomenon is probably related to the luminescence quenching by the surface organic molecules, and to some extent to the smaller average size of the nanoparticles.

In Fig. 10 the luminescence decay curves of the nanophosphors obtained, recorded at λ_{ex} = 254 nm and λ_{em} = 596 nm are presented. The luminescence lifetimes were calculated on the basis of the measured decay profiles. The decay curves of the HT samples were fitted to the $y = A^*\exp(-x/\tau) + y0$ mathematic function of the monoexponential decay, whereas the decay profiles of the precipitated (non-HT) samples were fitted well to the $y = A_1^*\exp(-x/\tau_1) + A_2^*\exp(-x/\tau_2) + y0$ mathematic function of the biexponential decay, both with R > 0.999. The calculated values of the averaged emission lifetimes were in the range of 4–12 ms, which reflects the significant differences between the samples (size, crystallinity and surface properties). The long luminescence lifetimes are characteristic of well crystallized lanthanide fluorides, whose activator ion (e.g. Sm^{3+}, Eu^{3+}) is situated in a highly symmetrical coordination environment [12,21,32,47]. In the bulk hexagonal CeF_3, all of the Ln^{3+} ions (host and dopant ions) should occupy only one type of the site having C_2 symmetry [48] and should reveal monoexponential luminescence decay. As we mentioned above, the HT nanocrystals exhibit monoexponentional decay, namely their lifetime values are 9.81 m (water), 8.70 ms (citric acid) and 11.91 ms (EDTA). This confirms that the emitting Sm^{3+} ions occupy one type of site in the nanocrystals synthesized. However, the precipitated (non-HT) products exhibited biexponential decay, namely their lifetime values are 7.63 (τ_1) and 3.21 (τ_2) ms (water), 6.58 (τ_1) and 2.39 (τ_2) ms (citric acid) and 5.61 (τ_1) and 1.77 (τ_2) ms (EDTA). Such behaviour suggests that the Sm^{3+} ions occupy two types of sites in those nanocrystals. This is because of the small size of the non-HT nanoparticles, resulting in a large surface-to-volume ratio, leading to an increased amount of surface and near surface ions. These surface ions are placed in a different coordination environment (surrounded by water/organic molecules, crystal defects, etc.) than the ions situated inside the nanocrystals (surrounded by other ions). That is why the values of τ_1 associated with the inner ions are much longer in comparison to the τ_2 values corresponding to the surface ions, which are effectively quenched by the external environment. Obviously the surface effects occur in both series of products, but they are not manifested enough to be detected in the bigger HT nanoparticles.

4. Conclusions

A series of brightly luminescent nanomaterials composed of lanthanide fluorides (CeF_3:Gd^{3+}, Sm^{3+}) were successfully synthesized via a coprecipitation method and subsequent hydrothermal treatment. The nanoparticles formed exhibited pink–orange emission originating from the Sm^{3+} ions. The products obtained were composed of small nanocrystals (≈5–10 nm), which grew after hydrothermal treatment into larger ones (≈50–100 nm). Due to the enhanced energy transfer (from Ce^{3+} and Gd^{3+} to Sm^{3+} ions) in the larger particles with improved crystallinity, the nanomaterials synthesized exhibited tuneable luminescence phenomenon. Their emission was altered from pink (smaller, coprecipitated particles) to orange (larger, hydrothermally treated ones). The use of organic modifiers (EDTA and citric acid) influenced the morphology and enhanced the homogeneity/monodispersity of the nanoparticles. The products obtained were analysed by powder XRD, TEM, EDX, spectrofluorometry, FT-IR spectroscopy, TG-DTA and elemental analysis. The prepared nanomaterials, revealing tuneable luminescence, can be employed as new light sources, luminescence tracers, biomarkers, multifunctional contrast agents as well as in multimodal imaging and forensics.

Acknowledgements

M.R. gratefully acknowledges the financial support from Polish Ministry of Science and Higher Education-scientific work was financed from the budget for science in 2012–2015 as a research project within the program called „Diamond Grant" Nr DI2011 011441. M.R. is a recipient of the scholarship from the Foundation of Adam Mickiewicz University in Poznań (2014/2015) and is a scholar supported by the Foundation for Polish Science (FNP).

Appendix A. Supplementary data

Supplementary data related to this article can be found at http://dx.doi.org/10.1016/j.jallcom.2015.11.182.

References

[1] S.A. Hilderbrand, F. Shao, C. Salthouse, U. Mahmood, R. Weissleder, Chem. Commun. 28 (2009) 4188–4190.
[2] M. Runowski, A. Ekner-Grzyb, L. Mrówczyńska, S. Balabhadra, T. Grzyb, J. Paczesny, A. Zep, S. Lis, Langmuir 30 (2014) 9533–9543.
[3] X. Xue, F. Wang, X. Liu, J. Mater. Chem. 21 (2011) 13107–13127.
[4] M. Runowski, T. Grzyb, A. Zep, P. Krzyczkowska, E. Gorecka, M. Giersig, S. Lis, RSC Adv. 4 (2014) 46305–46312.
[5] S. Hsu, Y.Y. Lin, S. Huang, K.W. Lem, D.H. Nguyen, D.S. Lee, Nanotechnology 24 (2013) 475102–475112.
[6] L. Lou, K. Yu, Z. Zhang, B. Li, J. Zhu, Y. Wang, R. Huang, Z. Zhu, Nanoscale 3 (2011) 2315–2323.
[7] R.S. Yadav, V.K. Shukla, P. Mishra, S.K. Pandey, K. Kumar, V. Baranwal, M. Kumar, A.C. Pandey, J. Alloys Compd. 547 (2013) 1–4.
[8] Y. Zeng, Z. Li, Y. Liang, X. Gan, M. Zheng, Inorg. Chem. 52 (2013) 9590–9596.
[9] A. Szczeszak, T. Grzyb, B. Barszcz, V. Nagirnyi, A. Kotlov, S. Lis, Inorg. Chem. 52 (2013) 4934–4940.
[10] T. Grzyb, RSC Adv. 4 (2014) 2590–2595.

[11] T. Grzyb, M. Runowski, A. Szczeszak, S. Lis, J. Phys. Chem. C 116 (2012) 17188–17196.
[12] K.H. Cheng, J. Aijmo, L. Ma, M. Yao, X. Zhang, J. Como, L.J. Hope-Weeks, J. Huang, W. Chen, J. Phys. Chem. C 112 (2008) 17931–17939.
[13] C. Galland, Y. Ghosh, A. Steinbrück, J.A. Hollingsworth, H. Htoon, V.I. Klimov, Nat. Commun. 3 (2012) 908–914.
[14] A. Orte, J.M. Alvarez-Pez, M.J. Ruedas-Rama, ACS Nano 7 (2013) 6387–6395.
[15] T. Grzyb, M. Runowski, K. Dąbrowska, M. Giersig, S. Lis, J. Nanopart. Res. 15 (2013) 1958–1972.
[16] M. Runowski, K. Dąbrowska, T. Grzyb, P. Miernikiewicz, S. Lis, J. Nanopart. Res. 15 (2013) 2068–2083.
[17] F. Gagné, D. Maysinger, C. André, C. Blaise, Nanotoxicology 2 (2008) 113–120.
[18] C. Kirchner, T. Liedl, S. Kudera, T. Pellegrino, A. Muñoz Javier, H.E. Gaub, S. Stölzle, N. Fertig, W.J. Parak, Nano Lett. 5 (2005) 331–338.
[19] C. Li, J. Lin, J. Mater. Chem. 20 (2010) 6831–6847.
[20] Y. Liu, D. Tu, H. Zhu, X. Chen, Chem. Soc. Rev. 42 (2013) 6924–6958.
[21] T. Grzyb, M. Runowski, S. Lis, J. Lumin. 154 (2014) 479–486.
[22] F. Wang, Y. Han, C.S. Lim, Y. Lu, J. Wang, J. Xu, H. Chen, C. Zhang, M. Hong, X. Liu, Nature 463 (2010) 1061–1065.
[23] F. Wang, X. Fan, M. Wang, Y. Zhang, Nanotechnology 18 (2007) 25701–25706.
[24] B.G. Wybourne, L. Smentek, Optical Spectroscopy of Lanthanides, CRC Press, New York, 2007.
[25] P.A. Tanner, Chem. Soc. Rev. 42 (2013) 5090–5101.
[26] G. Blasse, Phys. Status Solidi A 73 (1982) 205–208.
[27] J.W. Stouwdam, M. Raudsepp, F.C.J.M. van Veggel, Langmuir 21 (2005) 7003–7008.
[28] S. Lis, J. Alloys Compd. 341 (2002) 45–50.
[29] L. Li, H. Lin, X. Zhao, Y. Wang, X. Zhou, C. Ma, X. Wei, J. Alloys Compd. 586 (2014) 555–560.
[30] X. Wu, Q. Zhang, X. Wang, H. Yang, Y. Zhu, Eur. J. Inorg. Chem. 2011 (2011) 2158–2163.
[31] C. Li, X. Liu, P. Yang, C. Zhang, H. Lian, J. Lin, J. Phys. Chem. C 112 (2008) 2904–2910.
[32] M. Runowski, S. Lis, J. Alloys Compd. 597 (2014) 63–71.
[33] B. Sojka, M. Kuricova, A. Liskova, M. Bartusova, M. Banski, J. Misiewicz, M. Dusinska, M. Horvathova, E. Jahnova, S. Ilavska, M. Szabova, E. Rollerova, A. Podhorodecki, J. Tulinska, J. Appl. Toxicol. 34 (2014) 1220–1225.
[34] H. Moos, J. Lumin 1–2 (1970) 106–121.
[35] H.-T. Wong, H.L.W. Chan, J.H. Hao, Appl. Phys. Lett. 95 (2009) 022512–022514.
[36] X. Zhang, T. Hayakawa, M. Nogami, Int. J. Appl. Ceram. Technol. 8 (2011) 741–751.
[37] D. Chen, Y. Yu, F. Huang, P. Huang, A. Yang, Y. Wang, JACS 132 (2010) 9976–9978.
[38] G. Wang, Q. Peng, Y. Li, Acc. Chem. Res. 44 (2011) 322–332.
[39] D. Chen, Z. Wan, Y. Zhou, P. Huang, J. Zhong, M. Ding, W. Xiang, X. Liang, Z. Ji, J. Alloys Compd. 638 (2015) 21–28.
[40] J.I. Langford, J.C. Wilson, J. Appl. Crystallogr. 11 (1978) 102–113.
[41] M.S. Wrighton, D.S. Ginley, D.L. Morse, J. Phys. Chem. 78 (1974) 2229–2233.
[42] A.M. Kłonkowski, S. Lis, M. Pietraszkiewicz, Z. Hnatejko, K. Czarnobaj, M. Elbanowski, Chem. Mater. 15 (2003) 656–663.
[43] J. Peng, Y. Sun, L. Zhao, Y. Wu, W. Feng, Y. Gao, F. Li, Biomaterials 34 (2013) 9535–9544.
[44] G.N. Kustova, L.R. Batsanova, J. Appl. Spectrosc. 4 (1966) 62–63.
[45] W. Su, B. Li, D. Liu, F. Zhang, J. Phys. D. Appl. Phys. 40 (2007) 3343–3347.
[46] X. Wang, L. Andrews, J. Phys. Chem. A 114 (2010) 2293–2299.
[47] T. Grzyb, M. Runowski, A. Szczeszak, S. Lis, J. Solid State Chem. 200 (2013) 76–83.
[48] W.T. Carnall, G.L. Goodman, K. Rajnak, R.S. Rana, J. Chem. Phys. 90 (1989) 3443–3457.

Supporting information for:

Synthesis of lanthanide doped CeF_3:Gd^{3+}, Sm^{3+} nanoparticles, exhibiting altered luminescence after hydrothermal post-treatment

Marcin Runowski, Stefan Lis[*]

Adam Mickiewicz University, Faculty of Chemistry, Department of Rare Earths, Umultowska 89b, 61-614 Poznań, Poland

The products synthesized, namely CeF_3:Gd^{3+} X%, Sm^{3+} 1% (X = 0-50%) and CeF_3:Gd^{3+} 15%, Sm^{3+} X% (X = 0.5-10%) fitted well the reference pattern of the hexagonal CeF_3 (P3c1 space group, ref. 086-0967) from the ICDD database, which confirms the successful substitution of Ce^{3+} by Gd^{3+} and Sm^{3+} (Figs. S1, S2). The experimental diffraction patterns obtained revealed significant broadening of reflexes caused by a small size of the crystals forming a given product.

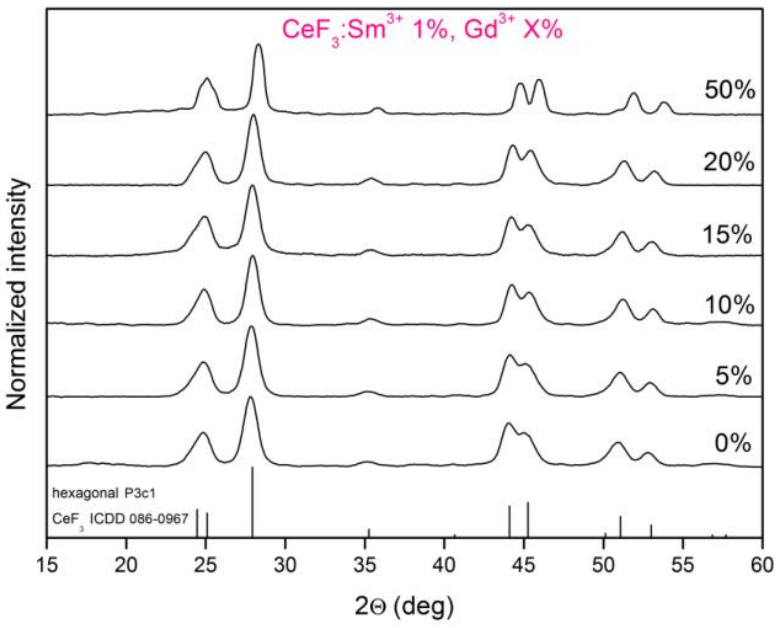

Fig. S1 XRD patterns of the CeF_3:Gd^{3+} X%, Sm^{3+} 1% nanocrystals.

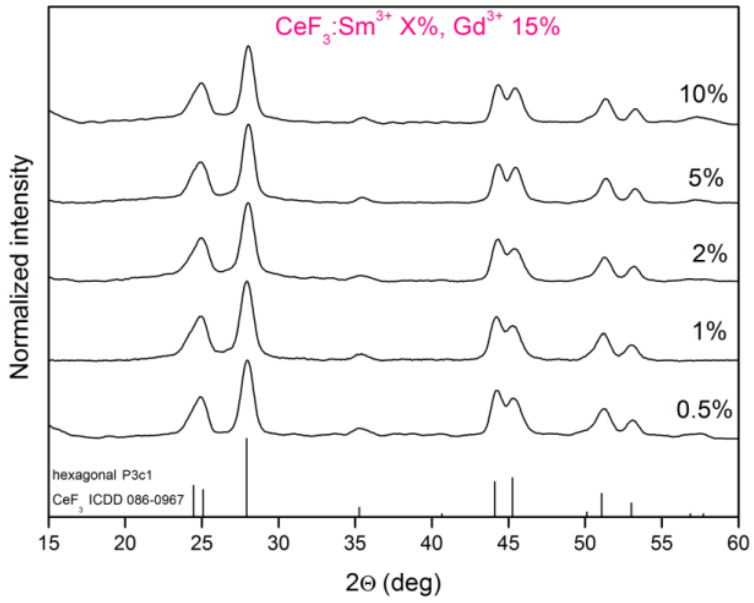

Fig. S2 XRD patterns of the CeF_3:Gd^{3+} 15%, Sm^{3+} X% nanocrystals.

The excitation spectra of the products, namely CeF_3:Gd^{3+} X%, Sm^{3+} 1% (X = 0-50%) and CeF_3:Gd^{3+} 15%, Sm^{3+} X% (X = 0.5-10%) were measured at λ_{em} = 596 nm (Figs. S3, S4). All of the spectra were normalized to the intensity of the most intense band. In the range of 300-450 nm the low intense and narrow bands corresponding to the forbidden $4f^5$-$4f^5$ intrinsic transitions of the Sm^{3+} ion can be observed in the presented spectra. All of the spectra reveal a very broad and intensive band ranging from 200-300 nm, corresponding to the allowed 4f→5d electric dipole transition of the Ce^{3+} ion. At 310 nm the low intensity band corresponding to the $^8S_{7/2}\rightarrow{}^6P_J$ transition of the Gd^{3+} ion (energy transfer (ET) to Sm^{3+}) was observed, except of the sample which did not contain Gd^{3+} ions (CeF_3:Gd^{3+} 0%, Sm^{3+} 1%). The mentioned sample exhibited also the least intense ET transition of Ce^{3+} (250-300 nm). This fact confirms the crucial role of the Gd^{3+} ions as mediators of energy (ET from Ce^{3+} via Gd^{3+} to Sm^{3+} ions), providing the intensive luminescence of Sm^{3+} ion. In both series of the spectra (Fig. S3 and S4) the products with optimal concentrations of dopant ions (Gd^{3+} 15%,

Sm^{3+} 1%) revealed the highest intensity ratio of ET band (200-300 nm) to 4f-4f bands within the Sm^{3+} ion (300-450 nm).

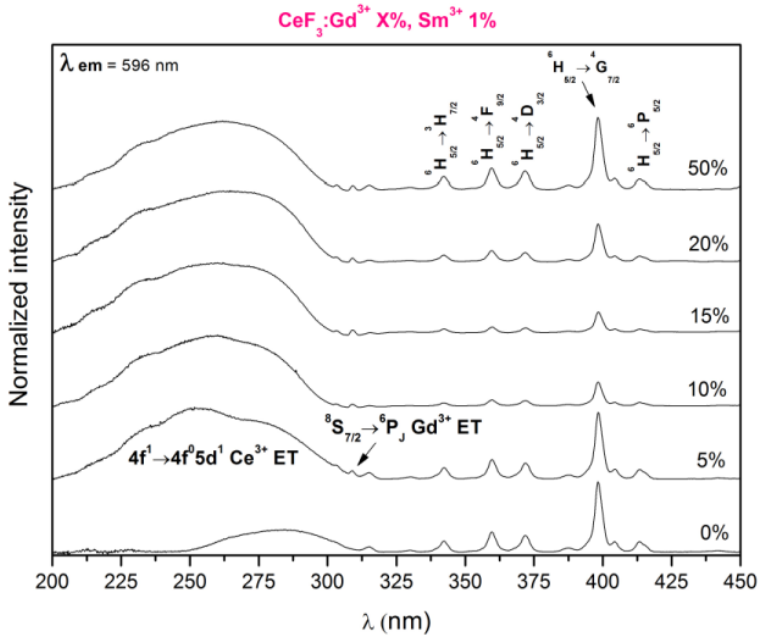

Fig. S3 Excitation spectra of the CeF_3:Gd^{3+} X%, Sm^{3+} 1% nanophosphors.

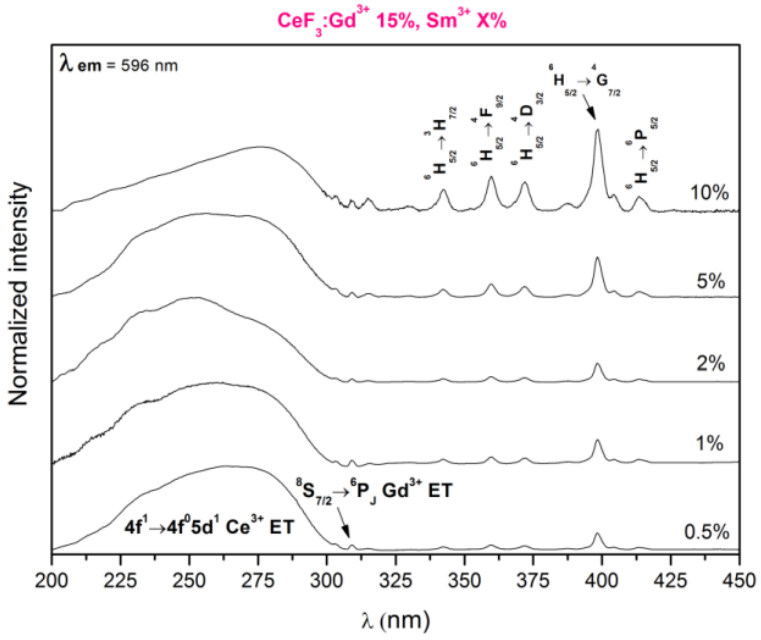

Fig. S4 Excitation spectra of the CeF_3:Gd^{3+} 15%, Sm^{3+} X% nanophosphors.

The emission spectra of the products, namely CeF_3:Gd^{3+} X%, Sm^{3+} 1% (X = 0-50%) and CeF_3:Gd^{3+} 15%, Sm^{3+} X% (X = 0.5-10%) are presented in Figs. S5 and S6. All of the spectra were recorded at λ_{ex} = 254. The spectra were normalized to the intensity of the most intense band. The intensity ratio of the bands corresponding to the transitions of the Sm^{3+} ion ($^4G_{5/2}\rightarrow{}^6H_J$) is generally the same in the presented series of the products. This is because the compounds synthesized are composed of the same hexagonal fluorides.

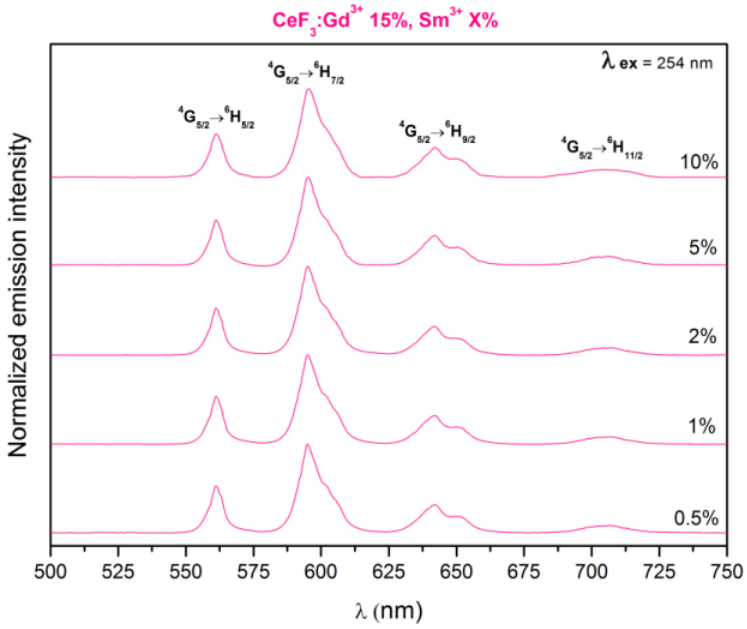

Fig. S5 Emission spectra of the CeF_3:Gd^{3+} 15%, Sm^{3+} X% nanophosphors.

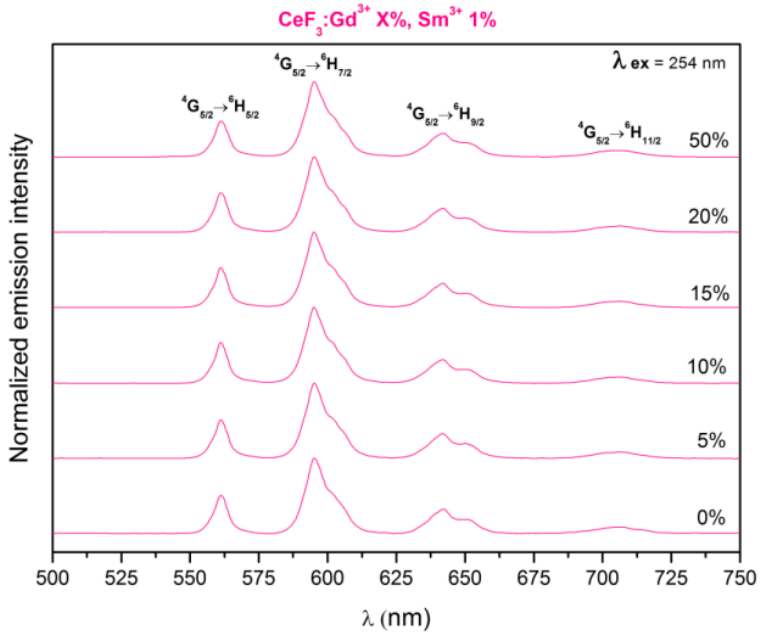

Fig. S6 Emission spectra of the $CeF_3:Gd^{3+}$ X%, Sm^{3+} 1% nanophosphors.

Figs. S7 and S8 present the luminescence decay profiles of $CeF_3:Gd^{3+}$ X%, Sm^{3+} 1% and $CeF_3:Gd^{3+}$ 15%, Sm^{3+} X%, recorded at λ_{ex} = 254 nm and λ_{em} = 596 nm. The decay curves of the samples fitted well the $y=A_1*\exp(-x/\tau_1)+A_2*\exp(-x/\tau_2)+y0$ mathematic function ($R > 0.999$). The biexponential decay of the precipitated nanoparticles confirms that the Sm^{3+} ions occupy two types of sites in the structure, which is commonly found in small nanoparticles, having large surface-to-volume ratio. The longer lifetime component (τ_1) is related to the inner ions (inside the crystals), whereas the shorter one (τ_2) corresponds to the surface Sm^{3+} ions. In Fig. S7 the longest lifetime (τ_1 = 7.63 ms; τ_2 = 3.21 ms) exhibits the $CeF_3:Gd^{3+}$ 15%, Sm^{3+} 1% sample, containing an optimal amount of the Gd^{3+} ions. The products having less or more the Gd^{3+} ions in their structure revealed shorter emission lifetimes. In Fig. S8 the products exhibited lifetime shortening together with the increasing concentration of the Sm^{3+} ions. This is because of the concentration quenching phenomenon, resulting in a shorter radiative lifetime of the products containing higher amount of emitting ions (luminescence activators). However, the $CeF_3:Gd^{3+}$ 15%, Sm^{3+} 1% product, having an optimal amount of the

Sm^{3+} ions, revealed the highest contribution of the first lifetime component (50.7% of τ_1 and 49.3% of τ_2) in comparison to the rest samples in the series.

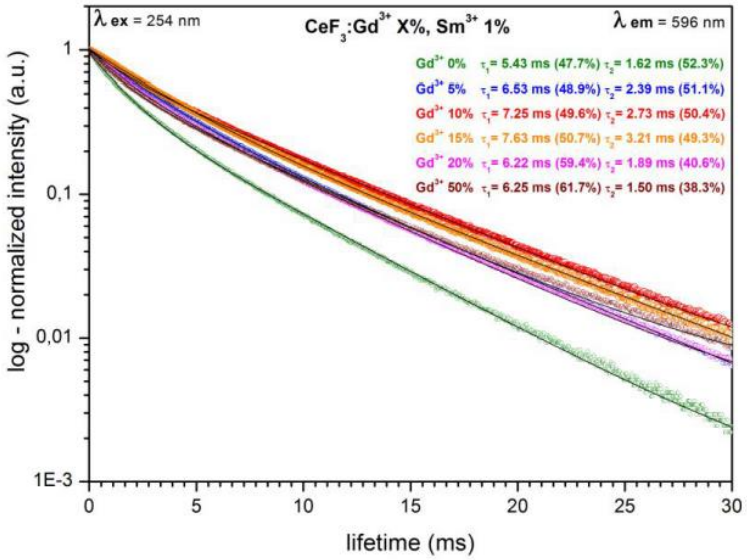

Fig. S7 Luminescence decay curves of the $CeF_3:Gd^{3+}$ X%, Sm^{3+} 1% nanophosphors.

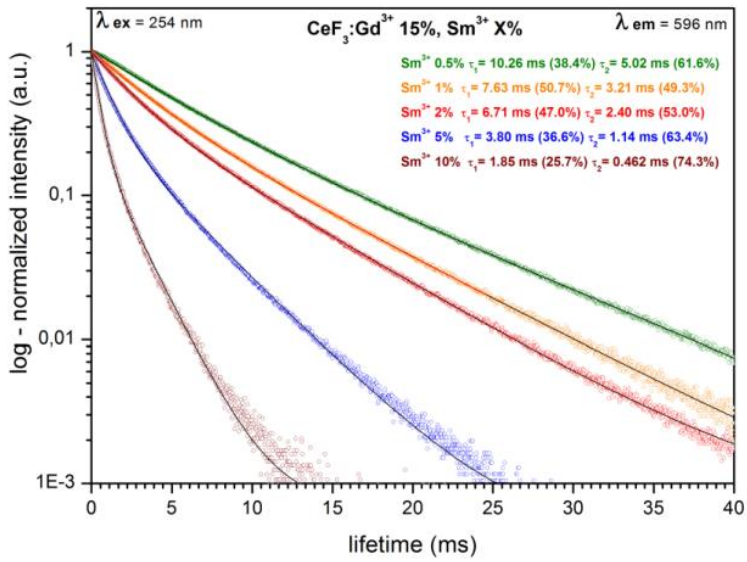

Fig. S8 Luminescence decay curves of the $CeF_3:Gd^{3+}$ 15%, Sm^{3+} X% nanophosphors.

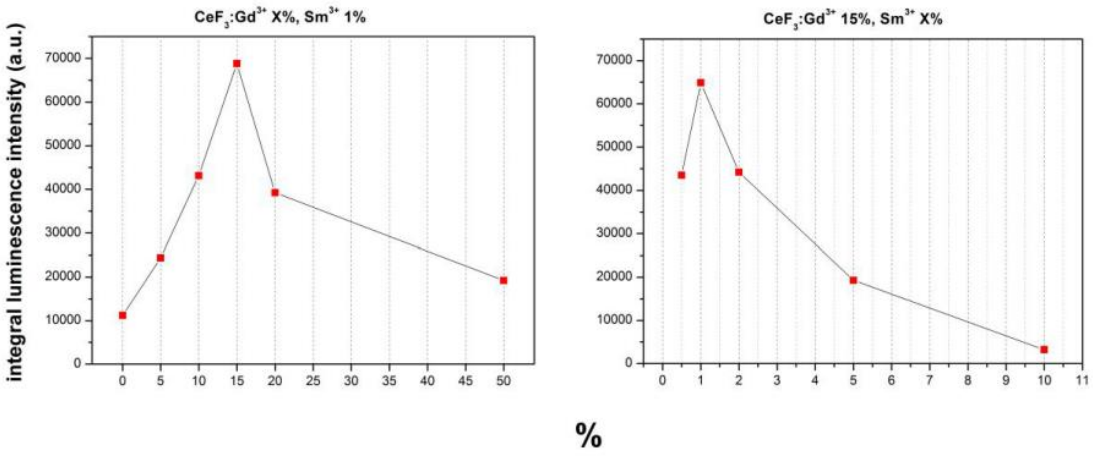

Fig. S9 Comparison of total luminescence intensity of the $CeF_3:Gd^{3+}$ X%, Sm^{3+} 1% and $CeF_3:Gd^{3+}$ 15%, Sm^{3+} X% nanophosphors.

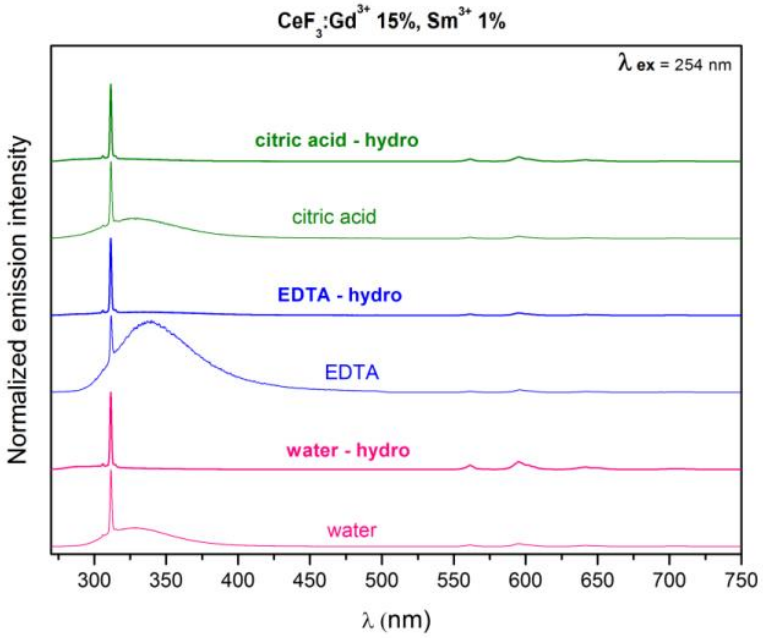

Fig. S10 Emission spectra of the $CeF_3:Gd^{3+}$ 15%, Sm^{3+} 1% nanomaterials, obtained by a coprecipitation method and by a hydrothermal post-treatment (hydro). The spectra were normalized to the most intense band.

In order to investigate the stability of the organic surface layer and confirm the composition of the nanomaterials synthesized (via co-precipitation method), thermogravimetry–differential thermal analysis (TG–DTA) measurements were performed. Below 100°C the first weight loss assigned to the moisture (absorbed water molecules) evaporation was observed. In the case of the product obtained in the presence of EDTA (left), two intense exothermic peaks around 206 and 312°C were observed. The first peak was probably related with structural changes/decarboxylation of EDTA molecules (partial weight loss), whereas the second peak was related to the total decomposition and detachment of the organic compound (from the nanoparticles surface). The product synthesized in the presence of citric acid (centre), revealed also two less intense exothermic peaks around 284 and 328°C. At higher temperature (>350°C) the lanthanide fluoride nanoparticles oxidize forming lanthanide oxyfluorides, and finally lanthanide oxides (≈800-1000°C).

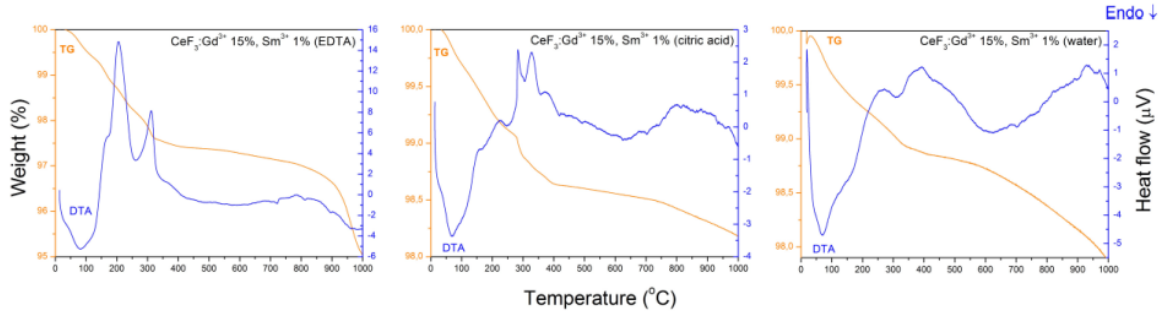

Fig. S11 TG-DTA curves of CeF_3:Gd^{3+} 15%, Sm^{3+} 1% obtained in pure water and in the presence of citric acid or EDTA.

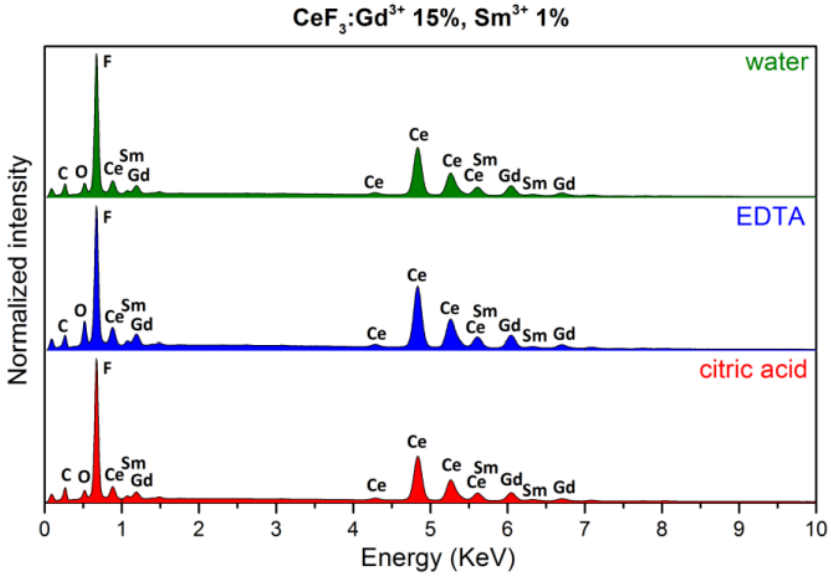

Fig. S12 EDX spectra of CeF_3:Gd^{3+} 15%, Sm^{3+} 1% nanophosphors, coprecipitated in pure water and in the presence of citric acid or EDTA.

Problemem badawczym, jaki podjąłem w pracy pt. „*Preparation and photophysical properties of luminescent nanoparticles based on lanthanide doped fluorides (LaF_3:Ce^{3+}, Gd^{3+}, Eu^{3+}), obtained in the presence of different surfactants*" było otrzymanie wydajnych nanoluminoforów wykazujących czerwoną luminescencję pod wpływem promieniowania UV oraz zbadanie wpływu modyfikatorów organicznych na strukturę, morfologię i właściwości spektroskopowe powstałych produktów. W tym celu wybrano fluorek lantanu jako wydajną matrycę, która domieszkowano jonami Ce^{3+}, Gd^{3+}, Eu^{3+}. Rolę emitera (aktywatora luminescencji) pełnił w tym układzie jon Eu^{3+}, natomiast jon Gd^{3+} pełnił role mediatora, pośrednicząc (zmniejszając przerwę energetyczna pomiędzy najniższymi stanami wzbudzonymi Ce^{3+} i Eu^{3+}) w przeniesieniu energii z jonu Ce^{3+} do jonu Eu^{3+}. W trakcie badań zmieniano kolejno stężenia wszystkich jonów w celu znalezienia optymalnego układu, wykazującego najbardziej intensywną luminescencję. Po ustaleniu optymalnych stężeń domieszek wykonano syntezę szeregu nanomateriałów luminescencyjnych o tym samym składzie fazy krystalicznej, ale przy użyciu różnych surfaktantów/anty-aglomerantów (metody micelarne). Czynnikami tymi były różne związki organiczne oddziaływujące na powierzchnię nanokryształów i mogące potencjalnie wpływać na właściwości fizykochemiczne nanocząstek. Okazało się, iż niektóre związki (w szczególności kwas poliakrylowy – PAA), powodowały znaczące zmniejszenie się rozmiaru nanocząstek i jednoczesny spadek intensywności ich emisji. Ponadto obserwowano wzrost objętości komórki elementarnej, wraz z zmniejszeniem się rozmiaru ziaren produktów. Wyznaczone wartości absolutnych i względnych wydajności kwantowych były zgodne z obserwowana zmianą intensywności luminescencji otrzymanych materiałów. Właściwości fizykochemiczne otrzymanych produktów zostały zbadane przy użyciu metod takich jak: XRD, TEM, FT-IR i spektrofluorymetria. W zależności od użytych organicznych modyfikatorów powierzchni, część otrzymanych nanocząstek tworzyła stabilne koloidy wodne. Przyczyniło się to do zastosowania takich związków organicznych w dalszych syntezach bardziej złożonych nanostruktur typu rdzeń/powłoka (core/shell).

Wkład własny w powstanie pracy: koncepcja badań, wykonanie syntezy i zbadanie właściwości fizykochemicznych otrzymanych produktów. Analiza uzyskanych wyników, opracowanie danych i zredagowanie publikacji.

Journal of Alloys and Compounds 597 (2014) 63–71

Contents lists available at ScienceDirect

Journal of Alloys and Compounds

journal homepage: www.elsevier.com/locate/jalcom

Preparation and photophysical properties of luminescent nanoparticles based on lanthanide doped fluorides (LaF_3:Ce^{3+}, Gd^{3+}, Eu^{3+}), obtained in the presence of different surfactants

Marcin Runowski, Stefan Lis *

Adam Mickiewicz University, Faculty of Chemistry, Department of Rare Earths, Grunwaldzka 6, 60-780 Poznań, Poland

ARTICLE INFO

Article history:
Received 12 December 2013
Received in revised form 28 January 2014
Accepted 28 January 2014
Available online 5 February 2014

Keywords:
Luminescence
Eu^{3+} doped lanthanide fluorides
Energy transfer
Nanophosphors
Nanomaterials
Organic surface modifiers

ABSTRACT

A series of nanomaterials composed of LaF_3:Ce^{3+} 10%, Gd^{3+} 30%, Eu^{3+} 1% was synthesized via a facile co-precipitation approach. The reaction between appropriate lanthanide (Ln^{3+}) and fluoride ions resulted in the formation of crystalline, Ln^{3+} doped fluorides and was performed in the presence of a series of organic modifiers, acting as surfactants and anti-agglomeration agents. Modifiers such as polyacrylic acid (PAA), ethylenediaminetetraacetic acid (EDTA), citric acid and oleylamine most significantly influenced the morphology and spectroscopic properties of the products. The product obtained in the presence of PAA was composed of the smallest nanoparticles (ca. 5–6 nm), with narrow size/shape distribution. All fluorides synthesized exhibited intensive, bright red luminescence under UV irradiation ($\lambda_{ex} \approx 250$ nm), because of the presence of Eu^{3+} ions in their structure. The efficient intensity of luminescence was a result of indirect excitation, via energy transfer (ET) phenomena occurring in the system ($Ce^{3+} \rightarrow Gd^{3+} \rightarrow Eu^{3+}$). The structure and morphology of the obtained nanomaterials were established by powder X-ray Diffraction (XRD) and Transmission Electron Microscopy (TEM) measurements. Optical properties of the obtained compounds were studied and discussed on the basis of excitation emission spectra and luminescence decay curves. On the basis of the performed measurements, luminescence quantum yield (absolute and relative) and radiative lifetimes were calculated and analyzed. FT-IR spectroscopy was applied to examine the presence of molecules of the organic modifiers on the nanoparticles surface.

1. Introduction

Luminescent materials have been extensively studied over the last two decades by many scientists and engineers [1–6]. Recently, much attention has been paid towards luminescent nanomaterials, namely the materials composed of small, luminescent nanoparticles. There are many classes of such compounds, i.e. luminescent organic compounds, semiconductive quantum dots (q-dots), inorganic materials based on lanthanide (Ln) doped compounds [7–11]. Each class of these compounds has their own benefits and drawbacks. Luminescent materials based on organic structures can exhibit strong and efficient emission, thanks to high quantum yield (QY) and molar absorption coefficient. However, they are often thermally and photochemically unstable, exhibiting variable luminescence in time, due to photobleaching effect after light irradiation. Luminescent q-dots are much more stable, they exhibit bright multicolor luminescence, and they can be easily obtained as nanosized particles. On the other hand, some of them are cytotoxic like the commonly studied ones based on cadmium, selenium and tellurium elements [12]. Inorganic materials doped with Ln^{3+} ions can exhibit multicolor luminescence under UV (down-conversion) or NIR (up-conversion) excitation, depending on the selected dopant ions (e.g. Tb^{3+} – green, Eu^{3+} – red, Tm^{3+} – blue) [13–16]. They can be also obtained as nanosized, crystalline materials. The color of their emission depends on the dopant ions used in a given system, the molar ratio of the ions used and crystal structure of the host material [17–19]. The mechanism responsible for their luminescence properties involves forbidden 4f–4f transitions within the 4f-electron shell of the Ln^{3+} ion. Because of the forbidden character of such transitions, their relative intensity is rather weak. In order to increase the luminescence intensity of the Ln^{3+} ions, the allowed energy transfer (ET) or charge transfer (CT) transitions are frequently used [20–22]. These phenomena occur for instance in Tb^{3+} doped CeF_3 nanoparticles, in which after UV excitation, the energy transfer from Ce^{3+} to Tb^{3+} ions occurs,

* Corresponding author. Tel.: +48 61 8291345.
E-mail address: blis@amu.edu.pl (S. Lis).

http://dx.doi.org/10.1016/j.jallcom.2014.01.209
0925-8388/

showing effective green emission of the Tb^{3+} ion being an activator [23]. Other advantages of Ln^{3+} doped nanomaterials are their high thermal stability, photostability, large Stokes shift and long radiative lifetime (in the range of ms) [7,24–27].

The luminescent materials/nanomaterials based on Ln^{3+} doped inorganic structures are usually composed of crystalline doped phosphates – $LnPO_4$ [28], oxides – Ln_2O_3 [29], oxyfluorides – LnOF [30], borates – $LnBO_3$ [31], vanadates $LnVO_3$ [32], fluorides LnF_3 [33] and their more complex analogues like $Ln_xO_yF_z$ [34] or $NaLnF_4$ [35]. All these structures have already been successfully synthesized as nanomaterials exhibiting different particle sizes, structures, morphology and spectroscopic properties.

Lanthanide doped fluorides (LnF_3) have been intensively studied as promising luminescent materials over the last decade [36–38]. LnF_3 are featured with low phonon energy of the crystal lattice (e.g. $LaF_3 \approx 350\ cm^{-1}$), resulting in a relatively high QY of luminescence and diminished nonradiative relaxation of their excited states [39–41]. Their other benefits are multicolor luminescence [17], long radiative lifetimes (several ms) [23], invariable luminescence in time [26], low cytotoxicity [42], well defined crystal structures [43] and possibilities of easy surface modifications. Additionally, LnF_3 can be very easily synthesized in the form of ultra-small nanoparticles, usually close to spherical in shape, which allows the formation of stable colloids. Such nanomaterials based on LnF_3 can be used in a variety of applications, e.g. novel light sources in optoelectronics [44], plasma display panels (PDP) [45], luminescent tracers in forensic [46], bio-imaging/labeling [47] as well as sophisticated core/shell type nanomaterials [42].

Here we report an easy coprecipitation synthesis of a series of nanocrystalline fluorides, based on LaF_3 codoped with Ce^{3+}, Gd^{3+} and Eu^{3+} ions. The nanophosphors obtained exhibited bright red luminescence due to the ET phenomena from Ce^{3+} to Gd^{3+} ions and then to the activator ion, i.e. Eu^{3+}. The products were synthesized in the presence of various organic compounds acting as anti-agglomeration/crystallization directing agents.

2. Experimental

2.1. Materials

The appropriate amounts of Eu_2O_3, Gd_2O_3, and La_2O_3 oxides (Stanford Materials, 99.99%) were separately dissolved in a concentrated, nitric acid, HNO_3 (POCh S.A., ultra-pure) in order to obtain $Eu(NO_3)_3$, $Gd(NO_3)_3$ and $La(NO_3)_3$ aqueous solutions of a known molar concentration, respectively. $CeCl_3{\cdot}7H_2O$ (99.9%), polyacrylic acid (PAA – average $M_w \approx 1800$), adypic acid (≥99.5%, HPLC), polyvinylpyrrolidone (PVP – pure p.a.), polyvinyl alcohol (PVA – pure p.a.) and oleylamine (70%, pure) were purchased from Sigma Aldrich. Ammonium fluoride, NH_4F (ACS grade, 98+%), citric acid (>99.5%, pure p.a., hydrate), ethylenediaminetetraacetic acid (EDTA – >98%, pure p.a.), Triton X-100, ethylene glycol (pure p.a.) and glycerine (pure p.a.) were purchased from POCh S.A. Polyethylene glycol 6000 (PEG – 98%, pure), cetyltrimethylammonium bromide (CTAB – 98%, pure) were purchased from Alfa Aesar. Distilled water was used in all experiments.

2.2. Synthesis

All syntheses were performed to get 0.5 g of the product. The typical synthesis of a given nanophosphor was as follows: NH_4F (50% stoichiometric excess) was dissolved in 25 mL of water/ethanol 50/50 solvent system. The second solution was prepared by mixing $Ln(NO_3)_3$ and $CeCl_3$ aqueous solutions at an appropriate molar ratio (0.1 $CeCl_3$, 0.3 $Gd(NO_3)_3$, 0.01 $Eu(NO_3)_3$ and 0.59 $La(NO_3)_3$ mol%). The obtained aqueous solution was filled with water up to 50 mL and mixed with 50 mL of ethanol. 1 wt.% of a chosen organic modifier was dissolved in both solutions. The as-prepared solutions were transferred onto a hot plate magnetic stirrer and heated to 333 K upon vigorous stirring. The pH of all as-prepared solutions during the syntheses was adjusted to be pH ≈ 5. The heated solution containing lanthanide ions was transferred into the addition funnel, and slowly dropped to the continuously heated and stirred solution containing F^- ions. The addition was completed in 30 min. Subsequently, the white precipitates formed were collected and washed several times with ethanol and water, in order to purify the compound synthesized. The final products were dried in an oven at 85 °C for 24 h. The scheme of synthesis in Fig. 1 illustrates a formation of LaF_3:Ce^{3+}, Gd^{3+}, Eu^{3+} nanoparticles, in the presence of surfactants/organic modifiers.

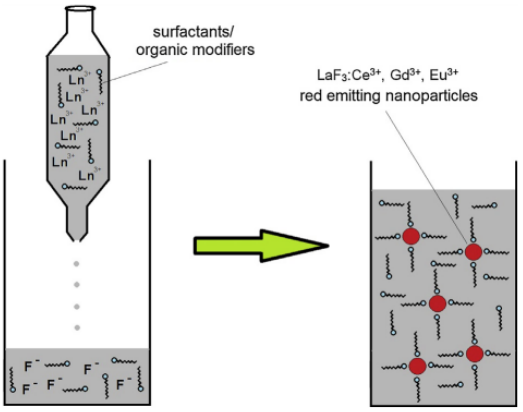

Fig. 1. Synthesis scheme of LaF_3:Ce^{3+}, Gd^{3+}, Eu^{3+} nanoparticles.

2.3. Characterization

Powder X-ray diffractograms were recorded using a Bruker AXS D8 Advance diffractometer, using Cu Kα radiation (λ = 1.5406 Å) in the 2θ ranges from 6° to 60° (resolution 0.05°/step). On the basis of the recorded diffractograms, the average grains sizes were estimated using Scherrer's equation [48]:

$$D = \frac{k\lambda}{\cos\theta\sqrt{\beta^2 - \beta'^2}}$$

where D is grain size, k is a shape factor (0.9 for spherical particles), λ is the wavelength of radiation, θ is an angle of diffraction, β is a Full Width at Half Maximum (FWHM) and β' stands for an instrumental effect. Transmission electron microscopy measurements were performed using a Transmission Electron Microscope JEM 1200 EXII, JEOL, operating at accelerating voltage 80 kV. FT-IR spectra were measured using an FT-IR spectrophotometer, JASCO 4200. The spectra were recorded in transmission mode at resolution of 4 cm^{-1}. Before each measurement, the samples were mixed with KBr, ground and pressed into disks. The excitation, emission spectra and luminescence decay curves were measured using a Hitachi F-7000 spectrofluorometer at 293 K. The excitation and emission spectra were recorded at resolution of 0.2 nm and appropriately corrected for the apparatus response. The luminescence QY of the obtained nanophosphors were determined by two different methods (absolute and relative) and compared. The first method was described by Wrighton et al. [49] and successfully used by others [23,50]. In order to measure the absolute QY of luminescence via this method, the diffuse reflectance of the sample relative to a nonabsorbing standard (e.g. KBr, MgO, La_2O_3) must be measured at the excitation and emission wavelengths of the sample under the same conditions. The obtained QY of luminescence is the ratio of photons emitted to the difference of diffuse reflected photons by the measured sample and the nonabsorbing standard. As a nonabsorbing standard we chose La_2O_3. The absolute QY of luminescence (φ) of the products was calculated from the following equation:

$$\varphi = \frac{E}{(R - R')} \quad (1)$$

where E is an integral emission intensity of the sample, R is an integral diffuse reflectance intensity of the nonabsorbing standard and R' is an integral diffuse reflectance intensity of the measured sample. All data were recorded at the same excitation wavelength (249 nm). The second method applied for determination of the luminescence QY of nanophosphors synthesized was a relative one. This method is based on Judd–Ofelt (J–O) theory, and allows the determination of QY, as well as J–O intensity parameters (see SI). This approach was used first by Kodaira et al. [51] and further successfully applied by others [43,52]. The method uses averaged lifetimes of luminescence ($\tau = \int I(t)\tau dt / \int I(\tau)dt$) and intensity ratio of the radiative transitions in the emitting Ln^{3+} ion (in our case $^5D_0 \rightarrow {}^7F_j$ transitions of the Eu^{3+} ion) for QY determination.

3. Results and discussion

3.1. Selection of the dopant concentrations

A series of nanocrystalline lanthanide fluorides (LaF_3:Ce^{3+}, Gd^{3+}, Eu^{3+}) was synthesized via an easy and low-cost coprecipitation method, in the presence of commonly used anti-agglomeration

agents/surface modifiers. The organic stabilizers used were the following: PAA, citric acid, adipic acid, EDTA, CTAB, Triton X-100, PEG, PVP, PVA, oleylamine, ethylene glycol and glycerine. They were used to investigate their influence on morphological, structural and spectroscopic properties of the nanophosphors synthesized. The goal of this work was to synthesize efficient and inexpensive nanophosphors, featured with small size and narrow size/shape distribution. Eu^{3+} ion was selected as an efficient luminescence activator, resulting in intensive red emission of the nanomaterials obtained. Our intention was to limit the total amount of expensive Ln^{3+} ions in the obtained nanophosphors (Eu^{3+} and Gd^{3+}), as well as Ce^{3+} ions, which can be relatively easily oxidized at elevated temperature and after high-energy light irradiation [53–55]. Altering single Ln^{3+} ion concentration in the crystal structure, with the amount of the remaining ions fixed, we were able to determine the optimal dopant concentrations/ratios, resulting in the most effective luminescence of the system. The structure and morphology of the synthesized LaF_3:Ce^{3+}, Gd^{3+}, Eu^{3+} were not changed upon doping with various concentrations of Ln^{3+} ions (see Fig. S1 in Supporting Information), except for slightly changed unit cell parameters, caused by small differences in the ionic radii of different Ln^{3+} ion. All products had the same hexagonal structure of LaF_3, isostructural with CeF_3, which will be discussed in the next paragraph. Fig. S2 shows a comparison of integral emission intensity, for the samples doped with different concentrations of Ln^{3+} ions (discussed further in the manuscript). As a result of this study, LaF_3:Ce^{3+} 10%, Gd^{3+} 30%, Eu^{3+} 1% was found to be the most efficient phosphor, exhibiting the highest integral emission intensity. This compound was used for further syntheses and photophysical studies with a series of the organic modifiers mentioned above.

3.2. Structure and morphology

The nanoparticles LaF_3:Ce^{3+} 10%, Gd^{3+} 30%, Eu^{3+} 1% crystallized in a hexagonal system, $P\bar{3}c1$ space group. Fig. 2 presents the recorded powder diffractograms of the products. They fitted well the reference pattern of hexagonal LaF_3, taken from Inorganic Crystal Structure Database (ICSD), card No. 04-005-4417. The recorded XRD patterns exhibited significant broadening of reflexes, which is common for nanocrystalline particles. On the basis on the Scherrer equation, the average grain sizes of the synthesized LaF_3:Ce^{3+} 10%, Gd^{3+} 30%, Eu^{3+} 1% nanoparticles were estimated [48], and presented in Fig. 3a. The samples obtained in the presence of PAA, oleylamine or citric acid revealed the smallest particle size in the range 7–9 nm. Other products had particle size in the range 10–11 nm, except for the sample denoted as EDTA with particles size of 17 nm. The values obtained correlated well with the TEM data. However, some differences, i.e. smaller values estimated from XRD than from TEM images, were explained by slight differences in the products crystallinity and the presence of crystal strains. One must remember that such small nanoparticles having high surface-to-volume ratio, have surface defects and crystal strains, which also contribute to the broadening of reflexes. In order to calculate cell volumes of the products, the unit cell parameters were obtained by standard Rietveld Analysis (for all samples $R_w < 5$), using anisotropic approach and Maud 2.0 software [56,57]. All calculated cell volumes of the nanomaterials synthesized (Fig. 3b) were smaller than the cell volume of the reference LaF_3 because of the smaller ionic radii of the Ln^{3+} dopant ions. However, in the series a tendency of the cell volume expansion correlating with the decreasing size of the nanomaterials could be observed. The samples denoted as PAA, oleylamine and citric acid having the smallest grain sizes, revealed the largest cell volumes. This phenomenon was related to the crystal strains in the small nanocrystalline particles, resulting in an elevated pressure inside nanocrystals, which caused unit cell expansion [58]. The effect increases with decreasing grain sizes of the products.

Fig. 4 presents TEM images of the nanomaterials synthesized. The images a–f depict LaF_3:Ce^{3+} 10%, Gd^{3+} 30%, Eu^{3+} 1% obtained in the presence of the following organic compounds: PAA (a), oleylamine (b), EDTA (c), citric acid (d), Triton X-100 (e), and PVP (f),

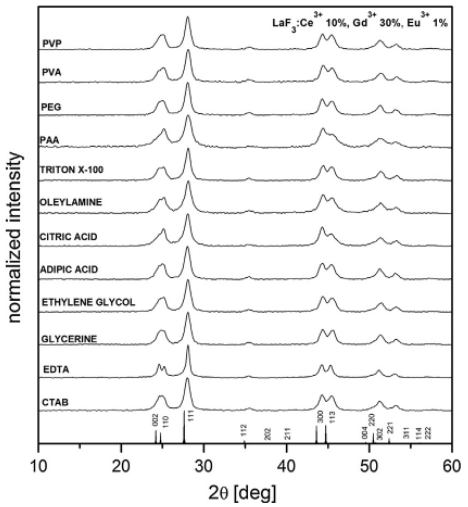

Fig. 2. XRD patterns of LaF_3:Ce^{3+} 10%, Gd^{3+} 30%, Eu^{3+} 1% series.

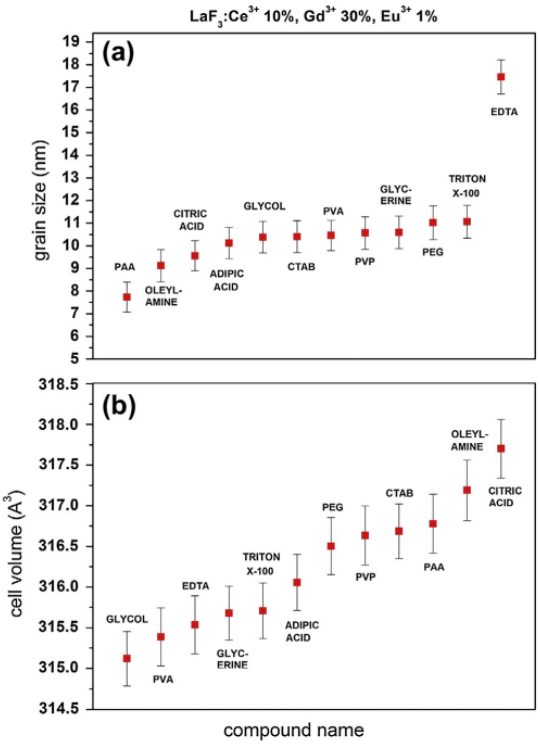

Fig. 3. Estimated grain size (a) and calculated cell volume (b) of LaF_3:Ce^{3+} 10%, Gd^{3+} 30%, Eu^{3+} 1% nanocrystals.

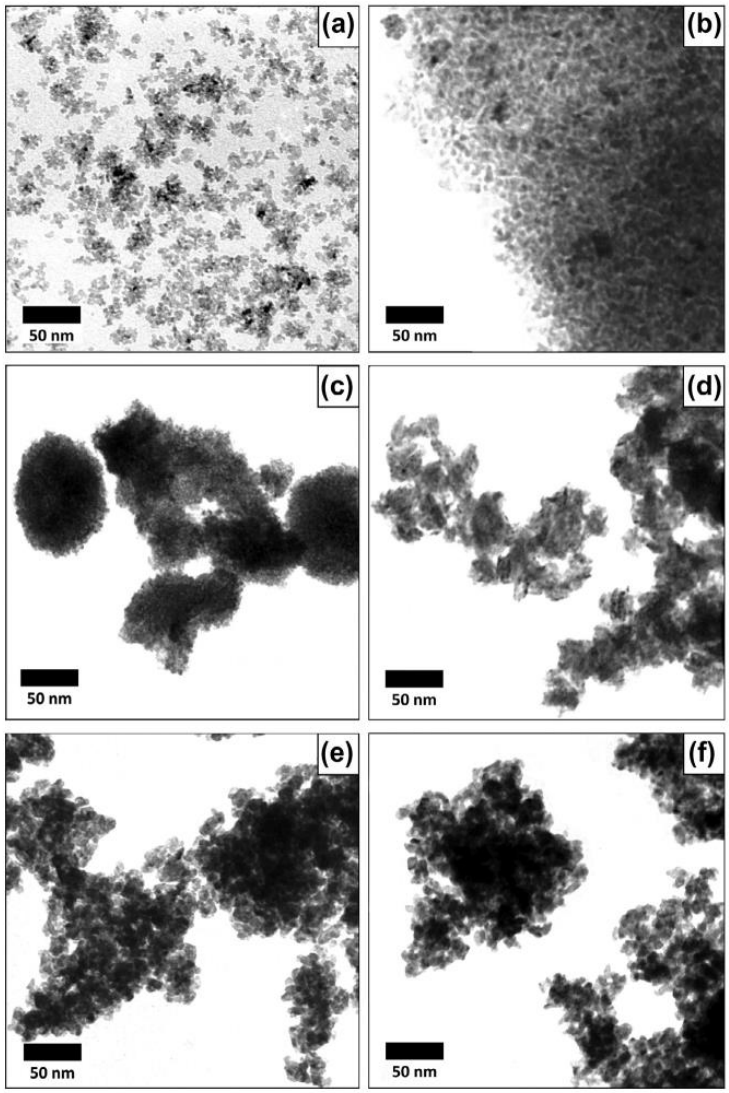

Fig. 4. TEM images of LaF_3:Ce^{3+} 10%, Gd^{3+} 30%, Eu^{3+} 1% nanostructures obtained in the presence of PAA (a), oleylamine (b), EDTA (c), citric acid (d), Triton X-100 (e), and PVP (f).

respectively. Because of a similar morphology (size/shape distribution) of the other nanomaterials to the samples e and f, the data for the other materials are presented (samples g–l) in the Supporting Information (Fig. S3). The product obtained using PAA (a) was composed of uniform and very small nanoparticles, which size was in the range of 5–6 nm. The particles did not agglomerate and formed very stable aqueous colloids (no observed sedimentation was noted over many days, which also resulted in difficulties with the product purification by centrifugation). PAA acted as a very effective crystallization directing agent, surfactant and surface modifier. Sample b synthesized in the presence of oleylamine also consisted of small nanoparticles whose sizes were in the range 7–9 nm. However, the particles exhibited higher level of agglomeration in comparison to those in sample a. The product obtained in the presence of EDTA (c) was composed of aggregates of about 80–100 nm and close to spherical shape and did not form stable colloidal systems. Sample d, synthesized in the presence of citric acid, consisted of aggregates of 30–40 nm of smaller nanoparticles. Samples e and f as well as g–l (see SI) exhibited similar morphologies. Their average grain sizes were in the range of 10–11 nm with slight differences depending on the agent used. This leads to a conclusion that the organic compounds used for the syntheses of the first four (a–d) nanomaterials significantly influenced the final morphology of the products obtained, whereas the other ones did not change noticeable the samples morphology. However these organic compounds acted as anti-agglomeration agents, decreasing the level in agglomeration of the final products, depending on the organic compound used.

Fig. 5 presents the FT-IR spectra of the nanomaterials synthesized. Four of them modified with PAA, EDTA, citric acid, oleylamine are discussed here in details, because of the presence of organic modifiers on their surface, manifested as the absorption

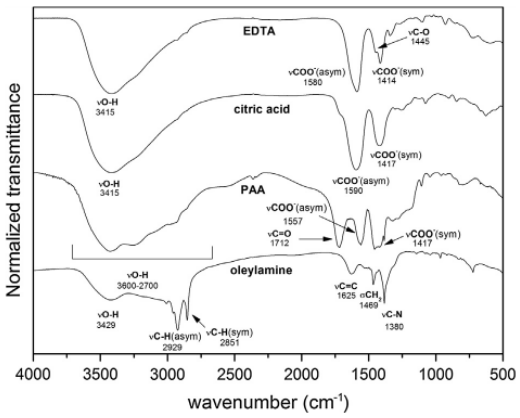

Fig. 5. FT-IR spectra of LaF_3:Ce^{3+} 10%, Gd^{3+} 30%, Eu^{3+} 1% nanomaterials synthesized in the presence of EDTA, citric acid, PAA, oleylamine.

peaks observed. In all spectra the broad and intensive band corresponding to the O—H stretching (ν) vibrations can be observed around 3400 cm^{-1}. This band originates from the adsorbed water molecules. The second band related to H_2O molecules (O—H deformation (σ) vibrations), which should at 1640 cm^{-1}, overlaps with different absorption bands, corresponding to the organic modifiers. In the spectrum of EDTA modified nanomaterial three are two absorption bands at 1580 and 1414 cm^{-1} assigned to asymmetric and symmetric vibrations of —COO^- groups, respectively. The band at 1445 cm^{-1} corresponds to νC—O vibrations. The spectrum of the nanomaterial obtained in the presence of citric acid exhibits similar bands, i.e. peaks at 1590 and 1417 cm^{-1} assigned to the asymmetric and symmetric ν vibrations of —COO^- groups, respectively. The presence of these bands confirms the deprotonated character of carboxylic groups in the organic acid molecules, and their attachment to the surface. These bands can be also observed in the PAA modified nanomaterial, at 1557 and 1417 cm^{-1}, assigned to the asymmetric and symmetric ν vibrations of —COO^- groups, respectively. Other bands in this spectrum are the one at 1712 cm^{-1} assigned to νC=O vibrations, and a very broad and intensive band in the range of 2700–3600 cm^{-1} assigned to νO—H vibrations of PAA molecules. The spectrum of the product synthesized in the presence of oleylamine exhibits the following bands: $\nu C{-}H_{(asym)}$ at 2929 cm^{-1}, $\nu C{-}H_{(sym)}$ at 2851 cm^{-1}, νC=C at 1625 cm^{-1}, σCH_2 at 1469 cm^{-1} and νC—N at 1380 cm^{-1}. The bands assigned to —NH_2 groups were not detected because of their overlapping with a broad band originating from water molecules (νO—H). The spectra of the other compounds are presented in the Supporting Information (Fig. S4). In those spectra the bands corresponding to the vibrations of water and ethanol molecules were dominant and the absorption band related to the organic modifiers could hardly be observed. It was probably related with weak interactions between the organic modifiers and fluoride nanocrystals, and their subsequent easy detachment in the purification process.

3.3. Luminescence properties

The obtained nanophosphors exhibited intensive luminescence, resulting from effective energy transfer (ET) process, commonly occurring in lanthanide based luminescent compounds, both organic and inorganic. Thanks to this phenomenon, indirectly excited (by ET) phosphors can exhibit increased luminescence intensity, as compared to directly excited ones, e.g. LaF_3:Eu^{3+}. Direct excitation of these phosphors is inefficient, because of the selection rules forbidden 4f–4f transitions in the emitting Ln^{3+} ions (e.g. Sm^{3+}, Eu^{3+}, Tb^{3+}, Dy^{3+}), and results in weak luminescence of these ions. Ce^{3+} ion is a well known luminescence sensitizer (energy donor) which can transfer energy to a desired Ln^{3+} ion [17,20,23]. Compounds doped with Ce^{3+} ions reveal broad and intensive band around 250 nm in their excitation spectrum. This band corresponds to the $4f^1 \rightarrow 4f^05d^1$ transition of the Ce^{3+} ion. Such ET phenomenon can be applied in many compounds, such as CeF_3:Tb^{3+} and $LaPO_4$:-Ce^{3+}, Tb^{3+}. However, in Ce^{3+}/Eu^{3+} doped compounds, the ET process does not occur effectively, and the energy cannot be efficiently transferred from the excited Ce^{3+} ions to the emitting Eu^{3+} ions. The reason for this is a too large energy gap between the lowest excited state of Ce^{3+} and the lowest excited state of Eu^{3+} [17,59]. That is why an energy mediator ion, whose lowest excited state is situated between the excited states of Ce^{3+} and Eu^{3+} should participate in ET between these ions. In the materials studied Gd^{3+} ion was embedded in the structure of the final nanophosphors, acting simultaneously as an energy acceptor from Ce^{3+} ions and as an energy donor to the emitting Eu^{3+} ions (see ET scheme in Fig. 6).

As mentioned above, the LaF_3:Ce^{3+} 10%, Gd^{3+} 30%, Eu^{3+} 1% compound was selected as the most efficient red phosphor, exhibiting the highest total emission in the visible spectral range. The selection was made from a series of variously doped fluorides. If the concentration of the dopant ions (Ce^{3+}, Gd^{3+}, Eu^{3+}) was too small, the ET via crystal lattice would be limited and ineffective. However, if their concentrations exceeded a certain threshold, the concentration quenching/cross relaxation process would take place, deteriorating the final emission intensity of the emitter ion (see Fig. S2). This effect was the most pronounced for Eu^{3+} ion, which is very sensitive to concentration quenching phenomena [60,61].

Luminescence properties of the synthesized nanomaterials are presented in Figs. 7–11. All spectra including luminescence decay curves were measured at 293 K, in ambient conditions.

Fig. 7 presents the excitation spectra of a series of fluorides, LaF_3:Ce^{3+} 10%, Gd^{3+} 30%, Eu^{3+} 1% obtained in the presence of different anti-agglomeration agents/surfactants. The spectra were measured at λ_{em} = 592 nm, at which the most intensive band corre-

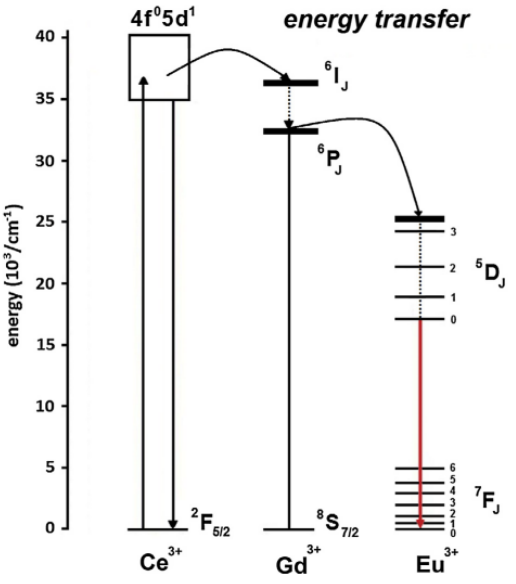

Fig. 6. Energy transfer (ET) scheme for LnF_3 codoped with Ce^{3+}, Gd^{3+} and Eu^{3+} ions.

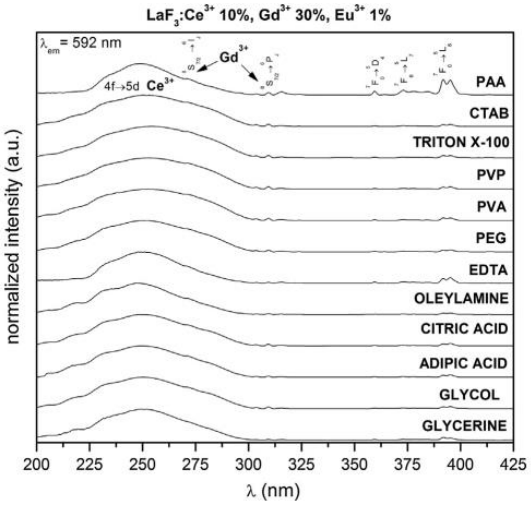

Fig. 7. Excitation spectra of $LaF_3:Ce^{3+}$ 10%, Gd^{3+} 30%, Eu^{3+} 1% nanophosphors; λ_{em} = 592 nm.

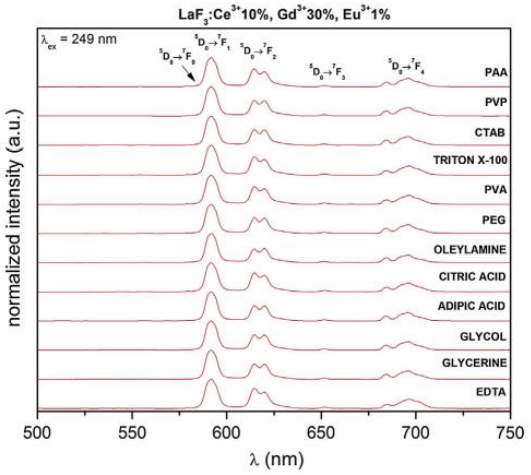

Fig. 8. Emission spectra of $LaF_3:Ce^{3+}$ 10%, Gd^{3+} 30%, Eu^{3+} 1% nanophosphors; λ_{ex} = 249 nm.

sponding to the $^5D_0 \rightarrow {}^7F_1$ transition was observed. All spectra were normalized to the intensity of the most intensive band, namely 4f → 5d Ce^{3+} ET, centred at 249 nm. In the range of ca. 300–400 nm, a series of sharp, less intensive bands corresponding to the intrinsic $4f^8$–$4f^8$ transitions in Eu^{3+} ion, can be observed. In the shorter wavelengths range, the bands assigned to Ce^{3+} and Gd^{3+} ET were recorded. As was mentioned above the very broad and intensive band at 249 nm, was assigned to $4f^1 \rightarrow 4f^05d^1$ transition within the Ce^{3+} ion, confirming ET to Gd^{3+} and Eu^{3+} ions. The other two bands at 272 and 310 nm were assigned to the $^8S_{7/2} \rightarrow {}^6I_J$ and $^8S_{7/2} \rightarrow {}^6P_J$ transitions in Gd^{3+} ion, respectively. These bands indicate that direct ET from Gd^{3+} to Eu^{3+} ions can occur. However, small intensity of the corresponding bands means that this process did not cause effective Eu^{3+} excitation. In the spectrum of PAA modified nanophosphors, the observed 4f–4f transitions exhibited relatively high intensity ratio in comparison to the analogous

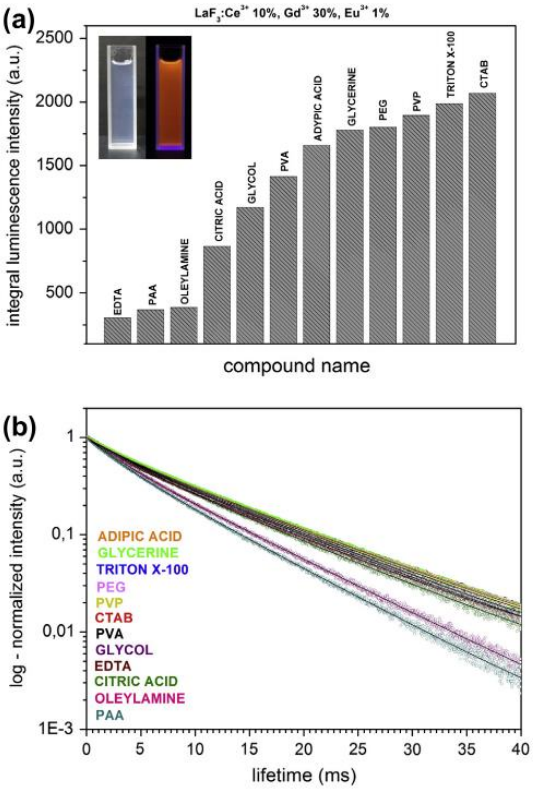

Fig. 9. Integral luminescence intensity (a) and luminescence decay curves: the top curve represents ADIPIC ACID sample, the bottom curve corresponds to PAA sample (b) of $LaF_3:Ce^{3+}$ 10%, Gd^{3+} 30%, Eu^{3+} 1% nanophosphors; λ_{ex} = 249 nm and λ_{em} = 592 nm.

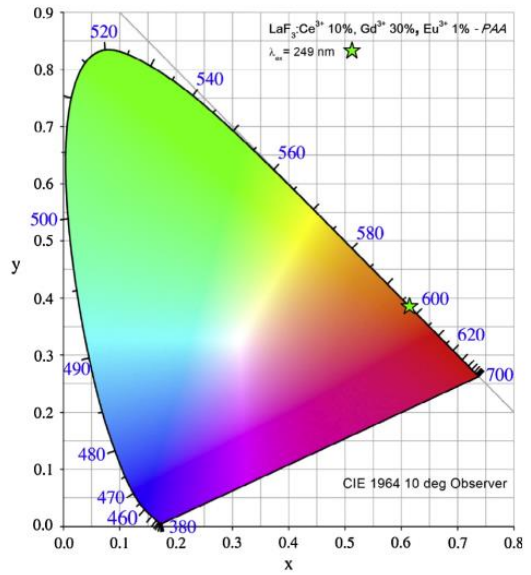

Fig. 10. CIE chromaticity diagram of $LaF_3:Ce^{3+}$ 10%, Gd^{3+} 30%, Eu^{3+} 1% nanophosphor obtained in the presence of PAA.

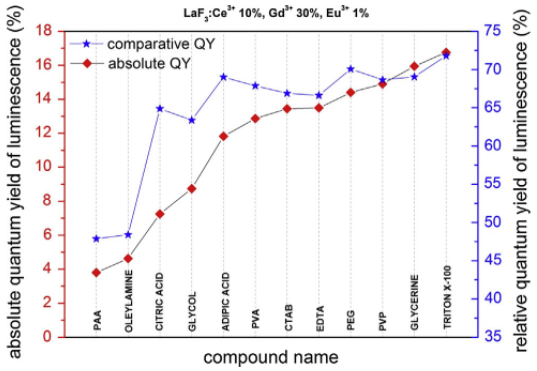

Fig. 11. Comparison of absolute and relative quantum yields for LaF_3:Ce^{3+} 10%, Gd^{3+} 30%, Eu^{3+} 1% nanophosphors; λ_{ex} = 249 nm.

Table 1
Calculated luminescence lifetimes, τ_1 and τ_2 (by fitting to the recorded decay profiles) for LaF_3:Ce^{3+} 10%, Gd^{3+} 30%, Eu^{3+} 1% nanophosphors; λ_{ex} = 249 nm and λ_{em} = 592 nm.

Compound	τ_1	τ_2
ADYPIC ACID	10.13 ms (77%)	3.03 ms (23%)
GLYCERINE	10.13 ms (77%)	3.04 ms (23%)
TRITON X-100	10.12 ms (77%)	3.02 ms (23%)
PEG	10.11 ms (78%)	2.97 ms (22%)
PVP	10.10 ms (78%)	2.80 ms (22%)
CTAB	10.01 ms (77%)	2.94 ms (23%)
PVA	9.80 ms (77%)	2.86 ms (23%)
EDTA	9.68 ms (71%)	4.01 ms (29%)
GLYCOL	9.64 ms (77%)	2.94 ms (23%)
CITRIC ACID	9.60 ms (78%)	2.78 ms (22%)
OLEYLAMINE	7.85 ms (73%)	2.88 ms (23%)
PAA	7.34 ms (77%)	2.77 ms (23%)

bands in the other spectra (because of the less intensive 4f → 5d band). The reason for this high intensity ratio was the UV light absorption by PAA molecules in the 200–300 nm range. Beside, these nanoparticles in the sample modified with PAA revealed the smallest size and one of the highest level of the organic modifier bonding to their surface (see IR spectra). Therefore, thanks to the effective overlapping of the donor (Ce^{3+}, Gd^{3+}) and acceptor (Gd^{3+}, Eu^{3+}) emission/absorption integrals, the sample modified with PAA exhibited intensive, bright red luminescence. One should remember that Gd^{3+} ion acted simultaneously as an energy acceptor and donor, being a mediator in the ET process.

Fig. 8 presents the emission spectra of all nanophosphors synthesized. All spectra were measured at λ_{ex} = 249 nm, at which the most intensive band corresponding to the $4f^1 \rightarrow 4f^05d^1$ transition was observed (Ce^{3+} excitation). All spectra were normalized to the intensity of the most intensive band, assigned to $^5D_0 \rightarrow {}^7F_1$ transition in Eu^{3+} ion, centred at 592 nm. The spectra showed the characteristic, sharp bands corresponding to $^5D_0 \rightarrow {}^7F_j$ (j = 0–4) transitions in Eu^{3+} ion. These transitions occur commonly in inorganic/organic compounds having Eu^{3+} ion in their structure. The presence of these bands in the emission spectra results in a bright red luminescence of the nanophosphors synthesized. The intensity ratio of the bands is similar in the spectra of the whole series of products, because of the same crystal structure and composition of the luminescent phase. The hypersensitive $^5D_0 \rightarrow {}^7F_2$ electric dipole transition (very sensitive to the changes in local symmetry of the Eu^{3+} coordination environment) in all spectra shows lower intensity than the $^5D_0 \rightarrow {}^7F_1$ magnetic dipole transition (insensitive to the changes in Eu^{3+} site symmetry). This fact implies that the Eu^{3+} ions were successfully incorporated in the crystalline structure of the synthesized doped fluorides, featured with high site symmetry. Here is worth noting that the $^5D_0 \rightarrow {}^7F_2$ transition is forbidden and its intensity increases along with decreasing site symmetry of the Eu^{3+} ion site [62]. The intensity ratio of the $^5D_0 \rightarrow {}^7F_2/{}^5D_0 \rightarrow {}^7F_1$ transitions (see Fig. S5) is known as the asymmetry parameter, and it is used to determine the symmetry of the coordination environment of the Eu^{3+} ion embedded in a given structure (crystalline compound or organic complex).

Fig. 9a presents a comparison of the total luminescence intensity of all nanophosphors obtained. The products synthesized in the presence of EDTA, PAA, oleylamine and citric acid revealed the lowest emission intensity. This observation is in a good agreement with IR and TEM data, which showed that the nanoparticles of these compounds exhibited the highest level of organic modification/surface binding and the smallest grain size. Small nanoparticles having surface modified with organic compounds exhibit lower emission intensity because of the UV light absorption by organic molecules and luminescence quenching due to the presence of surface defects. The inset in the Fig. 9 shows bright orange–red[1] luminescence of the aqueous colloidal LaF_3:Ce^{3+} 10%, Gd^{3+} 30%, Eu^{3+} 1% nanophosphor synthesized in the presence of PAA. Left image presents the colloid in daylight, and the right image presents its emission under UV lamp irradiation (254 nm).

Fig. 9b presents the luminescence decay curves measured for the nanophosphors synthesized in this study. On the basis of the recorded curves, the luminescence lifetimes were calculated, and their values are shown in the Table 1. All decay profiles fit well to the mathematic function $y = A_1 * \exp(-x/\tau_1) + A_2 * \exp(-x/\tau_2) + y_0$, with $R > 0.999$, revealing a biexponential character of the decay curves. The calculated values of the radiative lifetimes were in the range of ms ($\tau_1 \approx 7$–10 ms, $\tau_2 \approx 3$ ms). Such relatively long lifetimes are typical of the Eu^{3+} ions embedded in a high symmetry structure of crystalline fluorides [43]. The observed biexponential character of the decay profiles can be explained by the presence of two emitting species of Eu^{3+} ions. In the bulk hexagonal lanthanide fluoride there should be only one site symmetry occupied by Eu^{3+} ion. However, in nanomaterials, whose particles size is in the range of several nm, the surface-to-volume ratio becomes significantly high to influence the measured spectroscopic properties [63]. That is why a second lifetime component appears in the measured luminescence decay curves. This short lived component, τ_2 is associated with surface and near surface Eu^{3+} ions being surrounded by water molecules, organic modifier molecules and other species, which quench the luminescence. In other words, such surface ions are in a different coordination environment than the bulk ions. Additionally, Eu^{3+} ions are very sensitive to changes in their site symmetry, which is manifested in altered spectroscopic properties, e.g. radiative lifetimes [62,64]. The nanophosphors synthesized in the presence of PAA and oleylamine exhibited the shortest lifetime, which agrees well with our predictions. As previously mentioned, these compounds showed the smallest particles size and the highest level of surface modification, manifested as luminescence quenching and lifetimes shortening.

The CIE1964 color coordinates were calculated to characterize the color of light emitted by the nanoluminophors studied. Obtained CIE charts are very similar for all of the samples studied, as shown in Fig. 10 for the nanoluminophor synthesized in the presence of PAA.

The calculated absolute QY of luminescence (Fig. 11) was in the range 4–16%, while the relative QY range was 48–73%. The results obtained were in a good agreement with literature data [23,43,50,52]. However, the values calculated by the absolute

[1] For interpretation of color in Fig. 9, the reader is referred to the web version of this article.

method were much smaller than those from the approach based on the J–O theory. This discrepancy between both series of data probably follows from the fact that the applied relative method (J–O) treats the radiative lifetime of the sample as a crucial parameter determining the final QY of the product. Ln^{3+} doped, inorganic compounds exhibit usually much longer radiative lifetimes (several ms) in comparison to those of the organic complexes of Ln^{3+} ions in solutions (from several to several hundred μs). That is why the QY calculated on the basis of the J–O theory were much higher. The measured and calculated values of QY (absolute and relative) were the smallest for PAA, oleylamine and citric acid modified nanophosphors and the highest for glycerine and Triton X-100 modified samples. The results obtained correlated with the luminescence intensity of the products synthesized, with their lifetimes and with the observed presence of large amount of organic modifiers in IR spectra. However one should remember that for potential bio-applications and tracing/labeling techniques, the compromise between effectiveness of luminescence of the products and their size/shape distribution including agglomeration processes, should be kept [65].

4. Conclusions

A series of Ln^{3+} doped fluorides was successfully synthesized by a simple, fast, low-cost and eco-friendly coprecipitation approach. All products exhibited intensive red luminescence, typical of Eu^{3+} ions in a highly symmetrical coordination environment. The products had small particle sizes, from 5 to 11 nm, depending on the organic modifier used. The product synthesized in the presence of PAA revealed the smallest particle size and narrow size/shape distribution and formed very stable aqueous colloid. The photophysical properties of the obtained nanomaterials were examined by XRD, TEM and spectrofluorometric measurements (excitation, emission spectra and luminescence decay curves). Luminescence quantum yields (QY) and radiative lifetimes were also determined. The obtained absolute and relative QY of luminescence were compared. A good correlation between both series of data was found, however the absolute QY were smaller than the relative ones. On the basis of the measured luminescence properties of the nanophosphors obtained, the Judd–Ofelt analysis was performed providing additional information about their structure and local site symmetry of Ln^{3+} ions. FT-IR spectroscopy confirmed the presence of organic modifiers molecules on the nanoparticles surface. The nanomaterials obtained can be applied in many fields of science, e.g. colored lighting, bio-imaging, luminescence tracing, detecting systems, forensic applications etc.

Acknowledgements

M.R. gratefully acknowledges the financial support from Polish Ministry of Science and Higher Education – scientific work financed from the budget for science in 2012-2015 as a research project within the program called "Diamond Grant" No. DI2011 011441.

Appendix A. Supplementary material

Supplementary material associated with this article can be found, in the online version, at http://dx.doi.org/10.1016/j.jallcom.2014.01.209.

References

[1] G. Blasse, B.C. Grabmaier, Luminescent Materials, Springer, Berlin, 1994.
[2] H. Chander, Mater. Sci. Eng., R Rep. 49 (2005) 113–155.
[3] S. Lis, J. Alloys Comp. 341 (2002) 45–50.
[4] M. Runowski, T. Grzyb, S. Lis, J. Nanopart. Res. 14 (2012) 1188–1195.
[5] H. Peng, G. Liu, X. Dong, J. Wang, J. Xu, W. Yu, J. Alloys Comp. 509 (2011) 6930–6934.
[6] D.V. Sunitha, H. Nagabhushana, S.C. Sharma, B.M. Nagabhushana, R.P.S. Chakradhar, J. Alloys Comp. 575 (2013) 434–443.
[7] K. Binnemans, Chem. Rev. 109 (2009) 4283–4374.
[8] Z. Tang, N.a. Kotov, M. Giersig, Science 297 (2002) 237–240.
[9] D. Dosev, M. Nichkova, I.M. Kennedy, J. Nanosci. Nanotechnol. 8 (2008) 1052–1067.
[10] R.S. Yadav, V.K. Shukla, P. Mishra, S.K. Pandey, K. Kumar, V. Baranwal, et al., J. Alloys Comp. 547 (2013) 1–4.
[11] X. Feng, L. Yang, N. Zhang, Y. Liu, J. Alloys Comp. 506 (2010) 728–733.
[12] F. Gagné, D. Maysinger, C. André, C. Blaise, Nanotoxicology 2 (2008) 113–120.
[13] N.O. Nuñez, H. Míguez, M. Quintanilla, E. Cantelar, F. Cussó, M. Ocaña, Eur. J. Inorg. Chem. 2008 (2008) 4517–4524.
[14] M. Runowski, T. Grzyb, S. Lis, J. Rare Earths 29 (2011) 1117–1122.
[15] H. Lin, D. Chen, M. Niu, Y. Yu, P. Huang, Y. Wang, Mater. Res. Bull. 45 (2010) 52–55.
[16] J.J. Zhao, Y. Sun, X. Kong, L. Tian, Y. Wang, L. Tu, et al., J. Phys. Chem. B 112 (2008) 15666–15672.
[17] F. Wang, X. Fan, M. Wang, Y. Zhang, Nanotechnology 18 (2007) 25701–25706.
[18] N. Niu, P. Yang, Y. Liu, C. Li, D. Wang, S. Gai, et al., J. Colloid Interface Sci. 362 (2011) 389–396.
[19] T. Grzyb, A. Gruszeczka, R.J. Wiglusz, Z. Śniadecki, B. Idzikowski, S. Lis, J. Mater. Chem. 22 (2012) 22989–22997.
[20] K. Riwotzki, H. Meyssamy, A. Kornowski, M. Haase, J. Phys. Chem. B 104 (2000) 2824–2828.
[21] G. Blasse, Phys. Status Solidi A 73 (1982) 205–208.
[22] L. Li, H. Lin, X. Zhao, Y. Wang, X. Zhou, C. Ma, et al., J. Alloys Comp. 586 (2014) 555–560.
[23] T. Grzyb, M. Runowski, A. Szczeszak, S. Lis, J. Phys. Chem. C 116 (2012) 17188–17196.
[24] J. Wang, S. Bo, L. Song, J. Hu, X. Liu, Z. Zhen, Nanotechnology 18 (2007) 465606–465611.
[25] I. Omkaram, G. Seeta Rama Raju, S. Buddhudu, J. Phys. Chem. Solids 69 (2008) 2066–2069.
[26] M.-Y. Xie, L. Yu, H. He, X.-F. Yu, J. Solid State Chem. 182 (2009) 597–601.
[27] Z. Xu, Y. Cao, C. Li, P. Ma, X. Zhai, S. Huang, et al., J. Mater. Chem. 21 (2011) 3686–3694.
[28] S. Lucas, E. Champion, D. Bregiroux, D. Bernache-Assollant, F. Audubert, J. Solid State Chem. 177 (2004) 1302–1311.
[29] N. Dhananjaya, H. Nagabhushana, S.C. Sharma, B. Rudraswamy, C. Shivakumara, B.M. Nagabhushana, J. Alloys Comp. 587 (2014) 755–762.
[30] T. Grzyb, M. Węcławiak, S. Lis, J. Alloys Comp. 539 (2012) 82–89.
[31] A. Szczeszak, T. Grzyb, B. Barszcz, V. Nagirnyi, A. Kotlov, S. Lis, Inorg. Chem. 52 (2013) 4934–4940.
[32] J.W. Stouwdam, M. Raudsepp, F.C.J.M. van Veggel, Langmuir 21 (2005) 7003–7008.
[33] C. Li, J. Yang, P. Yang, H. Lian, J. Lin, Chem. Mater. 20 (2008) 4317–4326.
[34] T. Passuello, F. Piccinelli, M. Trevisani, M. Giarola, G. Mariotto, L. Marciniak, et al., J. Mater. Chem. 22 (2012) 10639–10649.
[35] M. Karbowiak, A. Mech, A. Bednarkiewicz, W. Stręk, Ł. Kępiński, J. Phys. Chem. Solids 66 (2005) 1008–1019.
[36] J.H. Zeng, Z.H. Li, J. Su, L. Wang, R. Yan, Y. Li, Nanotechnology 17 (2006) 3549–3555.
[37] J. Wang, W. Miao, Y. Li, H. Yao, Z. Li, Mater. Lett. 63 (2009) 1794–1796.
[38] E.N.M. Cheung, R.D.a. Alvares, W. Oakden, R. Chaudhary, M.L. Hill, J. Pichaandi, et al., Chem. Mater. 22 (2010) 4728–4739.
[39] H. Moos, J. Lumin. 1–2 (1970) 106–121.
[40] H.-T. Wong, H.L.W. Chan, J.H. Hao, Appl. Phys. Lett. 95 (2009) 022512–022514.
[41] X. Zhang, T. Hayakawa, M. Nogami, Int. J. Appl. Ceram. Technol. 8 (2011) 741–751.
[42] T. Grzyb, M. Runowski, K. Dąbrowska, M. Giersig, S. Lis, J. Nanopart. Res. 15 (2013) 1958–1972.
[43] T. Grzyb, M. Runowski, A. Szczeszak, S. Lis, J. Solid State Chem. 200 (2013) 76–83.
[44] D. Zhang, C. Chen, F. Wang, D.M. Zhang, Appl. Phys. B 98 (2009) 791–795.
[45] J. Mahakhode, S. Dhoble, C. Joshi, S. Moharil, J. Alloys Comp. 438 (2007) 293–297.
[46] K.H. Cheng, J. Aijmo, L. Ma, M. Yao, X. Zhang, J. Como, et al., J. Phys. Chem. C 112 (2008) 17931–17939.
[47] D. Hu, M. Chen, Y. Gao, F. Li, L. Wu, J. Mater. Chem. 21 (2011) 11276–11282.
[48] J.I. Langford, a.J.C. Wilson, J. Appl. Crystallogr. 11 (1978) 102–113.
[49] M.S. Wrighton, D.S. Ginley, D.L. Morse, J. Phys. Chem. 78 (1974) 2229–2233.
[50] A.M. Kłonkowski, S. Lis, M. Pietraszkiewicz, Z. Hnatejko, K. Czarnobaj, M. Elbanowski, Chem. Mater. 15 (2003) 656–663.
[51] C. Kodaira, H.F. Brito, O.L. Malta, O.A. Serra, J. Lumin. 101 (2003) 11–21.
[52] R.J. Wiglusz, T. Grzyb, S. Lis, W. Strek, J. Lumin. 130 (2010) 434–441.
[53] C. Canevali, M. Mattoni, F. Morazzoni, R. Scotti, M. Casu, A. Musinu, et al., JACS 127 (2005) 14681–14691.
[54] S. Agnello, G. Iovino, G. Buscarino, R. Boscaino, F. Costa, J. Sol–Gel. Sci. Technol. 58 (2010) 56–61.
[55] J.L. Rygel, C.G. Pantano, J. Non-Cryst. Solids 355 (2009) 2622–2629.
[56] H.M. Rietveld, J. Appl. Crystallogr. 2 (1969) 65–71.
[57] L. Lutterotti, S. Matthies, H.R. Wenk, Int. Union Crystallogr.: Newslett. CPD 21 (1999) 14–15.

[58] K. Kamala Bharathi, N.R. Kalidindi, C.V. Ramana, J. Appl. Phys. 108 (2010) 083529–083533.
[59] G. Blasse, Mater. Chem. Phys. 16 (1987) 201–236.
[60] G. Blasse, J. Chem. Phys. 46 (1967) 2583–2585.
[61] D.R. Tallant, C.H. Seager, R.L. Simpson, J. Appl. Phys. 91 (2002) 4053–4064.
[62] B.R. Judd, J. Chem. Phys. 44 (1966) 839–840.
[63] K. Ostrikov, E.C. Neyts, M. Meyyappan, Adv. Phys. 62 (2013) 113–224.
[64] S. Polizzi, M. Battagliarin, M. Bettinelli, A. Speghini, G. Fagherazzi, J. Mater. Chem. 12 (2002) 742–747.
[65] M. Runowski, K. Dąbrowska, T. Grzyb, P. Miernikiewicz, S. Lis, J. Nanopart. Res. 15 (2013) 2068–2083.

Supporting Information for:

Preparation and photophysical investigation of luminescent nanoparticles based on lanthanide doped fluorides (LaF_3:Ce^{3+}, Gd^{3+}, Eu^{3+}), obtained in the presence of different surfactants

*Marcin Runowski, Stefan Lis**

Adam Mickiewicz University, Faculty of Chemistry, Department of Rare Earths, Grunwaldzka 6, 60-780 Poznań, Poland

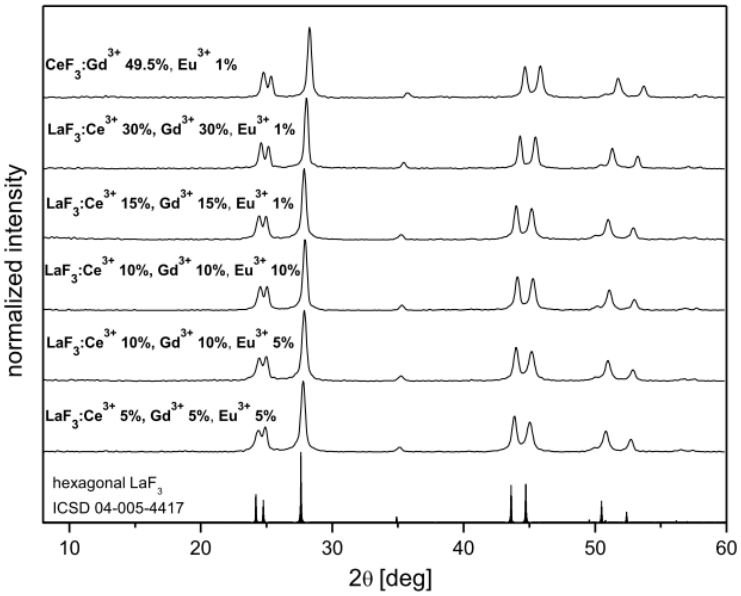

Fig. S1 XRD patterns of LaF_3 doped with Ce^{3+}, Gd^{3+}, Eu^{3+} ions.

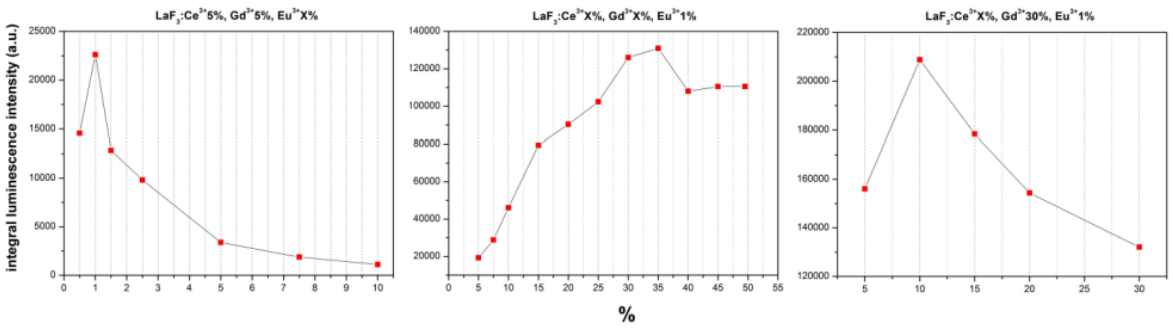

Fig. S2 Comparison of integral luminescence intensity of LaF_3 codoped with Ce^{3+}, Gd^{3+}, Eu^{3+} ions; λ_{ex} = 249 nm.

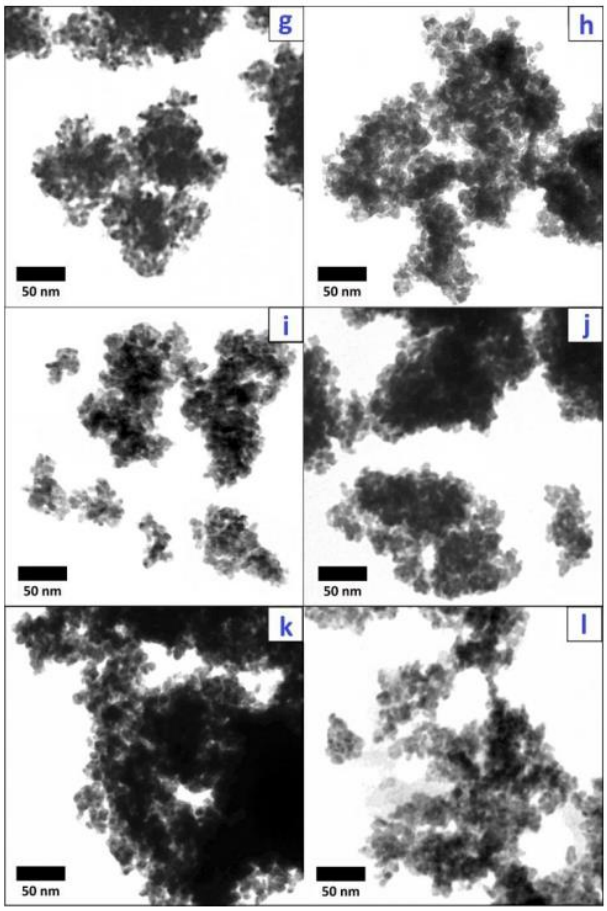

Fig. S3 TEM images of LaF_3:Ce^{3+} 10%, Gd^{3+} 30%, Eu^{3+} 1% nanostructures obtained in the presence of glycol (g), glycerine (h), PEG (i), CTAB (j), PVA (k), adipic acid (l).

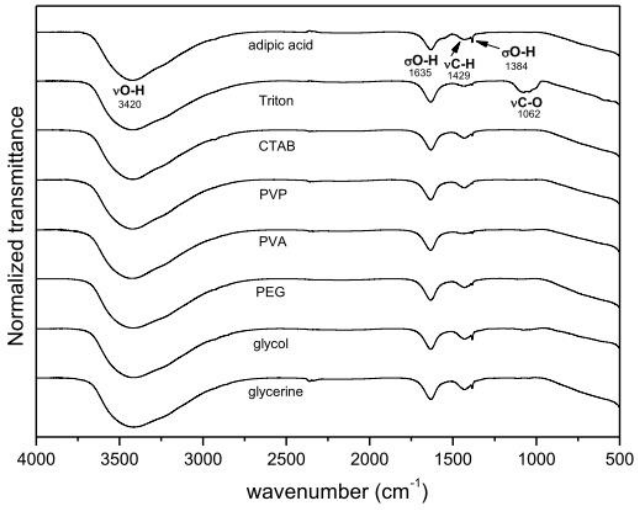

Fig. S4 FT-IR spectra of LaF_3:Ce^{3+} 10%, Gd^{3+} 30%, Eu^{3+} 1% nanomaterials synthesized in the presence of adipic acid, Triton X-100, CTAB, PVP, PVA, PEG, glycol and glycerine.

On the basis of the recorded emission spectra and luminescence lifetimes, the analysis of Judd-Ofelt (J-O) intensity parameters was performed. This analysis provided additional information concerning structural and photophysical features of the nanophosphors synthesized. The analysis was performed according to the well-known procedure described by Kodaira et al.[1] and later successfully applied by the others[2,3]. The refractive index for all compounds was assumed to be 1.71. Generally, the Ω_2 intensity parameter corresponds to the symmetry of the local coordination environment of the Eu^{3+} ion, and its polarizability. The value of this parameter increases along with increasing asymmetry of the local coordination environment of the Eu^{3+} ions embedded in the given crystal structure. Whereas, the Ω_4 intensity parameter corresponds to the bonds covalency of the system studied (electron density of the ligands) and its rigidity. Larger value of this parameter corresponds to the larger bonds covalency (smaller iconicity) in the given system.

The calculated J-O parameters (Ω_2 and Ω_4), averaged lifetimes, relative quantum yields and other parameters are presented in the Table S1. Generally, both intensity parameters, Ω_2 and Ω_4 revealed only small variances in the whole series of products, because of the same hexagonal crystal structure of the synthesized nanomaterials. However, the values of Ω_2 parameter are slightly higher for the products obtained in the presence of PAA, PVA, EDTA, citric acid and Triton X-100, in comparison to the rest of compounds. This fact correlates with the high intensity ratio of $^5D_0 \rightarrow {}^7F_2/{}^5D_0 \rightarrow {}^7F_1$ transitions for these compounds, presented in Fig. S5. It means that for the discussed products the local site symmetry of Eu^{3+} ion is the lowest in the series. In other words, the highest asymmetry of the coordination environment of Eu^{3+} ion in these structures was probably caused by the presence of coordinated ligands to the nanoparticles surface (which was observed in the presented IR spectra), and the crystal defects in these nanomaterials. The product synthesized in the presence of oleylamine revealed the smallest value of the Ω_2 parameter and intensity ratio of the mentioned transitions. We suppose that it was caused by interactions of the oleylamine molecules with nanoparticles surface, resulting in increased symmetry of the system. The possible explanation can be that the oleylamine molecules are hydrophobic and can assembly/arrange on the nanoparticles surface, simultaneously limiting the contact of water molecules with superficial Eu^{3+} ions. That is why the final effect was converse in comparison to the other products having large amount of the organic modifier in the structure. However, the presented explanation requires further studies which could confirm our assumptions. The similar trend was observed for Ω_4 intensity parameter, namely its value was the highest for the products denoted as PAA, PVA, EDTA, citric acid and Triton X-100 (higher covalency of Ln-F bonds), and the lowest for oleylamine (lower covalency). This phenomenon was related to the increased covalency of the Ln-F bond.

Table 1 Radiative (A_{rad}) and non-radiative (A_{rad}) decay rates, total processes of $^5D_0 \rightarrow {}^7F_J$ transitions (A_{tot}), luminescence lifetimes (τ), intensity parameters (Ω_2 and Ω_4) and quantum yield of luminescence (η) for the $LaF_3:Ce^{3+}$ 10%, Gd^{3+} 30%, Eu^{3+} 1% series.

compound name	A_{rad} [s^{-1}]	A_{nrad} [s^{-1}]	A_{tot} [s^{-1}]	τ [ms]	Ω_2 [10^{-20} cm^2]	Ω_4 [10^{-20} cm^2]	η [%]
PAA	132.22	144.02	276.24	3.62	5.01	7.05	47.86
oleylamine	122.52	130.64	253.16	3.95	4.26	6.48	48.40
glycol	127.77	73.84	201.61	4.96	4.52	7.15	63.38
citric acid	138.95	75.18	214.13	4.67	5.34	7.64	64.89
EDTA	135.96	68.12	204.08	4.90	5.35	7.42	66.62
CTAB	128.63	63.68	192.31	5.20	4.66	7.15	66.89
PVA	133.34	63.12	196.46	5.09	4.95	7.49	67.87
PVP	129.77	59.26	189.04	5.29	4.65	7.22	68.65
adipic acid	126.39	56.76	183.15	5.46	4.57	6.84	69.01
glycerine	128.34	57.53	185.87	5.38	4.62	7.08	69.05
PEG	131.95	56.38	188.32	5.31	4.72	7.51	70.06
Triton X-100	134.71	52.91	187.62	5.33	4.99	7.73	71.80

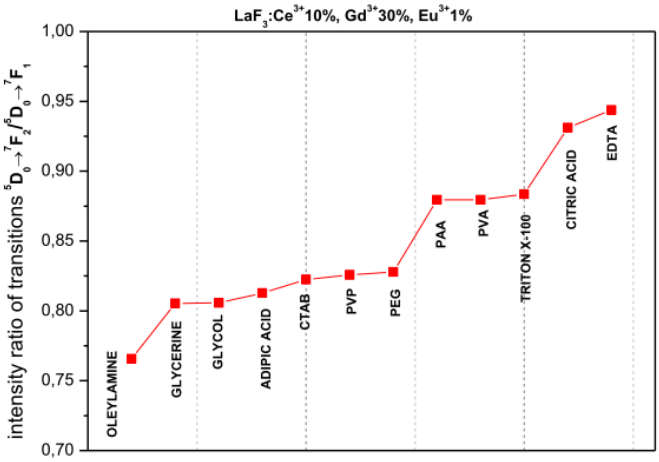

Fig. S5 Intensity ratios of $^5D_0 \rightarrow {}^7F_2/{}^5D_0 \rightarrow {}^7F_1$ transitions for $LaF_3:Ce^{3+}$ 10%, Gd^{3+} 30%, Eu^{3+} 1% nanophosphors.

References

[1] C. Kodaira, H.F. Brito, O.L. Malta, O.A. Serra, Luminescence and energy transfer of the europium (III) tungstate obtained via the Pechini method, J. Lumin. 101 (2003) 11-21.

[2] R.J. Wiglusz, T. Grzyb, S. Lis, W. Strek, Hydrothermal preparation and photoluminescent properties of $MgAl_2O_4:Eu^{3+}$ spinel nanocrystals, J. Lumin. 130 (2010) 434-441.

[3] T. Grzyb, M. Runowski, A. Szczeszak, S. Lis, Structural, morphological and spectroscopic properties of Eu^{3+} doped rare earth fluorides synthesized by the hydrothermal method, J. Solid State Chem. 200 (2013) 76-83.

Problemem badawczym jaki podjąłem w pracy pt. „*Nanosized complex fluorides based on* Eu^{3+} *doped* Sr_2LnF_7 *(Ln = La, Gd)*" było otrzymanie złożonych, nanokrystalicznych luminoforów, wykazujących intensywną czerwoną luminescencję. W tym celu wybrano struktury złożonych fluorków, tj. strontowo-lantanowego i strontowo-gadolinowego. Układy te domieszkowano rosnącą ilością jonów Eu^{3+}, w zakresie 0-30%. Syntezę prowadzono metoda współstrąceniową w obecności glikolu polietylenowego (PEG 6000), pełniącego zarówno rolę surfaktantu i modyfikatora powierzchni. Obecność cząsteczek modyfikatora organicznego na powierzchni krystalitów była widoczna na zarejestrowanych widmach IR. W wyniku syntezy otrzymano małe (≈ 15 nm) i homogeniczne nanoczastki wykazujące czerwoną luminescencję. Właściwości fizykochemiczne otrzymanych luminoforów zostały zbadane metodami dyfrakcji proszkowej (XRD), transmisyjnej mikroskopii elektronowej (TEM), spektroskopii w podczerwieni (FT-IR) i spektrofluorymetrii. W przypadku fluorku strontowo-gadolinowego (Sr_2GdF_7:Eu^{3+}) obserwowano na widmach wzbudzenia pasma związane z przeniesieniem energii $Gd^{3+}\rightarrow Eu^{3+}$. W przypadku obu struktur wyznaczono optymalne stężenie jonu Eu^{3+} (≈ 20%), zapewniające najbardziej intensywną emisję próbki. Obserwowano również wpływ ilości domieszki na krzywe zaniku luminescencji i obliczone na ich podstawie czasy życia. Wraz ze zwiększaniem stężenia Eu^{3+}, następowało skrócenie się emisyjnych czasów życia.

Wkład własny w powstanie pracy: koncepcja badań, znaczący udział w syntezie i zbadaniu właściwości fizykochemicznych otrzymanych nanoluminoforów. Analiza uzyskanych wyników, opracowanie danych i zredagowanie publikacji.

Available online at www.sciencedirect.com
ScienceDirect
JOURNAL OF RARE EARTHS, Vol. 32, No. 3, Mar. 2014, P. 242
JOURNAL OF RARE EARTHS
www.re-journal.com/en/

Nanosized complex fluorides based on Eu^{3+} doped Sr_2LnF_7 (Ln=La, Gd)

M. Runowski, S. Balabhadra, S. Lis*

(Department of Rare Earths, Faculty of Chemistry, Adam Mickiewicz University, Grunwaldzka 6, 60-780 Poznan, Poland)

Received 8 June 2013; revised 27 January 2014

Abstract: A simple co-precipitation approach taking place between Ln^{3+}, Sr^{2+} cations and F^- anions, led to the formation of nanocrystalline Eu^{3+} doped Sr_2LnF_7 (Ln=La and Gd) complex fluorides. The reaction was carried out in the presence of polyethylene glycol, PEG 6000 as a surfactant/surface modifier, providing small size and homogeneity of the products. The synthesized compounds were composed of small nanoparticles with an average size of 15 nm. All obtained Eu^{3+} doped compounds exhibited an intensive red luminescence. In the case of gadolinium based compounds, the energy transfer phenomena could be observed from Gd^{3+} ions to Eu^{3+} ions. In order to study the structure and morphology of the synthesized fluorides, powder X-ray diffraction (XRD) and transmission electron microscopy (TEM) measurements were performed. Also FT-IR spectra of the products were recorded, revealing the presence of PEG molecules on the nanoparticles surface. A spectrofluorometry technique was applied to examine optical properties of the synthesized nanoparticles. Excitation and emission spectra as well as luminescence decay curves were measured and analysed. The performed analysis revealed a red luminescence, typical for the Eu^{3+} ion situated in the inorganic, highly symmetric matrix. Concentration quenching phenomena and lifetimes shortening, together with an increasing of the Eu^{3+} doping level, were observed and discussed. Judd-Ofelt analysis was also performed for all doped samples, in order to support the registered spectroscopic data and examine in details structural and optoelectronic properties of the synthesized nanomaterials.

Keywords: luminescence; Eu^{3+} doping; complex strontium lanthanide fluorides; nanoparticles; Sr_2LnF_7; $Sr_{0.69}La_{0.31}F_{2.31}$; rare earths

Rare-earth-doped inorganic nanomaterials have been applied or considered for applications in modern lighting, displays and optical communication fields, such as fluorescent lamps, field emission displays, plasma display panels (PDPs)[1–5]. Recently, many researchers are paying much attention on lanthanide fluorides[6–8], alkaline earth metal fluorides[9,10] and complex ones[11–13]. Moreover, scientists successfully investigated Eu^{3+} doped alkaline earth fluorides as white light-emitting-diodes (WLEDs) materials[14].

The alkaline earth fluorides are important optical raw materials with high solubility of both sensitizer and activator ions, which have been applied as crystal laser hosts. Because the radii of the luminescent lanthanide ions are similar to the Sr^{2+} host cations, the Ln^{3+} ions can be successfully embedded in the Sr_2LnF_7 structure[14,15]. The concentration of the dopant ions also shows a predominant effect on their structural and optical characteristics in the strontium fluorides. Among all of the lanthanides, Eu^{3+} is most convenient for these kind of studies, due to narrow emission bands and long radiative lifetimes of the excited states. More importantly Eu^{3+} doping is regarded to be a luminescent probe that allows extraction of necessary information concerning a local chemical environment of lanthanide ion and crystal structure, directly from the emission spectra. Also an intensive red emission from the Eu^{3+} ion is a factor improving the color rendering index (CRI).

The fluoride hosts, such as the one studied in the current work, are strong and efficient luminescent materials. Nowadays, fluoride hosts, are intensively investigated due to their potential applications in many areas including lighting, optoelectronics, detection systems or more advanced forensic medical applications[16–18]. The lanthanide fluorides are especially interesting due to the low phonon energy of their crystal lattice, which suppresses nonradiative relaxations of dopant ions, like Eu^{3+} [19]. This value is significantly lower in comparison to lanthanide oxides, phosphates or borates, often used as phosphors. Due to their photostability, lanthanide fluorides can be used as special materials in novel applications[14].

In the this work we reported the luminescent nanomaterials containing Eu^{3+} doped Sr_2LnF_7:Eu^{3+} (Ln= La, Gd) nanocrystals. The structure, morphology and spectroscopic properties of the obtained products were examined, and the obtained results were analysed and discussed. The Judd-Ofelt theory was applied to calculate the radiative properties of the prepared materials, and to investigate their electron structure.

Foundation item: Project supported by Polish Ministry of Science and Higher Education (Diamond Grant" Nr DI2011 011441)

* **Corresponding author:** S. Lis (**E-mail:** blis@amu.edu.pl; **Tel.:** +48 61 829 1345)

DOI: 10.1016/S1002-0721(14)60058-2

1 Experimental

1.1 Synthesis

1.1.1 Materials

La_2O_3, Eu_2O_3 and Gd_2O_3 oxides (Stanford Materials, 99.99%) were separately dissolved in a concentrated, nitric acid, HNO_3 (POCh S.A., ultra-pure) to obtain $La(NO_3)_3$, $Eu(NO_3)_3$ and $Gd(NO_3)_3$ aqueous solutions, respectively. Strontium nitrate, $Sr(NO_3)_2$ (pure, 99%) and ammonium fluoride, NH_4F (ACS grade, ≥98%) were purchased from POCh S.A. Polyethylene glycol - PEG 6000 (Alfa Aesar, 98%) was used as a surfactants/surface modifier. In all experiments, only ultra-pure distilled water was used.

1.1.2 Synthesis

The synthesis of complex, nanocrystalline fluorides based on Eu^{3+} doped Sr_2LnF_7 (Ln=La and Gd) was performed via a simple wet chemical route, namely co-precipitation. To synthesize the Sr_2LnF_7:Eu^{3+} nanocrystals, the stoichiometric amounts of appropriate lanthanide salts were dissolved in 50 mL of ethanol/water solvent system. After that, 0.25 g of PEG 6000 was added and dissolved. Polyethylene glycol was used as a surfactant/surface modifier to provide small size and homogeneity for desired nanocrystals. Afterwards, second solution was prepared by dissolving NH_4F (50% excess) in 50 mL of the same water/ethanol system, with the addition of 0.25 g of PEG 6000, as well. Subsequently, the first solution was dropped into the solution containing fluoride ions, which was heated up to approx. 50 °C. The dropping process lasted approx. 20 min. Afterwards, the formed transparent precipitate was collected and washed with water for several times. The final obtained product was dried in vacuum at 85 °C for 12 h.

1.2 Characterization

Electron microscopy measurements were performed using a transmission electron microscope JEM 1200 EXII, JEOL, operating at accelerating voltage equal to 80 kV. Powder X-ray diffractograms were registered using Bruker AXS D8 Advance diffractometer, using Cu Kα radiation (λ=0.15406 nm). Based on the experimental XRD patterns, the average grains sizes were estimated using Scherrer's equation:

$$D = \frac{k\lambda}{\cos\theta\sqrt{\beta - \beta'^2}} \quad (1)$$

Where D is grain size, k is a shape factor (0.9 for spherical particles), λ is a wavelength of radiation, θ is an angle of diffraction, β is a full width at half maximum (FWHM) and β'^2 is an instrumental effect. IR spectra were measured with FT-IR spectrophotometer, JASCO 4200. The IR spectra were measured in transmission mode; the samples were mixed with KBr, ground and pressed into pellets. The excitation, emission spectra and luminescence decay curves were registered using Hitachi F-7000 spectrofluorometer at ambient conditions. The excitation and emission spectra were appropriately corrected for the apparatus response.

2 Results and discussion

The structures of the synthesized products were studied using powder XRD technique. Both series of the obtained Eu^{3+} doped fluorides crystallize as cubic, complex fluoride $Sr_xLn_{1-x}F_y$ (Ln=La, Gd) isostructural with SrF_2[14]. Because of the similarity of the ionic radii of Sr^{2+} and Ln^{3+}, both Ln^{3+} ions can easily substitute the Sr^{2+} ions in the crystal lattice, forming the above mentioned complex fluorides[15]. The occurring phenomenon was also confirmed as a presence of one, crystalline phase in the presented powder diffractograms (Fig. 1) of the synthesized nanomaterials, in the whole doping range (0–30% Eu^{3+}). All diffractograms were compared and fitted well to the $Sr_{0.69}La_{0.31}F_{2.31}$ (ICDD card No. 04-006-8267), crystallising in a cubic crystal system, *Fm*3*m* space group. The Sr/Ln ratio is close to 2 in the discussed structure, like the molar ratios of Sr^{2+} and Ln^{3+} ions used as starting materials in the synthesis process. For the convenience of the reader the empiric formula Sr_2LnF_7:Eu^{3+} *x*% (equal to $Sr_2Ln_{1-x}Eu_xF_7$) was used throughout this article. The synthesized doped Sr_2GdF_7 reveal shifted XRD patterns towards higher 2θ angles, compared to the analogic Sr_2LaF_7 compounds, which means that their unit cell parameters decreased. The mentioned phenomenon is in good agreement with the well-known lanthanide contraction, due to the fact that the Gd^{3+} ion has smaller ionic radius than the La^{3+} ion. Because of the same reasons, increasing amount of the Eu^{3+} ions in the Sr_2LaF_7:Eu^{3+} series (ranging from 0 to 30%), the same shift towards higher angles can be observed. In the case of Sr_2GdF_7:Eu^{3+} series, a slight shift, however towards smaller angle can be observed, as well (unit cell volume expansion, due the slightly larger Eu^{3+} ionic radius in comparison with substituted Gd^{3+} ion). All measured XRD patterns of the synthesized nanomaterials reveal significant broadening effect of their reflexes, which is characteristic for nanocrystalline products, and confirms their small, nanometric size. Based on Scherrer equation[20], the average grain size for the obtained Eu^{3+} doped Sr_2LaF_7 and Sr_2GdF_7 series were estimated as 8.26±0.76 nm and 8.76±0.94 nm, respectively (because of the same reflexes broadening in each series, the estimated grain sizes are averaged values for each Eu^{3+} doped series). The obtained grain size values correspond well to the data calculated from TEM images. However, they are a bit smaller, probably because of the presence of strains/defects in the crystal structure of the synthesized nanomaterials, which is common in such small nanoparticles and causes reflexes broadening, as well.

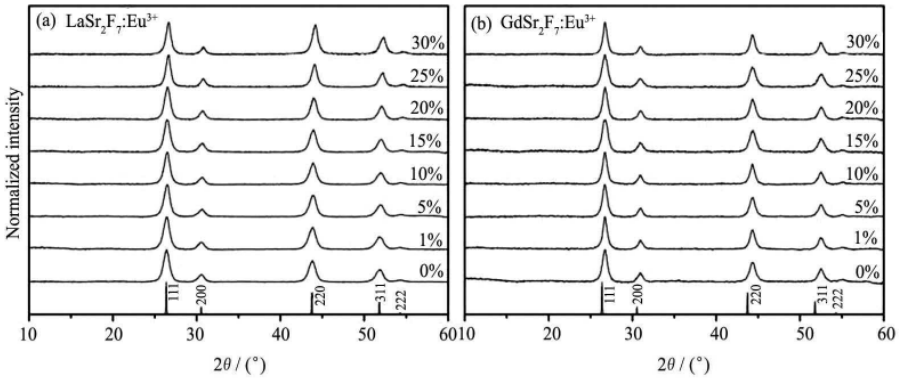

Fig. 1 XRD patterns of Eu^{3+} doped Sr_2LaF_7 (a) and Sr_2GdF_7 (b)

The complementary information about the structure and morphology of the obtained nanomaterials are provided using transmission electron microscopy (TEM) technique. Fig. 2 depicts TEM images of Sr_2LaF_7:20%Eu^{3+} (a) and Sr_2GdF_7:20%Eu^{3+} (b) nanocrystals. By using PEG 6000 as a surfactant, the obtained nanomaterials are composed of relatively uniform, small and homogeneous nanocrystals, which is clearly seen in the depicted pictures. The synthesized nanoparticles of both products are in the range of 10–15 nm. The morphology of the obtained nanostructures is also similar in each series with the varying Eu^{3+} level (data not shown), however La^{3+} based fluorides are generally less agglomerated than Gd^{3+} based ones.

In the depicted FT-IR spectra (Fig. 3) of the Sr_2LaF_7:20%Eu^{3+} and Sr_2GdF_7:20%Eu^{3+} products, the presence of the organic compound (PEG 6000 – surface modifier) attached to the nanoparticles surface can be observed. This fact is confirmed by the presence of absorption peaks, originating from organic moieties oscillations of polyethylene glycol molecules. Peaks at 2933 and 2884 cm^{-1} are related with stretching vibrations of C–H bonds in $–CH_2$ groups, and the peak at 1436 cm^{-1} corresponds to the bending vibrations of these groups. The strong and sharp peak at 1384 cm^{-1} originates from bending vibrations within –OH groups of polyethylene glycol. The rest of the peaks are related to absorbed, surface water molecules (νO–H at 3400 cm^{-1} and σO–H at 1640 cm^{-1}) and CO_2 molecules (approx. 2360 cm^{-1}).

Here we presented luminescence properties of the obtained nanomaterials, expressed as a comparison of their excitation and emission spectra, luminescence decay curves and Judd-Ofelt analysis.

The measured excitation spectra presented in Fig. 4, were registered at λ_{em}=593 nm (the range of the most prominent band corresponding to the $^5D_0 \rightarrow {}^7F_1$ transition), in the range of 200–450 nm, and normalized to the intensity of the most intensive band in each spectrum. The first series of excitation spectra for Sr_2LaF_7 (Fig. 4) exhibit numerous sharp, characteristic bands, related with intrinsic $4f^8$-$4f^8$ transitions within Eu^{3+} ions, visible mainly in the 240–400 nm range. All transitions reveal similar intensities in the whole range of the applied doping. The second set of the excitation spectra registered for Sr_2GdF_7 (Fig. 4), besides the same bands typical for transitions in Eu^{3+} ions, reveals two additional bands related with $^8S_{7/2} \rightarrow {}^6I_J$ (*ca.* 272 nm) and $^8S_{7/2} \rightarrow {}^6P_J$ (*ca.* 310 nm) transitions of the Gd^{3+} ions, corresponding to $Gd^{3+} \rightarrow Eu^{3+}$ energy transfer (ET)[7]. The high intensity of those bands is caused by an effective overlapping of the donor (Gd^{3+}) emission and acceptor (Eu^{3+}) absorption integral. Because of this phenomenon the ET process is very efficient in the obtained nanomaterials. Together with the increment of the amount of dopant ions (Eu^{3+}),

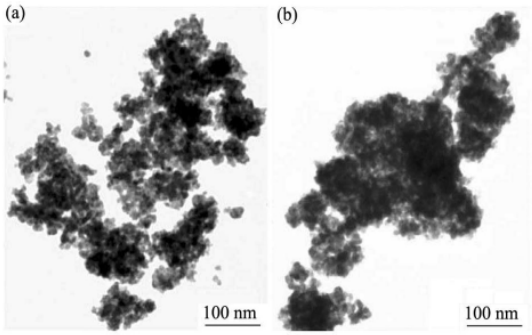

Fig. 2 TEM images of $Sr_2LaF_7:Eu^{3+}$ 20% (a) and $Sr_2GdF_7:Eu^{3+}$ 20% (b)

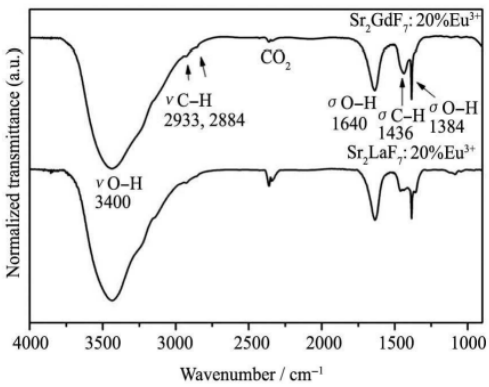

Fig. 3 FT-IR spectra of Sr_2LaF_7:20%Eu^{3+} and Sr_2GdF_7:20%Eu^{3+}

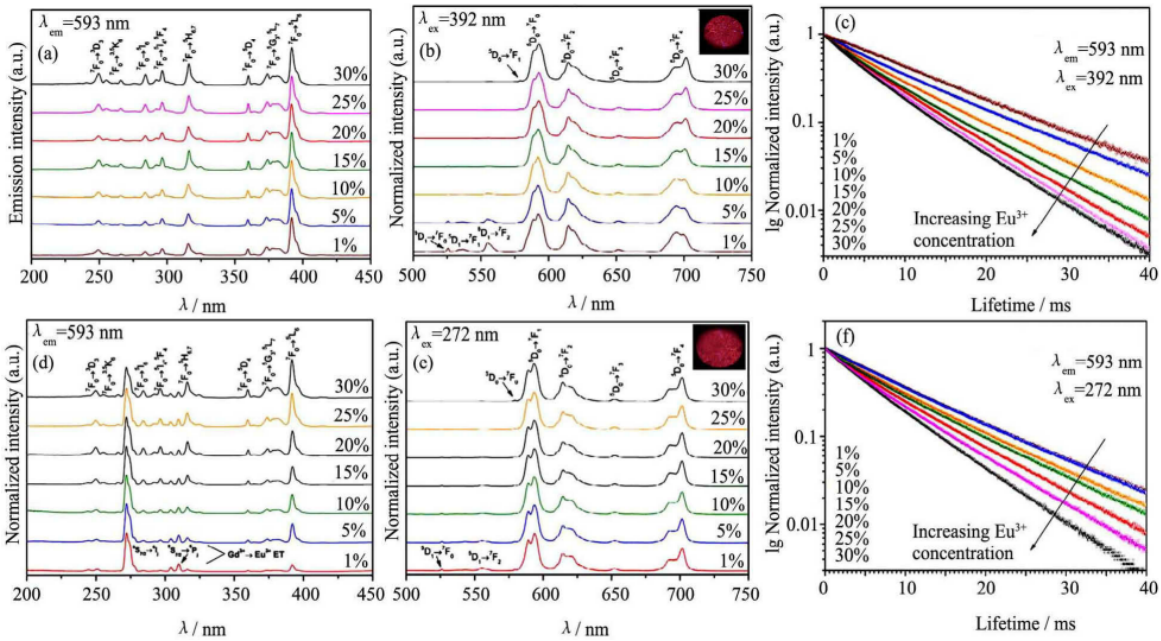

Fig. 4 Excitation (a, d), emission (b, e) spectra and luminescence decay curves (c, f) of Eu^{3+} doped Sr_2LaF_7 (a–c) and Sr_2GdF_7 (d–f)

the most prominent band, namely $^8S_{7/2}\rightarrow{}^6I_J$ related with $Gd^{3+}\rightarrow Eu^{3+}$ ET, becomes less intensive in comparison to the rest bands originating from intrinsic transitions in the Eu^{3+} ions, which can be observed in the discussed spectra. In the case of the $Sr_2Gd_{0.7}Eu_{0.3}F_7$ sample with the highest doping level, the $^7F_0\rightarrow{}^5L_6$ band (related with intrinsic transitions in Eu^{3+} ion) is even more intense than the $^8S_{7/2}\rightarrow{}^6I_J$ band. The discussed altering of the mentioned transitions ratio is directly related with decreasing amount of Gd^{3+} ions in the samples together with an increase of Eu^{3+} doping.

Emission of the observed bands is generally similar in all synthesized products. In both, La and Gd based compounds the emission from higher energy excited levels is the most efficient in the samples with lower doping levels (1% and 5% of Eu^{3+}), because when the concentration of Eu^{3+} ions increases in the sample, the mentioned higher excited levels are effectively quenched, which is a well-known phenomenon in the case of Eu^{3+} doped materials[21]. The hypersensitive $^5D_0\rightarrow{}^7F_2$ electric dipole transition (forbidden transition, the intensity increases when the site symmetry of Eu^{3+} ion decreases[22]) in all spectra is relatively weak, in comparison with $^5D_0\rightarrow{}^7F_1$ magnetic dipole transition, which acts usually as an internal standard in the case of transitions ratio comparisons in Eu^{3+} doped compounds. The mentioned fact clearly states that a local symmetry of the environment of the Eu^{3+} ions in the obtained nanomaterials is relatively high. This is in a good agreement with our predictions, and states that the Eu^{3+} dopant ions were successfully incorporated in the ordered, highly crystalline, cubic structure of the synthesized fluorides, where the site symmetry is high.

Luminescence lifetimes were analysed based on registered luminescence decay curves of the obtained nanophosphors, and are shown in Fig. 4. All curve profiles were fitted well (R>0.999) to the mathematic function $y=A_1*\exp(-x/\tau)+y_0$, demonstrating the monoexponential character of the measured luminescence decay curves. This was in good accordance with our prediction, due to the presence of only one coordination site which can be occupied by Ln^{3+} ions, in the synthesized fluoride crystal structures. In both series of obtained compounds, the general trend expressed by the lifetimes shortening together with an increment of doping level (more Eu^{3+} ions in the crystal structure) can be observed. All calculated lifetimes are relatively long and are in the range of ms (3.9–7.6 ms), which is typical for crystalline Eu^{3+} doped fluorides[7]. The exact values of lifetimes for all obtained compounds were calculated as averaged luminescence lifetimes, namely $\tau=\int I(\tau)\tau dt/\int I(\tau)dt$, and are presented in Table 1, together with data obtained from Judd-Ofelt analysis.

Based on the measured luminescence properties of the synthesized nanophosphors, the comparison of their integral luminescence intensity was plotted and is presented in Fig. 5. In both examples, Sr_2LaF_7:Eu^{3+} (λ_{ex}=392 nm) and Sr_2GdF_7:Eu^{3+} (λ_{ex}=272 nm), the most intensive luminescence exhibited compounds doped with 20% of Eu^{3+} ($Sr_2La_{0.8}Eu_{0.2}F_7$). This observation is in good agreement with cross relaxation model, which is at the higher doping level (using luminescence activator ion as a dopant e.g. Eu^{3+}), the concentration quenching phenomenon occurs[21]. In the case of our nanophosphors

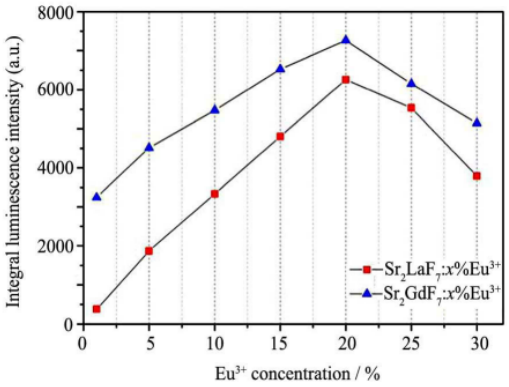

Fig. 5 Integral luminescence intensity for Eu^{3+} doped Sr_2LaF_7 and Sr_2GdF_7

that critical doping level was achieved when more than 20% of the Ln^{3+} ions were substituted by Eu^{3+} ions. The gadolinium based products exhibit generally more intensive luminescence than lanthanum based ones, which can be observed in the depicted plot.

The analysis of Judd-Ofelt intensity parameters was performed in order to support and extend the registered spectroscopic data, as well as to provide more detailed information concerning the structural and photophysical aspects of the obtained nanomaterials. The mentioned analysis has been carried out based on the well-known procedure described by Kodaira et al.[23] and successfully applied by others[7,24]. The refractive index for all compounds was assumed to be 1.44, as for isostructural SrF_2. In general, the Ω_2 intensity parameter is related to the local site symmetry of the Eu^{3+} ion, and its polarizability. The value of this parameter increases with increasing asymmetry of the coordination environment of the Eu^{3+} ions present in the crystalline host. The Ω_4 intensity parameter is related to the bond covalency in the system (electron density within the ligands) and its rigidity. Higher value of this parameter corresponds to higher covalency (lesser iconicity) of the system. In both series of products the values of the Ω_2 parameters are similar because of the same cubic crystal structure of all doped compounds, in which the symmetry is generally similar. However, in the Sr_2LaF_7:Eu^{3+} series a slight decrease of the Ω_2 value with increasing Eu^{3+} concentration was observed (decreasing $^5D_0 \rightarrow {}^7F_2/{}^5D_0 \rightarrow {}^7F_1$ transitions ratio in the emission spectra). The Ω_4 value increases in the Sr_2LaF_7:Eu^{3+} series with the increase of Eu^{3+} doping. This phenomenon is related with increasing covalency of the Ln–F bond. Due to the well-known lanthanide contraction[25], Eu^{3+} has smaller ionic radius than La^{3+}, that is why the average distance between Ln^{3+} and F^- decreases, resulting in increased bond covalency in this system. There are no clear tendencies of the $\Omega_{2,4}$ parameters in the Sr_2GdF_7:Eu^{3+} series, because of the similar ionic radii of Eu^{3+} and Gd^{3+} ions[26]. In the case of the calculated quantum yield of luminescence, also the decreasing tendency (from approx. 98% to 50%) in both series is visible. Therefore an increasing Eu^{3+} concentration in the samples causes decreasing of quantum yield, because of the stronger cross-relaxation process between Eu^{3+} ions in the compounds of higher doping level.

Table 1 Radiative (A_{rad}) and non-radiative (A_{nrad}) decay rates, total processes of $^5D_0 \rightarrow {}^7F_J$ transitions (A_{tot}), luminescence lifetimes (τ), intensity parameters (Ω_2 and Ω_4) and quantum yield of luminescence (η) for Eu^{3+} doped Sr_2GdF_7 (top) and Sr_2LaF_7 (bottom)

Sr_2GdF_7: x%Eu^{3+}	A_{rad}/ s^{-1}	A_{nrad}/ s^{-1}	A_{tot}/ s^{-1}	τ/ ms	Ω_2/ 10^{-20} cm^2	Ω_4/ 10^{-20} cm^2	η/ %
1	126.13	26.54	152.67	6.55	5.44	12.34	82.61
5	125.78	27.12	152.91	6.54	5.28	12.30	82.26
10	125.45	50.29	175.75	5.69	5.41	12.68	71.38
15	124.75	69.42	194.17	5.15	4.88	12.85	64.25
20	127.92	86.68	214.59	4.66	5.31	12.73	59.61
25	126.98	111.10	238.09	4.20	5.28	12.73	53.34
30	128.92	128.15	257.07	3.89	5.59	12.66	50.15
Sr_2LaF_7: x%Eu^{3+}	A_{rad}/ s^{-1}	A_{nrad}/ s^{-1}	A_{tot}/ s^{-1}	τ/ ms	Ω_2/ 10^{-20} cm^2	Ω_4/ 10^{-20} cm^2	η/ %
1	130.180	2.09	132.27	7.56	5.85	12.22	98.41
5	130.63	26.35	156.98	6.37	6.07	12.21	83.21
10	129.84	56.72	186.56	5.36	5.96	12.23	69.59
15	129.42	80.22	209.64	4.77	5.75	12.54	61.73
20	129.15	95.56	224.71	4.45	5.67	12.58	57.47
25	131.58	105.38	236.96	4.22	5.64	13.11	55.52
30	133.64	119.52	253.16	3.95	5.63	14.05	52.78

3 Conclusions

The synthesis of complex, nanocrystalline fluorides based on Eu^{3+} doped Sr_2LnF_7 (Ln=La and Gd) was successfully performed via a simple and low-cost co-precipitation route. The synthesized products were composed of small (approx. 15 nm) nanoparticles. Polyethylene glycol was used as a surfactant/surface modifier, providing small size and homogeneity of the obtained nanocrystals, and its presence was confirmed by FT-IR spectroscopy. The structure and morphology of the synthesized nanomaterials were examined and confirmed by transmission electron microscopy (TEM) and powder X-ray diffraction (XRD) techniques. Spectroscopic studies (excitation, emission spectra and luminescence decay curves measurements) for all synthesized samples were supported by detailed Judd-Ofelt analysis, revealing structural and local site symmetry changes after Ln^{3+} substitution in the crystal structure. The obtained compounds could be potentially used as efficient nanophosphors due to their bright and intensive red luminescence under UV irradiation, as well as for the sophisticated, hybrid core/shell type nanostructures functioning as small and luminescent nanocrystalline core.

References:

[1] Hölsä J. Persistent luminescence beats the afterglow: 400 years of persistent luminescence. *Electrochem. Soc. Interface*, 2009, winter: 42.

[2] Chander H. Development of nanophosphors - A review. *Mater. Sci. Eng*., 2005, **49**: 113.

[3] Shionoya S, Yen W M. Phosphor Handbook. Boca Raton, Florida: CRC Press, 1999.

[4] Kim C. Phosphors for plasma display panels. *J. Alloys Compd*., 2000, **311**: 33.

[5] Shyichuk A, Lis S. Green-emitting nanoscaled borate phosphors $Sr_3RE_2(BO_3)_4:Tb^{3+}$. *Mater. Chem. Phys.*, 2013, **40**: 447.

[6] Grzyb T, Runowski M, Szczeszak A, Lis S. Influence of matrix on the luminescent and structural properties of glycerine-capped, Tb^{3+} doped fluoride nanocrystals. *J. Phys. Chem. C*, 2012, **116**: 17188.

[7] Grzyb T, Runowski M, Szczeszak A, Lis S. Structural, morphological and spectroscopic properties of Eu^{3+} doped rare earth fluorides synthesized by the hydrothermal-method. *J. Solid State Chem*., 2013, **200**: 76.

[8] Li C X, Ma P A, Yang P P, Xu Z H, Li G G, Yang D M, Peng C, Lin J. Fine structural and morphological control of rare earth fluorides REF_3 (RE=La–Lu, Y) nano/microcrystals: microwave-assisted ionic liquid synthesis, magnetic and luminescent properties. *CrystEngComm*, 2011, **13**: 1003.

[9] Moore D S. Laser spectroscopy of defect chemistry in $CaF_2:Er^{3+}$, *J. Chem. Phys*., 1981, **74**: 1626.

[10] Wang J S, Miao W R, Li Y X, Yao H C, Li Z J. Water-soluble Ln^{3+}- doped calcium fluoride nanocrystals: Controlled synthesis and luminescence properties. *Mater. Lett.*, 2009, **63**: 1794.

[11] Marcazzó J, Santiago M, D'Angelo C, Furetta C, Caselli E, Study of the luminescent properties of $KMgF_3$:Sm. *Nucl. Instrum. Methods Phys. Res*., *Sect. B*, 2010, **268**: 183.

[12] Wang F, Fan X P, Wang M Q, Zhang Y. Multicolour PEI/$NaGdF_4:Ce^{3+}$, Ln^{3+} nanocrystals by single-wavelength excitation. *Nanotechnology*, 2007, **8**: 25701.

[13] Wang L L, Chen H, Zhang D S, Zhao D, Qin W P. Dual-mode luminescence from lanthanide tri-doped $NaYF_4$ nanocrystals. *Mater. Lett*., 2011, **65**: 504.

[14] Fu H Y, Qiao X S, Cui S, Luo Q, Qian J Y, Fan X P, Zhang X H. Tunable white light emission from glass-ceramics containing Eu^{2+}, Tb^{3+}, Eu^{3+} co-doped $SrLaF_5$ nanocrystals. *Mater. Lett.*, 2012, **71**: 15.

[15] Qiao X S, Fan X P, Wang M Q, Yang H, Zhang X F. Luminescence behavior of Er^{3+} doped glass ceramics containing Sr_2RF_7 (R=Y, Gd, La) nanocrystals. *J. Appl. Phys*., 2008, **104**: 43508.

[16] Wegh R.T. Visible quantum cutting in $LiGdF_4:Eu^{3+}$ through downconversion. *Science*, 1999, **283**: 663.

[17] Cui S S, Chen H Y, Zhu H Y, Tian J M, Chi X M, Qian Z Y, Achilefu S, Gu Y Q. Amphiphilic chitosan modified upconversion nanoparticles for in vivo photodynamic therapy induced by near-infrared light. *J. Mater. Chem.*, 2012, **22**: 4861.

[18] Singh K, Kumar K, Pandey C, Parkash O, Rai S B, Kumar D. Photon avalanche upconversion and pump power studies in $LaF_3:Er^{3+}/Yb^{3+}$ phosphor. *Appl. Phys. B*, 2011, **104**: 1035.

[19] Wang J S, Bo S H, Song L M, Hu J, Liu X H, Zhen Z. One-step synthesis of highly water-soluble $LaF_3:Ln^{3+}$ nanocrystals in methanol without using any ligands. *Nanotechnology*, 2007, **18**: 465606.

[20] Langford J I, Wilson J C. Scherrer after sixty years: A survey and some new results in the determination of crystallite size. *J. Appl. Crystallogr.*, 1978, **11**: 102.

[21] Blasse G. Concentration quenching of Eu^{3+} fluorescence. *J. Chem. Phys*., 1967, **46**: 2583.

[22] Judd B R. Hypersensitive transitions in rare-earth ions. *J. Chem. Phys*. 1966, **44**: 839.

[23] Kodaira C, Brito H F, Malta O L, Serra O A. Luminescence and energy transfer of the europium (III) tungstate obtained via the Pechini method. *J. Lumin*., 2003, **101**: 11.

[24] Wiglusz R J, Grzyb T, Lis S, Strek W. Hydrothermal preparation and photoluminescent properties of $MgAl_2O_4:Eu^{3+}$ spinel nanocrystals. *J. Lumin*., 2010, **130**: 434.

[25] Runowski M, Grzyb T, Lis S. Bifunctional luminescent and magnetic core/shell type nanostructures Fe_3O_4@CeF_3: Tb^{3+}/SiO_2. *J. Rare Earths*, 2011, **29**: 1117.

[26] Runowski M, Grzyb T, Lis S. Magnetic and luminescent hybrid nanomaterial based on Fe_3O_4 nanocrystals and $GdPO_4:Eu^{3+}$ nanoneedles. *J. Nanopart. Res*., 2012, **14**: 1188.

Oprócz nanokrystalicznych fluorków domieszkowanych jonami lantanowców, również fosforanowe nanocząstki domieszkowane tymi jonami wykazują intensywną luminescencję i pożądane właściwości strukturalne oraz morfologiczne. Dlatego też, kolejnym problemem badawczym jaki podjąłem w pracy pt. „*Eu^{3+} and Tb^{3+} doped $LaPO_4$ nanorods, modified with luminescent organic compound, exhibiting tunable multicolour emission*" było zbadanie wybranych struktur fosforanowych (tj. $LaPO_4$:Eu^{3+} i $LaPO_4$:Tb^{3+}) celem wytworzenia hybrydowych, nieroganiczno-organicznych nanoluminoforów o zmodyfikowanej powierzchni, wykazujących przestrajalną luminescencję. Ważnymi aspektami wspominanych fosforanów jest ich wydłużony kształt przypominający nanodruty/nanoigły (duży *aspect ratio*). Do modyfikacji powierzchni użyto wielkocząsteczkowych związków organicznych o właściwościach ciekłokrystalicznych i luminescencyjnych. Udało się otrzymać nowe hybrydowe nanomateriały nieorganiczno-organiczne złożone z nanodrutów fosforanów lantanowców oraz organicznej nanowarstwy powierzchniowej. Powstałe nanomateriały wykazywały przestrajalną luminescencję, pochodzącą zarówno od fazy nieorganicznej jak i organicznej. Zmiana koloru barwy (przestrojenie koloru emisji) następowało na skutej zmiany długości fali światła wzbudzającego w zakresie 200-400 nm (UV). Możliwa była modulacja koloru emisji od zielonego, poprzez żółty aż do czerwonego. Otrzymane nanomateriały zostały szczegółowo zbadane pod kątem ich właściwości strukturalnych, morfologicznych (HR-TEM, STEM i DLS) i spektroskopowych (widma IR potwierdzające obecność struktur fosforanowych oraz powierzchniowych cząsteczek związku organicznego) ze szczególnym uwzględnieniem badań luminescencyjnych (widma wzbudzenia/emisji, krzywe zaniku luminescencji, zdjęcia emisji i diagram chromatyczności). Zsyntetyzowane produkty mogą zostać potencjalnie zastosowane jako nowe zaawansowane źródła światła, znaczniki luminescencje, biomarkery, trudne do podrobienia zabezpieczenia dokumentów, etc.

Wkład własny w powstanie pracy: koncepcja badań oraz znaczący udział w syntezie i zbadaniu właściwości fizykochemicznych otrzymanych nanostruktur. Analiza uzyskanych wyników, opracowanie danych i zredagowanie publikacji.

RSC Advances

PAPER

View Article Online
View Journal | View Issue

Cite this: *RSC Adv.*, 2014, **4**, 46305

Eu^{3+} and Tb^{3+} doped $LaPO_4$ nanorods, modified with a luminescent organic compound, exhibiting tunable multicolour emission†

Marcin Runowski,[a] Tomasz Grzyb,[a] Anna Zep,[b] Paulina Krzyczkowska,[b] Ewa Gorecka,[b] Michael Giersig[ac] and Stefan Lis*[a]

Received 24th June 2014
Accepted 12th September 2014

DOI: 10.1039/c4ra06168c

www.rsc.org/advances

Co-precipitation reaction followed by hydrothermal treatment were used to synthesise Eu^{3+} or Tb^{3+} doped $LaPO_4$ nanorods, of 5–10 nm in width and 50–100 nm in length. Surface modification of the as-prepared nanoparticles with a selected luminescent organic compound resulted in formation of hybrid inorganic–organic nanomaterials. The products obtained exhibited tunable multicolour luminescence, dependent on the surface modification and applied excitation wavelength. The colour of their emission can be altered from red-orange to yellow-green. Powder X-ray diffraction (XRD), high resolution transmission electron microscopy (HRTEM) and scanning transmission electron microscopy (STEM) confirmed the structure and morphology of the products synthesized. Successful surface modification of the nanophosphors was evidenced by analytical and spectroscopic techniques such as dynamic light scattering (DLS) – providing size distribution histograms and zeta potentials of the nanoparticles; IR spectroscopy and elemental analysis which proved the presence of an organic phase in the structure; spectrofluorometry (excitation/emission spectra and luminescence decay curves) which confirmed the formation of hybrid, surface modified nanomaterials revealing tunable multicolour emission.

1. Introduction

Luminescent nanomaterials based on lanthanide ions (Ln^{3+}) have fascinated researchers for over the last two decades.[1–5] The spectroscopic properties of Ln^{3+} ions are unique among the other elements, which result from their electronic configuration $[Xe]4f^n$ ($n = 0$–14). 4f orbitals of lanthanide ions are shielded by 5p and 6s shells, which makes the 4f–4f electronic transitions nearly insensitive to the coordination environment of Ln^{3+} ion, and provides narrow spectral width of emission or absorption bands as well as long-lived luminescence.[6] The parity-forbidden character of the 4f–4f transitions results in a very low molar absorption coefficients and also low efficiencies of Ln^{3+} emission, when the direct excitation of 4f–4f absorption bands is applied. However, some Ln^{3+} ions, like Tb^{3+} and Ce^{3+}, can be effectively excited *via* the allowed 4f–5d transitions, which strongly enhances the luminescence efficiency.[7] Also the other, partially allowed processes like charge transfer (CT) observed in O^{2-} containing host materials and energy transfer (ET), can increase absorption of the excitation light and therefore luminescence intensity.[8,9] These specific properties of Ln^{3+} ions allow the design of nanomaterials revealing effective luminescence by applying ET and CT phenomena (indirect excitation). Much effort has been made to study ET between, *e.g.*: Ce^{3+} and Tb^{3+}, Gd^{3+} and Eu^{3+} or in up-converting systems: Yb^{3+} and Er^{3+}, Yb^{3+} and Tb^{3+}.[10–13] Also ET from the host or ligand to Ln^{3+} ion has been extensively investigated.[14] The emission bands of Ln^{3+} ions can be observed in the ultraviolet, visible and near infrared ranges.

The high potential of Ln^{3+}-doped nanomaterials is used in many different applications like lighting, phosphors production, organic light emitting diodes (OLEDs and LEDs), lasers, optical amplifiers or waveguides and such areas like medicine and biology.[4,15–19] Some of these applications result from the strong interest in Ln^{3+}-doped hybrid inorganic–organic materials.[20–22] In general, hybrid materials have altered properties that can be tailored according to the needs, *e.g.* they can show increased mechanical resistance, thermal stability, luminescence efficiency *etc.*[23–25] Also the multifunctionality and the possibility to modulate their properties are important factors increasing development of such hybrid materials.[26–31] Such sophisticated bi- or multifunctional hybrid/composite nanomaterials can exhibit simultaneously different desired properties like luminescence and magnetism, which are crucial for

[a]*Adam Mickiewicz University, Faculty of Chemistry, Umultowska 89b, 61-614 Poznań, Poland. E-mail: blis@amu.edu.pl*

[b]*University of Warsaw, Faculty of Chemistry, Laboratory of Physical Chemistry of Dielectrics and Magnetics, Żwirki i Wigury 101, 02-089 Warszawa, Poland*

[c]*Freie Universität Berlin, Institute of Experimental Physics, Arnimallee 14, 14195 Berlin, Germany*

† Electronic supplementary information (ESI) available: TG-DTA curves of the $LaPO_4$:Eu^{3+} 10%, $LaPO_4$:Tb^{3+} 10%, surface modified $LaPO_4$:Eu^{3+} 10%@organic and $LaPO_4$:Tb^{3+} 10%@organic nanomaterials (Fig. S1†). See DOI: 10.1039/c4ra06168c

development of advanced bioimaging, drug delivery, luminescence tracing, document protection *etc.*[28,29,32,33] One of the areas most recently studied is surface modification of nanocrystals (NCs). Significantly increased stability of colloids, lowered cytotoxicity of NCs and their higher biocompatibility, possibility of NCs use as drug carriers, production of biological sensors and detectors are only a few examples of the numerous applications that result from the inorganic–organic characteristics of hybrid nanomaterials.[20,34–36]

In this study we report the preparation of hybrid inorganic–organic nanomaterials based on $LaPO_4$ nanorods doped with Tb^{3+} or Eu^{3+} ions, having organically modified surface. Our aim was to synthesize the nanomaterials exhibiting tunable luminescence dependent on the excitation wavelength used and study their photophysical properties. Such nanocomposites exhibit bright, multicolour luminescence originating from inorganic and organic components. They can be applied as advanced phosphors, luminescence tracers, biomarkers, *etc.* What is more, nanomaterials based on lanthanide phosphates reveal low cytotoxicity,[24] and the use of functional organic compound as a surface modifier can alter the surface properties of the nanostructures modified and extend the range of their potential applications.

2. Experimental section

2.1. Materials

Eu_2O_3, Tb_4O_7 and La_2O_3 (Stanford Materials, 99.99%) were separately dissolved in a concentrated HNO_3 (POCh S.A., ultrapure) to obtain $Eu(NO_3)_3$, $Tb(NO_3)_3$ and $La(NO_3)_3$ aqueous solutions, respectively. Ammonium phosphate monobasic $NH_4H_2PO_4$ (Sigma-Aldrich, ReagentPlus®, ≥98.5%) was used as a source of phosphate ions. Polyethylene glycol (PEG) 6000 (Alfa Aesar, 98%) was used as a surfactant. The synthetic procedure leading to 2,3-di(3,4-dioctyloxyphenyl)-quinoxaline-6-carboxylic acid starts with the preparation of the appropriate ketone – 3,3,4,4-tetraoctyloxydibenzoyl, which has already been described in literature.[37] From this ketone and 3,4-diaminobenzoic acid, final compound was prepared according to the method described by E. J. Foster[38,39] and H.-J. Chen.[40] In all experiments, ultra-pure distilled water and absolute ethanol were used.

2.2. Synthesis of nanophosphors – $LaPO_4$:Ln^{3+} 10% (Ln^{3+} = Eu^{3+} or Tb^{3+})

The typical synthesis was carried out to get 1.5 g of the final product. The co-precipitation reaction was performed in ambient conditions, using a hot-plate magnetic stirrer. The initial pH of the prepared $RE(NO_3)_3$ solutions was around 5. Solution A: $La(NO_3)_3$ (11.62 mL, 0.494 M) and $Eu(NO_3)_3$ (1.52 mL, 0.419 M) were mixed together at 9/1 molar ratio, and filled with water up to 75 mL. 50 mL of ethanol was added to the as-prepared solution. Subsequently, 0.75 g of PEG was dissolved in this solution. Solution B: 25% molar excess of $NH_4H_2PO_4$ was dissolved in the same solvent systems, with addition of the same amount of PEG. The as-prepared solution B was added dropwise to solution A during 20 minutes. Afterwards the obtained white precipitate was centrifuged and washed with water and ethanol several times. To get well-crystallised nanomaterial, the as-prepared product was dispersed in 70 mL of water, transferred into a Teflon lined vessel and treated under hydrothermal conditions for 120 minutes at 200 °C and 40 bar (microwave autoclave – ERTEC, Magnum II, 600 W). When the reaction was complete, the purification procedure was repeated. The final product was dried under vacuum overnight. Tb^{3+} doped product was prepared in the same way, using $Tb(NO_3)_3$ instead of $Eu(NO_3)_3$.

2.3. Surface modification of nanorods

The following organic compound was selected as an exemplary surface modifier because of its complex character, presence of functional groups allowing further chemical modification, potential liquid crystal properties and intensive luminescence.[41] 5 mg of 2,3-di(3,4-dioctyloxyphenyl)-quinoxaline-6-carboxylic acid ($C_{53}H_{78}N_2O_6$ – for the reader's convenience the simple abbreviation the "organic" will be used throughout the article) dissolved in 10 mL of THF was added slowly to a stirred suspension of nanorods (50 mg) in 25 mL of THF. The reaction mixture was stirred at room temperature for further 72 h and the obtained yellow precipitate was then centrifuged (5 min, 13 000 rpm). In the next step, pure THF was added to the nanomaterial. Afterwards, the mixture was sonicated for 60 s and then centrifuged once more (5 min, 13 000 rpm). The procedure was repeated until no trace of excess of the organic compound was found as determined by TLC. The final, hybrid nanomaterials (yellow powders), revealed tunable multicolour luminescence originating from both inorganic and organic components. Here is worth noting, that there was no observed release of the organic compound from the nanoparticles surface, after washing the product in water. Only a long sonication and washing with THF or toluene caused a slow release of the organic compound. Fig. 1 illustrates a scheme of the nanomaterials surface modification.

2.4. Characterization

Electron microscopy measurements were carried out using transmission electron microscope-TEM Zeiss LIBRA 200FE, operating at 200 kV. Powder XRD (X-ray diffractograms) were recorded on a Bruker AXS D8 Advance diffractometer, using Cu Kα radiation (λ = 1.5406 Å). The elemental analysis of the products was performed using an Elementar Analyser Vario EL III. Setaram Setsys 1200 device, was used for simultaneous thermogravimetric-differential thermal analysis (TG-DTA), with a heating rate of 5 °C min^{-1} in air. IR spectra were recorded on FT-IR spectrophotometer, JASCO 4200. The IR spectra were measured in transmission mode, the samples were mixed with KBr, ground and pressed forming transparent discs. The particle size distribution (hydrodynamic diameter) and zeta (ζ) potential of the nanomaterials synthesized were recorded on Malvern Zetasizer Nano ZS, equipped with dynamic light scattering (DLS) module (He–Ne laser 633 nm, max 4 mW). Before measurements each product was dispersed in MiliQ quality water, forming stable aqueous colloid (0.1 mg mL^{-1}). The

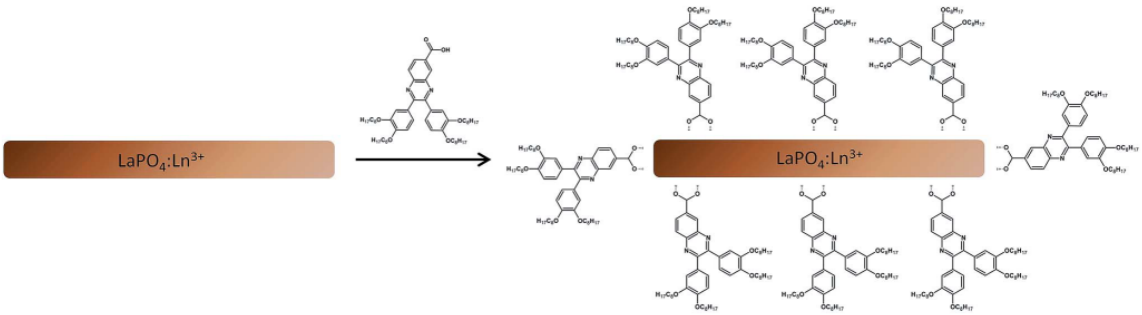

Fig. 1 Scheme of organic surface modification of $LaPO_4:Ln^{3+}$ 10% nanoparticles.

excitation/emission spectra and luminescence decay curves of the dried products were measured in ambient conditions, using a Hitachi F-7000 spectrofluorometer. All spectra were appropriately corrected for the apparatus response.

3. Results and discussion

3.1. Structure and morphology

The recorded powder XRD patterns of $LaPO_4:Tb^{3+}$ 10% and $LaPO_4:Eu^{3+}$ 10% were compared with the pattern from ICDD (International Centre for Diffraction Data) standards database (Fig. 2). Both diffractograms are similar and fit well to that of the hexagonal, hydrated lanthanum phosphate, $LaPO_4 \cdot 0.5H_2O$ (ICDD 000-046-1439). However, the diffractograms reveal also some very small reflexes (overlapping with the background noise), which are probably related to the monoclinic phase (monazite). The obtained XRD patterns exhibit broadened reflexes, which indicate the nanocrystallinity of the products synthesized, and at some extent, it can be due to the superposition of reflexes of hexagonal and monoclinic phase.

Fig. 3 presents electron microscope images of the nanomaterials synthesized. TEM images of $LaPO_4:Eu^{3+}$ 10% (a) and $LaPO_4:Tb^{3+}$ 10% (b), HR-TEM image of $LaPO_4:Eu^{3+}$ 10% including FFT (Fast Fourier Transform) inset (c), STEM image of $LaPO_4:Eu^{3+}$ 10%. TEM images (a and b) reveal numerous phosphate nanorods similar in shape. The nanorods synthesized are of 5–10 nm in width and 50–100 nm in length, revealing high aspect ratio. The presented HRTEM image of $LaPO_4:Eu^{3+}$ 10% (c) shows its interplanar distances, namely 0.35 nm (110) and 0.31 nm (200). The observed orientation of the planes and their calculated interplanar distances are consistent with FFT (Fig. 3c inset) of HR-TEM image and XRD analysis. The characteristic hexagonal pattern of the performed FFT undoubtedly confirms the crystal structure of the product obtained. The STEM image provides additional information about the $LaPO_4:Eu^{3+}$ 10% morphology (d), confirming the elongated shape of the synthesized nanoparticles.

Surface modification. Surface modification of the prepared inorganic nanophosphors by coating with luminescent organic modifier was carried out to get hybrid nanomaterials, exhibiting tunable multicolour luminescence, dependent on the excitation

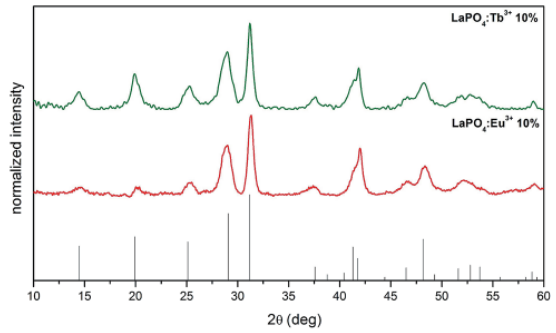

Fig. 2 XRD patterns of $LaPO_4:Eu^{3+}$ 10% ($0.5H_2O$) and $LaPO_4:Tb^{3+}$ 10% ($0.5H_2O$).

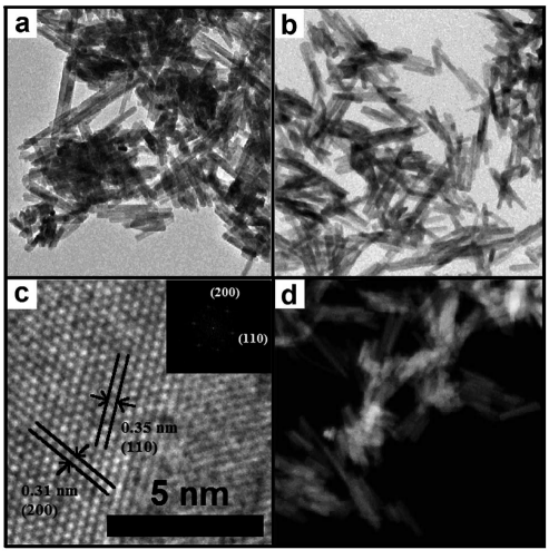

Fig. 3 TEM images of $LaPO_4:Eu^{3+}$ 10% (a), $LaPO_4:Tb^{3+}$ 10% (b); HR-TEM image and its FFT inset for $LaPO_4:Eu^{3+}$ 10% (c); STEM image of $LaPO_4:Eu^{3+}$ 10% (d).

wavelength. The morphology and structure of the nanoparticles obtained, were not affected by the organic surface modification. The presence of the organic modifier molecules on the nanoparticles surface was confirmed and examined by elemental analysis, FT-IR spectroscopy, DLS studies (ζ-potential and particle size distribution) and luminescence spectroscopy.

In order to determine the amount of organic modifiers in the nanomaterials obtained, the elemental analysis of $LaPO_4$:Eu^{3+} 10%, $LaPO_4$:Tb^{3+} 10%, $LaPO_4$:Eu^{3+} 10%@organic and $LaPO_4$:Tb^{3+} 10%@organic was performed. For $LaPO_4$:Eu^{3+} 10% product, the content of N, C, H was 0.004, 0.157 and 0.732 (wt%), respectively, whereas for $LaPO_4$:Tb^{3+} 10% product, the corresponding contents were 0.005, 0.155 and 0.746 (wt%), respectively. In the products modified with the organic compound ($C_{53}H_{78}N_2O_6$), the contents of N, C, H for $LaPO_4$:Eu^{3+} 10%@organic was 0.085, 2.267 and 0.942 (wt%), respectively, whereas for $LaPO_4$:Tb^{3+} 10%@organic product, the values obtained were 0.087, 2.249 and 0.955 (wt%), respectively. On the basis of the results, the molar concentration of the organic compound bound to the surface is 0.0332 mmol (2.79 wt%) and 0.0329 mmol (2.76 wt%) per one gram of $LaPO_4$:Eu^{3+} 10%@organic and $LaPO_4$:Tb^{3+} 10%@organic products, respectively. The results presented confirm a successful functionalization of the nanomaterials surface. The excessive hydrogen content in their structure was related to the adsorbed water molecules.

Additionally, TG-DTA measurements were performed to investigate the stability of the organic surface layer and confirm the composition of the nanomaterials synthesized. The results obtained agree well with the elemental analysis data, and they are presented in full in ESI (Fig. S1†).

Fig. 4 illustrates the IR spectra of $LaPO_4$:Eu^{3+} 10%, $LaPO_4$:Tb^{3+} 10%, $LaPO_4$:Eu^{3+} 10%@organic, $LaPO_4$:Tb^{3+} 10%@organic, and pure organic compound. All spectra recorded reveal broad absorption peaks around 3400 cm^{-1} and 1640 cm^{-1}, corresponding to the O–H stretching (ν) and deformation (σ) vibrations, respectively. The observed O–H bonds correspond to water molecules adsorbed on the nanorods surface and structural water molecules (hydration of phosphates). The absorption peaks around 2924 and 2865 cm^{-1} are related to νC–H vibrations of $-CH_2$ groups of organic compound molecules (adsorbed on the surface of phosphate nanorods). The spectra of the pure and modified phosphates exhibit very intensive and broad peaks assigned to the vibrations of phosphate groups. The peaks around 1050, 950 cm^{-1} were assigned to the stretching vibrations within PO_4 groups, and around 615, 542 cm^{-1} to the bending vibrations within these groups.[42,43] What is more, the quite intensive band observed at ~960 cm^{-1} confirms the coexistence of monoclinic phosphate (minor phase) together with the hexagonal lanthanum phosphate (major phase), which was mentioned during discussion of the XRD patterns. The peaks below 1700 cm^{-1} in the spectrum of the pure organic compound, correspond to the vibrations of numerous bonds in the very complex structure of this compound. The presence of peaks around 2900 and 1200 cm^{-1} in the spectra of the organically modified phosphates ($LaPO_4$:Eu^{3+} 10%@organic and $LaPO_4$:Tb^{3+} 10%@organic), confirms their successful modification with the organic compound used.

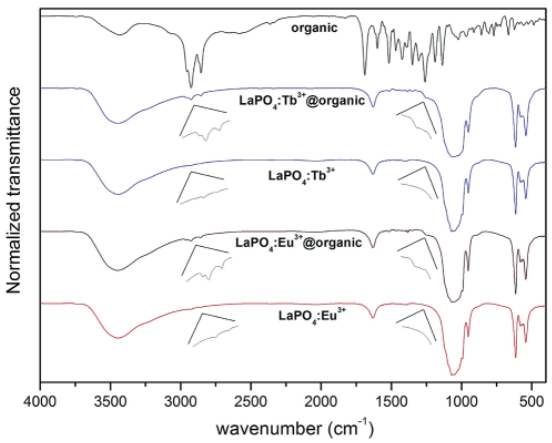

Fig. 4 IR spectra of pure organic compound (surface modifier), unmodified $LaPO_4$:Eu^{3+} 10% and $LaPO_4$:Tb^{3+} 10%, surface modified $LaPO_4$:Eu^{3+} 10%@organic and $LaPO_4$:Tb^{3+} 10%@organic.

The ζ-potential and average particle size distribution of the nanomaterials synthesized were measured by the DLS method. All of the measurement were carried out at pH = 7. The ζ-potential recorded for $LaPO_4$:Eu^{3+} 10% was +29.3 mV, and for $LaPO_4$:Tb^{3+} 10% it was +34.6 mV. The ζ-potential recorded for the surface modified $LaPO_4$:Eu^{3+} 10%@organic and $LaPO_4$:Tb^{3+} 10%@organic nanorods decreased to +17.8 mV and +27.3 mV, respectively. The decreased ζ-potential values confirmed surface modification of the nanomaterials synthesized. What is more, all of the nanomaterials exhibited relatively high surface charge, additionally confirming their stability at neutral pH, which is important in potential bioapplications. The average particle size distribution of the products synthesized is presented in Fig. 5. The approximate sizes of $LaPO_4$:Eu^{3+} 10% (a) and $LaPO_4$:Tb^{3+} 10% (b) particles are about 300 nm, and increase after surface modification for $LaPO_4$:Eu^{3+} 10%@organic (c) and $LaPO_4$:Tb^{3+} 10%@organic (d) to about 500 nm. This fact clearly confirms surface alterations of the nanomaterials modified, manifested by increased hydrodynamic diameter of the nanoparticles. However, the recorded DLS curves revealed the polydispersity of the nanomaterials obtained, which was caused by particles agglomeration and their "sticking" to bigger clusters after surface modification. The hydrodynamic radius/diameter of the particles analysed is usually larger in comparison to the real particle sizes from TEM data, since the DLS method takes into account surface solvation of the particles, and their agglomeration/aggregation in the colloidal solution. One must remember, that the data presented are onlya rough approximation of the nanoparticles sizes because of their highly anisotropic shape (DLS size measurements assume the spherical shape of the analysed objects).

3.2. Luminescent properties

Fig. 6–8 show the spectroscopic properties of Eu^{3+} and Tb^{3+} doped phosphate nanorods and the corresponding surface

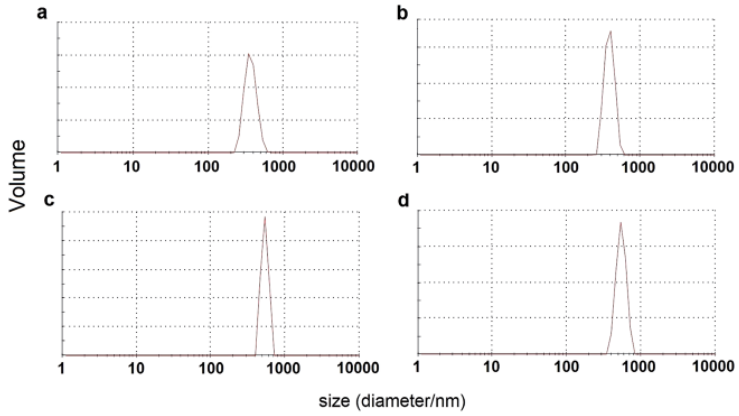

Fig. 5 Particle size distribution for $LaPO_4$:Eu^{3+} 10% (a) and $LaPO_4$:Tb^{3+} 10% (b) $LaPO_4$:Eu^{3+} 10%@organic (c) and $LaPO_4$:Tb^{3+} 10%@organic (d), measured by DLS method.

modified products, namely $LaPO_4$:Eu^{3+} 10%@organic and $LaPO_4$:Tb^{3+} 10%@organic. All spectra were recorded for solid products (dried powders). Fig. 6a presents three excitation spectra of $LaPO_4$:Eu^{3+}10% ($\lambda_{em} = 620$ nm) and $LaPO_4$:Eu^{3+} 10% @organic ($\lambda_{em} = 500$, 620 nm). For bare $LaPO_4$:Eu^{3+} 10% ($\lambda_{em} =$ 620 nm – the maximum of $^5D_0 \rightarrow {}^7F_2$ transition in Eu^{3+} ion), a dominant broad band centred at 256 nm related to $O^{2-} \rightarrow Eu^{3+}$ charge transfer (CT) transition can be observed. This band is the

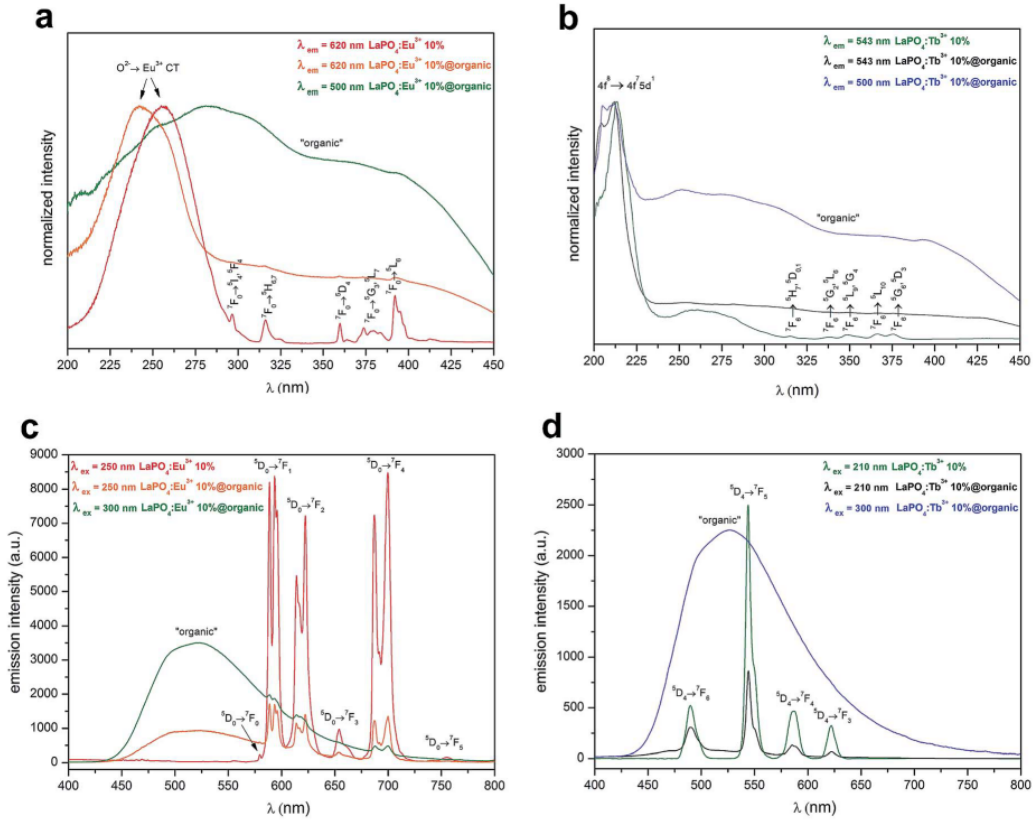

Fig. 6 Excitation spectra of $LaPO_4$:Eu^{3+} 10%, $LaPO_4$:Eu^{3+} 10%@organic (a) and $LaPO_4$:Tb^{3+} 10%, $LaPO_4$:Tb^{3+} 10%@organic (b); emission spectra of $LaPO_4$:Eu^{3+} 10%, $LaPO_4$:Eu^{3+} 10%@organic (c) and $LaPO_4$:Tb^{3+} 10%, $LaPO_4$:Tb^{3+} 10%@organic (d).

most intensive one in the whole spectrum because the mentioned CT transition is allowed by selection rules, in contrast to the forbidden 4f–4f transitions within Eu^{3+} ion (the series of narrow bands observed at 300–400 nm). For the surface modified $LaPO_4$:Eu^{3+} 10%@organic nanomaterial, the same dominant band can be observed (λ_{em} = 620 nm). The series of intrinsic 4f–4f transitions is hardly visible in this spectrum, because they overlap with the appearing absorption band of the organic surface modifier. The third plot obtained for the same modified nanomaterial, whose excitation spectrum was recorded at λ_{em} = 500 nm (the maximum of emission band for the organic compound) does not reveal the characteristic bands related to the transitions in Eu^{3+} ions. In this spectrum only a very broad absorption band centred at 282 nm corresponding to the surface organic compound can be observed in the whole presented wavelength range.

Fig. 6b shows three excitation spectra of $LaPO_4$:Tb^{3+} 10% (λ_{em} = 543 nm) and $LaPO_4$:Tb^{3+} 10%@organic (λ_{em} = 500, 543 nm). The spectrum of $LaPO_4$:Tb^{3+} 10% (λ_{em} = 543 nm is the maximum of the most intensive in the emission spectrum $^5D_4 \rightarrow {}^7F_5$ transition, within Tb^{3+} ions), shows a dominant broad band centred at 213 nm corresponding to $4f^8 \rightarrow 4f^75d^1$ (f–d) allowed transition. The bands at higher wavelengths are assigned to the forbidden 4f–4f transitions in Tb^{3+} ion. In the spectrum of $LaPO_4$:Tb^{3+} 10%@organic recorded at the same λ_{em} = 543 nm, the slightly shifted f–d transition is also dominant. The other 4f–4f transitions are not visible. The last excitation spectrum of this modified nanomaterial (λ_{em} = 500 nm) also reveals the dominant band related to f–d transition in Tb^{3+} ion. However, the very broad absorption band (with maximum ranging from 250 to 280 nm) assigned to the surface organic modifier, can be observed in the whole spectrum, as well.

Fig. 6c presents three emission spectra of $LaPO_4$:Eu^{3+}10% (λ_{ex} = 250 nm) and $LaPO_4$:Eu^{3+} 10%@organic (λ_{ex} = 250, 300 nm). In the first spectrum of $LaPO_4$:Eu^{3+}10% recorded at λ_{ex} = 250 nm (the position of the most intensive CT transition in the excitation spectrum), six narrow, split bands corresponding to the $^5D_0 \rightarrow {}^7F_J$ (J = 0–5) transitions can be observed. The hypersensitive electric dipole $^5D_0 \rightarrow {}^7F_2$ transition is sensitive to the site symmetry alterations.[44,45] The ratio between integrated areas of the $^5D_0 \rightarrow {}^7F_2$ and $^5D_0 \rightarrow {}^7F_1$ transition bands is informative about the presence of symmetry centre in the site occupied by the Eu^{3+} ions. The values calculated both for $LaPO_4$:Eu^{3+} 10% and $LaPO_4$:Eu^{3+} 10%@organic are close to 1 (1.04 and 1.01 respectively). The ratio higher than 1 indicates that the Eu^{3+} ions are situated at sites without inversion symmetry. However, in the $LaPO_4$:Eu^{3+} material the Eu^{3+} ions occupy sites with D_2 symmetry in the $LaPO_4$ structure which is non-centrosymmetric and the presence of an inversion centre cannot be assumed.[46–48]

The product exhibits an intense, bright red luminescence. When the surface modified nanomaterial was excited at the same wavelength, the intensity of the mentioned transitions decreased, and a new broad band appeared in the range of 500–550 nm. This band corresponds to the emission of the organic compound. As a consequence of these alternations in the spectrum shape, the observed luminescence of the product was tuned to yellowish emission. Upon exciting the organic modified nanomaterial at 300 nm (absorption range of the organic compound), the characteristic bands of Eu^{3+} ions can hardly be observed, in contrast to the very high intensity and broad emission band of the organic compound. The resulting emission of the product is green.

Fig. 6d shows three emission spectra of $LaPO_4$:Tb^{3+} 10% (λ_{ex} = 210 nm) and $LaPO_4$:Tb^{3+} 10%@organic (λ_{ex} = 210, 300 nm). The spectrum of $LaPO_4$:Tb^{3+} 10%, recorded at λ_{ex} = 210 nm (the position of the most intensive transition in the excitation spectrum), presents four narrow bands assigned to the $^5D_4 \rightarrow {}^7F_J$ (J = 6–3) transitions, characteristic of Tb^{3+} ions.[7] The product exhibits bright green luminescence. The spectrum of the $LaPO_4$:Tb^{3+} 10%@organic nanophosphor excited at the same wavelength reveals four bands typical of Tb^{3+} ions, as well.

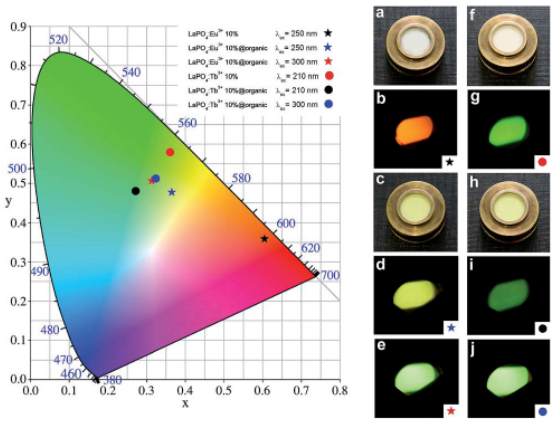

Fig. 7 Chromaticity diagram and photographs of $LaPO_4$:Eu^{3+} 10% (a and b), $LaPO_4$:Eu^{3+} 10%@organic (c–e), $LaPO_4$:Tb^{3+} 10% (f and g) and $LaPO_4$:Tb^{3+} 10%@organic (h–j), taken in daylight (a, c, f and h) and under UV light irradiation (λ_{ex} = 210 nm – g and i; λ_{ex} = 250 nm – b and d; λ_{ex} = 300 nm – e and j).

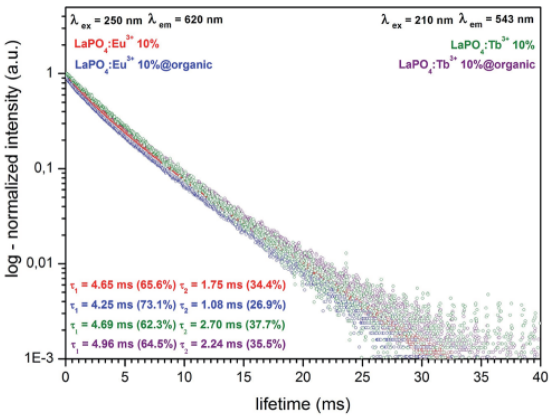

Fig. 8 Luminescence decay curves of $LaPO_4$:Eu^{3+} 10%, $LaPO_4$:Eu^{3+} 10%@organic and $LaPO_4$:Tb^{3+} 10%, $LaPO_4$:Tb^{3+} 10%@organic.

However, the intensity of these bands decreased in comparison to that in the spectrum of the unmodified product. Besides these bands, less intensive bands around 500–550 nm, corresponding to the organic modifier can also be observed. The colour of the product emission is still green, however shifted towards blue. The spectrum of the modified nanomaterial excited at 300 nm reveals only the intensive, broad band assigned to the organic compound. Its luminescence is greenish, namely the colour of emission is slightly altered when compared to that of the unmodified nanophosphor.

For more detailed specification of the luminescence colours one can refer to the included chromaticity diagram (CIE 1964 10 deg observer), presented in Fig. 7. The photographs of the products synthesized, taken in daylight and under UV light, showing their multicolour emission, are included in Fig. 7, as well.

Fig. 8 presents the luminescence decay curves and calculated radiative lifetimes for the $^5D_0 \rightarrow {}^7F_2$ and $^5D_4 \rightarrow {}^7F_5$ transitions of Eu^{3+} and Tb^{3+} ions, respectively. All data were recorded at 293 K; $\lambda_{em} = 620$ nm, $\lambda_{ex} = 250$ nm for the Eu^{3+} doped compounds and $\lambda_{em} = 543$ nm and $\lambda_{ex} = 210$ nm, for the Tb^{3+} doped compounds. In hexagonal lanthanum phosphate, all lanthanide ions should be at the sites of the same type (coordination environment).[24] However, the experimental profiles were successfully fitted to the biexponential function of decay, namely $y = A_1 \exp(-x/\tau_1) + A_2 \exp(-x/\tau_2) + y0$. The nanomaterials synthesized exhibit high surface-to-volume ratio. Therefore a large part of ions forming the material is placed on or near the surface of nanocrystals. Hence, after surface modification with the organic compound used, a significant number of the surface/near surface ions were localised in a new coordination environment (altered local site symmetry). The reason for this phenomenon was a strong coordination/binding of the organic molecules to the nanoparticles surface. This is why, the nanophosphors obtained exhibit a shorter second component of luminescence decay. Here is worth noting, that the presence of a small amount of monoclinic $LaPO_4$ in the sample can affect the lifetime components and disturb their decay profiles. However, because of the large contribution ($\approx$30%) of the second lifetime components and their significant shortening after the surface modification, we assume that the discussed biexponential character of the luminescence decay is predominantly caused by the differently emitting surface ions. The calculated luminescence lifetimes for the products synthesized are in the range of 4.25–4.96 ms (τ_1) and 1.08–2.70 ms (τ_2). The detailed values are presented in Fig. 8. Such relatively long radiative lifetimes are in line with literature data for lanthanide doped inorganic phosphors.[49,50] The observed lifetimes for Eu^{3+} and Tb^{3+} doped products are generally similar, however the lifetimes of Eu^{3+} ions are slightly shorter when compared to those of Tb^{3+} ions. Analysis of the decay profiles leads to a conclusion that the modified nanomaterials exhibit a shorter average lifetime, in comparison to their unmodified analogues. The lifetime shortening is particularly pronounced in the second lifetime component (τ_2), assigned to the surface ions (shortening from 1.75 to 1.08 ms and from 2.70 to 2.24 ms for Eu^{3+} and Tb^{3+} ions, respectively). This phenomenon can be explained by a strong interaction between surface ions and organic molecules attached to the nanoparticles surface, resulting in enhanced luminescence quenching. The results obtained are in agreement with the data on the emission decrease of the modified nanorods (see the emission spectra in Fig. 6a and b).

4. Conclusions

The highly luminescent, crystalline nanomaterials doped with Eu^{3+} and Tb^{3+} ions were synthesized *via* the co-precipitation approach followed by hydrothermal treatment. The nanomaterials formed were in the form of elongated nanorods (5–10 nm in width and 50–100 nm in length) composed of hexagonal $LaPO_4 \cdot 0.5H_2O$. Subsequently, the products obtained were modified with a luminescent organic compound. The surface modification resulted in a formation of hybrid inorganic–organic nanomaterials, which exhibited tunable and multimodal luminescence. The products emission could be tuned from red-orange to yellow-green luminescence. Successful modification of the surface of nanocrystals was checked by DLS, IR spectroscopy, elemental analysis, TG-DTA and spectrofluorometry. These novel, functional nanomaterials can be applied in luminescence tracing, detection techniques, multicolour imaging, as novel light sources and in many other special applications requiring sophisticated, hybrid nanomaterials exhibiting tunable emission. The products synthesized can be also used in biomedical applications requiring multifunctionality of nanomaterials.

Acknowledgements

Financial support from the National Science Centre (Grant no. UMO-2012/06/M/ST5/00325) is kindly acknowledged. M.R. gratefully acknowledges the financial support from the Polish Ministry of Science and Higher Education - scientific work financed from the budget for science in 2012–2015 as a research project within the program called “Diamond Grant” Nr DI2011 011441. A.Z. and E.G. gratefully acknowledges the financial support from the National Science Centre (Grant 2013/08/M/ST5/00781). P.K. gratefully acknowledges the financial support from the National Science Centre (Grant 2012/05/N/ST5/01505). M.G. thanks the National Science Centre “Maestro Project NR DEC-2012/06/A/ST4/00373” and the Foundation for Polish Science in Warsaw for financial support.

Notes and references

1 R. Bhargava, *J. Lumin.*, 1996, **70**, 85–94.
2 S. Heer, O. Lehmann, M. Haase and H.-U. Güdel, *Angew. Chem., Int. Ed.*, 2003, **42**, 3179–3182.
3 Z.-G. Yan and C. Yan, *J. Mater. Chem.*, 2008, **18**, 5046–5059.
4 W. Feng, C. Han and F. Li, *Adv. Mater.*, 2013, 1–17.
5 Q. Lü, A. Li, F. Guo, L. Sun and L. Zhao, *Nanotechnology*, 2008, **19**, 145701.
6 P. A. Tanner, *Chem. Soc. Rev.*, 2013, **42**, 5090–5101.

7 T. Grzyb, M. Runowski, A. Szczeszak and S. Lis, *J. Phys. Chem. C*, 2012, **116**, 17188–17196.
8 T. Grzyb, R. J. Wiglusz, V. Nagirnyj, A. Kotlov and S. Lis, *Dalton Trans.*, 2014, **43**, 6925–6934.
9 F. Wang, X. Fan, M. Wang and Y. Zhang, *Nanotechnology*, 2007, **18**, 25701–25706.
10 T. Grzyb, *RSC Adv.*, 2014, **4**, 2590–2595.
11 T. Grzyb, M. Runowski, K. Dąbrowska, M. Giersig and S. Lis, *J. Nanopart. Res.*, 2013, **15**, 1958–1972.
12 C. Cao, S. Guo, B. K. Moon, B. C. Choi and J. H. Jeong, *Solid State Sci.*, 2013, **19**, 99–103.
13 F. Auzel, *Chem. Rev.*, 2004, **104**, 139–173.
14 S. Lis, M. Elbanowski, B. Mąkowska and Z. Hnatejko, *J. Photochem. Photobiol., A*, 2002, **150**, 233–247.
15 S. Wang, J. Feng, S. Song and H. Zhang, *CrystEngComm*, 2013, **15**, 7142–7151.
16 C. C. Lin and R.-S. Liu, *J. Phys. Chem. Lett.*, 2011, **2**, 1268–1277.
17 Q. Y. Zhang and X. Y. Huang, *Prog. Mater. Sci.*, 2010, **55**, 353–427.
18 S. V. Eliseeva and J.-C. G. Bünzli, *Chem. Soc. Rev.*, 2010, **39**, 189–227.
19 G. Boulon, *Opt. Mater.*, 2012, **34**, 499–512.
20 K. Binnemans, *Chem. Rev.*, 2009, **109**, 4283–4374.
21 P. Escribano, B. Julián-López, J. Planelles-Aragó, E. Cordoncillo, B. Viana and C. Sanchez, *J. Mater. Chem.*, 2008, **18**, 23–40.
22 L. D. Carlos, R. A. S. Ferreira, V. de Zea Bermudez, B. Julián-López and P. Escribano, *Chem. Soc. Rev.*, 2011, **40**, 536–549.
23 J.-N. Park, P. Zhang, Y.-S. Hu and E. W. McFarland, *Nanotechnology*, 2010, **21**, 225708.
24 M. Runowski, K. Dąbrowska, T. Grzyb, P. Miernikiewicz and S. Lis, *J. Nanopart. Res.*, 2013, **15**, 2068.
25 E. He, H. Zheng, J. Dong, W. Gao, Q. Han, J. Li, L. Hui, Y. Lu and H. Tian, *Nanotechnology*, 2014, **25**, 045603–045611.
26 S. A. Corr, Y. P. Rakovich and Y. K. Gun'ko, *Nanoscale Res. Lett.*, 2008, **3**, 87–104.
27 S. T. Selvan, T. T. Y. Tan, D. K. Yi and N. R. Jana, *Langmuir*, 2009, **26**, 11631–11641.
28 S. X. C. Mi, J. Zhang, H. Gao, X. Wu, M. Wang, Y. Wu, Y. Di, Z. Xu and C. Mao, *Nanoscale*, 2010, **2**, 1141–1148.
29 M. Runowski, T. Grzyb and S. Lis, *J. Nanopart. Res.*, 2012, **14**, 1188.
30 B. Lu, Z. Zhang, J. Hao and J. Tang, *RSC Adv.*, 2014, **4**, 21909.
31 Y. He, S. Vasiraju and L. Que, *RSC Adv.*, 2014, **4**, 2433.
32 M. Liong, J. Lu, M. Kovochich, T. Xia, S. G. Ruehm, A. E. Nel, F. Tamanoi and J. I. Zink, *ACS Nano*, 2008, **2**, 889–896.
33 P. Kulpinski, M. Namyslak, T. Grzyb and S. Lis, *Cellulose*, 2012, **19**, 1271–1278.
34 J. Wang, J. Hu, D. Tang, X. Liu and Z. Zhen, *J. Mater. Chem.*, 2007, **17**, 1597–1601.
35 L. Lou, K. Yu, Z. Zhang, B. Li, J. Zhu, Y. Wang, R. Huang and Z. Zhu, *Nanoscale*, 2011, **3**, 2315–2323.
36 M. Runowski, A. Ekner-Grzyb, L. Mrówczyńska, S. Balabhadra, T. Grzyb, J. Paczesny, A. Zep and S. Lis, *Langmuir*, 2014, **30**, 9533–9543.
37 B. Mohr, V. Enkelmann and G. Wegner, *J. Org. Chem.*, 1994, **59**, 635–638.
38 E. J. Foster, C. Lavigueur, Y.-C. Ke and V. E. Williams, *J. Mater. Chem.*, 2005, **15**, 4062–4068.
39 E. J. Foster, R. B. Jones, C. Lavigueur and V. E. Williams, *J. Am. Chem. Soc.*, 2006, **128**, 8569–8574.
40 C.-J. Chen, Y.-C. Wu, H.-S. Sheu, G.-H. Lee and C. K. Lai, *Tetrahedron*, 2011, **67**, 114–124.
41 J. Szydłowska, P. Krzyczkowska, M. Salamończyk, E. Górecka, D. Pociecha, B. Maranowski and A. Krówczyński, *J. Mater. Chem. C*, 2013, **1**, 6883–6889.
42 S. Lucas, E. Champion, D. Bregiroux, D. Bernache-Assollant and F. Audubert, *J. Solid State Chem.*, 2004, **177**, 1302–1311.
43 Z. Xu, Y. Cao, C. Li, P. Ma, X. Zhai, S. Huang, X. Kang, M. Shang, D. Yang, Y. Dai and J. Lin, *J. Mater. Chem.*, 2011, **21**, 3686–3694.
44 B. R. Judd, *J. Chem. Phys.*, 1966, **44**, 839.
45 M. Runowski, S. Balabhadra and S. Lis, *J. Rare Earths*, 2014, **32**, 242–247.
46 T. Anfimova, Q. Li, J. O. Jensen, and N. J. Bjerrum, *Int. J. Electrochem. Sci.* 2014, **9**, 2285–2300.
47 J. a. Diaz-Guillén, A. F. Fuentes, S. Gallini and M. T. Colomer, *J. Alloys Compd.*, 2007, **427**, 87–93.
48 K. Binnemans and C. Görller-Walrand, *J. Rare Earths*, 1996, **14**, 173–180.
49 I. Omkaram, G. Seeta Rama Raju and S. Buddhudu, *J. Phys. Chem. Solids*, 2008, **69**, 2066–2069.
50 M. Runowski and S. Lis, *J. Alloys Compd.*, 2014, **597**, 63–71.

Supporting Information for:

Eu^{3+} and Tb^{3+} doped $LaPO_4$ nanorods, modified with luminescent organic compound, exhibiting tunable multicolour emission

Marcin Runowski[1], Tomasz Grzyb[1], Anna Zep[2], Paulina Krzyczkowska[2], Ewa Gorecka[2], Michael Giersig[1,3] and Stefan Lis[1*]

[1]*Adam Mickiewicz University, Faculty of Chemistry, Umultowska 89b, 61-614 Poznań, Poland*

[2]*University of Warsaw, Faculty of Chemistry, Laboratory of Physical Chemistry of Dielectrics and Magnetics, Żwirki i Wigury 101, 02-089 Warszawa, Poland*

[3]*Freie Universität Berlin, Institute of Experimental Physics, Arnimallee 14, 14195 Berlin, Germany*

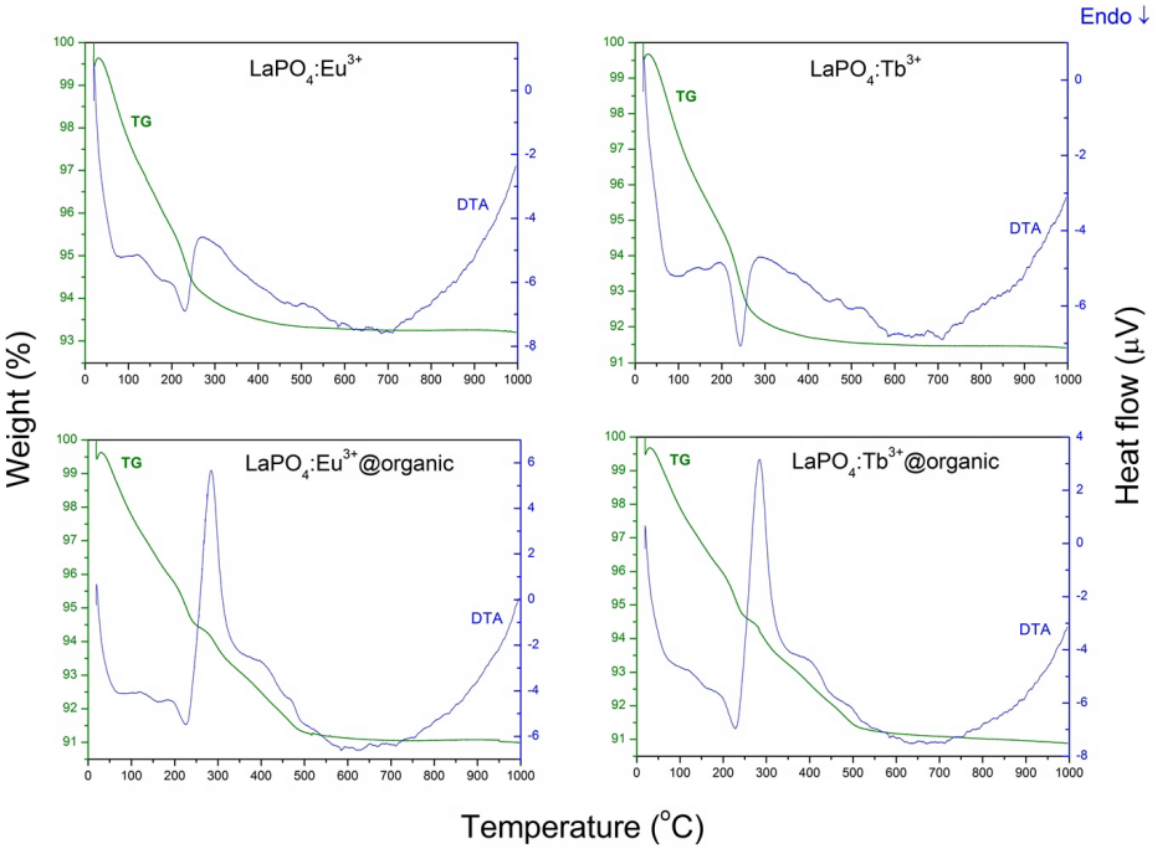

Fig. S1 TG-DTA curves of the $LaPO_4:Eu^{3+}$ 10%, $LaPO_4:Tb^{3+}$ 10%, surface modified $LaPO_4:Eu^{3+}$10%@organic and $LaPO_4:Tb^{3+}$10%@organic nanomaterials.

In order to investigate the stability of the organic surface layer and confirm the composition of the nanomaterials obtained, thermogravimetry–differential thermal analysis (TG–DTA) measurements were performed. Below 120°C the first weight loss assigned to the moisture (absorbed water

molecules) evaporation was observed. At around 170°C and 230°C two other endothermic peaks were observed. They are related to the release of structural water (zeolitically bound water) from the lanthanide phosphates. The mentioned peaks were observed in all samples. In the case of the surface modified products - $LaPO_4:Eu^{3+}$10%@organic and $LaPO_4:Tb^{3+}$10%@organic, the very intensive exothermic peaks at 285°C were observed. They were followed by the significant weight loss because of the decomposition of the organic surface modifier. The recorded change in mass was about 3 wt. %, which was close to the value obtained by elemental analysis (about 2.8 wt. %).

Synteza nanostruktur typu rdzeń/powłoka (core/shell) opartych o jony pierwiastków ziem rzadkich

Problemem badawczym, jaki podjąłem w pracy pt. „*Synthesis and Organic Surface Modification of Luminescent, Lanthanide-Doped Core/Shell Nanomaterials (*LnF_3*@*SiO_2*@*NH_2*@Organic Acid) for Potential Bioapplications: Spectroscopic, Structural, and in Vitro Cytotoxicity Evaluation*" było otrzymanie oraz zbadanie właściwości nowego luminescencyjnego nanomateriału hybrydowego typu core/shell (rdzeń/powłoka), o potencjalnych zastosowaniach biologicznych. Materiał ten miał wykazywać intensywną luminescencję, mały rozmiar oraz dużą monodyspersyjność cząstek. W oparciu o nanokrystaliczną matrycę fluorkową i odpowiednio zaprojektowany układ domieszek, otrzymano nanocząstki luminescencyjne, użyte następnie jako rdzenie nanostruktur typu core/shell. Cząstki te wykazywały po naświetleniu światłem ultrafioletowym bardzo intensywną zieloną luminescencję, na skutek efektywnego przeniesienia energii ($Ce^{3+}\rightarrow Gd^{3+}\rightarrow Tb^{3+}$), a dzięki małemu rozmiarowi (≈12 nm) tworzyły stabilne koloidy wodne. Otrzymany rdzeń został następnie zmodyfikowany powierzchniowo przy użyciu funkcyjnych silanów takich jak TEOS i APTES. Skutkiem tego było utworzenie wielowarstwowych nanostruktur typu core/shell (≈50 nm), mających nanopowłokę krzemionkową sfunkcjonalizowanej grupami aminowymi. Układy te zostały poddano dalszej modyfikacji powierzchni na skutek reakcji z reaktywną pochodną wybranego kwasu organicznego (chlorek kwasu p-metoksybenzoesowego). Zsyntetyzowane nanomateriały zostały szczegółowo zbadane pod kątem ich właściwości strukturalnych (XRD), morfologicznych (TEM) i spektroskopowych (spektrofluorymetria oraz spektroskopia FT-IR), ujawniając obecność krzemionki, grup aminowych i związku organicznego na powierzchni otrzymanych nanocząstek. Wykonano również pomiary wielkości hydrodynamicznych cząstek oraz ich uśrednionych ładunków powierzchniowych (zeta-potencjał), przy użyciu metody dynamicznego i elektroforetycznego rozpraszania światła (DLS i ELS). Na podstawie pomiarów potencjału zeta w różnych wartościach pH (miareczkowanie zeta-potencjometryczne) ustalono punkty izoelektryczne powstałych produktów. Analiza ich wartości pozwoliła na ostateczne potwierdzenie modyfikacji i charakteru powierzchni tych nanomateriałów. Co więcej przeprowadzono szczegółowe badania właściwości biologicznych otrzymanych nanocząstek, a mianowicie zbadano ich

cytotoksyczność względem ludzkich erytrocytów, w ramach badań *in-vitro*. Badania te potwierdziły interakcje nanocząstek z błoną komórkową erytrocytów i ujawniły różny wpływ poszczególnych nanostruktur na morfologie badanych erytrocytów. Warto podkreślić, że same nanocząstki CeF_3:Gd^{3+}, Tb^{3+} nie wykazywały cytotoksyczności i nie wpływały na morfologię erytrocytów. Natomiast otrzymane nanostruktury typu core/shell mające na powierzchni nanopowłokę krzemionkową wpływały znacząco na morfologię erytrocytów. Nanostruktury core/shell typu CeF_3:Gd^{3+}, Tb^{3+}/SiO_2 o niezmodyfikowanej powłoce krzemionkowej wykazywały najwyższą cytotoksyczność względem badanych komórek. Okazało się również, iż nanostruktury mające zmodyfikowaną grupami aminowymi powłokę krzemionkową (CeF_3:Gd^{3+},Tb^{3+}/SiO_2/NH_2) lub przyłączone związki organiczne do powierzchni (CeF_3:Gd^{3+},Tb^{3+}/SiO_2/NH_2/organic acid) wykazywały znacząco zmniejszoną cytotoksyczność i nie wykazywały negatywnego wpływu na badane komórki. Należy dodać, że taki nanomateriał został otrzymany po raz pierwszy, jak również w czasie jego opublikowania nie było dostępnych danych literaturowych na temat oddziaływania na komórki erytrocytów oraz cytotoksyczności nanokrystalicznych fluorków lantanowców i opartych o nie modyfikowanych powierzchniowo nanostruktur typu core/shell. Potwierdziło to znaczący wpływ charakteru powierzchni nanocząstek na właściwości biologiczne nanomateriałów i możliwość zmiany tych właściwości poprzez odpowiednią modyfikację powierzchni danych nanostruktur. Niska cytotoksyczność, stabilność tworzonych koloidów, biokompatybilność zapewniona poprzez odpowiednią modyfikację powierzchni nanocząstek oraz intensywna luminescencja, pozwala na potencjalne zastosowanie otrzymanych nanostruktur w aplikacjach medycznych i bio-chemicznych jako nośniki leków, w obrazowaniu luminescencyjnym jako biomarkery i środki kontrastowe, zaawansowane znaczniki luminescencyjne, nowe źródła światła, etc.

Wkład własny w powstanie pracy: koncepcja badań oraz znaczący udział w syntezie i zbadaniu właściwości fizykochemicznych otrzymanych nanostruktur. Analiza uzyskanych wyników, opracowanie danych i zredagowanie publikacji.

Langmuir

Article

pubs.acs.org/Langmuir

Synthesis and Organic Surface Modification of Luminescent, Lanthanide-Doped Core/Shell Nanomaterials (LnF_3@SiO_2@NH_2@Organic Acid) for Potential Bioapplications: Spectroscopic, Structural, and *in Vitro* Cytotoxicity Evaluation

Marcin Runowski,[†] Anna Ekner-Grzyb,*[,‡] Lucyna Mrówczyńska,[§] Sangeetha Balabhadra,[†] Tomasz Grzyb,[†] Jan Paczesny,[∥] Anna Zep,[⊥] and Stefan Lis*[,†]

[†]Department of Rare Earths, Faculty of Chemistry, Adam Mickiewicz University, Grunwaldzka 6, 60-780 Poznań, Poland

[‡]Department of Behavioural Ecology, Faculty of Biology, Adam Mickiewicz University, Umultowska 89, 61-614 Poznań, Poland

[§]Department of Cell Biology, Faculty of Biology, Adam Mickiewicz University, Umultowska 89, 61-614 Poznań, Poland

[∥]Department of Soft Condensed Matter and Fluids, Institute of Physical Chemistry of the Polish Academy of Sciences, Kasprzaka 44/52, 01-224 Warsaw, Poland

[⊥]Laboratory of Physicochemistry of Dielectrics and Magnetics, Faculty of Chemistry, University of Warsaw, Żwirki i Wigury 101, 02-089 Warsaw, Poland

Supporting Information

ABSTRACT: A facile coprecipitation reaction between Ce^{3+}, Gd^{3+}, Tb^{3+}, and F^- ions, in the presence of glycerine as a capping agent, led to the formation of ultrafine, nanocrystalline CeF_3:Tb^{3+} 5%, Gd^{3+} 5% (LnF_3). The as-prepared fluoride nanoparticles were successfully coated with an amine modified silica shell. Subsequently, the obtained LnF_3@SiO_2@NH_2 nanostructures were conjugated with 4-ethoxybenzoic acid in order to prove the possibility of organic modification and obtain a new functional nanomaterial. All of the nanophosphors synthesized exhibited intense green luminescence under UV light irradiation. Based on TEM (transmission electron microscopy) measurements, the diameters of the cores (≈12 nm) and core/shell particles (≈50 nm) were determined. To evaluate the cytotoxic activity of the nanomaterials obtained, their effect on human erythrocytes was investigated. LnF_3 nanoparticles were bound to the erythrocyte membrane, without inducing any cytotoxic effects. After coating with silica, the nanoparticles revealed significant cytotoxicity. However, further functionalization of the nanomaterial with $-NH_2$ groups as well as conjugation with 4-ethoxybenzoic acid entailed a decrease in cytotoxicity of the core/shell nanoparticles.

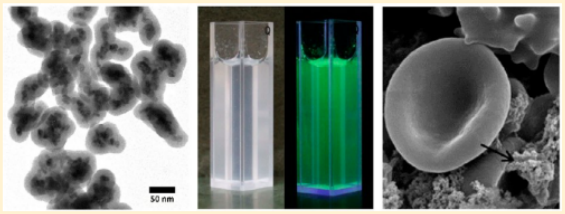

1. INTRODUCTION

Nanoscience and nanotechnology are broad and interdisciplinary areas of research that have been growing explosively worldwide in the past years.[1−3] Nanoparticles (NPs) have large surface area to volume ratios, which causes changes in their optoelectronic, magnetic, and catalytic properties in comparison to their bulk counterparts.[3−5] Because of their nanometric size, which is much smaller than living cells, they are suitable for numerous bioapplications. They can form stable aqueous colloids, which are useful for bioimaging.[1,2]

Nowadays, luminescent nanomaterials doped with lanthanide ions (Ln^{3+}) have attracted considerable attention as a result of their potential applications in various areas, such as field-effect transistors (FET), optoelectronics, optical storage, solar cells, and color displays.[6,7] Moreover, their unique properties allow for applications in biorelated areas, as biomedical markers *in vitro* and *in vivo*, in bioimaging, cancer therapy, or drug delivery.[6,8] The alternative particles, such as organic dyes and semiconductor quantum dots (QDs), have also been employed as phosphor materials in industry and luminescent markers in biology.[1,3] However, both of them have some limitations. Organic dyes often exhibit rapid photobleaching, and QDs can be cytotoxic, which limit their *in vivo* applications.[9] Hence, Ln^{3+}-doped nanophosphors are promising and novel nanomaterials due to their excellent properties such as narrow emission lines, long radiative lifetimes, large Stokes shifts, high quantum yields of luminescence, nonphotobleaching, and low toxicity.[2,7,8] However, Ln^{3+} ions have relatively low absorption coefficients, in comparison to organic dyes and QDs, which makes it necessary to use energy transfer (ET) phenomenon in lanthanide-doped NPs. This process can effectively increase the luminescence efficiency and allows for the possibility of designing the system for sensitivity to selected spectral regions; e.g., Yb^{3+} or Ce^{3+} ions are sensitizers for near-infrared or UV

Received: March 25, 2014
Revised: July 16, 2014
Published: July 18, 2014

radiation, respectively.[10,11] In particular, the Ce^{3+}/Tb^{3+} ion couple has been utilized in a number of traditional phosphors for the generation of green light.[11,12] Hence, numerous dispersible NPs doped with Ce^{3+} and Tb^{3+} ions have been synthesized through a variety of techniques.[12,13] Additionally, Gd^{3+} ion decreases the energy gap between the lowest excited states of Ce^{3+} and Tb^{3+} ions which facilitates ET to Tb^{3+} ions and enhances the luminescence intensity of the system.[14]

For optical applications rare earth fluoride (REF_3) host matrices are very attractive because of their low vibrational energy (<400 cm^{-1}).[15] Because of this feature, phosphors based on REF_3 exhibit high quantum efficiencies of luminescence and low nonradiative relaxation of their electronic excited states.[16] Nowadays, several REF_3 are used or are being tested for use in such fields as optoelectronics, medicine, and industry as luminescent fibers, amplifiers, lasers, various biomaterials, etc.[17−19]

Core/shell type nanoparticles are a special kind of nanomaterial, in which the core containing the desired functional nanoparticles is covered with a nanometric shell, e.g., silica or titania.[20,21] Therefore, such hybrid nanomaterials can be multifunctional, as they reveal simultaneously the properties of the core and the shell. The core usually consists of an inorganic phase, which can exhibit the desired properties, dependent on its further applications. The formed silica shell allows for its further surface modification, simultaneously protecting the core from the environment (oxidation, aggressive agents).[22]

A simple approach is to coat the given NPs with an external silica shell.[23] Silica is stable under acidic conditions and inert against redox reactions as compared with many organic coating materials. That is why such NPs coated with silica reveal high stability of colloids in water and biological systems, resistance to aggressive agents, and radiation as well as large surface area, which is beneficial in drug delivery systems and fluorescence labeling.[24] Additionally, the silica coating provides an abundance of surface active silanol groups, which can easily undergo further functionalization and improve the ability for bioconjugation of various functional groups to such NPs.[25]

However, nanomaterials containing silica can be cytotoxic.[26−29] The toxicity of such nanostructures depends on their phase composition, size, porosity, hydrophilicity, and surface charge.[27,30,31] The mechanism of their cytotoxicity is related to the abnormal expression of oxidative stress-associated molecules. Exposure to SiO_2 may decrease a cell's viability and proliferation, induce apoptosis and protein expression, as well as change mitochondrial activity, and induce hemolysis.[27,28,32]

Amine-functionalized silica nanoparticles have been studied to achieve a reactive and biocompatible modified surface by the formation of covalent bonds and electrostatic interactions between the interfacial amino groups and other organic coupling agents, working as receptors for biomolecules.[26,33]

It is an essential issue to evaluate cytotoxicity properties of potentially biocompatible nanostructures, before their application in biology or medicine. Nanoparticles may impair a cell's function, e.g., by cell membrane integrity disruption, interference with organelle function, or disruption of the cytoskeleton. They may cause oxidative stress, apoptosis, or epigenetic effect as well.[28,34,35] Moreover, nanoparticles can adsorb biomolecules, creating a "corona" of biomolecules on their surface, which may affect biological systems.[36] Despite all these potential dangers, only a few studies dealing with the cytotoxicity of Ln^{3+}-doped nanocrystals have been conducted. Cell viability depends on the dosage, exposure time, and size of studied nanoparticles as well as on the particles' crystallinity and the presence of ligands in a given system.[27,37] The increased use of nanomaterials in many areas of life and the confirmed cytotoxic properties of many of them implies the necessity of such research.

Erythrocytes are the dominant cells (99%) in human blood, and therefore they are the most convenient systems for the study of cytotoxicity activity of new chemical compounds. Red blood cells treated with nanostructures may aggregate and potentially create a thrombus.[38] Moreover, nanoparticles can bind to the erythrocyte membrane and induce changes in its molecular structure, resulting in cell shape alterations and hemolysis.[32,39,40] However, to the best of our knowledge, there is no study on the influence of nanocrystals doped with lanthanide ions on red blood cells.

In this study, we present a synthesis and photophysical characterization of multifunctional, luminescent core/shell type nanomaterials forming stable aqueous colloids and being easily functionalized. To better understand the biological features of the nanoparticles synthesized, the impact of bare nanocrystals and surface modified core/shell type nanostructures on human erythrocytes was investigated. Our intention was to synthesize efficient and monodispersive core/shell type nanophosphors and to modify their surfaces. We wanted to obtain noncytotoxic nanomaterial, which could be further applied as contrast agents, biomarkers or simple model materials for drug delivery, tracing techniques, selective detection, etc. CeF_3 nanoparticles doped with Gd^{3+} and Tb^{3+} ions were selected as an excellent luminescent system because of its tendency to crystallize as fine nanocrystals, which can form stable aqueous colloids, exhibiting very intense green emission. The last feature is especially important in potential bioimaging applications since to opens the possibility of eliminating short-lived background radiation. The formation of core/shell NPs was achieved using lanthanide fluoride as an inorganic luminescent core, and subsequent formation of an amine functionalized silica shell, via a modified Stöber method.[41] The amine-terminated NPs were further functionalized with 4-ethoxybenzoic acid, as an exemplary reactive organic compound, which can be used for further modifications. The performed surface modifications altered the biological features of the nanomaterials synthesized, especially their cytotoxicity and the possibility of selective binding to the desired organic structures.

2. EXPERIMENTAL SECTION

2.1. Materials. Tb_4O_7 and Gd_2O_3 (Stanford Materials, 99.99%) were dissolved in a concentrated, ultrapure nitric acid, HNO_3 (POCh S.A., 67%) to prepare $Tb(NO_3)_3$ and $Gd(NO_3)_3$ aqueous solutions. $CeCl_3 \cdot 7H_2O$ (99.9%) was purchased from Sigma-Aldrich. Ammonium fluoride, NH_4F (POCh S.A., ACS grade, 98%), was used as a source of fluoride ions. Tetraethyl orthosilicate, TEOS, and 3-aminopropyltriethoxysilane, APTES (Sigma-Aldrich, reagent grade, ≥98%), were used as a source of silica and amino groups, respectively. An aqueous solution of concentrated ammonium hydroxide (Chempur, pure p.a., 25%) was used to increase the pH during the hydrolysis of silanes. 4-Ethoxybenzoyl chloride (synthetic process described in the Supporting Information) was used as a surface modifier. Glycerin, ethanol, toluene, and THF (tetrahydrofuran) were purchased from POCh S.A. (pure p.a.). Glutaraldehyde and osmium tetroxide (OsO_4) were purchased from Sigma-Aldrich. Double distilled water was used for all syntheses.

2.2. Synthesis of Luminescent Core—CeF_3:Tb^{3+} 5%, Gd^{3+} 5%. The luminescent nanoparticles were synthesized via a well-known coprecipitation method.[2,11] The synthesis was performed to obtain 1 g

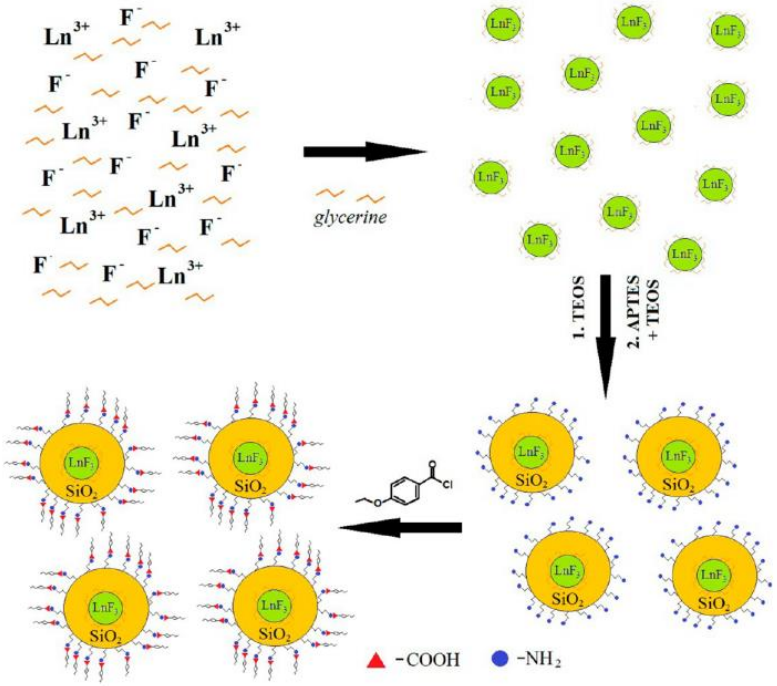

Figure 1. Synthesis scheme of CeF_3:Tb^{3+} 5%, Gd^{3+} 5%@SiO_2@NH_2@4-ethoxybenzoic acid core/shell type nanoparticles.

of the product. In order to synthesize the CeF_3:Tb^{3+} 5%, Gd^{3+} 5% nanomaterials, the solution A was prepared as follows: aqueous solutions of $Tb(NO_3)_3$, $Gd(NO_3)_3$, and $CeCl_3$ were mixed in molar ratio 5:5:90, respectively. The obtained solution containing rare earth ions was diluted with water up to 80 mL and subsequently mixed with 20 mL of glycerin (antiagglomerating agent). Subsequently solution B containing a fluoride ions source was prepared as follows: NH_4F (20% excess) was dissolved in 80 mL of water and subsequently mixed with 20 mL of glycerin. To the continuously stirred solution B, the solution A was added dropwise (the process of addition lasted approximately 20 min). After this time the reaction was finished, and a white precipitate of CeF_3:Tb^{3+} 5%, Gd^{3+} 5% was obtained. The precipitate was purified by centrifugation and washed several times with water. The product exhibited bright, green luminescence under UV lamp irradiation (λ_{ex} = 254 nm). The as-prepared product was dispersed in 50 mL of water using ultrasonication, forming a stable, homogeneous colloid.

2.3. Synthesis of Amine Modified Core/Shell Type—CeF_3:Tb^{3+} 5%, Gd^{3+} 5%@SiO_2@NH_2. A portion of 100 mg of colloidal CeF_3:Tb^{3+} 5%, Gd^{3+} 5% was transferred into a beaker, dispersed in 30 mL of water with the use of ultrasound. After that, 160 mL of ethanol and 10 mL of concentrated ammonia (hydrolysis catalyst) were added to the aqueous colloid obtained. The colloid was ultrasonicated again and then continuously stirred at ambient conditions. Subsequently, 0.25 mL of TEOS was added to the colloidal solution. After 30 min, 0.25 mL of TEOS and 0.25 mL of APTES were added to the solution. The whole process lasted 2.5 h. When the reaction was completed, the product was purified by centrifugation and washed several times with water and ethanol. The final amine modified core/shell type product exhibited bright, green luminescence under UV lamp irradiation (λ_{ex} = 254 nm) as well.

2.4. Synthesis of Core/Shell Type—CeF_3:Tb^{3+} 5%, Gd^{3+} 5%@SiO_2. In order to compare physicochemical properties of the amine modified core/shell nanomaterial with the nonmodified core/shell nanomaterial, an additional synthesis was performed using the same method as described above, but without the addition of APTES.

2.5. Surface Modification of CeF_3:Tb^{3+} 5%, Gd^{3+} 5%@SiO_2@NH_2. To the suspension of CeF_3:Tb^{3+} 5%, Gd^{3+} 5%@SiO_2@NH_2 core/shell type nanoparticles (0.8 g) in anhydrous toluene (75 mL) at ambient conditions, redistilled and dried triethylamine was added (1.0 g, 0.010 mol). The obtained mixture was stirred at 323 K for 15 min. Afterward, a solution of 4-ethoxybenzoyl chloride (1.7 g, 0.009 mol) in 10 mL of toluene was added dropwise. The mixture was stirred at 343 K for 24 h. After that, the reaction system was cooled, and then the toluene was removed using a rotary evaporator. The crude product was washed with water (100 mL) and then collected by filtration (in order to remove the triethylamine chloride formed during the process). Afterward, the resultant product was washed with methanol to remove the residual water. Subsequently, the as-prepared product was redispersed using ultrasound in THF, centrifuged, and washed several times. Here it is worth noting that the used organic compound could be easily solubilized in THF and toluene. However, toluene has a higher boiling point than THF, which was why toluene was used in the reaction.

The scheme depicted in Figure 1 presents the formation of the core/shell type luminescent nanomaterials and their surface modification.

3. CHARACTERIZATION

Microscopy measurements were performed with the transmission electron microscope JEM 1200 EXII, operating at an accelerating voltage of 80 kV. Powder XRD patterns were recorded with a Bruker AXS D8 Advance diffractometer, using Cu Kα radiation (λ = 1.5406 Å). Using the data collected from XRD, the average grain size of the nanocrystals synthesized was estimated based on Scherrer's equation:[42]

$$D = \frac{k\lambda}{\cos\theta\sqrt{\beta^2 - \beta'^2}} \quad (1)$$

where D is grain size, k is a shape factor (0.9 for spherical particles), λ is a wavelength of radiation, θ is an angle of

diffraction, β is a full width at half-maximum (fwhm), and β' is an instrumental effect. IR spectra were recorded using an FT-IR spectrophotometer, JASCO 4200, in the transmission mode. The excitation and emission spectra were measured using a Hitachi F-7000 spectrofluorometer, at 293 K. All spectra were appropriately corrected for the instrumental response. Luminescence decay curves were collected on a QuantaMasterTM 40 spectrophotometer equipped with an Opolette 355LD UVDM tunable laser, which had a repetition rate of 20 Hz, as the excitation source and a Hamamatsu R928 photomultiplier as the detector. The hydrodynamic diameter and zeta (ζ) potential of the obtained nanoparticles were measured using Malvern Zetasizer Nano ZS equipped with a dynamic light scattering (DLS) module (He−Ne laser 633 nm, maximum 4 mW). Before measurements each compound was dispersed in Milli-Q quality water forming diluted aqueous colloids (0.2 mg/mL). The pH value in all systems was adjusted using HCl and NaOH aqueous solutions. The elemental analysis was performed using an elementar analyzer (Vario EL III). The detailed characterization of erythrocyte preparation, cytotoxicity assays, and morphology alterations is presented in the Supporting Information.

4. RESULTS AND DISCUSSION

4.1. Structure, Morphology, and Surface Properties.

Figure 2 shows the powder XRD patterns of the materials

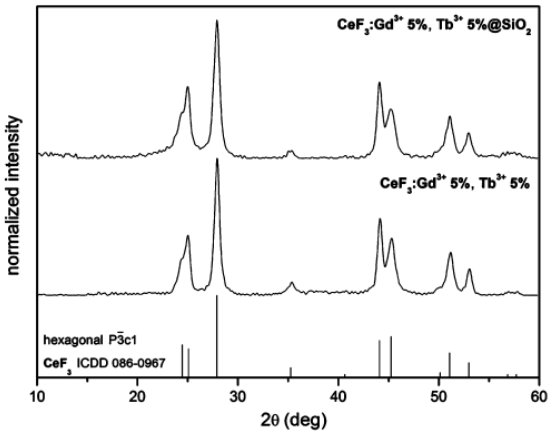

Figure 2. XRD patterns of CeF_3:Tb^{3+} 5%, Gd^{3+} 5% and CeF_3:Tb^{3+} 5%, Gd^{3+} 5%@SiO_2 nanostructures.

synthesized compared to the reference pattern from the ICDD (Inorganic Crystal Diffraction Data) database, card no. 086-0967. The CeF_3:Tb^{3+} 5%, Gd^{3+} 5% product was successfully synthesized as small, crystalline nanoparticles by coprecipitation in the presence of glycerin used as an antiagglomeration agent. The experimental diffractogram fits well to the hexagonal CeF_3 fluoride ($P\bar{3}c1$ space group). The second diffractogram recorded for the core/shell CeF_3:Tb^{3+} 5%, Gd^{3+} 5%@SiO_2 nanomaterial was similar to the pattern corresponding to the bare core because the crystalline phase in both compounds was the same. However, a slight difference could be found in the range of 20°−30° 2θ, where a small and broad reflex (overlapping with LnF_3 reflexes) assigned to the amorphous silica shell was observed (because of the partial ordering of the silica structure).[20,43] The subsequent surface modifications did not influence crystal structure of the luminescent core as well. The recorded diffractograms revealed significant reflexes broadening, which is typical of small nanoparticles. On the basis of the Scherrer equation,[42] the average grain size of the CeF_3:Tb^{3+} 5%, Gd^{3+} 5% nanocrystals synthesized was estimated as 11 ± 2 nm.

TEM images obtained for all samples are presented in Figure 3. The calculated average size of the core nanoparticles CeF_3:Tb^{3+} 5%, Gd^{3+} 5% (LnF_3) was about 12 nm (Figure 3A). The size of the LnF_3@SiO_2 nanostructures (Figure 3B) was in the range of 30−50 nm (averaged total size of the cores coated by silica shell). Larger agglomerates of the nanoparticles discussed were observed, as well. The average sizes of LnF_3@SiO_2@NH_2 (Figure 3C) and LnF_3@SiO_2@NH_2@4-ethoxybenzoic acid (Figure 3D) were similar for both nanomaterials, namely approximately 50−80 nm. Their larger size in comparison to sample B was related to the higher total amount of silanes in the reaction system, and probably to a sparser silica structure, caused by the presence of amine groups. Organic modification did not influence the nanoparticles size observed in the TEM images (similar size/shape for both C and D samples). The nanoparticles obtained revealed relatively narrow size/shape distributions. TEM measurements of the core/shell type nanostructures did not reveal bare silica particles (core-free silica).

Zeta-potential measurements of the nanoparticles synthesized were carried out on their diluted aqueous colloids at adjusted pH ranging from 2 to 13. The results are presented in Figure 4. Here we must consider approximate values due to the uncertainties of the values measured (represented by the depicted error bars). Also, the measurements were performed for discrete values of the pH. Core nanoparticles (LnF_3) exhibited a positive ζ-potential of around +35 mV in a wide pH range (from 2 to 9). There was a sudden drop of the ζ-potential which appeared upon changing the pH from 9 to 10. The isoelectric point (Ip), i.e., the pH at which the value of the ζ-potential equals 0, was around pH 10. The high ζ-potential values are typical for REF_3, which allows them to create stable colloidal systems. The reported literature value of Ip for bare (ligand free) REF_3 was estimated to be around pH ≈ 6.[44] In our case the difference from the literature data was probably caused by the presence of glycerine molecules attached to the nanoparticles' surface during the synthesis. Because of this fact, their aqueous colloids were very stable in a wide pH range (2−9). LnF_3/SiO_2 nanostructures had positive ζ-potential in the pH range from 2 to 3, which decreased to around −20 mV at pH = 5. The Ip was at pH = 4. It is well-known that the isoelectric point of amorphous silica is around pH 2−4 and its pK_a ≈ 7.[45,46] That was why below pH 4 the measured ζ-potential was positive (protonated $-SiOH_2^+$ surface moieties), decreased to −20 mV at pH around 5, and then dropped to −30 mV above pH 7 (deprotonated $-SiO^-$). LnF_3@SiO_2@NH_2 nanoparticles exhibited a change of ζ-potential from +45 to −20 mV when pH was changed from 4 to 7. Two steps were observed. First we noticed a decrease to around 0 mV above pH = 4, which was probably connected with unbounded silicon groups. The second drop (to −20 mV) above pH 6 was related to amine deprotonation and the formation of neutral amino groups ($-NH_3^+ \rightarrow -NH_2$) as well as further silica deprotonation. The determined Ip was around pH 6, which undoubtedly confirmed the silica surface modification. It is in good agreement with literature data for amine modified silica particles.[33,47] LnF_3@SiO_2@NH_2@4-ethoxybenzoic acid nano-

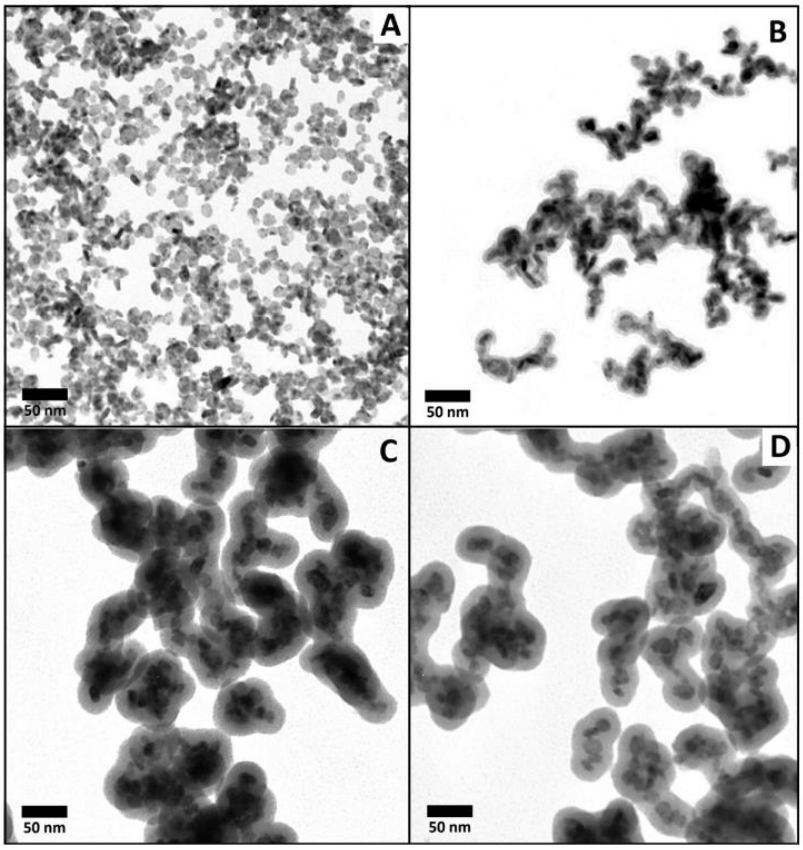

Figure 3. TEM images of CeF_3:Tb^{3+} 5%, Gd^{3+} 5% (A), CeF_3:Tb^{3+} 5%, Gd^{3+} 5%@SiO_2 (B), CeF_3:Tb^{3+} 5%, Gd^{3+} 5%@SiO_2@NH_2 (C), and CeF_3:Tb^{3+} 5%, Gd^{3+} 5%@SiO_2@NH_2@4-ethoxybenzoic acid (D) nanomaterials.

structure exhibited an isoelectric point (Ip) at around pH 4.5. No two step change was observed. The decreased Ip in comparison to the amine modified core/shell nanoparticles was due to the surface binding between amino groups and 4-ethoxybenzoic acid. In acidic and basic conditions the organic molecules were probably released. In range of low and high pH the value of the ζ-potentials of samples C and D were almost identical. Two peaks of the ζ-potential were visible at pH = 4 and 11. This was probably due to nonideal saturation of amino groups with organic molecules at values of the pH close to the release points.

The behavior of nanostructures in the pH range changing from 5 to 7 is interesting due to possible bioapplications. For such values of the pH, the high positive ζ-potential for the core nanoparticles became negative after silica coating. The amine modified silica exhibited much a higher ζ-potential then the nonmodified silica. After surface modification with 4-ethoxybenzoic acid, the ζ-potential became more negative comparedto the nonconjugated LnF_3@SiO_2@NH_2 nanostructures. Generally, all of the samples were stable at this pH range due to nonzero ζ-potentials. Changing the nature of the surface might be of interest for different bioimaging assays. The recorded size distribution histograms of the obtained nanomaterials are presented and discussed in the Supporting Information (Figure S1).

The recorded FT-IR spectra of all synthesized nanomaterials as well as their detailed interpretation are presented in the Supporting Information (Figures S2 and S3). The spectra revealed the presence of silica, amino groups, and 4-ethoxybenzoic acid in the nanomaterials obtained, confirming the desired surface modification of the nanoparticles.

In order to determine the amount of organic acid and amino groups in the nanomaterials obtained, elemental analyses of LnF_3@SiO_2@NH_2 and LnF_3@SiO_2@NH_2@4-ethoxybenzoic acid were performed. For the amine modified sample C, the obtained content of N, C, and H was 1.011, 2.737, and 1.550 wt %, respectively, whereas for sample D, modified with organic acid, the values were 0.740, 6.464, and 1.680 wt %, respectively. On the basis of the values obtained, the molar concentrations of the amino groups for the sample C (0.722 mmol/g) and 4-ethoxybenzoic acid molecules for sample D (0.345 mmol/g) were determined. The results obtained proved the high concentration of surface functional groups, confirming a successful nanomaterials functionalization, and revealed that approximately half of the amino groups were conjugated with the organic acid molecules.

4.2. Luminescent Properties. In Figures 5a–c spectroscopic properties of the nanomaterials synthesized are presented. All of the measurements were performed in the solid state (dried powders). The luminescent phase of the nanomaterials synthesized was composed of the crystalline

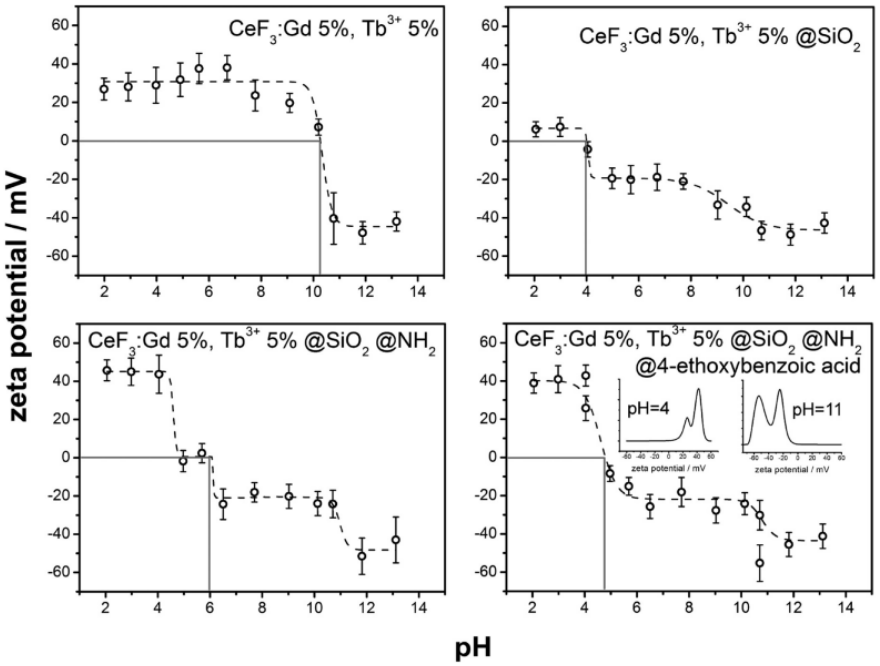

Figure 4. ζ-potential titration plots of CeF_3:Tb^{3+} 5%, Gd^{3+} 5%, CeF_3:Tb^{3+} 5%, Gd^{3+} 5%@SiO_2, CeF_3:Tb^{3+} 5%, Gd^{3+} 5%@SiO_2@NH_2 and CeF_3:Tb^{3+} 5%, Gd^{3+} 5%@SiO_2@NH_2@4-ethoxybenzoic acid diluted aqueous colloids.

CeF_3:Tb^{3+} 5%, Gd^{3+} 5% exhibiting ET phenomenon, in order to get the intense green emission of the Tb^{3+} ions. Direct Tb^{3+} excitation does not provide efficient luminescence because of the forbidden character of the 4f−4f transitions within Tb^{3+} ions.[11] In this system Ce^{3+} ions acted as energy donors, Tb^{3+} as energy acceptors (luminescence activators), and Gd^{3+} facilitated the ET from Ce^{3+} to Tb^{3+} ions, decreasing the energy gap between their lowest excited states.[14] The amount of dopants was fixed at 5% to provide efficient luminescence of the nanomaterials synthesized (due to energy transfer from Ce^{3+} and Gd^{3+} do Tb^{3+} ions) as well as to limit concentration quenching of Tb^{3+} ions and the amount of the precious Ln^{3+} ions used.[48] The concentration quenching phenomenon is commonly observed in the case of Ln^{3+}-doped materials and results in luminescence decrease and lifetime shortening.[2,11,48]

Figure 5a represents the normalized excitation spectra of the four products, recorded at λ_{em} = 543 nm (the highest emission band of Tb^{3+}). All spectra exhibited a very intense and broad absorption band around 250 nm, corresponding to the allowed $4f^1 \rightarrow 4f^05d^1$ transition in the Ce^{3+} ions (excitation of the Ce^{3+} ions), causing efficient ET to the Tb^{3+} ions.[11] Also, low-intensity absorption bands at lower energy related to the forbidden 4f → 4f transitions in the Tb^{3+} ions were observed. The core/shell type compounds obtained, having a silica shell in their structure, revealed slight shifts of the ET band and altered shapes in comparison to the pure core nanoparticles. This was because of the light absorption/scattering by the silica shell.[23,43] Also, the nanomaterial modified with 4-ethoxybenzoic acid exhibited a changed shape of the mentioned band due to UV light absorption by the organic acid in this region.

The emission spectra of the nanostructures were recorded under excitation at λ_{ex} =247 nm, in the range of the most intense ET band (Figure 5b). The products exhibited four narrow bands, characteristic of the Tb^{3+} ions, namely, $^5D_4 \rightarrow {}^7F_6$, $^5D_4 \rightarrow {}^7F_5$, $^5D_4 \rightarrow {}^7F_4$, and $^5D_4 \rightarrow {}^7F_3$ transitions corresponding to the magnetic dipole transitions in the 4f shell of the Tb^{3+} ions. When the concentration of the Tb^{3+} ions is low (usually much below 1%), a blue emission from the $^5D_3$ manifold can occur, if an appropriately remote distance between neighboring Tb^{3+} ions is preserved.[49] In our case emission bands connected with transitions from this level were not observed. All emission spectra had the same shape because of the similar chemical environment around Tb^{3+} ions. Such transitions are generally not sensitive to the coordination environment symmetry of the emitting ions.[11,26] Nanoparticles of the bare core exhibited the highest emission intensities, which can be clearly seen in the discussed spectra (red curve). The three products bearing silica shells exhibited similar intensity to each other, however significantly lower in comparison to the core nanoparticles (without silica). This was caused by light absorption/scattering by the silica shells.[43] Among these compounds, the one having a nonmodified silica shell (CeF_3:Tb^{3+}, Gd^{3+}@SiO_2) revealed the smallest emission intensity. The efficient luminescence quenching by O−H oscillators from water molecules was a reason for this behavior. In the spectrum of the product modified with 4-ethoxybenzoic acid, an intense broad emission band centered at 400 nm was observed (green curve). This band was assigned to the luminescence of the 4-ethoxybenzoic acid, attached to the nanoparticles' surface. It was an additional confirmation of the successful organic modification of our nanomaterial. In the Supporting Information (Figure S4) the excitation and emission spectra of the pure 4-ethoxybenzoic acid are shown. The discussed organic acid attached to the surface of nanoparticles exhibited a bathochromic shift in comparison to

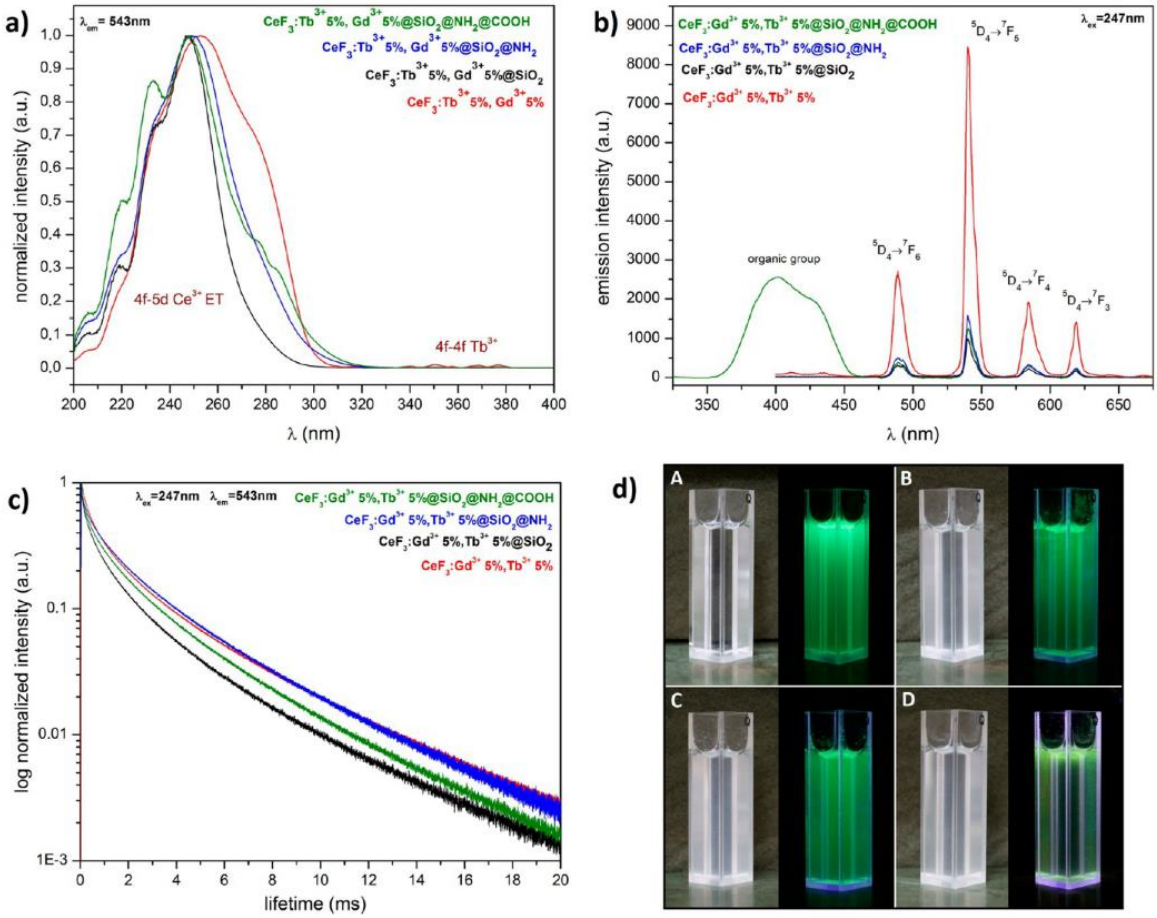

Figure 5. Excitation (a), emission spectra (b), and luminescence decay curves (c) of CeF_3:Tb^{3+} 5%, Gd^{3+} 5%, CeF_3:Tb^{3+} 5%, Gd^{3+} 5%@SiO_2, CeF_3:Tb^{3+} 5%, Gd^{3+} 5%@SiO_2@NH_2 and CeF_3:Tb^{3+} 5%, Gd^{3+} 5%@SiO_2@NH_2@4-ethoxybenzoic acid, recorded at λ_{em} = 543 nm and λ_{ex} = 247 nm. Photographs (d) of the obtained aqueous colloids of CeF_3:Tb^{3+} 5%, Gd^{3+} 5% (A), CeF_3:Tb^{3+} 5%, Gd^{3+} 5%@SiO_2 (B), CeF_3:Tb^{3+} 5%, Gd^{3+} 5% @SiO_2@NH_2 (C), and CeF_3:Tb^{3+} 5%, Gd^{3+} 5%@SiO_2@NH_2@4-ethoxybenzoic acid (D) nanomaterials, taken in a daylight (left) and under UV (254 nm) lamp irradiation (right).

the free acid because of the alternations of its coordination environment.

The measured luminescence decay curves depicted in Figure 5c showed nonexponential character, because of the quenching processes of the Tb^{3+} ions embedded in the crystalline structures. However, in order to compare the luminescence lifetimes of the nanomaterials synthesized, the recorded decay profiles were fitted to a mathematical function representing biexponential character ($R > 0.99$), namely, $y = A_1 \exp(-x/t_1) + A_2 \exp(-x/t_2) + y_0$. The bulk CeF_3 should reveal only one site symmetry for all Ln^{3+} ions, resulting in monoexponential luminescence decay. Therefore, we assumed that the second short-lived lifetime component corresponded to the surface and near surface ions because of a high quenching probability of such Tb^{3+} ions. The calculated lifetime values are presented in Table 1. In all samples the short-lived components were dominant. This proved there was a significant contribution of surface ions to the total luminescence of the products and also the relatively high surface to volume ratio of the NPs. The shortest average lifetime was observed in the nanomaterial modified with the organic acid, which confirmed the quenching

Table 1. Calculated Radiative Lifetimes Values (τ_1 and τ_2) of the Nanophosphors Obtained

compound	τ_1 (ms)	τ_2 (ms)
LnF_3 (CeF_3:Tb^{3+} 5%, Gd^{3+} 5%)	3.48 (31%)	0.59 (69%)
LnF_3@SiO_2	3.05 (28%)	0.55 (72%)
LnF_3@SiO_2@NH_2	3.43 (40%)	0.67 (60%)
LnF_3@SiO_2@NH_2@4-ethoxybenzoic acid	3.18 (32%)	0.49 (68%)

influence of the organic compound on Tb^{3+} emission. The longest emission lifetimes were recorded for the bare core and the amine modified core/shell type product. The observed increase of the lifetime for LnF_3@SiO_2@NH_2 nanomaterial in comparison to the LnF_3@SiO_2 was probably caused by the protecting role of the amino groups against the quenching influence of water molecules. The relatively long lifetimes obtained for the nanomaterials synthesized are in good agreement with data reported in the literature for Tb^{3+}-doped inorganic systems.[11,13]

The photographs of the aqueous colloidal solutions of the nanomaterials obtained are presented in Figure 5d, namely,

dx.doi.org/10.1021/la501107a | Langmuir 2014, 30, 9533−9543

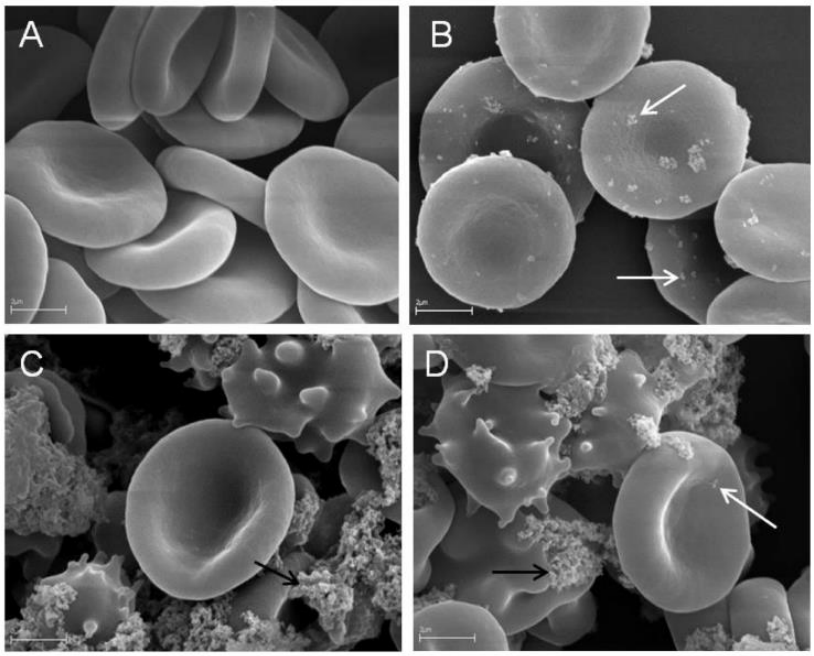

Figure 6. Effect of (A) PBS (control), (B) CeF_3:Tb^{3+} 5%, Gd^{3+} 5%, (C) CeF_3:Tb^{3+} 5%, Gd^{3+} 5%@SiO_2@NH_2, and (D) CeF_3:Tb^{3+} 5%, Gd^{3+} 5%@SiO_2@NH_2@4-ethoxybenzoic acid at the concentration 1 mg/mL, on human erythrocytes morphology as observed by scanning electron microscope. White arrows: single particles; black arrows: particles aggregates. Scale bars indicate 2 μm. CeF_3:Tb^{3+} 5%, Gd^{3+} 5%@SiO_2 treated cells are not shown because of 100% hemolysis.

LnF_3 (A), LnF_3@SiO_2 (B), LnF_3@SiO_2@NH_2 (C), and LnF_3@SiO_2/NH_2/4-ethoxybenzoic acid (D). Each colloid was prepared by dispersing the given nanomaterial in water, with the use of ultrasound, at a fixed concentration of the solid phase, equal to 0.5 mg/mL. The pictures of the colloids prepared were taken in daylight (left) and under a UV (254 nm) lamp irradiation (right), revealing their bright green luminescence. All of the colloids obtained were stable over many days. The colloid containing pure cores showed the most intense emission. Modification of the cores (surface coating) decreased the total amount of the luminescent phase in the final products, which is the direct reason for the lowered luminescence intensity observed in Figure 5d (photos B−D).

4.3. Cytotoxicity Properties of the Nanoparticles. The cytotoxicity properties of the nanoparticles synthesized were studied using human erythrocytes as a simple cell model. The CeF_3: Tb^{3+}, Gd^{3+} (LnF_3) nanomaterials were bound to the erythrocyte membrane as single particles or as small particle aggregates. However, it did not induce cell shape alterations (Figure 6B, compare with Figure 6A—control cells, dyscocytes) and did not increase membrane permeability and hemolysis, in the concentrations tested. The erythrocytes under the bare core treatment settled with a different rate as compared with the control erythrocytes (Figure S5), at the concentrations of 1 and 0.1 mg/mL. No influence of LnF_3 nanocrystals at the concentration of 0.01 mg/mL on the erythrocyte sedimentation rate was observed. Our data confirm the results presented in other studies, where rare-earth-based nanoparticles had no or only a small effect on mammalian cells tested *in vitro*, both cancer and normal ones.[23,50,51] However, different lanthanide-doped nanocrystals, like cerium oxide, demonstrated toxic properties, especially for cancer cells.[52,53]

In contrast, the analysis of LnF_3 encapsulated in silica shells revealed significant toxicity properties toward human erythrocytes (100% hemolysis), at concentrations of 1 and 0.1 mg/mL, and less cytotoxicity (more than 10% hemolysis) at the concentration of 0.01 mg/mL (Figure S5). The negative effect of LnF_3@SiO_2 on the erythrocyte membrane structure (hemolysis) and the sedimentation rate disappeared at a concentration of 0.001 mg/mL. The results of this study are in agreement with other data showing substantial cytotoxicity of nanomaterials containing SiO_2.[27,28] In those earlier investigations, the toxicity effects were also in a dose-dependent manner; however, the cells (such as human lung cancer cells, HaCaT cells, bone marrow mesenchymal stem cells, or skeletal myoblasts) were treated with NPs at a concentration higher than 0.001 mg/mL (the concentration which was nontoxic for the erythrocytes in our study). Here it is worth noting that according to the other research,[32,54] silica can exert negligible cytotoxic effects toward erythrocytes, dependent on the size of the silica particles and their surface properties mostly.

Both LnF_3@SiO_2@NH_2 and LnF_3@SiO_2@NH_2@4-ethoxybenzoic acid induced shape alterations (echinocytosis) and hemolysis ($\geq$ 10%) in the erythrocytes at the concentration of 1 mg/mL. Large self-aggregates of NPs bound to the erythrocytes induced their echinocytic transformations (Figure 6C,D). At NPs concentrations of 0.1 and 0.01 mg/mL, there was no cell hemolysis observed, and the erythrocyte's sedimentation rate was not affected (Figure S5). These outcomes confirmed previous investigations which demonstrated that functionalization of silica-coated nanoparticles with amino or carboxyl groups can reduce their cytotoxicity properties.[55] Amino groups may protect cells from interactions with surface silane. However, other studies indicated that

functionalization of silica nanoparticles with amino groups may increase their cytotoxic properties, depending of their surface structure and charge.[32,39]

In summary, the CeF_3:Tb^{3+} 5%, Gd^{3+} 5% nanoparticles could bind to red blood cell membranes as single particles without any cell shape transformation (Figure 6B), and they did not induce any changes in the structure of the membranes of the erythrocytes. The NPs binding to the erythrocytes occurred probably by interactions of the positive bare core with the negatively charged cell membrane. In contrast, NPs coated with silica revealed substantial cytotoxic properties, whereas the nanoparticles having silica functionalized with $-NH_2$ groups as well as with 4-ethoxybenzoic acid formed self-aggregates in the solution and revealed weak hemolytic activity. These aggregates bound to the erythrocytes surface inducing their echinocytic transformation (Figure 6C,D). The similar results to our were obtained by Zhao et al., in the case of 100−200 nm size mesoporous silica nanoparticles.[40] A silanol-rich surface of the silica was bound to the phosphatidylcholine-rich erythrocytes' membrane.

5. CONCLUSIONS

The luminescent CeF_3:Tb^{3+} 5%, Gd^{3+} 5% (LnF_3 core), LnF_3@SiO_2, and LnF_3@SiO_2@NH_2 (core/shell) nanoparticles were successfully synthesized and surface modified via facile, low-cost, and easy to scale-up methods. The nanostructures obtained were composed of nanocrystalline LnF_3 cores exhibiting intense green luminescence under UV light irradiation. The cores synthesized were coated with an external amine modified silica shell. Subsequently, the nanostructures obtained were successfully functionalized with 4-ethoxybenzoic acid, as an exemplary reactive and functional organic compound, which can be used for surface modifications. The formation of core/shell type nanoparticles, their structure, and surface modification with amino groups and carboxylic acid molecules were confirmed by XRD, TEM, and DLS measurements. On the basis of the performed ζ-potential titrations, the isoelectric points (Ip) of all of the obtained nanomaterials were determined. All synthesized nanomaterials formed stable aqueous colloids exhibiting green luminescence under UV lamp irradiation (λ_{ex} = 254 nm). The cytotoxicity assays revealed that all of the prepared nanomaterials can interact with human erythrocyte membranes. Silica coating and functionalization of the nanoparticles with $-NH_2$ groups as well as conjugation with 4-ethoxybenzoic acid induced significant changes of erythrocyte membrane perturbing properties, resulting in altered cytotoxic properties. These findings may be useful in the process of creating new NPs safe for living cells and for subsequent studies conducted on biomolecule delivery, e.g., in the organism. The results obtained can increase the impact of inorganic, lanthanide doped nanophosphors on fundamental biomedical research, as biomarkers, contrast agents, drug-delivery systems, etc.

■ ASSOCIATED CONTENT

Supporting Information

Preparation of 4-ethoxybenzoyl chloride; characterization of cytotoxicity assays; hydrodynamic diameters plots of CeF_3:Tb^{3+} 5%, Gd^{3+} 5%, CeF_3:Tb^{3+} 5%, Gd^{3+} 5%@SiO_2, CeF_3:Tb^{3+} 5%, Gd^{3+} 5%@SiO_2@NH_2, and CeF_3:Tb^{3+} 5%, Gd^{3+} 5%@SiO_2@NH_2@4-ethoxybenzoic acid, recorded at different pH values (2−13), and the insets presenting grain size distribution histograms for each compound, recorded at pH = 7 (Figure S1); FT-IR spectra of the nanomaterials synthesized (Figure S2) and spectra comparison of CeF_3:Tb^{3+} 5%, Gd^{3+} 5%@SiO_2@NH_2@4-ethoxybenzoic acid nanomaterial, before (a) and after (b) organic acid release from the surface at acidic pH (Figure S3); excitation (dotted line) and emission (continuous line) spectra of pure 4-ethoxybenzoic acid, recorded at λ_{em} = 335 nm and λ_{ex} = 247 nm, respectively (Figure S4); effect of the nanoparticles synthesized on the erythrocyte sedimentation rate (Figure S5). This material is available free of charge via the Internet at http://pubs.acs.org.

■ AUTHOR INFORMATION

Corresponding Authors

*E-mail blis@amu.edu.pl (S.L.).
*E-mail anna.ekner@gmail.com (A.E.G.).

Notes

The authors declare no competing financial interest.

■ ACKNOWLEDGMENTS

S.L., A.E.G., and T.G. kindly acknowledge the financial support from the National Science Centre (Grant DEC-2012/06/M/ST5/00325). M.R. gratefully acknowledges the financial support from Polish Ministry of Science and Higher Education—scientific work was financed from the budget for science in 2012−2015 as a research project within the program called "Diamond Grant" Nr DI2011 011441. J.P.'s work was supported by the National Science Centre within SONATA grant according to decision number DEC-2012/07/D/ST5/02240. A.Z. gratefully acknowledges the financial support from FNP Project TEAM/2010-5/4, "Self-assembly of functionalized inorganic−organic liquid crystalline hybrids for multifunctional nanomaterials". T.G. holds a scholarship from the Foundation for Polish Science for Young Scientists (FNP).

■ REFERENCES

(1) Selvan, S. T.; Tan, T. T. Y.; Yi, D. K.; Jana, N. R. Functional and Multifunctional Nanoparticles for Bioimaging and Biosensing. *Langmuir* **2009**, *26*, 11631−11641.

(2) Runowski, M.; Lis, S. Preparation and Photophysical Properties of Luminescent Nanoparticles Based on Lanthanide Doped Fluorides (LaF_3:Ce^{3+}, Gd^{3+}, Eu^{3+}), Obtained in the Presence of Different Surfactants. *J. Alloys Compd.* **2014**, *597*, 63−71.

(3) Xing, Y.; Chaudry, Q.; Shen, C.; Kong, K. Y.; Zhau, H. E.; Chung, L. W.; Petros, J. A.; O'Regan, R. M.; Yezhelyev, M. V.; Simons, J. W.; Wang, M. D.; Nie, S. Bioconjugated Quantum Dots for Multiplexed and Quantitative Immunohistochemistry. *Nat. Protoc.* **2007**, *2*, 1152−1165.

(4) Skumryev, V.; Stoyanov, S.; Zhang, Y.; Hadjipanayis, G.; Givord, D.; Nogués, J. Beating the Superparamagnetic Limit with Exchange Bias. *Nature* **2003**, *423*, 850−853.

(5) Yu, J. C.; Yu, J.; Zhang, L.; Ho, W. Enhancing Effects of Water Content and Ultrasonic Irradiation on the Photocatalytic Activity of Nano-sized TiO_2 Powders. *J. Photochem. Photobiol. A: Chem.* **2002**, *148*, 263−271.

(6) Bünzli, J.-C. G.; Eliseeva, S. V. Lanthanide NIR Luminescence for Telecommunications, Bioanalyses and Solar Energy Conversion. *J. Rare Earths* **2010**, *28*, 824−842.

(7) Eliseeva, S. V.; Bünzli, J.-C. G. Rare Earths: Jewels for Functional Materials of the Future. *New J. Chem.* **2011**, *35*, 1165−1176.

(8) Kang, X.; Yang, D.; Ma, P.; Dai, Y.; Shang, M.; Geng, D.; Cheng, Z.; Lin, J. Fabrication of Hollow and Porous Structured $GdVO_4$:Dy^{3+} Nanospheres as Anticancer Drug Carrier and MRI Contrast Agent. *Langmuir* **2013**, *29*, 1286−1294.

(9) Gagné, F.; Maysinger, D.; André, C.; Blaise, C. Cytotoxicity of Aged Cadmium-telluride Quantum Dots to Rainbow Trout Hepatocytes. *Nanotoxicology* **2008**, *2*, 113−120.
(10) Grzyb, T.; Gruszeczka, A.; Wiglusz, R. J.; Lis, S. The Effects of Down- and Up-conversion on Dual-Mode Green Luminescence from Yb^{3+}- and Tb^{3+}-Doped $LaPO_4$ Nanocrystals. *J. Mater. Chem. C* **2013**, *1*, 5410−5418.
(11) Grzyb, T.; Runowski, M.; Szczeszak, A.; Lis, S. Influence of Matrix on the Luminescent and Structural Properties of Glycerine-Capped, Tb^{3+}-Doped Fluoride Nanocrystals. *J. Phys. Chem. C* **2012**, *116*, 17188−17196.
(12) Kömpe, K.; Borchert, H.; Storz, J.; Lobo, A.; Adam, S.; Möller, T.; Haase, M. Green-Emitting $CePO_4$:Tb/$LaPO_4$ Core-Shell Nanoparticles with 70% Photoluminescence Quantum Yield. *Angew. Chem., Int. Ed.* **2003**, *42*, 5513−5516.
(13) Li, C.; Liu, X.; Yang, P.; Zhang, C.; Lian, H.; Lin, J. LaF_3, CeF_3, CeF_3:Tb^{3+}, and CeF_3:Tb^{3+}@LaF_3 (Core-Shell) Nanoplates: Hydrothermal Synthesis and Luminescence Properties. *J. Phys. Chem. C* **2008**, *112*, 2904−2910.
(14) Wang, F.; Fan, X.; Wang, M.; Zhang, Y. Multicolour PEI/$NaGdF_4$:Ce^{3+},Ln^{3+} Nanocrystals by Single-Wavelength Excitation. *Nanotechnology* **2007**, *18*, 25701−25706.
(15) Weber, M. J. Probabilities for Radiative and Nonradiative Decay of Er^{3+} in LaF_3. *Phys. Rev.* **1967**, *157*, 262−272.
(16) Zhang, Q.; Wang, X.; Zhu, Y. Multicolor Upconverted Luminescence-encoded Superparticles via Controlling Self-assembly Based on Hydrophobic Lanthanide-Doped $NaYF_4$ Nanocrystals. *J. Mater. Chem.* **2011**, *21*, 12132−12138.
(17) Stouwdam, J. W.; Hebbink, G. A.; Huskens, J.; van Veggel, F. C. J. M. Lanthanide-Doped Nanoparticles with Excellent Luminescent Properties in Organic Media. *Chem. Mater.* **2003**, *15*, 4604−4616.
(18) Lemyre, J.-L.; Ritcey, A. M. Synthesis of Lanthanide Fluoride Nanoparticles of Varying Shape and Size. *Chem. Mater.* **2005**, *17*, 3040−3043.
(19) Boulon, G. Fifty Years of Advances in Solid-state Laser Materials. *Opt. Mater.* **2012**, *34*, 499−512.
(20) Yang, P.; Quan, Z.; Hou, Z.; Li, C.; Kang, X.; Cheng, Z.; Lin, J. A Magnetic, Luminescent and Mesoporous Core-Shell Structured Composite Material as Drug Carrier. *Biomaterials* **2009**, *30*, 4786−4795.
(21) Runowski, M.; Grzyb, T.; Lis, S. Magnetic and Luminescent Hybrid Nanomaterial Based on Fe_3O_4 Nanocrystals and $GdPO_4$:Eu^{3+} Nanoneedles. *J. Nanopart. Res.* **2012**, *14*, 1188−1195.
(22) Joo, S. H.; Park, J. Y.; Tsung, C.-K.; Yamada, Y.; Yang, P.; Somorjai, G. A. Thermally Stable Pt/Mesoporous Silica Core-Shell Nanocatalysts for High-Temperature Reactions. *Nat. Mater.* **2009**, *8*, 126−131.
(23) Grzyb, T.; Runowski, M.; Dąbrowska, K.; Giersig, M.; Lis, S. Structural, Spectroscopic and Cytotoxicity Studies of TbF_3@CeF_3 and TbF_3@CeF_3@SiO_2 Nanocrystals. *J. Nanopart. Res.* **2013**, *15*, 1958−1972.
(24) Mahon, E.; Hristov, D. R.; Dawson, K. A. Stabilising Fluorescent Silica Nanoparticlesagainst Dissolution Effects for Biological Studies. *Chem. Commun.* **2012**, *48*, 7970−7972.
(25) Jana, N. R.; Earhart, C.; Ying, J. Y. Synthesis of Water-Soluble and Functionalized Nanoparticles by Silica Coating. *Chem. Mater.* **2007**, *19*, 5074−5082.
(26) Runowski, M.; Dąbrowska, K.; Grzyb, T.; Miernikiewicz, P.; Lis, S. Core/Shell-Type Nanorods of Tb^{3+}-Doped $LaPO_4$, Modified with Amine Groups, Revealing Reduced Cytotoxicity. *J. Nanopart. Res.* **2013**, *15*, 2068−2083.
(27) Lin, W.; Huang, Y.-W.; Zhou, X.-D.; Ma, Y. In Vitro Toxicity of Silica Nanoparticles in Human Lung Cancer Cells. *Toxicol. Appl. Pharmacol.* **2006**, *217*, 252−259.
(28) Yang, X.; Liu, J.; He, H.; Zhou, L.; Gong, C.; Wang, X.; Yang, L.; Yuan, J.; Huang, H.; He, L.; Zhang, B.; Zhuang, Z. SiO_2 Nanoparticles Induce Cytotoxicity and Protein Expression Alteration in HaCaT Cells. *Part. Fibre Toxicol.* **2010**, *7*, 1−12.
(29) Corbalan, J. J.; Medina, C.; Jacoby, A.; Malinski, T.; Radomski, M. W. Amorphous Silica Nanoparticles Aggregate Human Platelets: Potential Implications for Vascular Homeostasis. *Int. J. Nanomedicine* **2012**, *7*, 631−639.
(30) Yu, T.; Malugin, A.; Ghandehari, H. Impact of Silica Nanoparticle Design on Cellular Toxicity and Hemolytic Activity. *ACS Nano* **2011**, *5*, 5717−5728.
(31) Napierska, D.; Thomassen, L. C. J.; Rabolli, V.; Lison, D.; Gonzalez, L.; Kirsch-Volders, M.; Martens, J. A.; Hoet, P. H. Size-dependent cytotoxicity of monodisperse silica nanoparticles in human endothelial cells. *Small* **2009**, *5*, 836−853.
(32) Yu, T.; Malugin, A.; Ghandehari, H. Impact of Silica Nanoparticle Design on Cellular Toxicity and Hemolytic Activity. *ACS Nano* **2011**, *5*, 5717−5728.
(33) Wang, J.; Zheng, S.; Shao, Y.; Liu, J.; Xu, Z.; Zhu, D. Amino-Functionalized Fe_3O_4@SiO_2 Core-Shell Magnetic Nanomaterial as a Novel Adsorbent for Aqueous Heavy Metals Removal. *J. Colloid Interface Sci.* **2010**, *349*, 293−299.
(34) Fröhlich, E. Europe PMC Funders Group Cellular Targets and Mechanisms in the Cytotoxic Action of Non- Biodegradable Engineered Nanoparticles. *Curr. Drug Metab.* **2013**, *14*, 976−988.
(35) Stoccoro, A.; Karlsson, H. L.; Coppedè, F.; Migliore, L. Epigenetic Effects of Nano-sized Materials. *Toxicology* **2013**, *313*, 3−14.
(36) Monopoli, M. P.; Åberg, C.; Salvati, A.; Kenneth, A.; Dawson, K. A. Biomolecular Coronas Provide the Biological Identity of Nanosized Materials. *Nat. Nanotechnol.* **2012**, *7*, 779−786.
(37) Park, M. V. D. Z.; Neigh, A. M.; Vermeulen, J. P.; de la Fonteyne, L. J. J.; Verharen, H. W.; Briedé, J. J.; van Loveren, H.; de Jong, W. H. The Effect of Particle Size on the Cytotoxicity, Inflammation, Developmental Toxicity and Genotoxicity of Silver Nanoparticles. *Biomaterials* **2011**, *32*, 9810−9817.
(38) Janowski, M.; Bulte, J. W. M.; Walczak, P. Personalized Nanomedicine Advancements for Stem Cell Tracking. *Adv. Drug Delivery Rev.* **2012**, *64*, 1488−1507.
(39) Shahbazi, M.-A.; Hamidi, M.; Mäkilä, E. M.; Zhang, H.; Almeida, P. V.; Kaasalainen, M.; Salonen, J. J.; Hirvonen, J. T.; Santos, H. The Mechanisms of Surface Chemistry Effects of Mesoporous Silicon Nanoparticles on Immunotoxicity and Biocompatibility. *Biomaterials* **2013**, *34*, 7776−7789.
(40) Zhao, Y.; Sun, X.; Zhang, G.; Trewyn, B. G.; Slowing, I. I.; Lin, V. S.-Y. Interaction of Mesoporous Silica Nanoparticles with Human Red Blood Cell Membranes: Size and Surface Effects. *ACS Nano* **2011**, *5*, 1366−1375.
(41) Stöber, W. Controlled Growth of Monodisperse Silica Spheres in the Micron Size Range. *J. Colloid Interface Sci.* **1968**, *26*, 62−69.
(42) Langford, J. I.; Wilson, A. J. C. Scherrer after Sixty Years: A Survey and Some New Results in the Determination of Crystallite Size. *J. Appl. Crystallogr.* **1978**, *11*, 102−113.
(43) Runowski, M.; Grzyb, T.; Lis, S. Bifunctional Luminescent and Magnetic Core/shell Type Nanostructures Fe_3O_4@CeF_3:Tb^{3+}/SiO_2. *J. Rare Earths* **2011**, *29*, 1117−1122.
(44) Bogdan, N.; Vetrone, F.; Ozin, G. A.; Capobianco, J. A. Synthesis of Ligand-Free Colloidally Stable Water Dispersible Brightly Luminescent Lanthanide-doped Upconverting Nanoparticles. *Nano Lett.* **2011**, *11*, 835−840.
(45) Philipse, A. P.; van Bruggen, M. P. B.; Pathmamanoharan, C. Magnetic Silica Dispersions: Preparation and Stability of Surface-modified Silica Particles with a Magnetic Core. *Langmuir* **1994**, *10*, 92−99.
(46) Leung, K.; Nielsen, I. M. B.; Criscenti, L. J. Elucidating the Bimodal Acid-Base Behavior of the Water-Silica Interface from First Principles. *J. Am. Chem. Soc.* **2009**, *131*, 18358−18365.
(47) Rosenholm, J. M.; Meinander, A.; Peuhu, E.; Niemi, R.; Eriksson, J. E.; Sahlgren, C.; Lindén, M. Targeting of Porous Hybrid Silica Nanoparticles to Cancer Cells. *ACS Nano* **2009**, *3*, 197−206.
(48) Holloway, W. W., Jr.; Kestigian, M. Concentration Quenching of the Tb^{3+} Ion Fluorescence in $Y_3Al_5O_{12}$ Crystals. *Phys. Lett.* **1966**, *21*, 364−366.

(49) Ricci, P. C.; Carbonaro, C. M.; Corpino, R.; Cannas, C.; Salis, M. Optical and Structural Characterization of Terbium-Doped Y_2SiO_5 Phosphor Particles. *J. Phys. Chem. C* **2011**, *115*, 16630−16636.
(50) Chatterjee, D. K.; Rufaihah, A. J.; Zhang, Y. Upconversion Fluorescence Imaging of Cells and Small Animals Using Lanthanide Doped Nanocrystals. *Biomaterials* **2008**, *29*, 937−943.
(51) Chen, X.; Zhao, Z.; Jiang, M.; Que, D.; Shi, S.; Zheng, N. Preparation and Photodynamic Therapy Application of $NaYF_4$:Yb, Tm−$NaYF_4$:Yb, Er Multifunctional Upconverting Nanoparticles. *New J. Chem.* **2013**, *37*, 1782−1788.
(52) Wason, M. S.; Zhao, J. Cerium Oxide Nanoparticles: Potential Applications for Cancer and Other Diseases. *Am. J. Transl. Res.* **2013**, *5*, 126−131.
(53) Cheng, G.; Guo, W.; Han, L.; Chen, E.; Kong, L.; Wang, L.; Ai, W.; Song, N.; Li, H.; Chen, H. Cerium Oxide Nanoparticles Induce Cytotoxicity in Human Hepatoma SMMC-7721 Cells via Oxidative Stress and the Activation of MAPK Signaling Pathways. *Toxicol. In Vitro* **2013**, *27*, 1082−1088.
(54) Zhao, Y.; Sun, X.; Zhang, G.; Trewyn, B. G.; Slowing, I. I.; Lin, V. S.-Y. Interaction of Mesoporous Silica Nanoparticles with Human Red Blood Cell Membranes: Size and Surface Effects. *ACS Nano* **2011**, *5*, 1366−1375.
(55) Nabeshi, H.; Yoshikawa, T.; Arimori, A.; Yoshida, T.; Tochigi, S.; Hirai, T.; Akase, T.; Nagano, K.; Abe, Y.; Kamada, H.; Tsunoda, S.; Itoh, N.; Yoshioka, Y.; Tsutsumi, Y. Effect of Surface Properties of Silica Nanoparticles on Their Cytotoxicity and Cellular Distribution in Murine Macrophages. *Nanoscale Res. Lett.* **2011**, *6*, 93−98.

Supporting Information for:

Synthesis and organic surface modification of luminescent, lanthanide doped core/shell nanomaterials (LnF_3@SiO_2@NH_2@organic acid), for potential bioapplications – spectroscopic, structural and *in vitro* cytotoxicity evaluation

Marcin Runowski[1], Anna Ekner-Grzyb[2*], Lucyna Mrówczyńska[3], Sangeetha Balabhadra[1], Tomasz Grzyb[1], Jan Paczesny[4], Anna Zep[5], and Stefan Lis[1*]

[1]*Adam Mickiewicz University, Faculty of Chemistry, Department of Rare Earths, Grunwaldzka 6, 60-780 Poznań, Poland*
[2]*Adam Mickiewicz University, Faculty of Biology, Department of Behavioural Ecology, Umultowska 89, 61-614 Poznań, Poland*
[3]*Adam Mickiewicz University, Faculty of Biology, Department of Cell Biology, Umultowska 89, 61-614 Poznań, Poland*
[4]*Institute of Physical Chemistry of the Polish Academy of Sciences, Department of Soft Condensed Matter and Fluids, Kasprzaka 44/52, 01-224 Warsaw, Poland*
[5]*University of Warsaw, Faculty of Chemistry, Laboratory of Physicochemistry of Dielectrics and Magnetics, Żwirki i Wigury 101, 02-089 Warszawa, Poland*

Preparation of 4-ethoxybenzoyl chloride

The synthesis was carried out according to the well-known, universal and low-cost method. To the round bottom flask 4-ethoxybenzoic acid (1.66g; 0.010 mol; Sigma-Aldrich, pure p.a., 99%) and thionyl chloride (2.16 mL; 0.0293 mol; Fluka, pure ≥99%) were added. The mixture was stirred at 90˚C for 24 h. The thionyl chloride was removed from the mixture by the vacuum distillation to achieve 1.7 g (92% yield) of transparent oil. No further purification was needed.

Cytotoxicity assays and erythrocytes shape under the test compounds.

Erythrocyte preparation. Fresh human erythrocyte suspensions were obtained from the blood bank. The erythrocytes were washed three times (3000 rpm, 10 min) in phosphate buffered saline (PBS, pH 7.4) supplemented with 10 mM glucose. After washing, cells were suspended in the buffer at 1.65×10^9 cells/ml, stored at 277 K and used within 5 h.

Erythrocyte sedimentation under nanomaterials treatment. Erythrocytes (1.65×10^8 cells/ml) were incubated with nanoparticles in Eppendorf vials for 60 min, at 310 K, under

gently mixing. Three different concentrations (1, 0.1, 0.01 mg/ml) of the nanoparticles were investigated. In the case of $LnF_3@SiO_2$, a 0.001 mg/ml concentration was also analyzed, in order to obtain a non-toxic concentration of the structure. The cells incubated only in PBS (pH 7.4), and supplemented with 10 mM glucose, were taken as a control series. The erythrocyte sedimentation rate (ESR) was recorded by the use of a digital camera. The cells agglutination and the morphology of both treated and control erythrocytes were estimated using a light microscope. After observation, erythrocytes were fixed in 0.1% glutaraldehyde for 1h, RT. Each sample was repeated three times, and the experiments were repeated 3 times with erythrocytes from different donors.

Hemolysis assays. Erythrocytes ($1.65x10^8$ cells/ml, ~1.5 hematocrit) were incubated in phosphate-buffered saline (PBS, pH 7.4) supplemented with 10 mM glucose and containing test compounds for 60 min at 310 K (or for 12 hours at room temperature) in a shaking water bath. Three different concentrations (1, 0.1, 0.01 mg/ml) for all of the nanoparticles were investigated. In case of $LnF_3@SiO_2$, a 0.001 mg/ml concentration was also analyzed. Erythrocytes incubated only in PBS were taken as the control. Following the incubation, the erythrocyte suspensions were centrifuged (3000 rpm, 10 min), and the degree of hemolysis was estimated by monitoring the hemoglobin in the supernatant. The results were expressed as a percentage (%) of hemolysis. Hemolysis 0% was taken as the absorbance of the supernatant of the erythrocyte suspensions in PBS only, while the total hemolysis (100%) was determined when PBS was replaced by distilled water. Each sample was repeated three times and the experiments were repeated 3 times with erythrocytes from different donors.

Scanning electron microscope studies of erythrocytes shape alterations. Erythrocytes were fixed in 0.1 glutaraldehyde for 1 hour at room temperature. The fixed cells were washed by exchanging of the supernatant with PBS. The samples were gently vortexed and the cells were fixed with 2% glutaraldehyde for another hour. After washing as above, the cells were

post-fixed with 1% OsO_4 for 30 min at room temperature. The supernatant was exchanged with PBS, and samples were gently vortexed. Fixed cells were dehydrated in a series of ethanol solutions (50%, 60%, 70%, 80%, 90%, 95% and 100%), gold-sputtered, and examined using an *EVO 40* (ZEISS, Germany) scanning electron microscope.

DLS - size measurements

Based on DLS measurements the hydrodynamic diameter of the particles can be calculated. The values obtained are usually larger than particles sizes calculated from TEM images, because the hydrodynamic parameters (radius/diameter) of the particles are much larger than their real dimensions. However the tendency/correlation between both values (TEM and DLS) is usually preserved and reflect particles growth/shrinking. The averaged sizes of the nanomaterials obtained in the pH ranges 2-13 are presented in Figure S1 (top graphs). Core nanoparticles, CeF_3:Gd^{3+} 5%, Tb^{3+} revealed the smallest size being in the range of 40-50 nm (pH 2-8), increasing at higher pH values up to 190 nm. This phenomenon was probably caused by particles agglomeration and superficial hydrolysis of the crystalline product, what correlates with luminescence deterioration of the Ln^{3+} doped crystalline nanomaterials at high pH values (data not shown). The size of the CeF_3:Gd^{3+} 5%, Tb^{3+}/SiO_2 and CeF_3:Gd^{3+} 5%, Tb^{3+}/SiO_2/NH_2 nanostructures was similar. In the neutral pH the particles size was around 200 nm, decreasing in the extreme pH (acidic and basic) to about 100-150. This phenomenon was caused by particles agglomeration near their isoelectric points (lack of the stabilizing surface charges). The presented data was extracted from recorded size distributions by volume. The corresponding histograms presenting size distribution by volume of the nanostructures synthesized were recorded in the pH range 6-7, and are presented in Figure S1 (bottom graphs), confirming monodispersity and stability of obtained colloidal solutions. In the case of the product modified with organic acid, the measured averaged hydrodynamic diameters of the particles and the corresponding size distribution histograms

were almost the same as the amine modified product, that is why they are not shown here. This fact is in good agreement with the presented TEM data (Figure 3 c and d), where the observed particles size is the same.

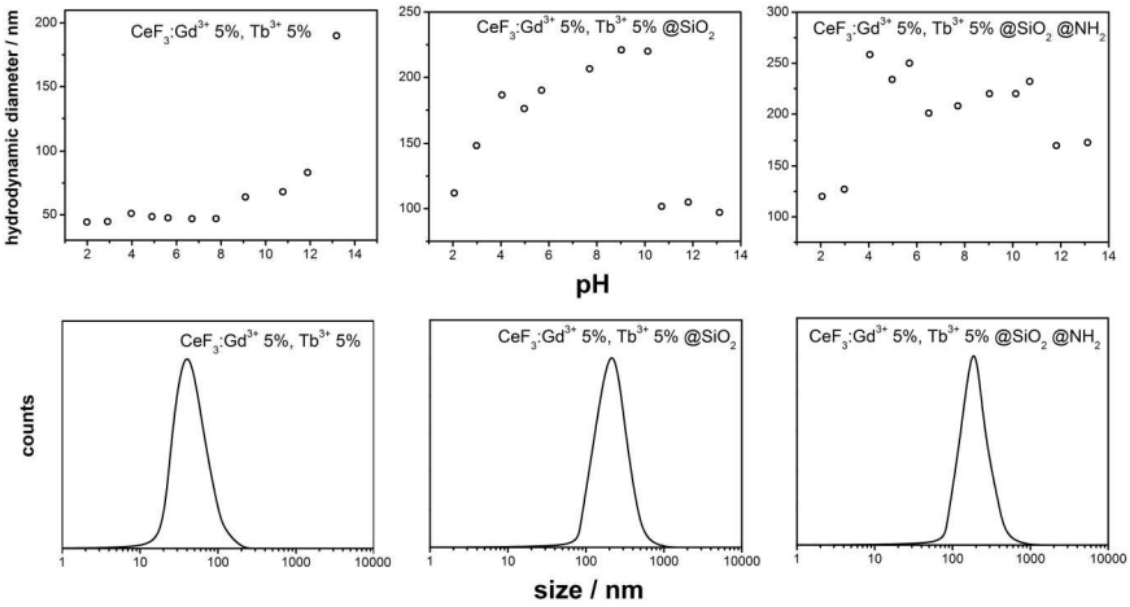

Figure S1. Hydrodynamic diameters plots of CeF_3:Tb^{3+} 5%, Gd^{3+} 5%, CeF_3:Tb^{3+} 5%, Gd^{3+} 5%@SiO_2, CeF_3:Tb^{3+} 5%, Gd^{3+} 5%@SiO_2@NH_2 and CeF_3:Tb^{3+} 5%, Gd^{3+} 5%@SiO_2@NH_2@4-ethoxybenzoic acid, recorded at different pH values (2-13). The insets present grain size distribution histograms for each compound, recorded at pH = 7. The histograms show size distribution by volume.

Figure S2 presents FT-IR spectra of LnF_3 (A), LnF_3@SiO_2 (B), LnF_3@SiO_2@NH_2 (C), LnF_3@SiO_2@NH_2@4-ethoxybenzoic acid (D) and pure 4-ethoxybenzoic acid. All spectra exhibited broad absorption peaks around 3400 cm^{-1} and 1640 cm^{-1} related to O-H stretching (ν) and deformation (σ) vibrations, respectively. They arose from the water adsorbed at the surface of the nanoparticles, trapped inside the silica shell, as well as from residual water molecules present in the KBr powder. In the case of samples B-D, they were also related to vibrations of the silanol groups of the amorphous silica. Absorption peaks at 2933, 2884 cm^{-1} (A-C) and at 2986, 2926 cm^{-1} (D and E) corresponded to νC-H vibrations of the aliphatic moieties of glycerine, ethanol, APTES and carboxylic acid, respectively. In the case of the

samples B-D, the spectra revealed several bands related to the silica shell, namely: νSi-O-Si(asym) at 1163,1085 cm^{-1}, νSi-O- at 956 cm^{-1}, νSi-O-Si(sym) at 797 cm^{-1}, and σO-Si-O at 466 cm^{-1}. The spectrum of the $LnF_3@SiO_2@NH_2$ nanomaterial (C) revealed additional peaks coming from amino groups, namely: around 3300 νN-H vibrations (overlapping with νO-H vibrations) and at 1537 cm^{-1} related to σN-H vibrations (scissoring). In the case of sample D, i.e. $LnF_3@SiO_2@NH_2$@4-ethoxybenzoic acid, additional absorption peaks were present: νC=O at 1681 cm^{-1}, νC=C at 1610 cm^{-1}, νC-O at 1384 cm^{-1}, $\nu C\text{-}O_{(aryl)}$ at 1266 cm^{-1}, σC-H at 1176 cm^{-1}, and several less intense bands related to the carboxylic acid used for the process of surface modification. We compared spectra of sample (D) and pure acid (E). Because most of the peak positions were the same in both spectra, especially the νC=O band, we assumed that there was no surface amide formation upon modification of the $–NH_2$ groups by carboxylic acid chloride (even after many attempts, long reaction time, different conditions and tedious product purification). After a scrupulous purification process (washing with THF/toluene and centrifugation), repeated many times, carboxylic acid was still detected in the IR spectra. This was probably due to strong electrostatic interactions between amino and carboxyl groups. Also a slight shift in the peak positions (νC=O from 1684 (E) to 1681 cm^{-1} (D)) and their intensity changes (e.g. νC-O, σN-H) confirmed such an explanation. This is beneficial for potential applications of the nanomaterials presented as drug carriers or organic/bio-sensors, since electrostatic interactions between surface groups/molecules are preferred over covalent bonds. In such a case a further release of the conjugated molecules is simplified. In order to additionally confirm that amino groups interacted with the organic acid molecules, a small amount of the product (several mg) was dispersed using ultrasound in acidic THF solution (1% HCl in 10 mL of THF) to extract the organic acid from our nanomaterial. The spectral comparison of $LnF_3@SiO_2@NH_2$@4-ethoxybenzoic acid before and after extraction (Figure S3) indicated a successful release of the discussed organic acid molecules in an acidic

solution. This phenomenon was caused by organic acid protonation, resulting in its release from the nanomaterial to the solution. The presented IR spectra confirmed the presence of a silica shell, an amine modified silica shell and its subsequent conjugation/modification with 4-ethoxybenzoic acid.

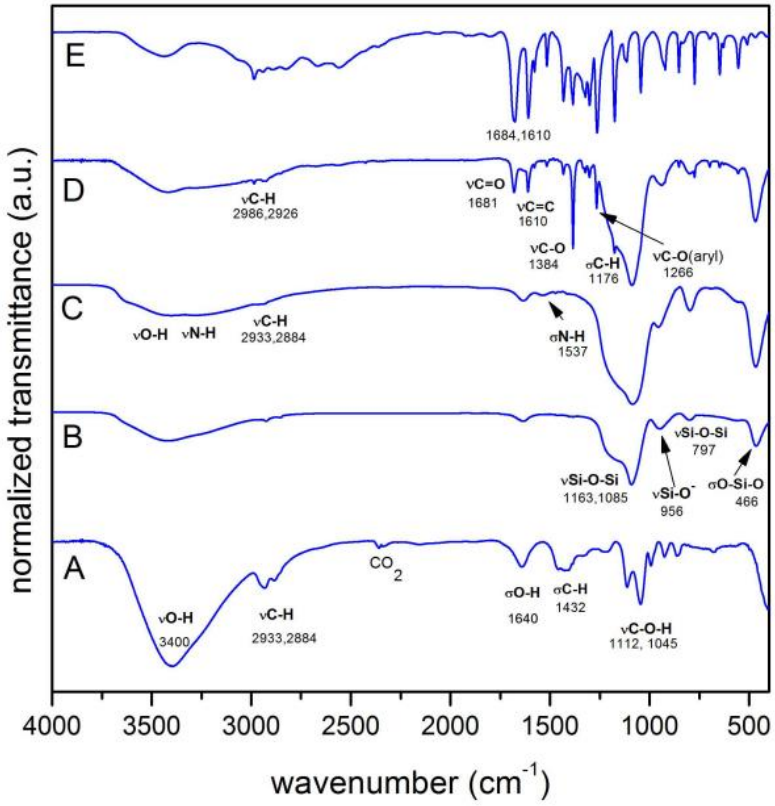

Figure S2. FT-IR spectra of CeF_3:Tb^{3+} 5%, Gd^{3+} 5% (a), CeF_3:Tb^{3+} 5%, Gd^{3+} 5%@SiO_2 (b), CeF_3:Tb^{3+} 5%, Gd^{3+} 5%@SiO_2@NH_2 (c), CeF_3:Tb^{3+} 5%, Gd^{3+} 5%@SiO_2@NH_2@4-ethoxybenzoic acid (d) and pure 4-ethoxybenzoic acid (e).

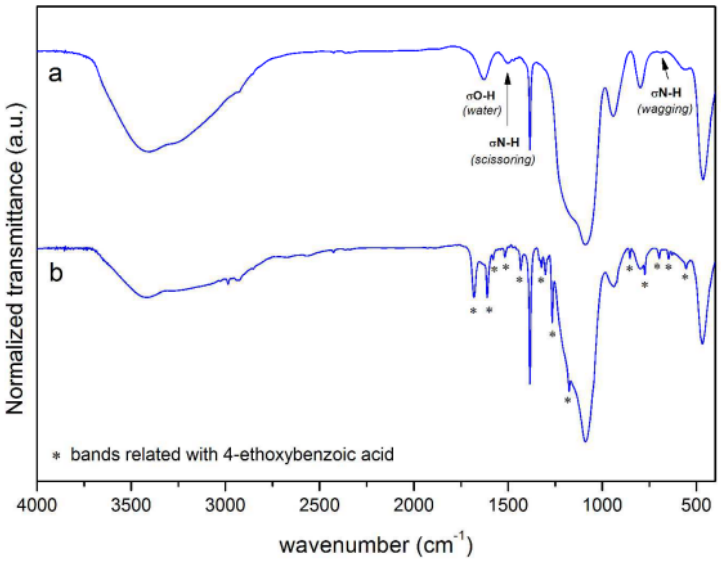

Figure S3. FT-IR spectra comparison of CeF_3:Tb^{3+} 5%, Gd^{3+} 5%@SiO_2@NH_2@4-ethoxybenzoic acid nanomaterial, before (a) and after (b) organic acid release from the surface at acidic pH.

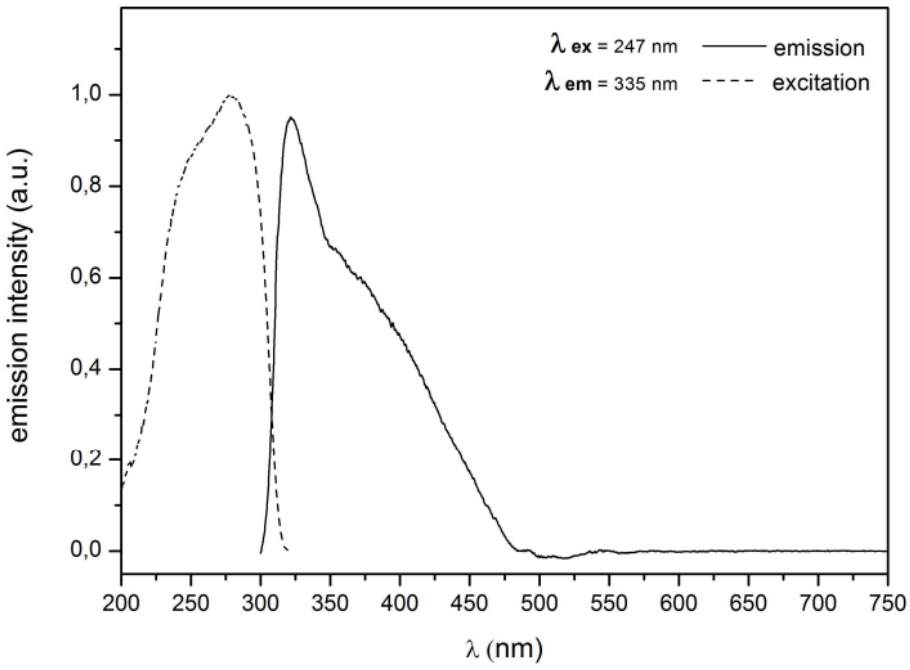

Figure S4. Excitation (dotted line) and emission (continuous line) spectra of pure 4-ethoxybenzoic acid, recorded at λ_{em} = 335 nm and λ_{ex} = 247 nm, respectively.

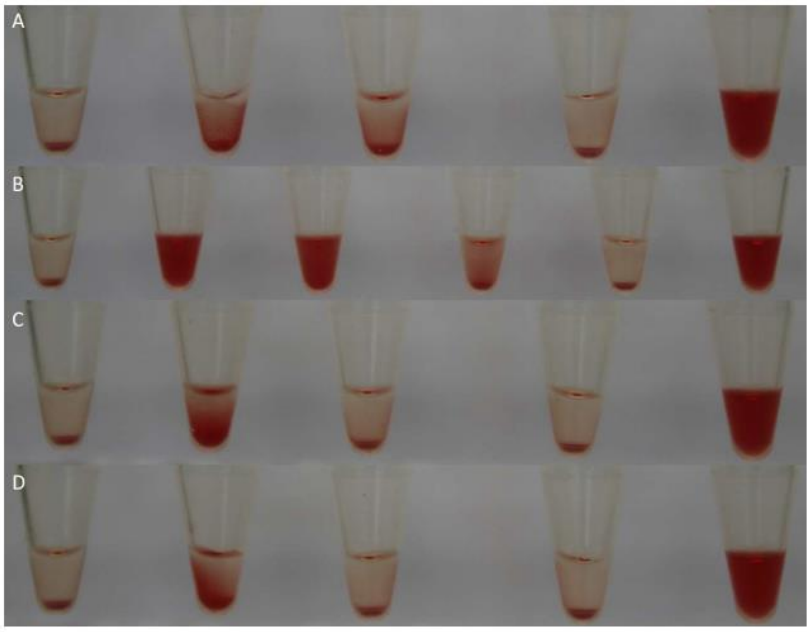

Figure S5. The effect of the nanoparticles: (a) - CeF_3:Tb^{3+} 5%, Gd^{3+} 5%, (b) - CeF_3:Tb^{3+} 5%, Gd^{3+} 5%@SiO_2, (c) - CeF_3:Tb^{3+} 5%, Gd^{3+} 5%@SiO_2@NH_2 and (d) - CeF_3:Tb^{3+} 5%, Gd^{3+} 5%@SiO_2@NH_2@4-ethoxybenzoic acid on the erythrocyte sedimentation rate. From the left: negative control (PBS), 1 mg/ml, 0.1 mg/ml, 0.01 mg/ml, and 0.001 mg/ml (in the case of (b) – CeF_3:Tb^{3+} 5%, Gd^{3+} 5%@SiO_2), and positive control (100% hemolysis; distilled water).

Jak już wspomniano, ciekawą i często pożądaną cechą niektórych fosforanów pierwiastków ziem rzadkich jest ich wydłużony kształt przypominający nanodruty/nanoigły (duży *aspect ratio*). Fakt ten wpływa znacząco na zmianę morfologii i charakteru takich nanocząstek w porównaniu do fluorków, które to często wykazują prawie sferyczną morfologie. Często zmianie ulegają także właściwości biologiczne takich podłużnych nanostruktur, w porównaniu do ich sferycznych odpowiedników. Problemem badawczym jaki podjąłem w pracy pt. „*Core/shell-type nanorods of Tb^{3+}-doped $LaPO_4$, modified with amine groups, revealing reduced cytotoxicity*" było otrzymanie luminescencyjnych nanomateriałów typu core/shell, o zmodyfikowanej powierzchni, wykazujących brak lub zmniejszoną cytotoksyczność. W wyniku przeprowadzonych badań udało się otrzymać nanodruty fosforanowe na bazie fosforanu lantanu domieszkowanego jonami terbu (III), $LaPO_4:Tb^{3+}$. Związku te wykazywały intensywną zieloną luminescencję dzięki obecności jonów Tb^{3+} w ich strukturze krystalicznej. Tak utworzone nanokrystality pokryto nanopowłoką krzemionkową otrzymując nanodruty $LaPO_4:Tb^{3+}/SiO_2$ typu core/shell. Następnie po powierzchniowej modyfikacji grupami aminowymi udało mi otrzymać sfunkcjonalizowane nanodruty $LaPO_4:Tb^{3+}/SiO_2/NH_2$ typu core/shell. Analiza strukturalna, przeprowadzona na podstawie wykonanych dyfraktogramów proszkowych (XRD) dla otrzymanych nanomateriałów potwierdziła utworzenie się pożądanej struktury krystalicznej. Otrzymane produkty miały formę nanodrutów pokrytych zewnętrzną powłoką krzemionkową co widać na wykonanych zdjęcia z mikroskopu elektronowego (SEM i TEM). Otrzymane produkty wykazywały zieloną luminescencję pod wpływem światła UV. Ich charakterystyka luminescencyjna potwierdziła zieloną luminescencję otrzymanych produktów, charakterystyczną dla krystalicznych materiałów domieszkowanych jonami Tb^{3+}. Dzięki zarejestrowanym widmom IR udało się potwierdzić obecność struktur fosforanowych, krzemionki i grup aminowych na powierzchni otrzymanych nanodrutów. Ponadto zmierzone krzywe adsorpcji i rozkłady wielkości porów ujawniły znaczną powierzchnię właściwą otrzymanych nanodrutów $LaPO_4:Tb^{3+}$ ($\approx$ 100 m^2/g), która uległa jeszcze większemu zwiększeniu po pokryciu krzemionką i utworzeniu się nanostruktur typu rdzeń powłoka - $LaPO_4:Tb^{3+}/SiO_2$ ($\approx$ 400 m^2/g). W wyniku pokrycia powierzchni grupami aminowymi, wielkość powierzchni właściwej uległa znacznemu zmniejszeniu ($\approx$ 30 m^2/g), co dodatkowo potwierdza udaną modyfikację powierzchni (grupy aminowe „zatykają" pory krzemionki). Korzystne właściwości luminescencyjne oraz ciekawa morfologia wytworzonych nanodrutów typu core/shell o zmodyfikowanej powłoce krzemionkowej przyczyniły się do przebadania ich

potencjalnej cytotoksyczności. Badania cytotoksyczności zostały wykonane *in vitro* na liniach komórkowych śródbłonka (HSkMEC) oraz czerniaka złośliwego (B16F0). Wyniki tych badań były bardzo zachęcające i interesujące gdyż wykazano iż „gołe" rdzenie fosforanowe, $LaPO_4:Tb^{3+}$ nie są cytotoksyczne, natomiast po pokryciu krzemionką, $LaPO_4:Tb^{3+}/SiO_2$ stają się znacząco cytotoksyczne powodując apoptozę komórek. Jednak co najważniejsze, dzięki przeprowadzonej modyfikacji powierzchni grupami aminowymi powstałe sfunkcjonalizowane nanomateriały $LaPO_4:Tb^{3+}/SiO_2/NH_2$ typu core/shell nie wykazywały objawów cytotoksyczności.

Wkład własny w powstanie pracy: koncepcja badań, wykonanie syntezy i zbadanie właściwości fizykochemicznych otrzymanych produktów. Analiza uzyskanych wyników, opracowanie danych i zredagowanie publikacji.

J Nanopart Res (2013) 15:2068
DOI 10.1007/s11051-013-2068-5

RESEARCH PAPER

Core/shell-type nanorods of Tb^{3+}-doped $LaPO_4$, modified with amine groups, revealing reduced cytotoxicity

Marcin Runowski · Krystyna Dąbrowska · Tomasz Grzyb · Paulina Miernikiewicz · Stefan Lis

Received: 23 January 2013 / Accepted: 11 October 2013

Abstract A simple co-precipitation reaction between Ln^{3+} cations (Ln = lanthanide) and phosphate ions in the presence of polyethylene glycol (PEG), including post-treatment under hydrothermal conditions, leads to the formation of Tb^{3+}-doped $LaPO_4$ crystalline nanorods. The nanoparticles obtained can be successfully coated with amorphous and porous silica, forming core/shell-type nanorods. Both products reveal intensive green luminescence under UV lamp irradiation. The surface of the core/shell-type product can also be modified with $–NH_2$ groups via silylation procedure, using 3-aminopropyltriethoxysilane as a modifier. Powder X-ray diffraction, transmission electron microscopy, and scanning electron microscopy confirm the desired structure and needle-like shape of the products synthesized. Fourier transform infrared spectroscopy and specific surface area measurements by Brunauer–Emmett–Teller method reveal a successful surface modification with amine groups of the core/shell-type nanoparticles prepared. The nanomaterials synthesized exhibit green luminescence characteristic of Tb^{3+} ions, as solid powders and aqueous colloids, examined by spectrofluorometry. The in vitro cytotoxicity studies reveal different degree toxicity of the products. $LaPO_4$:Tb^{3+}@SiO_2@NH_2 exhibits the smallest toxicity against B16F0 mouse melanoma cancer cells and human skin microvascular endothelial cell lines, in contrast to the most toxic $LaPO_4$:Tb^{3+}@SiO_2.

Keywords Core/shell nanorods · Cytotoxicity · Surface modification · Amine groups $–NH_2$ · Luminescence · Tb^{3+}-doped phosphates

M. Runowski · T. Grzyb · S. Lis (✉)
Department of Rare Earths, Faculty of Chemistry, Adam Mickiewicz University, Grunwaldzka 6, 60-780 Poznań, Poland
e-mail: blis@amu.edu.pl

K. Dąbrowska · P. Miernikiewicz
Bacteriophage Laboratory, Institute of Immunology and Experimental Therapy, Polish Academy of Sciences, Rudolfa Weigla 12, 53-114 Wrocław, Poland

Published online: 30 October 2013

Introduction

Nanoparticles revealing interesting and useful properties such as luminescence, magnetism, biocompatibility, high-capacity carriers (e.g., drug delivery), resistance for photo-bleaching and thermal-degradation, plasmonic effects, and other optoelectronic properties have been intensively studied over the last decade and their synthesis has been aimed by many researchers (Wang et al. 2010a; Grzyb et al. 2012; Limaye et al. 2011; Yang et al. 2009; Corr et al. 2008; Warren and Chan 2009; Park et al. 2010; Barnes et al. 2003; Zhang et al. 2009). In this group of nanostructures, nanophosphors doped with lanthanide ions exhibiting intensive luminescence, are materials of special importance (Grzyb et al. 2013a). Most of such

crystalline, inorganic phosphors are resistant to high temperature and UV irradiation. They also usually do not bleach over a long period of time and they can form stable aqueous colloids (Grzyb et al. 2012), which is very important for bio-applications (Nyk et al. 2008). The properties crucial for bio-applications are the small size, low-toxicity, and intensive luminescence. Lanthanide-doped nanophosphors and Q-dots show such properties. However, both classes of nanoparticles have certain benefits and drawbacks, e.g., some Q-dots based on heavy metals exhibit not only more efficient luminescence than the lanthanide-doped nanomaterials but also higher cytotoxicity (Xu et al. 2011; Gagné et al. 2008). There are many well-known inorganic phosphors based on lanthanide ions, e.g., simple fluorides, borates, vanadates, manganates, phosphates, and their complex analogs. Phosphates with the general formula: $LnPO_4$ or hydrated ones ($LnPO_4 \cdot nH_2O$) doped with activator ions (e.g., Eu^{3+}, Tb^{3+}, Tm^{3+}) can exhibit bright, multicolor luminescence dependent on their crystal structure, chemical composition and morphology (Yu et al. 2006; Phaomei et al. 2010; Phaomei et al. 2011); high refractive index and thermal stability (Ghosh et al. 2010; Blasse and Grabmaier 1994); biocompatibility, which are the well-known properties of many phosphate species (Hirsch et al. 2007). As the nanostructures discussed reveal such properties, the phosphates have been successfully applied fluorescent lamps, tracers, sensors and bio-sensors, contrast agents, drug carriers, and as other biocompatible species (Xu et al. 2011; Hölsä 2009; Kim 2000; Chander 2005; Shionoya and Yen 1999).

Silica is a well-known compound thoroughly studied over last decades (Stöber 1968; Zhao 1998; Jal et al. 2004). Amorphous silica has been commonly applied in chromatography, catalysis, and as a desiccant. Modified nanosilica has been recently used in many bio-applications, e.g., drug delivery, imaging, tracing techniques, and targeting therapies (Slowing et al. 2008; Selvan et al. 2009; Haidar 2010). These applications have been possible because of its inertness, availability, low-cost, ease of fabrication (also on industrial scale), large specific surface area, porosity, simple surface modification, and biocompatibility.

The novel class of nanomaterials, the so called core/shell-type compounds, can combine all the above-mentioned properties of luminescent phase and amorphous silica. When silica is a shell surrounding an internal core, it makes it resistant to oxidation, pH changes, temperature, and many aggressive agents which normally could change the properties of the core or decompose it (Joo et al. 2009; Park et al. 2010; Hu et al. 2010; Runowski et al. 2011). Literature gives many examples of such core/shell-type structures, e.g., nanoparticles with magnetic core like Fe_3O_4/SiO_2 (Correa-Duarte et al. 1998; Stjerndahl et al. 2008), luminescent core $NaYF_4/SiO_2$ (Tan et al. 2010), semiconducting core ZnO/SiO_2 (Wang et al. 2010b), metallic cores $FePt/SiO_2$, Au/SiO_2 (Warren and Chan 2009; Liz-Marzán et al. 1996), and more complex structures like $Fe_3O_4/SiO_2@GdPO_4:Eu^{3+}$ or $Fe_3O_4/SiO_2/Ag$ (Runowski et al. 2012; Lv et al. 2010). Thanks to the multifunctional character of these nanomaterials, they can be potentially used in novel, sophisticated systems and techniques in industry, biochemistry, medicine, trace analytics, etc.

In order to make nanomaterials biocompatible and capable of further reactions, usually their surface can be easily modified with functional groups like: –SH, –COOH, $–NH_2$, etc. 3-Aminopropyltriethoxysilane (APTES) is a well-known reagent used for introducing amine groups into many compounds. To the best of our knowledge there are two main approaches to the hydrolysis of APTES. The first one demands the use of non-polar, organic solvents like toluene and the absence of water traces in the reaction system (Cauvel and Renard 1997; Mello et al. 2011; Garg et al. 1996). This method is effective but restricted to the use of waterless, cytotoxic organic solvents. The molecules of the solvents can be bound to the silica shell or trapped in its pores, what could be the reason for difficulties with its removal in potential bio-applications. The second approach can be carried out in an ethanol/water system (Deng et al. 2000; Pham et al. 2002; Jung et al. 2012).

Nanomaterials usually exhibit different toxicity than that of the bulk ones or solvated ions, hence their toxicity can be altered, and the crucial factors responsible for the differences are: the size, crystallinity/amorphous, surface charge, ligands present on the surface, etc. (Love et al. 2012; Shaw and Handy 2011). Prior to applications, each nanomaterial should be thoroughly examined against its potential cytotoxicity. Nanosized silica is a representative example of a well-known nanomaterials suitable for numerous of potential applications. The cytotoxicity of silica in

micro and submicro size forms is usually negligible, but its nanoforms may often reveal significant cytotoxicity against various cell lines, which has been investigated in vitro and in vivo by many researchers in various biological trials. Previous studies have shown a dose-dependent toxicity of silica nanoparticles. This effect was related to general oxidative stress and apoptosis of nanoparticle-treated cells. Lipid peroxidation and membrane damage were indicated by malondialdehyde and lactate dehydrogenase release. Silica nanoparticles may probably induce genotoxic effects in cells. It is not clear if they act directly by internalization or by cell signaling pathways; however, important changes in the structure of genetic material have been also observed (Lin et al. 2006; Yang et al. 2010; Wang et al. 2007). Surface modification of cytotoxic nanomaterials can be an effective way for altering its toxicity and biocompatibility. As has been originally proposed by Nabeshi et al., nanoparticle surface alternations result in changes in their interactions with surrounding molecules and further, in their biocompatibility with living cells. These changes may influence the processes of internalization and intracellular distribution resulting in a reduction of unfavorable interactions and lower toxicity (Nabeshi et al. 2011).

Here we report a simple approach to the synthesis of a novel, hybrid luminescent nanomaterial composed of small and uniform core/shell-type nanorods, having modified surface with amine groups. The nanostructures obtained reveal bright green luminescence, thanks to the presence of Tb^{3+} ions, and anisotropic morphology. Because of the surface modified with amine groups, they can be easily covalently bound/linked to many organic and biocompatible molecules, via simple organic synthesis reactions. The in vitro cytotoxicity studies have revealed that the level of toxicity of the nanomaterials obtained depends on the type of species present on the surface.

Experimental

Materials

Tb_4O_7 and La_2O_3 (Stanford Materials, 99.99 %) were separately dissolved in a concentrated, nitric acid, HNO_3 (POCh S.A., ultra-pure) in order to prepare $Tb(NO_3)_3$ and $La(NO_3)_3$ aqueous solutions. Ammonium phosphate monobasic $(NH_4)H_2PO_4$ (Sigma-Aldrich, ReagentPlus®, ≥98.5 %) provided phosphate ions during the synthesis of $LnPO_4$. Tetraethyl orthosilicate, TEOS (Sigma-Aldrich, reagent grade, 98 %) was used as a source of silica. 3-Aminopropyltriethoxysilane, APTES (Sigma-Aldrich, ≥98 %) acted as a surface modifier providing aminopropyl moiety. 1-Hexadecyltrimethylammonium bromide, CTAB, and polyethylene glycol 6000, PEG (Alfa Aesar, 98 %) were used as surfactants and structure directing agents. Aqueous solution of 25 % ammonium hydroxide, NH_4OH (Chempur, pure p.a.) was used for pH adjusting in silanes hydrolysis reactions. In all reactions, ultra-pure distilled water and absolute ethanol were used.

Synthesis of luminescent nanorods: $LaPO_4$:Tb^{3+} 10 %

The synthesis was performed to get 1 g of the product. At first, lanthanide nitrates, $Ln(NO_3)_3$ were mixed at appropriate molar ratio (La^{3+}/Tb^{3+} 9/1), and filled with water up to 50 ml. To the prepared solution, 50 ml of absolute ethanol and 0.5 g of PEG 6000 were added. The obtained solution was clear and transparent. The second solution containing 120 % of stoichiometric amount of $NH_4H_2PO_4$ needed for precipitation of all $LnPO_4$ was prepared in the same solvent systems as the previous one, with addition of 0.5 g of PEG 6000 as well. In order to precipitate the doped lanthanide phosphate, the solution containing a source of phosphate was slowly added, drop-by-drop to the first solution. The addition was completed in 30 min. When the precipitation was finished, the whole system was still continuously stirred in ambient conditions, for another 30 min. When the reaction was complete, the precipitate was centrifuged several times and washed with water and ethanol to purify the product. In order to improve the crystallinity of the product, the as-prepared wet precipitate was transferred into Teflon lined vessel and placed in a microwave autoclave (ERTEC, Magnum II, 600 W). The subsequent hydrothermal process lasted for 2 h at 180 °C and 40 bar. After this time, the obtained white, crystalline product was centrifuged several times again and washed with water and ethanol. It is worth noting that after the hydrothermal reaction the wet product irradiated with UV lamp, exhibited intensive green luminescence in contrast to the precipitate

before hydrothermal treatment, which did not exhibit any observable luminescence.

Synthesis of core/shell-type nanorods: $LaPO_4:Tb^{3+}$ 10 %@SiO_2

The silica shell was prepared according to the modified Stöber method (Stöber 1968). The as-prepared, hydrothermally treated product—$LaPO_4:Tb^{3+}$ 10 % (core) was ultrasonicated in water forming a colloidal solution. Afterward, 100 mg of the colloidal core dispersed in a solvent system composed of 40 ml of water, 180 ml of ethanol, and 10 ml of concentrated ammonia (25 %, aqueous solution) were mixed together and ultrasonicated again. Afterward, 200 mg of CTAB was dissolved in the same mixture, in order to improve stability of the colloid formed and acting as a template facilitating the formation of amorphous and porous silica shell. Subsequently, the whole system was ultrasonicated once again. Finally, to the vigorously stirred colloidal solution, 1 ml of TEOS, as a source of silica shell was added. The reaction lasted for 2 h at ambient conditions, upon continuous magnetic stirring. When the reaction was complete the core/shell-type product obtained was left over night in the mother solution. On the next day the product was purified by centrifugation and washed several times with acidic ethanol (95/5 ethanol/HCl) and water. The reason for the use of acidic ethanol was to remove CTAB (template) from silica pores. In order to improve the level of purification, the mixture was ultrasonicated during the washing process. The as-prepared core/shell-type product was dispersed in water forming a colloidal solution.

Surface modification: $LaPO_4:Tb^{3+}$ 10 %@SiO_2@NH_2

A portion of 25 mg of colloidal $LaPO_4:Tb^{3+}$ 10 %@SiO_2 was dispersed in 2 ml of water with the use of ultrasounds. Afterward 45 ml of ethanol and 5 ml of 25 % aqueous ammonia solution were added to the colloid prepared. The system was vigorously stirred at ambient conditions. Subsequently, 0.1 ml of APTES and 0.1 ml of TEOS were injected into the prepared colloid. The reaction was continued for 3 h, at 50–60 °C. When the reaction was complete, the products were purified by centrifugation and washed several times with water and ethanol. Part of the final product was dispersed in water forming a colloidal solution, and the rest of the product was dried in vacuum for measurements.

Figure 1 shows a scheme of the formation of nanorods, their coating with silica and subsequent surface modification with amine groups.

Characterization

Electron microscopy measurements were performed using a Transmission Electron Microscope LEO 912AB, ZEISS operating at accelerating voltage 120 kV, and a Scanning Electron Microscope LEO 435VP, ZEISS operating at 3 kV. The nitrogen adsorption–desorption isotherms recorded at 77 K were measured using a Quantachrome NOVA 1000e apparatus. Specific surface area, pore volume and pore size distribution were calculated by the Brunauer–Emmett–Teller (BET) and Barrett–Joyner–Halenda (BJH) methods, respectively. Before measurements, all samples were preheated at 300 °C overnight in vacuum. Powder X-ray diffractograms (XRD) were recorded on a Bruker AXS D8 Advance diffractometer, using CuKα radiation ($\lambda = 1.5406$ Å), accelerating voltage 40 kV and emission current 40 mA. IR spectra were measured with an Fourier transform infrared (FT-IR) spectrophotometer, JASCO 4200. The IR spectra were measured in the transmission mode, the samples were mixed with KBr, ground, and pressed into pellets. The excitation and emission spectra including luminescence decay curves (dried, solid powders) were carried out with a Hitachi F-7000 spectrofluorometer in ambient conditions. The excitation and emission spectra were appropriately corrected for the apparatus response.

The cytotoxicity of nanorods

Cytotoxicity of the nanoparticles investigated was tested in proliferation assays and by cell imaging. Both cancer cells and normal cells were used. The human skin microvascular endothelial (HSkMEC) cell line was obtained from Cell Culture Collection of the IIET (Wroclaw, Poland). The B16F0 mouse melanoma cancer cell line was obtained from the American Type Culture Collection (ATCC, USA). Both lines are kept at the Cell Culture Collection of the IIET (Wroclaw, Poland). The cells were cultured in

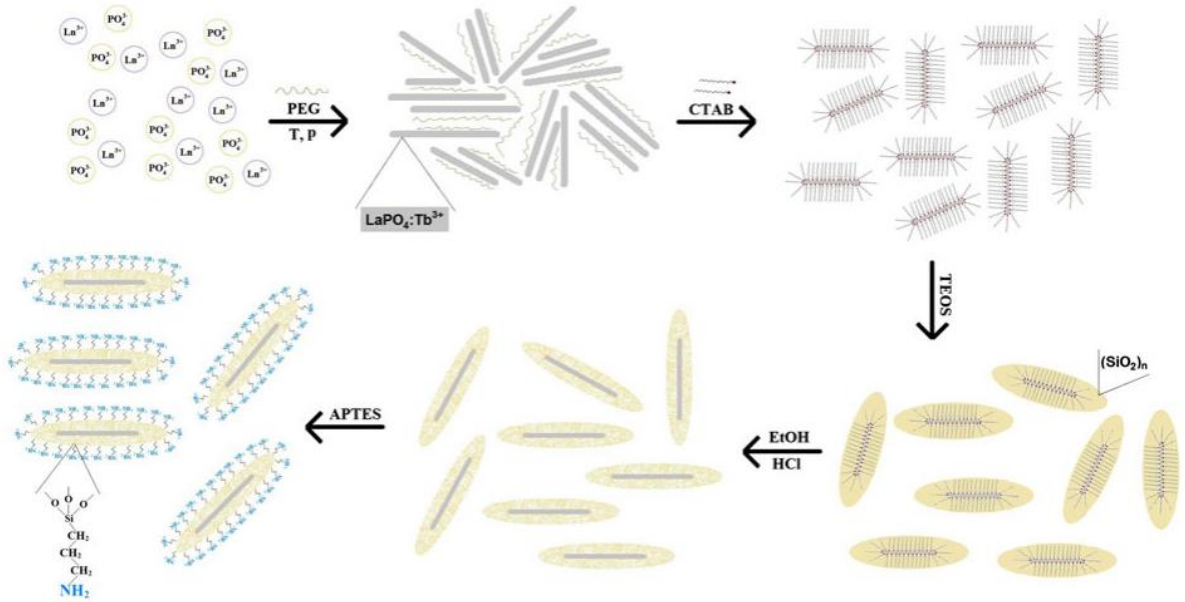

Fig. 1 Scheme of formation of $LaPO_4:Tb^{3+}$ 10 %@SiO_2@NH_2—surface-modified core/shell-type nanorods

OptiMEM (Invitrogen, Cergy Pontoise, France) supplemented with 5 % fetal bovine serum, 40 µg/ml gentamycin (Invitrogen) and 0.05 µg/ml fungizone (Invitrogen). The cells were seeded at 5×10^4 cells/cm^2 at 96-well plate or 6-well plate 2 h before experiments and maintained at 37° in a 5 % CO_2/95 % air atmosphere during the incubation prior to the experiment. Final concentrations of the nanoparticles were: 0.005, 0.01, 0.05, 0.1, 0.5, 1 mg/ml. All cultures including controls were supplemented with PBS to the same final volume. The effect of nanorods on the cells was assessed as follows: (i) cell condition and morphology was assessed by optical microscopy in sequential imaging, (ii) total cell material production was assessed by SRB assay (sulforhodamine B assay). The details of this technique were described by Skehan et al. (1990). The assay was performed after 48-h exposure of the cultured cells to the agents tested. The cells attached to the plastic were fixed by gently layering cold 50 % TCA (trichloroacetic acid, Aldrich-Chemie, Germany) on the top of the culture medium in each well. The plates were incubated at 4 °C for 1 h and then washed five times with tap water. The background optical density was measured in the wells filled with culture medium, without the cells. The cellular material fixed with TCA was stained with 0.4 % sulforhodamine B (SRB, Sigma, Germany)

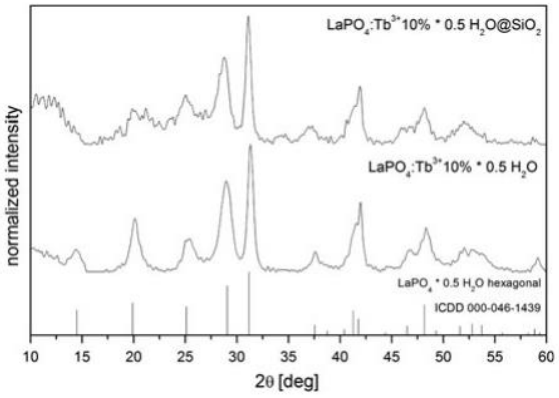

Fig. 2 XRD patterns of $LaPO_4:Tb^{3+}$ 10 % (·0.5H_2O) and $LaPO_4:Tb^{3+}$ 10 % (·0.5H_2O)@SiO_2 nanostructures

dissolved in 1 % acetic acid (POCh, Gliwice, Poland) for 30 min. Unbound dye was removed by rinsing with 1 % acetic acid. The protein-bound dye was extracted with 100 µl 10 mM unbuffered tris base (POCh, Gliwice, Poland) for determination of optical density (at 540 nm) in a computer-interfaced, 96-well microtiter plate reader Multiskan RC photometer (Labsystems, Helsinki, Finland). Each nanoparticle type and concentration in each cell line culture was tested two or three times, each test in 12-well groups, one exemplary experiment results of each type was presented ($N = 12$). The results were analyzed by

Table 1 Comparison of crystal lattice parameters from reference database (ICDD 000-046-1439) and XRD data of synthesized $LaPO_4:Tb^{3+}$ 10 % nanorods

Data	a (Å^3)	c (Å^3)	Cell volume (Å^3)
Reference	7.100	6.494	283.5
XRD	7.104 (6)	6.479 (7)	283.2 (4)

ANOVA with the Statistica 8.0 software package (www.statsoft.pl).

Results and discussion

Structure and morphology

The experimental X-ray powder diffractograms of $LaPO_4:Tb^{3+}$ 10 % and $LaPO_4:Tb^{3+}$ 10 %@SiO_2 were compared with pattern from International Centre for Diffraction Data (ICDD) standards database (Fig. 2). Both diffractograms are similar and fit well to the XRD pattern, number 000-046-1439, corresponding to the hexagonal, hydrated lanthanum phosphate, $LaPO_4{\cdot}0.5H_2O$ (for the reader convenience, compounds hydration is neglected in all formulas within the article). The diffractogram of core/shell-type product reveals an extra broad reflex in the 2θ range of 10°–15°, characteristic of amorphous silica (Musić et al. 2011). Both obtained powder XRD have broadened reflexes, which indicates the nanocrystallinity of the products.

Table 1 presents a comparison of cell parameters from reference database (hydrated $LaPO_4$) with the results of calculations based on XRD of the product obtained (doped $LaPO_4:Tb^{3+}$ 10 %). As follows from comparison of the data, a decrease in the unit cell volume takes place after Tb^{3+} doping. The reason for this phenomenon is the ionic radius of Tb^{3+} (dopant) smaller than that of La^{3+} ion (host). The above observation also confirms successful substitution of Ln^{3+} ions in the crystalline product.

The scanning electron microscopy (SEM) images presented in Fig. 3 reveal a uniform, needle-like shape of all nanoparticles of the core (a, b) and core/shell-type (c, d) products. The clusters of nanoparticles are in the range of nanometers. However, the core/shell-type products consist of larger nanostructures, because of the presence of an external silica shell. It is also worth mentioning that there is no any other phase present among the core/shell-type product's nanoparticles. In other words, the coating of lanthanum phosphate nanorods with silica is successful and uniform, without the presence of spherical particles in the final nanomaterial, characteristic of pure silica.

The next set of pictures (Fig. 4) shows transmission electron microscopy (TEM) images of the core (a, b) and core/shell-type (c, d) products. The average dimensions of $LaPO_4:Tb^{3+}$ 10 % are the width in the range of 7–11 nm and length of 80–110 nm. The bottom images (c, d) show a clear evidence of formation of a thin (15–20 nm) external silica shell, deposited on crystalline cores. What is also important, there are no traces of bare silica spheres among the core/shell-type nanorods. It means that the synthesized nanomaterial is homogeneous and uniform, which is important in many applications.

Figures 5, 6, and 7 illustrate the spectroscopic properties of the core and core/shell-type products. The spectroscopic studies (emission spectra and luminescence lifetimes) of the nanostructures obtained were performed in colloidal state (aqueous colloids), preserving the same amount of the luminescent phase in a fixed volume of a given colloid, in order to compare its relative emission intensity. Such measurements, allow the studies of luminescence quenching effect by water molecules. The dried products (powders) were used for the measurements of excitation spectra, because the spectra of the colloids were difficult for interpretation. Figure 5 presents the excitation spectra of the compounds studied recorded at $\lambda_{em} = 543$ nm (the center of Tb^{3+} emission main peak). Both spectra reveal the same dominant band in the range of 210–214 nm, corresponding to the allowed $4f^8 \rightarrow 4f^7 5d^1$ transition within Tb^{3+} ions. The slight change in its position and shape in the spectra of core/shell products is due to the absorption of silica present in the system. The minor peaks in the higher wavelengths correspond to the forbidden f → f transitions in Tb^{3+} ions. Again, because of the silica absorption in this region, these peaks are not observable in the core/shell spectrum.

Figure 6 presents the emission spectra of the core and core/shell nanophosphors ($\lambda_{ex} = 210$ nm), revealing four narrow bands, typical of Tb^{3+}-doped phosphors, namely: $^5D_4 \rightarrow {}^7F_6$, $^5D_4 \rightarrow {}^7F_5$, $^5D_4 \rightarrow {}^7F_4$, $^5D_4 \rightarrow {}^7F_3$, related to magnetic dipole transitions within 4f shell of Tb^{3+} ions (Lis 2002). Both spectra

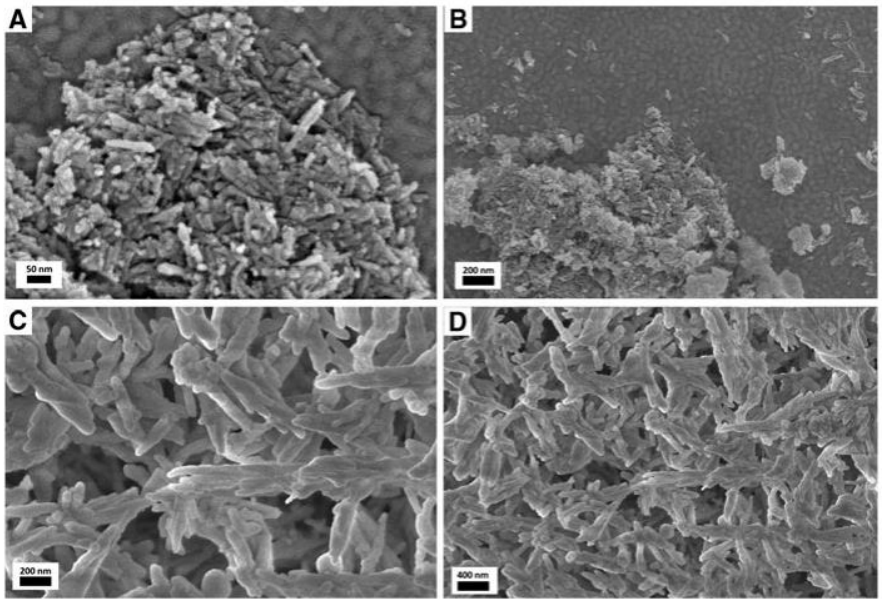

Fig. 3 SEM images of $LaPO_4:Tb^{3+}$ 10 %—core (**a**, **b**) and $LaPO_4:Tb^{3+}$ 10 %@SiO_2—core/shell (**c**, **d**) nanorods

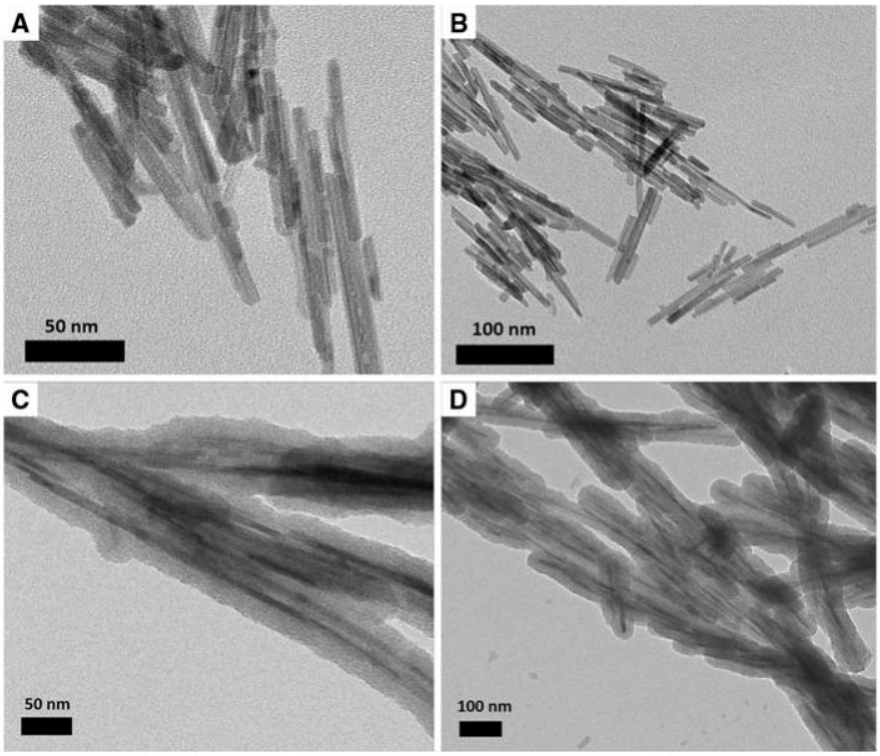

Fig. 4 TEM images of $LaPO_4:Tb^{3+}$ 10 %—core (**a**, **b**) and $LaPO_4:Tb^{3+}$ 10 %@SiO_2—core/shell (**c**, **d**) nanorods

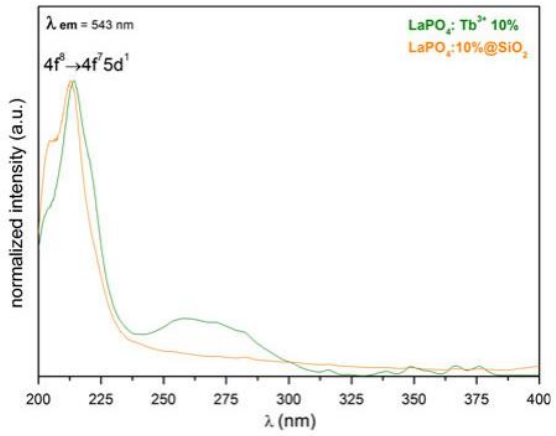

Fig. 5 Excitation spectra of $LaPO_4$:Tb^{3+} 10 % and $LaPO_4$:Tb^{3+} 10 %@SiO_2, recorded for dried samples

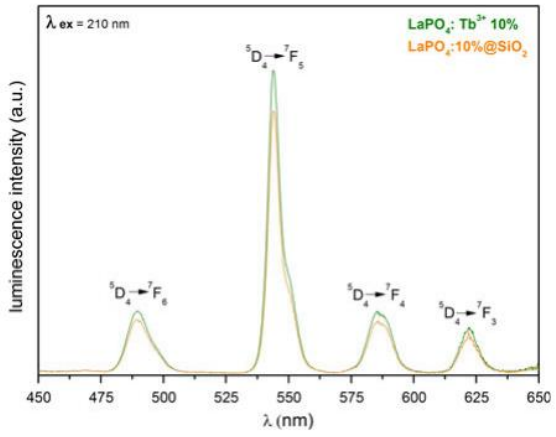

Fig. 6 Emission spectra of $LaPO_4$:Tb^{3+} 10 % and $LaPO_4$:Tb^{3+} 10 %@SiO_2, recorded for aqueous colloids

exhibit the same shape because of magnetic dipole nature of the transitions in Tb^{3+} ions, which are not sensitive to the site symmetry of the emitting ion. Their relative intensities are similar, however, the total intensity of luminescence of the bare core—$LaPO_4$:Tb^{3+} 10 % is slightly higher. We assume that this decrease is related to the thin silica shell on the surface of emitting nanorods which scatter and absorb light (Grzyb et al. 2013b).

Figure 7 shows the luminescence decay curves and calculated radiative lifetimes for the $^5D_4 \rightarrow {}^7F_5$ transition of the Tb^{3+} ions. The data were collected at 293 K, $\lambda_{em} = 543$ nm and $\lambda_{ex} = 210$ nm, for both products. The profiles recorded are fitted by a mono-exponential decay, (τ), $y = A1 \times \exp(-x/t) + y0$. In

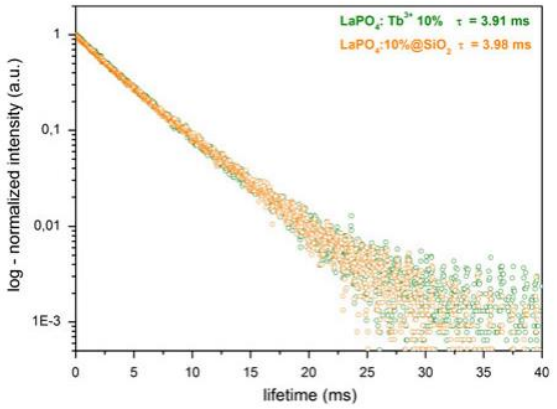

Fig. 7 Luminescence decay curves of $LaPO_4$:Tb^{3+} 10 % and $LaPO_4$:Tb^{3+} 10 %@SiO_2 observed at $\lambda_{em} = 543$ nm and $\lambda_{ex} = 210$ nm

hexagonal lanthanum phosphate, all lanthanide ions are situated in the same type of coordination site, which is confirmed by monoexponential decay of the luminescence. The calculated values of lifetimes are 3.91 and 3.98 ms for the core and core/shell-type products, respectively. These values are in good correspondence to the relatively long lifetimes of lanthanide-doped inorganic phosphors (Omkaram et al. 2008; Grzyb et al. 2012). An explanation of the slight increase in lifetime of the core/shell-type product can be a protective effect of the external thin layer of the silica shell, which decreases the quenching of the excited states of Tb^{3+} ions by O–H oscillators of water molecules (Wu et al. 2011).

Figure 8 presents the previously discussed aqueous colloids of $LaPO_4$:Tb^{3+} 10 % and $LaPO_4$:Tb^{3+} 10 %@SiO_2 are presented. They were prepared by ultrasonication of the products in water, and as mentioned before, the same concentration/amount of the luminescent phase was used for both dispersions. Colloidal solutions of both nanostructures are stable, and the colloidal particles do not settle down for a few days. Photographs on the left side present colloids of the core (a, b) and those on the right side present colloids of the core/shell-type product (c, d), taken under day light (a, c) and under UV light, 254 nm (b, d). Both of them exhibit bright, green luminescence characteristic of Tb^{3+} ions. In the core/shell-type compound, the silica shell scatters light and that is why its emission reveals a bit different hue.

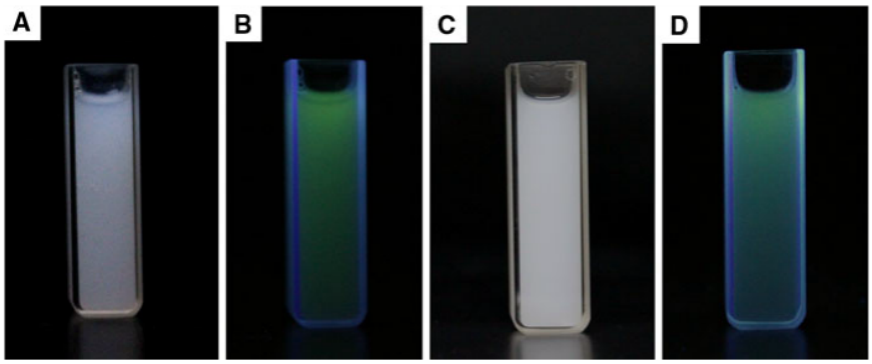

Fig. 8 Photographs of the aqueous colloids of $LaPO_4$:Tb^{3+} 10 %—core (**a**, **b**) and $LaPO_4$:Tb^{3+} 10 %@SiO_2—core/shell (**c**, **d**), taken under ambient light (**a**, **c**) and under 254 nm UV light (**b**, **d**)

Surface modification

In order to show that a modification of the surface of core/shell-type, $LaPO_4$:Tb^{3+} 10 %@SiO_2 nanoparticles is feasible and simple to perform, the surface was modified with $–NH_2$ groups. The reasons for such a choice were: multifunctional character of amines, i.e., biocompatibility, the use for water purification from heavy metals, the use as chelating agents, as reagents in many chemical reactions, a possibility of linking/binding to other organic molecules, availability of literature data on modifications with $–NH_2$ groups, a possibility of further modifications based on organic synthesis reactions. The reaction was carried out in a polar, non-toxic ethanol/water solvent system. However, the hydrolysis of APTES in a system without TEOS was ineffective as evidenced by the absence of the absorption peaks assigned to $–NH_2$ and $–CH_2$ groups in the IR spectra (data not shown). This fact is also described in literature (Bagwe et al. 2006), which is in agreement with the results of our study, therefore we used a mixture of APTES and TEOS for the surface modification. Their hydrolysis and subsequent co-condensation permitted successful modification of the core/shell nanomaterial surface with amine groups ($\equiv$Si–$(CH_2)_3$–NH_2).

The crystalline structure, shape and spectroscopic properties of the core/shell-type nanoparticles obtained, were not changed after surface modification with amine groups. The presence of amine groups was checked by FT-IR spectroscopy, analysis of specific surface area of the products and their cytotoxicity.

Figure 9 presents the IR spectra of $LaPO_4$:Tb^{3+} 10 %, $LaPO_4$:Tb^{3+} 10 %@SiO_2 and $LaPO_4$:Tb^{3+} 10 %@SiO_2@NH_2. All spectra reveal broad absorption peaks centered at 3,440 and 1,640 cm^{-1} corresponding to the O–H stretching (ν) and deformation (σ) vibrations, respectively. The O–H bonds come from water adsorbed on the surface and inside the mesopores of silica as well as silanol groups of amorphous silica. Absorption peaks around 2965, 2924, and 2855 cm^{-1} are assigned to νC–H vibrations of $–CH_2$ groups of PEG molecules (adsorbed on the surface of phosphate nanorods) and aminopropyl moiety (after APTES modification). All the spectra show also very intensive peaks corresponding to the vibrations of phosphate groups (partially overlapping with bands from silica) at 1049, 951 and at 615, 542 cm^{-1} and they are assigned to the stretching and bending vibrations within PO_4 groups, respectively

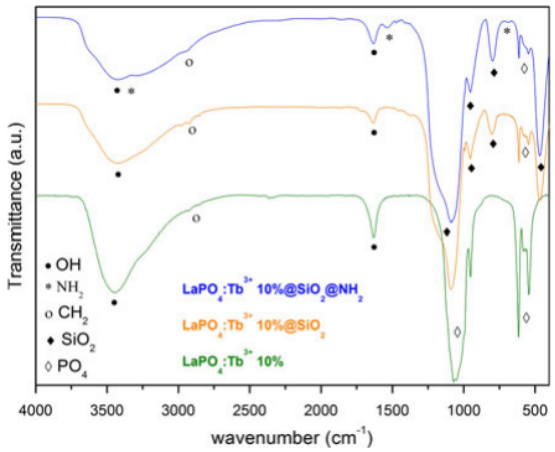

Fig. 9 FT-IR spectra of $LaPO_4$:Tb^{3+} 10 %, $LaPO_4$:Tb^{3+} 10 %@SiO_2, and amine-modified $LaPO_4$:Tb^{3+} 10 %@SiO_2@NH_2 nanomaterials

(Xu et al. 2011; Lucas et al. 2004). In the spectra of core/shell-type product and APTES-modified one, three bands related to the silica, are visible, and they are assigned to the following vibrations: νSi–O–Si(asym) at 1178,1085 cm^{-1}, νSi–O– at 952 cm^{-1}, νSi–O–Si(sym) at 800 cm^{-1}, and σO–Si–O at 467 cm^{-1} (Musić et al. 2011; Mello et al. 2011; Wang et al. 2010c). In the spectrum of the amine-modified product, the following additional peaks are observed: around 3,400 and 3,300 cm^{-1} assigned to νN–H vibrations (overlapping with νO–H vibrations), at 1,540 cm^{-1} σN–H (scissoring) and at 690 cm^{-1} σN–H (wagging) (Mello et al. 2011; Wang et al. 2010c). The presented spectra undoubtedly confirm the presence of silica shell and its successful modification with amine groups.

Specific surface area and porosity of the products were examined by nitrogen adsorption–desorption method. Figure 10 presents the N_2 adsorption–desorption isotherms recorded for the nanostructures studied in the temperature range 77–573 K. According to BET method, the specific surface area of $LaPO_4:Tb^{3+}$ 10 % nanorods is 126.100 m^2/g, while that of the core/shell-type product—$LaPO_4:Tb^{3+}$ 10 %@SiO_2 it is equal to 431.725 m^2/g, and that of $LaPO_4:Tb^{3+}$ 10 %@SiO_2@NH_2 it is 34.518 m^2/g. All compounds reveal N_2 sorption isotherms characteristic of mesoporous materials, namely type IV isotherm for both core/shell-type products, and type V isotherm for core nanomaterial (Sing et al. 1985). These values are in a good agreement with predictions, because they reflect an increased surface area of the core/shell-type product after its coating with porous silica which has high surface area (usually hundreds of m^2/g). Inorganic compounds have usually small specific surface area, in the range from several to several tens of m^2/g. In contrast, $LaPO_4:Tb^{3+}$ 10 % nanorods reveal prominent surface areas, which reflects small size of its nanocrystals, large surface area to volume ratio and porosity. On the other hand, a significantly decreased specific surface area of the $LaPO_4:Tb^{3+}$ 10 %@SiO_2@NH_2, confirms a successful modification of its surface and the presence of pores filled with the silanes applied. The total pore volume is similar for the core and core/shell-type nanomaterials, namely 0.327 and 0.343 cm^3/g for the core and core/shell-type product, respectively. These values are typical of inorganic, porous compounds. However, for the core/shell

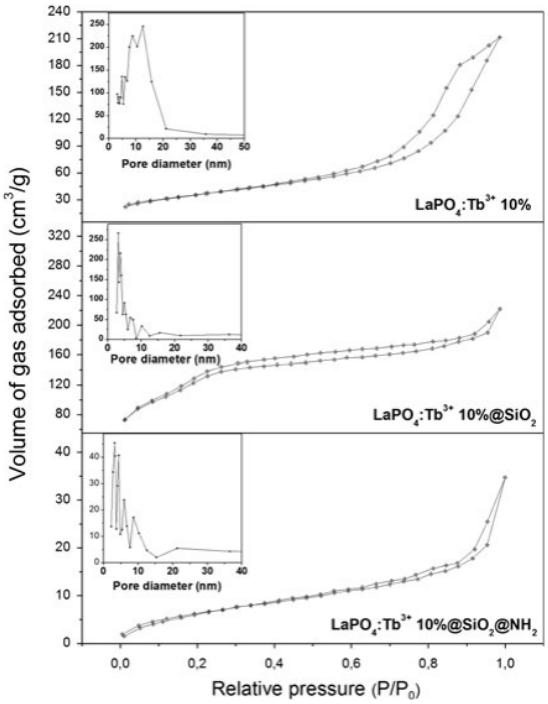

Fig. 10 Nitrogen adsorption–desorption isotherms and pore size distribution insets of $LaPO_4:Tb^{3+}$ 10 %—core, $LaPO_4:Tb^{3+}$ 10 %@SiO_2—core/shell, and amine-modified $LaPO_4:Tb^{3+}$ 10 %@SiO_2@NH_2 hybrid, core/shell-type nanostructures

modified with –NH_2 groups, the total pore volume is much smaller and equals to 0.054 cm^3/g. This decrease in the pore volume is probably related to the presence of covalently bound amine groups inside the pores and on the surface of the core/shell-type nanorods (linked by propyl moiety). The distribution of pore size (Fig. 10 insets) is calculated by BJH method. The average pore diameter in $LaPO_4:Tb^{3+}$ 10 % is 10.371 nm, for the core/shell-type product it is equal to 3.179 nm, and for the amine-modified core/shell-type nanomaterial it is 6.766 nm. Crystalline nanorods of the core are featured with mesopores, which can be attributed to the interstitial spaces/gaps between nanorods (Xu et al. 2011). Both, the core/shell-type product and the amine-modified one, have smaller pores, which is typical of compounds based on porous silica. The average pore diameter for the amine-modified nanomaterial is bigger than for the unmodified core/shell, because of a broader distribution of its pore diameter. We assume that this phenomenon is related to the formation of some additional superficial pores as a result of surface modification.

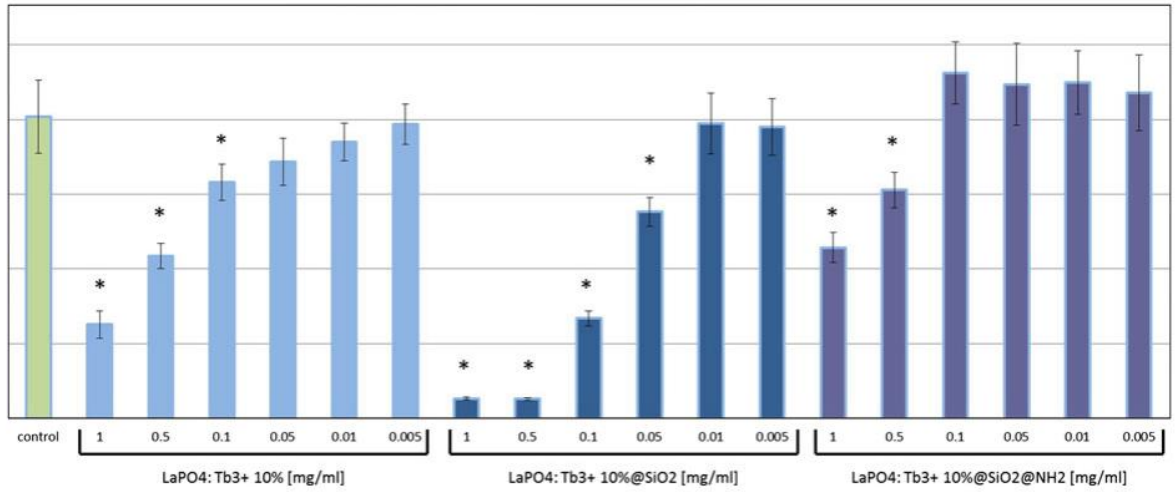

Fig. 11 Cell viability in the cultures treated with nanorods evaluated by SRB assay on B16F0 cells. *Bars* present 540 nm absorbance in the assay reflecting the amount of cell material in the cultures treated with gradient concentrations of $LaPO_4$:Tb^{3+} 10 % or $LaPO_4$:Tb^{3+} 10 %@SiO_2 or $LaPO_4$:Tb^{3+} 10 %@SiO_2@NH_2. Control cell cultures were supplemented with adequate volume of PBS. Groups of wells that significantly differ from the control wells (by ANOVA) are marked with *asterisks*

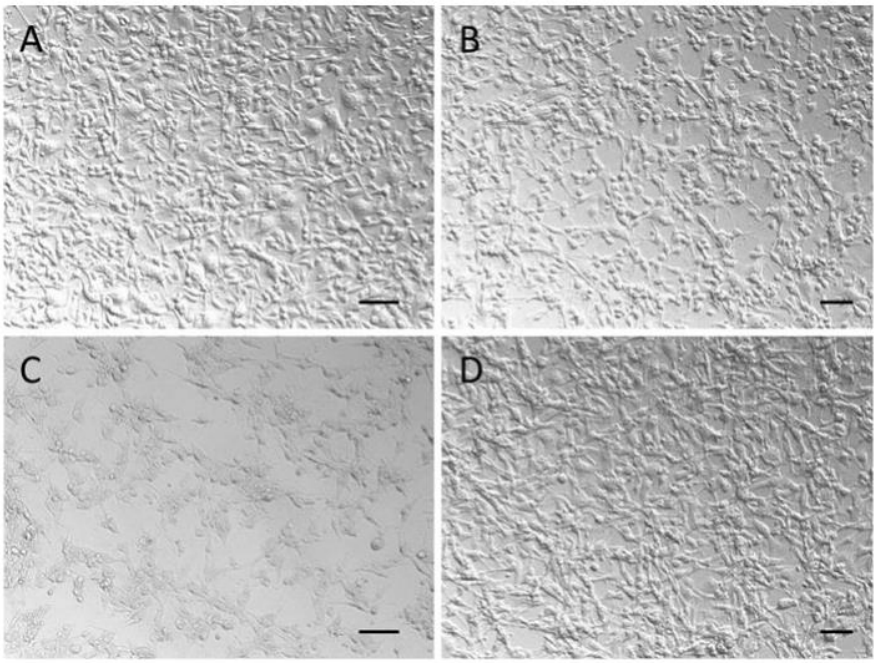

Fig. 12 Microscopic images of 48-h culture of B16F0 cells treated with nanorods: **a** control cells; **b** cells cultured with 0.05 mg/ml $LaPO_4$:Tb^{3+} 10 %; **c** cells cultured with 0.05 mg/ml $LaPO_4$:Tb^{3+} 10 %@SiO_2; **d** cells cultured with 0.05 mg/ml $LaPO_4$:Tb^{3+} 10 %@SiO_2@NH_2 (*scale bars* represent 500 μm)

In order to determine the amount of amine groups in the obtained nanomaterials the elemental analysis of $LaPO_4$:Tb^{3+} 10 %@SiO_2, and $LaPO_4$:Tb^{3+} 10 %@SiO_2@NH_2 was performed. For the $LaPO_4$:Tb^{3+} 10 %@SiO_2 product the obtained content of N, C, H was 0.021, 3.449, and 2.417

(wt%), respectively, whereas for amine-modified product, $LaPO_4:Tb^{3+}$ 10 %@SiO_2@NH_2 the obtained content of N, C, H was 2.902, 7.839, and 3.373 (wt%), respectively. On the basis of the results, the molar concentration of amine groups was determined for 2.058 mmol per one gram of the product. The results additionally confirmed the successful surface modification of the synthesized $LaPO_4:Tb^{3+}$ 10 %@SiO_2@NH_2 nanomaterial and large amount of amine groups present in its structure.

The effect of nanorods on mammalian cells in vitro

The effect of nanorods on mammalian cells (B16F0 and HSkMEC) was investigated by cell proliferation studies in in vitro cultures. In these conditions, the cells were directly exposed to interactions with nanorods, without physiological co-factors or background. 48-h exposition of the cells to nanorods revealed substantial differences in the cell sensitivity to the three products investigated: $LaPO_4:Tb^{3+}$ 10 %, $LaPO_4:Tb^{3+}$ 10 %@SiO_2, and $LaPO_4:Tb^{3+}$ 10 %@SiO_2@NH_2. In general, mammalian cells were most vulnerable to the core/shell-type product; however, surface modification with NH_2 groups resulted in an important increase in safety and substantial decrease in attenuating effect on the cells.

Potential toxic effects of $LaPO_4:Tb^{3+}$ 10 %, $LaPO_4:Tb^{3+}$ 10 %@SiO_2, and $LaPO_4:Tb^{3+}$ 10 %@SiO_2@NH_2 were assessed by determination of their tolerable concentrations for B16F0 cultures. These concentrations were: 0.05 mg/ml of non-modified $LaPO_4:Tb^{3+}$ 10 %, 0.01 mg/ml of the core/shell-type product, while as much as 0.1 mg/ml of the core/shell modified with NH_2 groups was (Fig. 11). Further, microscopic imaging of the cultures revealed dramatic changes in B16F0 cell number and morphology in the group treated with unmodified core/shell products already in concentrations 0.05 mg/ml. In the same conditions only minor changes were noticed in the group treated with 0.05 mg/ml of $LaPO_4:Tb^{3+}$ 10 % or $LaPO_4:Tb^{3+}$ 10 %@SiO_2@NH_2 (Fig. 12). Visualization of the cell condition suggests that the exposure of cells to unmodified core/shell-type products leads not only to the loss of cell viability and their slower growth, but rather to substantial membrane damage, which

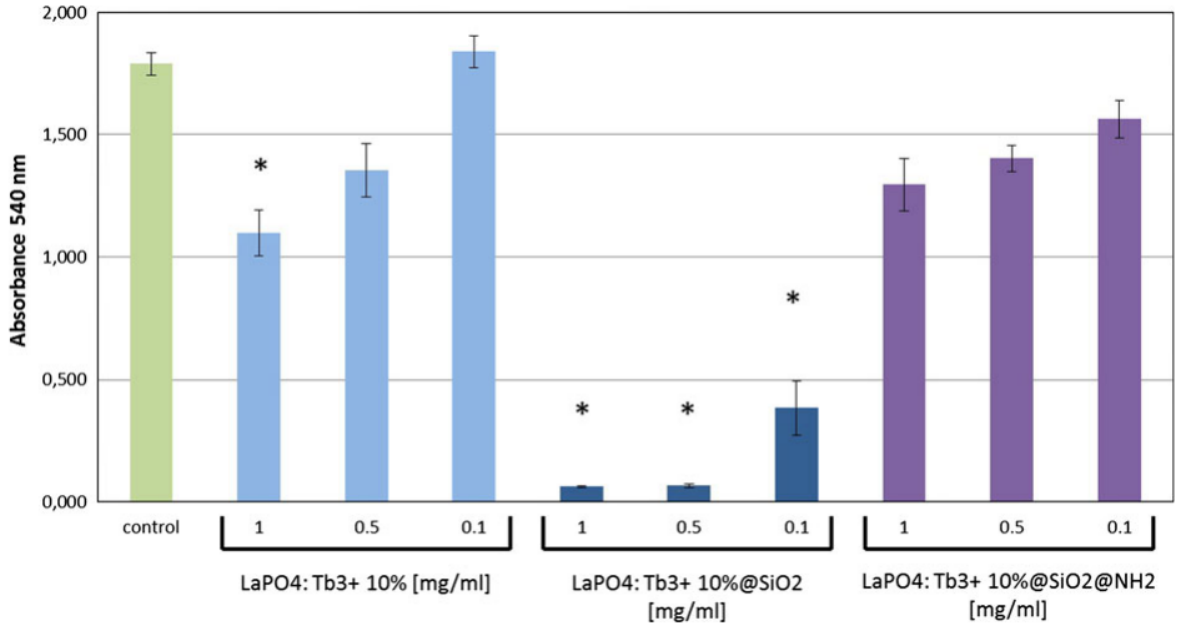

Fig. 13 Cell viability in the cell cultures treated with nanorods studied by SRB assay on HSkMEC cells. *Bars* present 540 nm absorbance in the assay reflecting the amount of cell material in the cultures treated with gradient concentrations of $LaPO_4:Tb^{3+}$ 10 % or $LaPO_4:Tb^{3+}$ 10 %@SiO_2 or $LaPO_4:Tb^{3+}$ 10 %@SiO_2@NH_2. Control cell cultures were supplemented with adequate volume of PBS. Groups of wells that significantly differ from the control wells (by ANOVA) were marked with *asterisks*

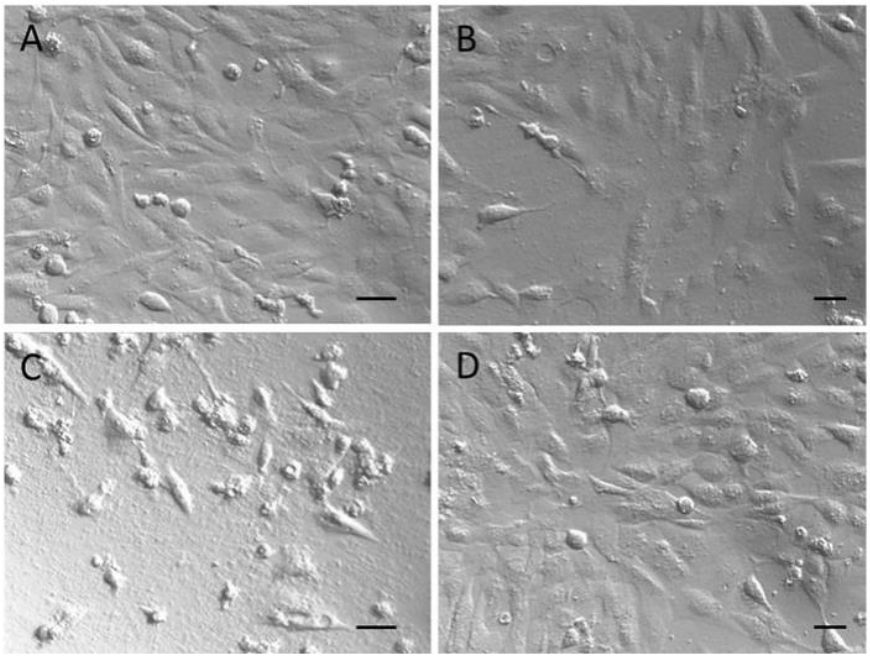

Fig. 14 Microscopic images of 48-h culture of HSkMEC cells treated with nanorods: **a** control cells; **b** cells cultured with 0.05 mg/ml $LaPO_4$:Tb^{3+} 10 %; **c** cells cultured with 0.05 mg/ml $LaPO_4$:Tb^{3+} 10 %@SiO_2; **d** cells cultured with 0.05 mg/ml $LaPO_4$:Tb^{3+} 10 %@SiO_2@NH_2 (*scale bars* represent 250 μm)

results in an apoptotic cell death. Similar effects were observed in HSkMEC cell cultures, which were most sensitive to toxic activity of silica shell products, but they tolerated well the same products modified with amine groups (Figs. 13, 14).

These observations are in line with a previous report of Nabeshi et al. (2011) who investigated model spherical silica nanoparticles and presented toxic effects of external silica shell, which were decreased by surface modification with amine groups. He used one cell line of murine macrophages, the range of silica products was 0.01–1 mg/ml. In our studies, the unmodified silica product was also the most toxic in two different cell lines. The remained residues of CTAB in the structure of silica could potentially contribute to increasing toxicity of $LaPO_4$:Tb^{3+} 10 %@SiO_2 (Zhang et al. 2012). However, we assume that the mentioned effect can be negligible or of minor influence, because of the large specific surface area of the mentioned product, which confirms that the template agent used has been successfully removed (CTAB was removed by washing the product several times with acidic ethanol, assisted with ultrasounds) from the silica pores located near the surface of the discussed core/shell-type nanomaterial. The surface modification with amine groups resulted in a product of approximately 10-times lower toxicity in comparison to the non-modified $LaPO_4$:Tb^{3+} 10 %@SiO_2. The amine coated surface was also better tolerated by the cells than the "bare" $LaPO_4$:Tb^{3+} 10 % (core). Surface alternations were postulated to change biological nature of small silica nanoparticles interactions with surrounding molecules, e.g., serum proteins or culture medium compounds. The surface modification may influence the processes of internalization and intracellular distribution resulting in a decrease in the unfavorable interactions and lower toxicity (Nabeshi et al. 2011). Our results show that the core/shell-type nanorods with the amine-modified silica shell can also be a better choice for biological applications. They are good candidates for further modifications, e.g., with targeting peptides or other biologically active organic compounds, but they are also the safer form of the products to which the mammalian cells show the highest tolerability.

Conclusions

Tb^{3+}-doped crystalline nanorods, exhibiting green luminescence, have been synthesized under hydrothermal conditions. Subsequently their surface has been coated with silica, forming the core/shell-type nanorods, which were further successfully modified with amine groups. The in vitro cytotoxicity studies unambiguously revealed significant toxicity of the core/shell-type nanorods against B16 and HSkMEC cells, and a negligible toxicity of the amine-modified core/shell-type nanomaterial against the same cells. Surface modification with $–NH_2$ groups also made the final nanomaterial biocompatible and provided a possibility of binding/linking desired molecules to the surface of nanorods, via simple organic synthesis reactions. The non-cytotoxic nanomaterial modified with amine groups can be potentially used in many areas and techniques, e.g., biotechnology, bio-imaging, nanoengineering, drug delivery, fluorescent labeling, tracing techniques, etc.

Acknowledgments M. R. gratefully acknowledges the financial support from Polish Ministry of Science and Higher Education—scientific work financed from the budget for science in 2012–2015 as a research project within the program called "Diamond Grant" No. DI2011 011441. P. M. is a recipient of the "Start" grant from Foundation for Polish Science.

References

Bagwe RP, Hilliard LR, Tan W (2006) Surface modification of silica nanoparticles to reduce aggregation and non-specific binding. Langmuir 22:4357–4362. doi:10.1021/la052797j

Barnes WL, Dereux A, Ebbesen TW (2003) Surface plasmon subwavelength optics. Nature 424:824–830. doi:10.1038/nature01937

Blasse G, Grabmaier BC (1994) Luminescent materials. Springer, Berlin

Cauvel A, Renard G (1997) Monoglyceride synthesis by heterogeneous catalysis using mcm-41 type silicas functionalized with amino groups. J Org Chem 62:749–751. doi:10.1021/jo9614001

Chander H (2005) Development of nanophosphors—a review. Mater Sci Eng R Rep 49:113–155. doi:10.1016/j.mser.2005.06.001

Corr SA, Rakovich YP, Gun'ko YK (2008) Multifunctional magnetic-fluorescent nanocomposites for biomedical applications. Nanoscale Res Lett 3:87–104. doi:10.1007/s11671-008-9122-8

Correa-Duarte MA, Giersig M, Kotov NA, Liz-Marzán LM (1998) Control of packing order of self-assembled monolayers of magnetite nanoparticles with and without SiO_2 coating by microwave irradiation. Langmuir 14:6430–6435. doi:10.1021/la9805342

Deng G, Markowitz MA, Kust PR, Gaber BP (2000) Control of surface expression of functional groups on silica particles. Mater Sci Eng C 11:165–172. doi:10.1016/S0928-4931(00)00203-4

Gagné F, Maysinger D, André C, Blaise C (2008) Cytotoxicity of aged cadmium-telluride quantum dots to rainbow trout hepatocytes. Nanotoxicology 2:113–120. doi:10.1080/17435390802245708

Garg BS, Bist JS, Sharma RK, Bhojak N (1996) Solid-phase extraction of metal ions and their estimation in vitamins, steel and milk using 3-hydroxy-2-methyl-1,4-naphthoquinone-immobilized silica gel. Talanta 43:2093–2099. doi:10.1016/S0039-9140(96)01994-7

Ghosh P, Kar A, Patra A (2010) Structural and photoluminescence properties of doped and core-shell $LaPO_4:Eu^{3+}$ nanocrystals. J Appl Phys 108:203–210. doi:10.1063/1.3514137

Grzyb T, Runowski M, Szczeszak A, Lis S (2012) Influence of matrix on the luminescent and structural properties of glycerine-capped, Tb^{3+}-doped fluoride nanocrystals. J Phys Chem C 116:17188–17196. doi:10.1021/jp3010579

Grzyb T, Runowski M, Szczeszak A, Lis S (2013a) Structural, morphological and spectroscopic properties of Eu^{3+}-doped rare earth fluorides synthesized by the hydrothermal method. J Solid State Chem 200:76–83. doi:10.1016/j.jssc.2013.01.012

Grzyb T, Runowski M, Dąbrowska K, Giersig M, Lis S (2013b) Structural, spectroscopic and cytotoxicity studies of $TbF_3@CeF_3$ and TbF_3 $@CeF_3@SiO_2$ nanocrystals. J Nanopart Res 15:1958–1972. doi:10.1007/s11051-013-1958-x

Haidar ZS (2010) Bio-inspired/-functional colloidal core-shell polymeric-based nanosystems: technology promise in tissue engineering, bioimaging and nanomedicine. Polymers 2:323–352. doi:10.3390/polym2030323

Hirsch AKH, Fischer FR, Diederich F (2007) Phosphate recognition in structural biology. Angew Chem Int Ed 46:338–352. doi:10.1002/anie.200603420

Hölsä J (2009) Persistent luminescence beats the afterglow: 400 years of persistent luminescence. Electrochem Soc Interface Winter 18:42–45

Hu H, Wang Z, Pan L (2010) Synthesis of monodisperse Fe_3O_4@silica core–shell microspheres and their application for removal of heavy metal ions from water. J Alloys Compd 492:656–661. doi:10.1016/j.jallcom.2009.11.204

Jal PK, Patel S, Mishra BK (2004) Chemical modification of silica surface by immobilization of functional groups for extractive concentration of metal ions. Talanta 62:1005–1028. doi:10.1016/j.talanta.2003.10.028

Joo SH, Park JY, Tsung C-K, Yamada Y, Yang P, Somorjai GA (2009) Thermally stable Pt/mesoporous silica core-shell

nanocatalysts for high-temperature reactions. Nat Mater 8:126–131. doi:10.1038/nmat2329

Jung HS, Moon D-S, Lee J-K (2012) Quantitative analysis and efficient surface modification of silica nanoparticles. J Nanomater 2012:1–8. doi:10.1155/2012/593471

Kim C (2000) Phosphors for plasma display panels. J Alloys Compd 311:33–39. doi:10.1016/S0925-8388(00)00856-2

Limaye MV, Singh SB, Das R, Poddar P, Kulkarni SK (2011) Room temperature ferromagnetism in undoped and Fe-doped ZnO nanorods: microwave-assisted synthesis. J Solid State Chem 184:391–400. doi:10.1016/j.jssc.2010.11.008

Lin W, Huang Y-W, Zhou X-D, Ma Y (2006) In vitro toxicity of silica nanoparticles in human lung cancer cells. Toxicol Appl Pharmacol 217:252–259. doi:10.1016/j.taap.2006.10.004

Lis S (2002) Luminescence spectroscopy of lanthanide(III) ions in solution. J Alloys Compd 341:45–50. doi:10.1016/S0925-8388(02)00055-5

Liz-Marzán LM, Giersig M, Mulvaney P (1996) Synthesis of nanosized gold-silica core-shell particles. Langmuir 12:4329–4335. doi:10.1021/la9601871

Love SA, Maurer-Jones MA, Thompson JW, Lin Y-S, Haynes CL (2012) Assessing nanoparticle toxicity. Annu Rev Anal Chem 5:181–205. doi:10.1146/annurev-anchem-062011-143134

Lucas S, Champion E, Bregiroux D, Bernache-Assollant D, Audubert F (2004) Rare earth phosphate powders $RePO_4{\cdot}nH_2O$ (Re = La, Ce or Y)—part I. Synthesis and characterization. J Solid State Chem 177:1302–1311. doi:10.1016/j.jssc.2003.11.003

Lv B, Xu Y, Tian H, Wu D, Sun Y (2010) Synthesis of Fe_3O_4 SiO_2 Ag nanoparticles and its application in surface-enhanced Raman scattering. J Solid State Chem 183:2968–2973. doi:10.1016/j.jssc.2010.10.001

Mello MR, Phanon D, Silveira GQ, Llewellyn PL, Ronconi CM (2011) Amine-modified MCM-41 mesoporous silica for carbon dioxide capture. Microporous Mesoporous Mater 143:174–179. doi:10.1016/j.micromeso.2011.02.022

Musić S, Filipović-Vincentović N, Sekovanić L (2011) Precipitation of amorphous SiO_2 particles and their properties. Braz J Chem Eng 28:89–94. doi:10.1590/S0104-66322011000100011

Nabeshi H, Yoshikawa T, Arimori A, Yoshida T, Tochigi S, Hirai T, Akase T, Nagano K, Abe Y, Kamada H, Tsunoda S-I, Itoh N, Yoshioka Y, Tsutsumi Y (2011) Effect of surface properties of silica nanoparticles on their cytotoxicity and cellular distribution in murine macrophages. Nanoscale Res Lett 6:93. doi:10.1186/1556-276X-6-93

Nyk M, Kumar R, Ohulchanskyy TY, Bergey EJ, Prasad PN (2008) High contrast in vitro and in vivo photoluminescence bioimaging using near infrared to near infrared up-conversion in Tm^{3+} and Yb^{3+}-doped fluoride nanophosphors. Nano Lett 8:3834–3838. doi:10.1021/nl802223f

Omkaram I, Seeta Rama Raju G, Buddhudu S (2008) Emission analysis of Tb^{3+}:$MgAl_2O_4$ powder phosphor. J Phys Chem Solids 69:2066–2069. doi:10.1016/j.jpcs.2008.03.005

Park JN, Zhang P, Hu YS, McFarland EW (2010) Synthesis and characterization of sintering-resistant silica-encapsulated Fe3O4 magnetic nanoparticles active for oxidation and chemical looping combustion. Nanotechnology 21:225708–225716. doi:10.1088/0957-4484/21/22/225708

Pham T, Jackson JB, Halas NJ, Lee TR (2002) Preparation and characterization of gold nanoshells coated with self-assembled monolayers. Langmuir 18:4915–4920. doi:10.1021/la015561y

Phaomei G, Ningthoujam RS, Singh WR, Singh NS, Luwang MN, Tewari R, Vatsa RK (2010) Low temperature synthesis and luminescence properties of re-dispersible Eu^{3+}-doped $LaPO_4$ nanorods by ethylene glycol route. Opt Mater 32:616–622. doi:10.1016/j.optmat.2009.12.009

Phaomei G, Ningthoujam RS, Singh WR, Loitongbam RS, Singh NS, Rath A, Juluri RR, Vatsa RK (2011) Luminescence switching behavior through redox reaction in Ce^{3+} co-doped LaPO4:Tb^{3+} nanorods: re-dispersible and polymer film. Dalton Trans 40:11571–11580. doi:10.1039/c1dt11264c

Runowski M, Grzyb T, Lis S (2011) Bifunctional luminescent and magnetic core/shell type nanostructures Fe_3O_4@-CeF_3:Tb^{3+}/SiO_2. J Rare Earths 29:1117–1122. doi:10.1016/S1002-0721(10)60609-6

Runowski M, Grzyb T, Lis S (2012) Magnetic and luminescent hybrid nanomaterial based on Fe_3O_4 nanocrystals and $GdPO_4$:Eu^{3+} nanoneedles. J Nanopart Res 14:1188–1195. doi:10.1007/s11051-012-1188-7

Selvan ST, Tan TTY, Yi DK, Jana NR (2009) Functional and multifunctional nanoparticles for bioimaging and biosensing. Langmuir 26:11631–11641. doi:10.1021/la903512m

Shaw BJ, Handy RD (2011) Physiological effects of nanoparticles on fish: a comparison of nanometals versus metal ions. Environ Int 37:1083–1097. doi:10.1016/j.envint.2011.03.009

Shionoya S, Yen WM (1999) Phosphor handbook. CRC Press, Boca Raton

Sing KSW, Everett DH, Haul RAW, Moscou L, Pierotti RA, Rouquerol J, Siemieniewska T (1985) Reporting physisorption data for gas/solid systems with special reference to the determination of surface area and porosity. Pure Appl Chem 57:603–619. doi:10.1351/pac198557040603

Skehan P, Storeng R, Scudiero D, Monks A, McMahon J, Vistica D, Warren JT, Bokesch H, Kenney S, Boyd MR (1990) New colorimetric cytotoxicity assay for anticancer-drug screening. J Natl Cancer Inst 82:1107–1112. doi:10.1093/jnci/82.13.1107

Slowing II, Vivero-Escoto JL, Wu C-W, Lin VS-Y (2008) Mesoporous silica nanoparticles as controlled release drug delivery and gene transfection carriers. Adv Drug Deliv Rev 60:1278–1288. doi:10.1016/j.addr.2008.03.012

Stjerndahl M, Andersson M, Hall HE, Pajerowski DM, Meisel MW, Duran RS (2008) Superparamagnetic $Fe_3O_4SiO_2$ nanocomposites: enabling the tuning of both the iron oxide load and the size of the nanoparticles. Langmuir 24:3532–3536. doi:10.1021/la7035604

Stöber W (1968) Controlled growth of monodisperse silica spheres in the micron size range. J Colloid Interface Sci 26:62–69. doi:10.1016/0021-9797(68)90272-5

Tan S, Yang P, Niu N, Gai S, Wang J, Jing X, Lin J (2010) Monodisperse and core–shell structured $NaYF_4$:Ln@SiO_2 (Ln = Yb/Er, Yb/Tm) microspheres: synthesis and characterization. J Alloys Compd 490:684–689. doi:10.1016/j.jallcom.2009.10.139

Wang JJ, Sanderson BJS, Wang H (2007) Cytotoxicity and genotoxicity of ultrafine crystalline SiO_2 particulate in cultured human lymphoblastoid cells. Environ Mol Mutagen 48:151–157. doi:10.1002/em

Wang F, Han Y, Lim CS, Lu Y, Wang J, Xu J, Chen H, Zhang C, Hong M, Liu X (2010a) Simultaneous phase and size control of upconversion nanocrystals through lanthanide doping. Nature 463:1061–1065. doi:10.1038/nature08777

Wang J, Tsuzuki T, Sun L, Wang X (2010b) Reverse microemulsion-mediated synthesis of SiO_2-coated ZnO composite nanoparticles: multiple cores with tunable shell thickness. ACS Appl Mater Interfaces 2:957–960. doi:10.1021/am100051z

Wang J, Zheng S, Shao Y, Liu J, Xu Z, Zhu D (2010c) Amino-functionalized Fe_3O_4@SiO_2 core-shell magnetic nanomaterial as a novel adsorbent for aqueous heavy metals removal. J Colloid Interface Sci 349:293–299. doi:10.1016/j.jcis.2010.05.010

Warren CW, Chan PD (2009) Bio-applications of nanoparticles. Springer, New York

Wu X, Zhang Q, Wang X, Yang H, Zhu Y (2011) One-pot synthesis of carboxyl-functionalized rare earth fluoride nanocrystals with monodispersity, ultrasmall size and very bright luminescence. Eur J Inorg Chem 2011:2158–2163. doi:10.1002/ejic.201001149

Xu Z, Cao Y, Li C, Ma P, Zhai X, Huang S, Kang X, Shang M, Yang D, Dai Y, Lin J (2011) Urchin-like $GdPO_4$ and $GdPO_4$:Eu^{3+} hollow spheres: hydrothermal synthesis, luminescence and drug-delivery properties. J Mater Chem 21:3686–3694. doi:10.1039/c0jm03333b

Yang P, Quan Z, Hou Z, Li C, Kang X, Cheng Z, Lin J (2009) A magnetic, luminescent and mesoporous core-shell structured composite material as drug carrier. Biomaterials 30:4786–4795. doi:10.1016/j.biomaterials.2009.05.038

Yang X, Liu J, He H, Zhou L, Gong C, Wang X, Yang L, Yuan J, Huang H, He L, Zhang B, Zhuang Z (2010) SiO_2 nanoparticles induce cytotoxicity and protein expression alteration in HaCaT cells. Part Fibre Toxicol 7:1–12. doi:10.1186/1743-8977-7-1

Yu L, Li D, Yue M, Yao J, Lu S (2006) Dependence of morphology and photoluminescent properties of $GdPO_4$:Eu^{3+} nanostructures on synthesis condition. Chem Phys 326:478–482. doi:10.1016/j.chemphys.2006.03.008

Zhang D, Chen C, Wang F, Zhang DM (2009) Optical gain and upconversion luminescence in LaF_3: Er, Yb nanoparticles-doped organic–inorganic hybrid materials waveguide amplifier. Appl Phys B 98:791–795. doi:10.1007/s00340-009-3851-y

Zhang Y, Xu D, Li W, Yu J, Chen Y (2012) Effect of size, shape, and surface modification on cytotoxicity of gold nanoparticles to human HEp-2 and canine MDCK cells. J Nanomater 2012:1–7. doi:10.1155/2012/375496

Zhao D (1998) Triblock copolymer syntheses of mesoporous silica with periodic 50 to 300 Angstrom pores. Science 279:548–552. doi:10.1126/science.279.5350.548

Nanomateriały luminescencyjno-magnetyczne

Problemem badawczym jaki podjąłem w pracy pt. „*Synthesis, surface modification/decoration of luminescent–magnetic core/shell nanomaterials, based on the lanthanide doped fluorides (*$Fe_3O_4/SiO_2/NH_2/PAA/LnF_3$*)*” było otrzymanie nowych nanomateriałów luminescencyjno-magnetycznych typu rdzeń/powłoka (core/shell), wykazujących jednocześnie intensywną, wielobarwną luminescencję pod wpływem promieniowania UV oraz odpowiedź na przyłożone pole magnetyczne. Spośród otrzymanych luminescencyjnych nanocząstek zostały wybrane struktury wykazujące pożądane właściwości spektroskopowe (intensywną emisję), strukturalne (nanokrystaliczność) i morfologiczne (homogeniczność i monodyspersyjność), które zostały użyte do otrzymania złożonych nanomateriałów luminescencyjno-magnetycznych typu rdzeń/powłoka. Związkami tymi były fluorki typu CeF_3: 10% Gd^{3+}, 10% Tb^{3+} i LaF_3: 10% Ce^{3+}, 30% Gd^{3+}, 1% Eu^{3+}, wykazujące odpowiednio zieloną i czerwoną luminescencję. W celu otrzymania nanomateriałów luminescencyjno-magnetycznych zsyntetyzowano nanocząstki magnetytu – Fe_3O_4, poprzez zastosowanie zmodyfikowanej metody Massart’a. Następnie pokryto je krzemionką sfunkcjonalizowaną grupami aminowymi $–NH_2$, poprzez użycie zmodyfikowanej metody Stöber’a. Źródłem krzemionki był tetraetoksysilan (TEOS) a grup aminowych 3-aminopropylotrietoksysilan (APTES). W wyniku wymienionych reakcji udało się otrzymać nanostruktury typu rdzeń/powłoka (core/shell) - $Fe_3O_4/SiO_2/NH_2$. Do dalszej modyfikacji powierzchni użyto kwasu poliakrylowego (PAA), którego molekuły zostały związane z powierzchniowymi grupami aminowymi, uprzednio otrzymanych magnetycznych nanostruktur. Dzięki temu możliwa była powierzchniowa koordynacja wprowadzonych do układu jonów lantanowców (Ln^{3+}) poprzez grupy karboksylowe PAA. W końcowym etapie syntezy wprowadzono do układu źródło fluoru jakim był roztwór NH_4F, co spowodowało utworzenie się nanostruktur typu $Fe_3O_4/SiO_2/NH_2/PAA/CeF_3$: 10% Gd^{3+}, 10% Tb^{3+} oraz $Fe_3O_4/SiO_2/NH_2/PAA/LaF_3$: 10% Ce^{3+}, 30% Gd^{3+}, 1% Eu^{3+}. Strukturę otrzymanych produktów zbadano za pomocą metody dyfraktometrii proszkowej (XRD), potwierdzając jednoczesną obecność refleksów zarówno od fazy magnetycznej jak i luminescencyjnej. Morfologia cząstek została zobrazowana za pomocą zdjęć TEM pokazujących utworzenie się powłoki krzemionkowej na cząstkach magnetycznych oraz przyłączenie się nanokrystalicznych fluorków

lantanowców do powierzchni krzemionki. Zarejestrowane widma FT-IR wykazały obecność fazy magnetycznej, krzemionki, grup aminowych i PAA w otrzymanych nanomateriałach. Powstałe nanomateriały wykazywały właściwości luminescencyjno-magnetyczne, czyli jednocześnie intensywną zielona lub czerwoną emisję po naświetleniu światłem UV (254 nm) oraz odpowiedź na przyłożone pole magnetyczne. Właściwości te były obserwowane zarówno w ciele stałym jak i w roztworze (po przyłożeniu silnego magnesu stałego do roztworu koloidalnego nanocząstek, następowała migracja całej luminescencyjno-magnetycznej fazy rozproszonej). Wykonana charakterystyka luminescencyjna otrzymanych nanomateriałów, tj. widma wzbudzenia/emisji, krzywe zaniku luminescencji i radiacyjne czasy życia, potwierdziły efektywną czerwoną lub zieloną emisję otrzymanych produktów, po naświetleniu światłem UV (≈ 250 nm). Wykonane widma EDX, potwierdziły zgodny z oczekiwanym skład pierwiastkowy otrzymanych luminescencyjno-magnetycznych nanomateriałów. Takie materiały mogą zostać użyte do detekcji i jednoczesnego obrazowania (luminescencyjnego i magnetycznego) różnych struktur organicznych i biologicznie czynnych, jak i do wzbogacania magnetycznego śladowych ilości substancji na powierzchni takich nanostruktur typu core/shell. Otrzymane związki mogą też być zastosowane w dziedzinach takich jak: medycyna, farmacja, kryminalistyka, optoelektronika i przemysł.

Wkład własny w powstanie pracy: koncepcja badań, wykonanie syntezy i zbadanie właściwości fizykochemicznych otrzymanych produktów. Analiza uzyskanych wyników, opracowanie danych i zredagowanie publikacji.

Journal of Luminescence 170 (2016) 484–490

Contents lists available at ScienceDirect

Journal of Luminescence

journal homepage: www.elsevier.com/locate/jlumin

Synthesis, surface modification/decoration of luminescent–magnetic core/shell nanomaterials, based on the lanthanide doped fluorides ($Fe_3O_4/SiO_2/NH_2/PAA/LnF_3$)

Marcin Runowski, Stefan Lis [1]

Adam Mickiewicz University, Faculty of Chemistry, Department of Rare Earths, Umultowska 89b, 61-614 Poznań, Poland

ARTICLE INFO

Article history:
Received 31 January 2015
Received in revised form
4 May 2015
Accepted 20 May 2015
Dedicated to Professor Oscar L. Malta on the occasion of his sixtieth birthday.
Available online 28 May 2015

Keywords:
Luminescence
Magnetism
Eu^{3+} and Tb^{3+} doping
Amine modified silica
Multifunctional nanoparticles
Energy transfer

ABSTRACT

The synthesized magnetite nanoparticles (10–15 nm) were successfully coated with amine modified silica nanoshell, which led to the formation of core/shell type nanostructures (30–50 nm). The as-prepared nanoparticles were surface modified with polyacrylic acid (PAA) via electrostatic interactions of $-NH_2$ and –COOH groups. Afterwards, the surface PAA molecules acted as complexing agents of the introduced lanthanide (Ln^{3+}) ions. Subsequently, the as-prepared nanostructures were surface decorated with luminescent LnF_3 nanoparticles, forming Eu^{3+} or Tb^{3+} doped $Fe_3O_4/SiO_2/NH_2/PAA/LnF_3$ nanomaterials (50–100 nm). The obtained luminescent–magnetic products exhibited simultaneously bright red or green emission under UV lamp irradiation (λ_{ex}=254 nm), and a response for the applied magnetic field (strong magnet attracts the colloidal particles, dispersed in aqueous medium). After the synthesis, properties of the nanomaterials were investigated by powder X-ray diffraction (XRD) technique, transmission electron microscopy (TEM), infrared spectroscopy (IR) and spectrofluorometry (analysis of excitation/emission spectra and luminescence decay curves). Such advanced nanomaterials can be potentially used in multimodal imaging, targeted therapies and as multifunctional contrast agents, novel luminescent–magnetic tracers, protection of documents, etc.

1. Introduction

The interest of multifunctional nanomaterials has been growing explosively over the last few years [1–7]. Such nanomaterials have dual or more complex structure, because their composition consists of two or more phases, resulting in unique properties. They can exhibit simultaneously two or more functionalities, namely tuneable multicolor luminescence, magnetic response, plasmonic properties, biological activity, drug-delivery capability, catalytic activity, etc. [8–14]. The multifunctionality and possibility of alterations of their properties are crucial factors promoting development of such nanocomposites and hybrid nanomaterials.

The core/shell type nanoparticles are usually composed of at least two separate phases of different chemical composition or crystal structure [6]. Therefore, such complex core/shell type nanomaterials become multifunctional, because they combine the properties of the core and the shell in a single nanomaterial. The inorganic core coated with a given nanoshell (e.g. modified silica/titania) can form core/shell nanostructures [6, 15–17]. Because the external shell exhibits different properties in comparison to the internal core, the final nanomaterials may reveal the desired properties depending on their phase composition, morphology, size and surface nature. Moreover, such shell protects the inner core from a damaging impact of the external environment (high temperature, aggressive agents, pH changes, oxidation, radiation, etc.) [18–20].

The compounds doped with lanthanide ions (Ln^{3+}) can exhibit different colors of emission, depending on the used dopant ion (e.g. Eu^{3+} – red, Tb^{3+} – green) [8,21–23]. They reveal also long luminescence lifetimes (several ms), narrow emission bands and a photostability [22,24,25]. However, their direct excitation does not provide efficient luminescence, because the 4f–4f electronic transitions are forbidden by the selection rules [21,26,27]. That is why, the charge transfer (CT) and energy transfer (ET) phenomena are commonly applied to increase the emission intensity of such systems, e.g. $O^{2-} \rightarrow Eu^{3+}$ CT, $Ce^{3+} \rightarrow Tb^{3+}$ ET [28–31].

Nowadays, the luminescent nanomaterials are intensively investigated, because they can be used in various scientific and industrial applications [32–35]. The organic dyes have been the most commonly used phosphors because of their significant molar absorption coefficient of UV light. However, they are not resistant to photo-bleaching and can be easily oxidized. Quantum-dots are

E-mail address: blis@amu.edu.pl (S. Lis).
[1] Tel.: +48 61 8291345.

http://dx.doi.org/10.1016/j.jlumin.2015.05.037
0022-2313/

photo-stable, resistant to high temperature and reveal simultaneously intense luminescence [36,37]. However, most of them are cytotoxic (CdSe, CdS), because of the presence of heavy metal ions in their structure [38,39]. That is why much attention has been paid to the phosphors based on lanthanide ions. The inorganic compounds such as lanthanide oxides, fluorides, phosphates, vanadates and borates, doped with the selected Ln^{3+} activator ion can exhibit intense, multicolor luminescence. They are also resistant to photo-bleaching, high temperature, redox processes, aggressive agents and UV radiation [31,40–44]. The phosphors based on rare earth elements are commonly utilized in plasma display panels, detection systems, optoelectronics, biomarkers, lighting, luminescence tracing and as luminescent cores in the core/shell type nanostructures [45–49]. Moreover, they reveal low cytotoxicities, which allow their potential use in various bioapplications [6,15,42].

The multifunctional nanomaterials exhibiting simultaneously luminescent and magnetic properties have been intensively examined recently [9,50–52]. The core/shell type nanostructures are especially suitable for such systems, because they can have a magnetic core coated by a protective shell (e.g. silica) which can be further functionalized and decorated with luminescent nanoparticles. Such luminescent–magnetic nanomaterials can be potentially used in multimodal imaging, hyperthermia treatment, targeted photodynamic therapy, selective drug delivery, water purification and enrichment of trace elements/substances, etc. [16,53–55].

Here we report the facile synthesis method, surface modification and decoration of luminescent–magnetic nanomaterials based on the lanthanide fluorides – $Fe_3O_4/SiO_2/NH_2/PAA/LnF_3$. The nanomaterials synthesized are composed of magnetite nanoparticles coated with amine modified silica shell, which was further modified with Ln^{3+} ions coordinated by PAA molecules (previously attached to the surface $–NH_2$ groups), and finally decorated with Eu^{3+} or Tb^{3+} doped LnF_3 nanoparticles. The products obtained formed stable aqueous colloids exhibiting bright red or green luminescence and a response for the applied magnetic field.

2. Experimental section

2.1. Materials

$FeCl_3 \cdot 6H_2O$ and $FeSO_4 \cdot 7H_2O$ (POCh S.A., pure p.a.) were used as precursors of magnetite nanoparticles. Polyacrylic acid (PAA) (average $Mw \approx 1800$) and $CeCl_3 \cdot 7H_2O$ (pure p.a., 99.9%) were purchased from Sigma-Aldrich. La_2O_3, Gd_2O_3, Eu_2O_3 and Tb_4O_7 (Stanford Materials 99.99%) were dissolved in a concentrated nitric acid (POCh S.A., pure p.a., 67%) to obtain $La(NO_3)_3$, $Gd(NO_3)_3$, $Eu(NO_3)_3$ and $Tb(NO_3)_3$ aqueous solutions, respectively. NH_4F (ACS grade, $\geq$98%), was purchased from POCh S.A. Tetraethyl orthosilicate (TEOS) and 3-aminopropyltriethoxysilane (APTES) (reagent grade, $\geq$98%) were purchased from Sigma-Aldrich. Ammonia aqueous solution (Chempur, pure p.a., 25%) was used to increase pH of the reaction system (acceleration of silanes hydrolysis).

2.2. Synthesis of Fe_3O_4

The nanoparticles of magnetite (Fe_3O_4) were prepared by a modified Massart method [56]. The water used was purged with nitrogen (for 15 min), to remove the oxygen dissolved. 0.3475 g of $FeSO_4 \cdot 7H_2O$ was dissolved in 5 mL of water containing 0.05 mL of 30% HCl (to suppress oxidation of Fe^{2+} ions) and mixed with 0.675 g of $FeCl_3 \cdot 6H_2O$, which was dissolved in 20 mL of water. Afterwards, 10 mL of concentrated ammonia was added drop by drop to the obtained solution of Fe^{2+} and Fe^{3+} ions. Immediately, the black precipitate of magnetite nanoparticles appeared in the solution. The reaction was performed in ambient conditions, with a continuous magnetic stirring. The synthesized Fe_3O_4 product was purified using a strong magnet and washing several times with water.

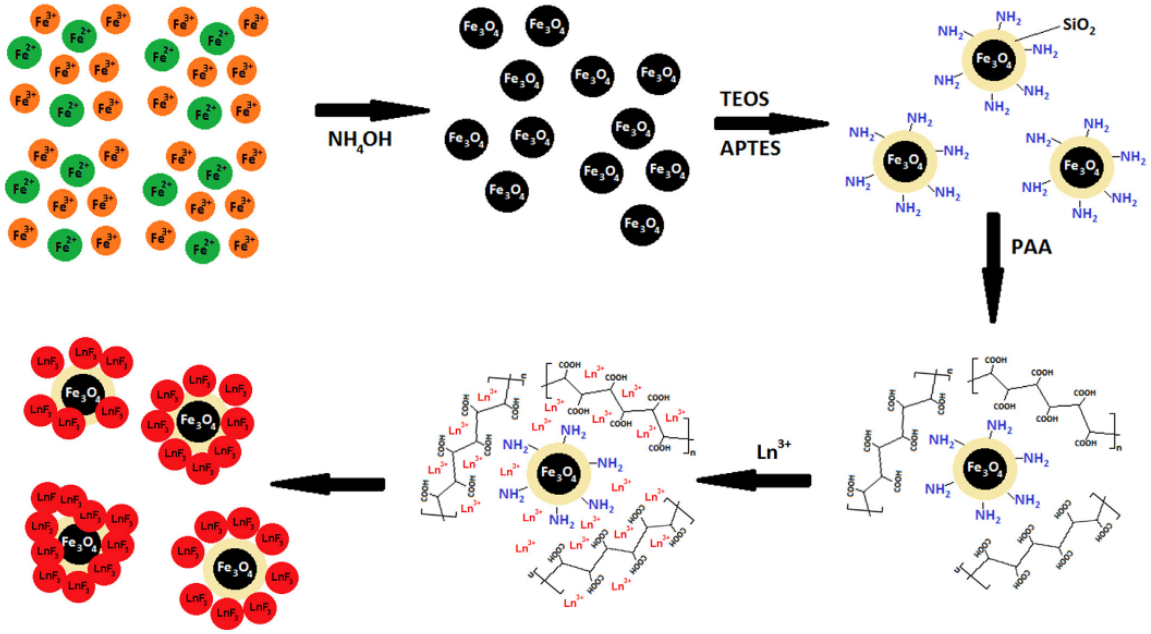

Fig. 1. Scheme of the synthesis, surface modification and decoration of $Fe_3O_4/SiO_2/NH_2/PAA/LnF_3$ core/shell type nanomaterials.

2.3. Synthesis of $Fe_3O_4/SiO_2/NH_2$

50 mg of Fe_3O_4 compound was transferred to a beaker, dispersed in 30 mL of water, assisted with ultrasounds. After that 160 mL of ethanol and 10 mL of concentrated ammonia were added to the obtained aqueous colloid. The mixture was continuously stirred in ambient conditions. Subsequently, 0.25 mL of TEOS was dropwise added to the beaker. After 30 min, 0.25 mL of APTES and 0.25 mL of TEOS were added to the stirred solution. The whole reaction was completed during 2.5 h. When the reaction was finished, the products were purified by the use of a magnet and washed several times with ethanol and water.

2.4. Synthesis of $Fe_3O_4/SiO_2/NH_2/PAA/LnF_3$

For the synthesis of $Fe_3O_4/SiO_2/NH_2/PAA/CeF_3$: 10% Gd^{3+}, 10% Tb^{3+} nanomaterial, the aqueous solutions of $CeCl_3$, $Gd(NO_3)_3$ and $Tb(NO_3)$, mixed at appropriate molar ratio, were used. Whereas, for the Fe_3O_4 /$SiO_2/NH_2/PAA/LaF_3$: 10% Ce^{3+}, 30% Gd^{3+}, 1% Eu^{3+} nanomaterial, the aqueous solutions of $La(NO_3)_3$, $CeCl_3$, $Gd(NO_3)_3$ and $Eu(NO_3)_3$ were used. 5 mL of the aqueous colloid containing 20 mg of the magnetic $Fe_3O_4/SiO_2/NH_2$ product was dispersed in 85 mL of water, assisted with ultrasounds. Subsequently, 10 mg of PAA was dissolved in the as-prepared colloidal solution, and ultrasonicated again. Afterwards, the appropriate amounts of lanthanide salts (aqueous chloride and nitrates) were added to the system (both syntheses were performed to get 100 mg of LnF_3). After that, 90 mL of ethanol was added to the colloidal solution. In a separate beaker, NH_4F (50% molar excess) was dissolved in the 60/60 mL ethanol/water solvent system. This solution was added dropwise to the solutions containing $Fe_3O_4/SiO_2/NH_2/PAA/Ln^{3+}$, in order to precipitate CeF_3: 10% Gd^{3+}, 10% Tb^{3+} or LaF_3: 10% Ce^{3+}, 30% Gd^{3+}, 1% Eu^{3+} nanocrystals on the surface of magnetic core/shell nanostructures, respectively. The reaction was performed in ambient conditions, with a continuous magnetic stirring, and lasted 30 min. When the reaction was completed, the obtained luminescent–magnetic nanomaterials were purified by the use of magnet and washed several times with ethanol and water.

Fig. 1 shows the scheme of the formation of luminescent–magnetic core/shell type nanostructures – Fe_3O_4 /$SiO_2/NH_2/PAA/LnF_3$.

2.5. Characterization

Transmission electron microscopy (TEM) images were performed using JEM 1200 EXII, JEOL transmission electron microscope, operating at an accelerating voltage of 80 kV. Powder X-ray diffraction patterns (XRD) were measured using a Bruker AXS D8 Advance diffractometer (6°–60° 2θ range), applying CuKα_1 radiation of $\lambda = 1.5406$ Å, at a resolution of 0.05 degree per step. Fourier transform infrared spectra (FT-IR) were recorded using a JASCO 4200 FT-IR spectrophotometer. The IR spectra were collected in a transmission mode, by mixing/grinding the analysed product with KBr, and pressing to transparent discs. The excitation and emission spectra as well as luminescence decay curves were recorded using a Hitachi F-7000 spectrofluorimeter. The spectra were corrected for the apparatus response.

3. Results and discussion

The magnetic core, Fe_3O_4 was synthesized in a form of small nanoparticles (10–15 nm), by a modified Massart method. Afterwards, the as-prepared nanoparticles were surface coated with an amine modified silica shell by a modified Stöber method [57]. In this approach TEOS was used as a source of silica, and APTES was a source of amino groups. The obtained magnetic core/shell type nanostructures – $Fe_3O_4/SiO_2/NH_2$ were subsequently modified with PAA, thanks to the strong affinity of $–NH_2$ groups to the –COOH groups (originating from PAA). The systems prepared were used for complexation of the given Ln^{3+} ions, and subsequent precipitation of the desired LnF_3 luminescent nanoparticles on the surface of the core/shell type nanostructures. This led to the formation of luminescent–magnetic nanomaterials, namely $Fe_3O_4/SiO_2/NH_2/PAA/CeF_3$: 10% Gd^{3+}, 10% Tb^{3+} or $Fe_3O_4/SiO_2/NH_2/PAA/LaF_3$: 10% Ce^{3+}, 30% Gd^{3+}, 1% Eu^{3+}.

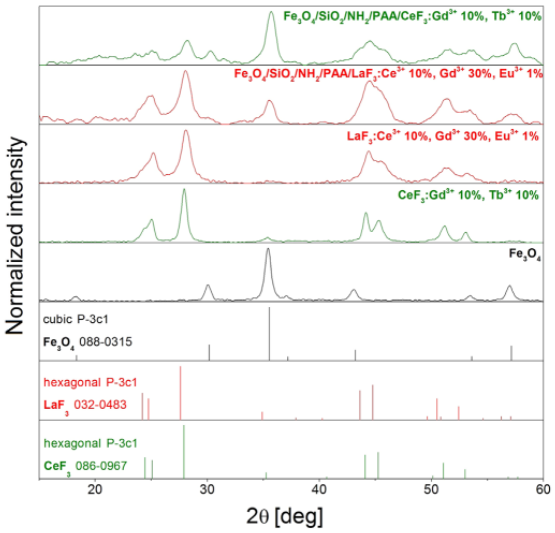

Fig. 2. Powder XRD patterns of Fe_3O_4, LnF_3, $Fe_3O_4/SiO_2/NH_2/PAA/LnF_3$ nanomaterials.

Fig. 2 presents the recorded powder diffractograms of the nanomaterials synthesized. The diffractograms of the luminescent–magnetic nanomaterials are similar and reveal reflexes corresponding to two crystalline phases, which fit well the reference patterns of cubic magnetite – Fe_3O_4 (ICDD 088-0315, Fd-3m) and hexagonal CeF_3 or LaF_3 (ICDD 086-0967 (Ce), 032-0483 (La), P-3c1). However, the XRD pattern (top) of the Tb^{3+} doped core/shell nanomaterial reveals smaller amount of CeF_3 in its structure, comparing to the Eu^{3+} doped one (lower level of surface decoration). There are no reflexes from silica shell because of its amorphous structure. In order to compare the reflexes positions of the structures corresponding to the core/shell nanomaterials, the diffractograms of the as-prepared Fe_3O_4, LaF_3: 10% Ce^{3+}, 30% Gd^{3+}, 1% Eu^{3+} and CeF_3: 10% Gd^{3+}, 10% Tb^{3+} are also presented in Fig. 2. The broadening of reflexes is related to the nanometric size of the crystals forming the nanomaterials obtained, which is characteristic for compounds composed of small nanoparticles. There are no extra reflexes, which confirm the successful substitution of the matrices obtained (LaF_3 and CeF_3) by the selected dopant Ln^{3+} ions, as well. The observed quite low signal-to-noise ratio in the case of the core/shell nanomaterials is caused by the presence of amorphous phase (silica) in their structure and low crystallinity of the surface lanthanide fluoride nanoparticles.

Fig. 3 shows TEM images of the nanomaterials synthesized, namely: Fe_3O_4 (A), $Fe_3O_4/SiO_2/NH_2$ (B), $Fe_3O_4/SiO_2/NH_2/PAA/LaF_3$: 10% Ce^{3+}, 30% Gd^{3+}, 1% Eu^{3+} (C), and $Fe_3O_4/SiO_2/NH_2/PAA/CeF_3$: 10% Gd^{3+}, 10% Tb^{3+} (D). The synthesized magnetite nanoparticles (A) have a size in the range of 10–15 nm. Their surface coating with amine modified silica shell, resulted in a formation of

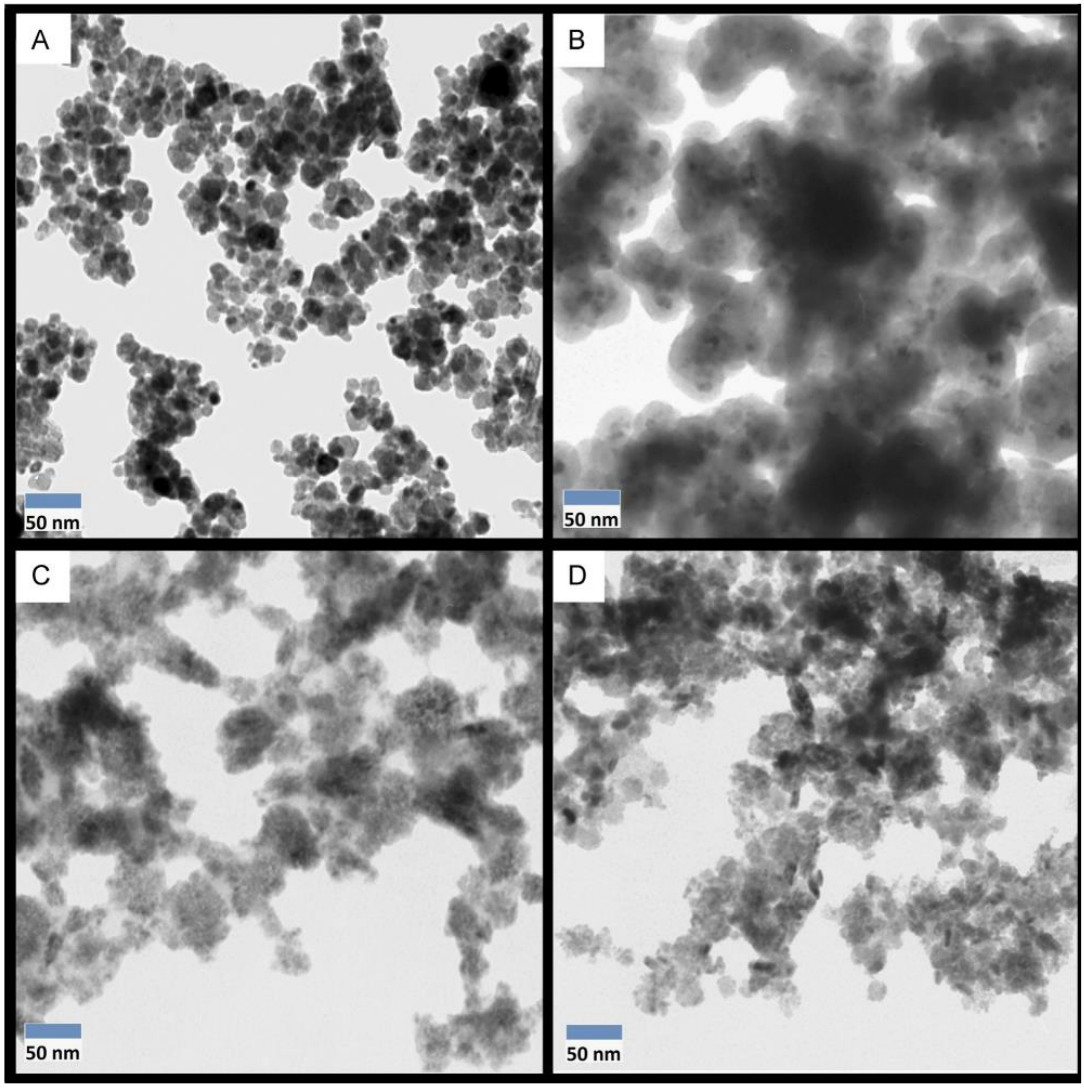

Fig. 3. TEM images of Fe_3O_4 (A), $Fe_3O_4/SiO_2/NH_2$ (B), $Fe_3O_4/SiO_2/NH_2/PAA/LaF_3$: 10% Ce^{3+}, 30% Gd^{3+}, 1% Eu^{3+} (C), $Fe_3O_4/SiO_2/NH_2/PAA/CeF_3$: 10% Gd^{3+}, 10% Tb^{3+} (D).

agglomerated core/shell type nanostructures – $Fe_3O_4/SiO_2/NH_2$ (B), which size is approx. 30–50 nm. The further surface decoration led to the larger nanostructures (≈ 50–100), covered with lanthanide fluoride nanoparticles – $Fe_3O_4/SiO_2/NH_2/PAA/LnF_3$ (C, D). Because of the abundance of LnF_3 nanoparticles decorated on the silica surface, the internal $Fe_3O_4/SiO_2/NH_2$ "core" is almost totally covered by the second, external luminescent shell, and hardly observed in the TEM images.

FT-IR spectra of the nanomaterials synthesized are presented in Fig. 4. All of the spectra reveal very broad bands centered at 3450 cm^{-1}, related to the O–H stretching (ν) vibrations and the less intense bands centered at 1630 cm^{-1} related to the O–H deformation (σ) vibrations. The mentioned O–H vibrations originate from the H_2O molecules adsorbed on the nanoparticles surface and silanol groups (–Si–OH) of the silica. The absorption peaks in the range of 550–650 cm^{-1} corresponding to νFe–O vibrations can be also observed for all of the samples, confirming the presence of magnetic phase in the nanomaterials synthesized. The spectra of the core/shell nanoparticles containing silica shell in their structure (B–D), exhibit intense bands characteristic of amorphous silica, i.e. νSi–O–Si(asym) vibration centered at 1080 cm^{-1}, νSi–O^- vibration at 950 cm^{-1}, νSi–O–Si(sym) vibration around 800 cm^{-1} and σO–Si–O vibration at 460 cm^{-1}. Moreover, the weak band related to σN–H vibrations (scissoring) of amino groups at 1545 cm^{-1} is present in these spectra, as well. The spectra of the luminescent–magnetic nanomaterials modified with PAA (C and D) reveal an absorption band at around 1715 cm^{-1} corresponding to the νC=O vibration of PAA molecules. The rest of undescribed peaks relate mostly to the vibrations of organic molecules present on the nanoparticles surface.

The nanomaterials synthesized exhibited a bright red or green luminescence, as a result of the effective energy transfer (ET) from the Ce^{3+} (energy donor ion) to the Eu^{3+} or Tb^{3+} ions [21,58]. Gd^{3+} ions act as energy mediators and decrease the energy gap

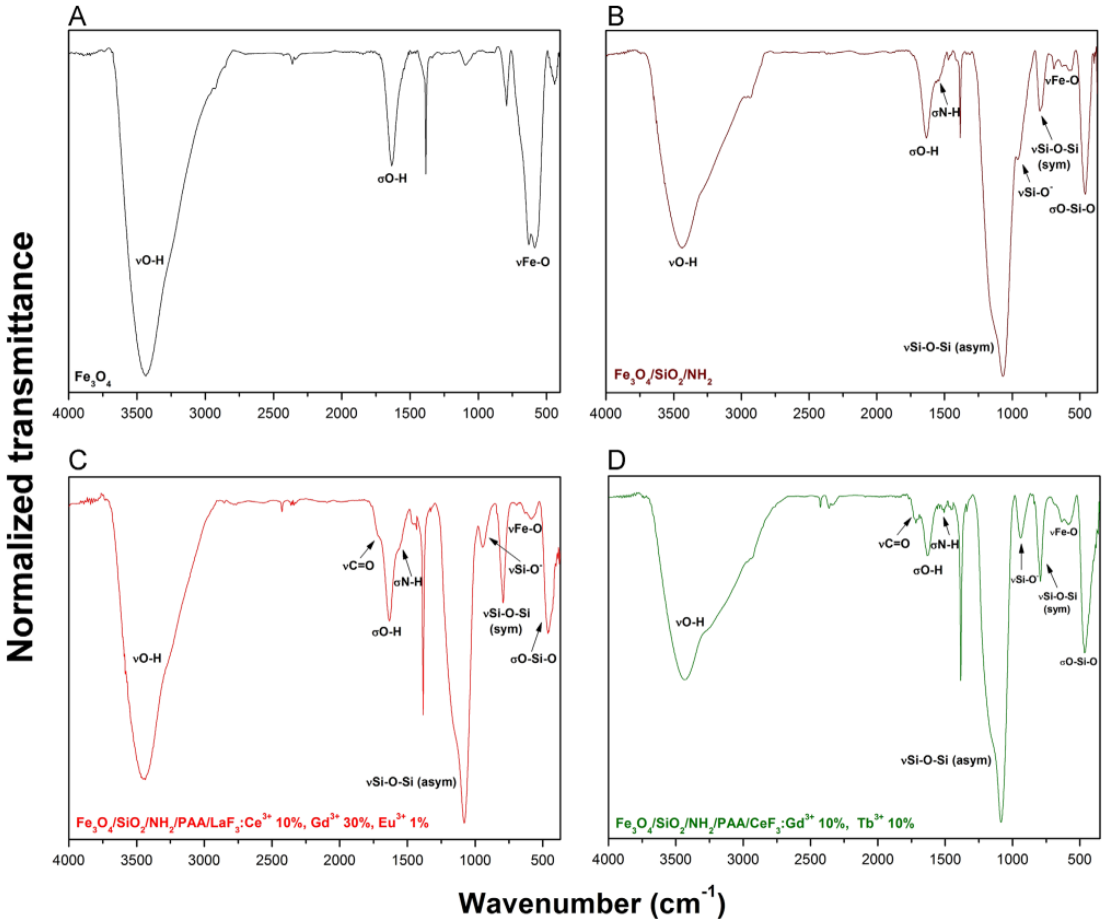

Fig. 4. FT-IR spectra of Fe_3O_4 (A), $Fe_3O_4/SiO_2/NH_2$ (B), $Fe_3O_4/SiO_2/NH_2/PAA/LaF_3$: 10% Ce^{3+}, 30% Gd^{3+}, 1% Eu^{3+} (C), $Fe_3O_4/SiO_2/NH_2/PAA/CeF_3$: 10% Gd^{3+}, 10% Tb^{3+} (D).

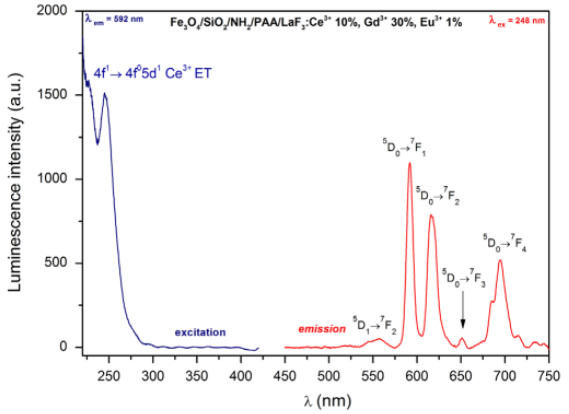

Fig. 5. Excitation (blue) and emission (red) spectra of $Fe_3O_4/SiO_2/NH_2/PAA/LaF_3$: 10% Ce^{3+}, 30% Gd^{3+}, 1% Eu^{3+} nanomaterial; λ_{ex}=248 nm, λ_{em}=592 nm.

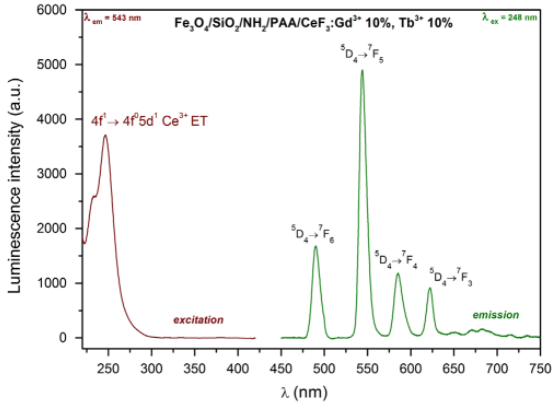

Fig. 6. Excitation (brown) and emission (green) spectra of $Fe_3O_4/SiO_2/NH_2/PAA/CeF_3$: 10% Gd^{3+}, 10% Tb^{3+} nanomaterial; λ_{ex}=248 nm, λ_{em}=543 nm.

between the lowest excited states of Ce^{3+} and Eu^{3+}/Tb^{3+} ions, enhancing the final luminescence intensity of the system [31,58]. The direct excitation of the Eu^{3+} or Tb^{3+} ions is ineffective, because of low values of absorption coefficients of the forbidden 4f–4f transitions in these ions. The composition of luminescent phases – lanthanide fluorides (concentration of dopant ions) was optimized as shown in our recent studies concerning the spectroscopic and structural characteristics of LnF_3 doped with Ce^{3+},

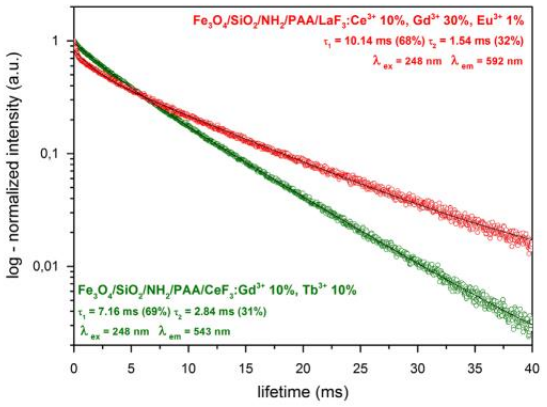

Fig. 7. Luminescence decay curves of $Fe_3O_4/SiO_2/NH_2/PAA/CeF_3$: 10% Gd^{3+}, 10% Tb^{3+} (green) and $Fe_3O_4/SiO_2/NH_2/PAA/LaF_3$: 10% Ce^{3+}, 30% Gd^{3+}, 1% Eu^{3+} (red) nanomaterials; λ_{ex}=248 nm, λ_{em}=592 nm (Eu^{3+}) and 543 nm (Tb^{3+}). (For interpretation of the references to color in this figure legend, the reader is referred to the web version of this article.)

Gd^{3+}, Eu^{3+} and Tb^{3+} ions (variously doped series of compounds) [6,21,58]. LaF_3: 10% Ce^{3+}, 30% Gd^{3+}, 1% Eu^{3+} and CeF_3: 10% Gd^{3+}, 10% Tb^{3+} revealed the most intense red/green emission, among other LnF_3 doped with Eu^{3+} or Tb^{3+} ions. That is why the systems were used as luminescent nanoshells, for preparation of the luminescent–magnetic core/shell type nanomaterials.

Luminescence properties of the nanomaterials obtained are shown in Figs. 5–8. The excitation/emission spectra and luminescence decay curves were recorded at 293 K, in ambient conditions. In the case of the emission spectra, both products were excited at λ_{ex}=248 nm (Ce^{3+} ET), whereas, the excitation spectra were measured at λ_{em}=592 and 543 nm (centers of the most intense bands in the corresponding emission spectra), for Eu^{3+} and Tb^{3+} doped samples, respectively. Fig. 5 presents the excitation and emission spectra of the $Fe_3O_4/SiO_2/NH_2/PAA/LaF_3$: 10% Ce^{3+}, 30% Gd^{3+}, 1% Eu^{3+} the nanomaterial, and Fig. 6 shows the spectra of the $Fe_3O_4/SiO_2/NH_2/PAA/CeF_3$: 10% Gd^{3+}, 10% Tb^{3+} nanomaterial.

In the both excitation spectra (Figs. 5 and 6), the broad and intense band related to the $4f^1 \rightarrow 4f^05d^1$ transition of the Ce^{3+} ion dominates in the whole range of the given spectrum. The intrinsic 4f–4f transitions of Eu^{3+} and Tb^{3+} are hardly observed (≈ 300–400 nm), because of the much more intense ET transitions (≈ 200–300 nm) occurring in the nanophosphors prepared.

The emission spectrum of the Eu^{3+} doped product shown in Fig. 5 reveals five characteristic bands of Eu^{3+} ion, corresponding to the $^5D_1 \rightarrow {}^7F_2$, $^5D_0 \rightarrow {}^7F_1$, $^5D_0 \rightarrow {}^7F_2$, $^5D_0 \rightarrow {}^7F_3$, and $^5D_0 \rightarrow {}^7F_4$ transitions. The presence of these bands results in a bright red luminescence of the nanomaterial obtained. The hypersensitive $^5D_0 \rightarrow {}^7F_2$ electric dipole transition exhibits lower intensity in comparison to the $^5D_0 \rightarrow {}^7F_1$ magnetic dipole transition. This confirms the successful substitution of the host ions (La^{3+}) by the Eu^{3+} ions, which are embedded in a highly symmetric (high site symmetry) crystal lattice of hexagonal LaF_3. It is worth noting, that the $^5D_0 \rightarrow {}^7F_2$ transition is very sensitive to the changes of local site symmetry (coordination environment) of Eu^{3+} ion, whereas the $^5D_0 \rightarrow {}^7F_1$ transition is insensitive to the changes of its local site symmetry. The intensity of the forbidden $^5D_0 \rightarrow {}^7F_2$ transition increases together with decreasing local site symmetry of the Eu^{3+} ion [59].

The emission spectrum of the Tb^{3+} doped product presented in Fig. 6 exhibits four characteristic bands of the Tb^{3+} ion, corresponding to the $^5D_4 \rightarrow {}^7F_6$, $^5D_4 \rightarrow {}^7F_5$, $^5D_4 \rightarrow {}^7F_4$ and $^5D_4 \rightarrow {}^7F_3$ magnetic dipole transitions. The presence of these bands results in a bright green luminescence of the product synthesized. Such magnetic dipole transitions are generally not sensitive to the changes of a local site symmetry of the Tb^{3+} ion [21].

Fig. 7 shows the recorded luminescence decay curves of the nanomaterials synthesized. On the basis of the measured decay profiles, the luminescence lifetimes were calculated. Both decay curves were fitted to the mathematic function:

$$y = A_1 * \exp(-x/\tau_1) + A_2 * \exp(-x/\tau_2) \quad (1)$$

representing a biexponential decay ($R > 0.999$). The obtained values of the emission lifetimes are following: τ_1=10.14 ms, τ_2=1.54 ms (Eu^{3+}) and τ_1=7.16 ms, τ_2=2.84 ms (Tb^{3+}). The values calculated are relatively long, which is characteristic of the Eu^{3+} and Tb^{3+} ions incorporated into a crystal structure of highly

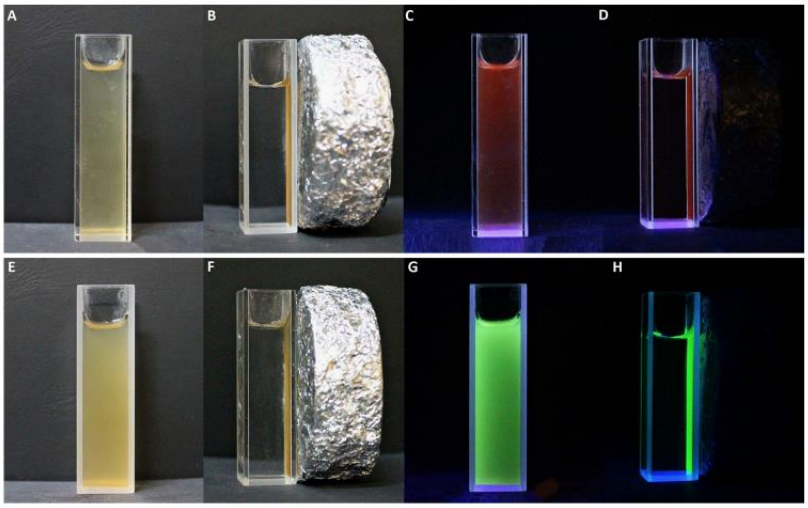

Fig. 8. Photographs of $Fe_3O_4/SiO_2/NH_2/PAA/LaF_3$: 10% Ce^{3+}, 30% Gd^{3+}, 1% Eu^{3+} (A–D) and $Fe_3O_4/SiO_2/NH_2/PAA/CeF_3$: 10% Gd^{3+}, 10% Tb^{3+} (E–H), taken before (A, C, E, and G) and after (B, D, F, and H) magnet capture, in a day-light (A, B, E, and F) and under UV light (λ_{ex}=254 nm) irradiation (C, D, G, and H). (For interpretation of the references to color in this figure, the reader is referred to the web version of this article.)

symmetrical lanthanide fluorides [21, 58]. The bulk hexagonal LnF_3 has one type of a site symmetry which can be occupied by the Eu^{3+} or Tb^{3+} ions. However, the presence of biexponential decay indicates the existence of two different coordination environments for the emitting Ln^{3+} ions. This is because of differences in emission intensities and decay lifetimes of the inner ions (inside nanocrystals) in comparison to the surface/near surface ions. Due to the small size of lanthanide nanoparticles, resulting in their high surface-to-volume ratio, the contribution of the surface ions can be detected [58,60]. The second lifetime component (τ_2) related to the surface ions, reveals the shorter decay time, because the surface and near surface Eu^{3+} or Tb^{3+} ions are surrounded by water molecules, surface impurities and defects which effectively quench their luminescence.

The photographs of the colloidal luminescent–magnetic nanomaterials dispersed in water (1 mg/mL), confirm their multifunctionality (Fig. 8). They were taken in a day-light (left) and under UV light (right). The as-prepared aqueous colloids were stable over many hours. It is clearly seen that the products are magnetic, because all of the particles are attracted by a strong magnet ($Nd_2Fe_{14}B$), making the solution transparent. Moreover, only the solid material is attracted to the cuvette wall, and brightly illuminate under a UV light irradiation, with the characteristic of Eu^{3+} red and Tb^{3+} green color, respectively. This confirms the absence of free Ln^{3+} ions in the solution, and a strong interaction/attachment of the luminescent and magnetic components in a single core/shell nanomaterial.

4. Conclusions

The multifunctional core/shell type nanomaterials $Fe_3O_4/SiO_2/NH_2$/PAA/LaF_3: 10% Ce^{3+}, 30% Gd^{3+}, 1% Eu^{3+} and $Fe_3O_4/SiO_2/NH_2$/PAA/CeF_3: 10% Gd^{3+}, 10% Tb^{3+} were obtained via facile syntheses in solution, followed by a surface modification and further decoration with luminescent nanoparticles. The products synthesized were composed of magnetic cores coated with amine modified silica, linked with polycarboxylic acid (PAA) and external fluoride nanoparticles, doped with luminescent lanthanide ions. The nanomaterials obtained exhibited simultaneously luminescent and magnetic properties. Under UV light ($\lambda_{ex} \approx 250$ nm) the products doped with the Eu^{3+} and Tb^{3+} ions revealed a bright red or green emission, respectively. Powder XRD, TEM, FT-IR spectroscopy and spectrofluorometry techniques were used to determine structural, morphological and spectroscopic properties of the products obtained. The prepared nanomaterials can potentially be applied as multimodal tracers, bifunctional luminescent–magnetic contrast agents, drug carriers, components of novel optomagnetic security/protection systems, etc.

Acknowledgments

M.R. gratefully acknowledges the financial support from Polish Ministry of Science and Higher Education-scientific work was financed from the budget for science in 2012–2015 as a research project within the program called “Diamond Grant” Nr DI2011 011441. M.R. is a recipient of the scholarship from the Foundation of Adam Mickiewicz University in Poznań, for the 2014/2015 academic year.

Appendix A. Supplementary material

Supplementary data associated with this article can be found in the online version at http://dx.doi.org/10.1016/j.jlumin.2015.05.037.

References

[1] M. Liong, J. Lu, M. Kovochich, T. Xia, S.G. Ruehm, A.E. Nel, F. Tamanoi, J.I. Zink, ACS Nano 2 (2008) 889.
[2] S.T. Selvan, T.T.Y. Tan, D.K. Yi, N.R. Jana, Langmuir 26 (2009) 11631.
[3] W. Di, X. Ren, H. Zhao, N. Shirahata, Y. Sakka, W. Qin, Biomaterials 32 (2011) 7226.
[4] N.O. Nuñez, S. Rivera, D. Alcantara, J.M. de la Fuente, J. García-Sevillano, M. Ocaña, Dalton Trans. 42 (2013) 10725.
[5] A.B. Deshmukh, R.R. Devarapalli, M.V. Shelke, J. Nanopart. Res. 16 (2014) 2372.
[6] M. Runowski, A. Ekner-Grzyb, L. Mrówczyńska, S. Balabhadra, T. Grzyb, J. Paczesny, A. Zep, S. Lis, Langmuir 30 (2014) 9533.
[7] X. Tian, Z. Dong, J. Hou, R. Wang, J. Ma, J. Lumin. 145 (2014) 459.
[8] M. Runowski, T. Grzyb, A. Zep, P. Krzyczkowska, E. Gorecka, M. Giersig, S. Lis, RSC Adv. 4 (2014) 46305.
[9] M. Runowski, T. Grzyb, S. Lis, J. Nanopart. Res. 14 (2012) 1188.
[10] S. Dutta Choudhury, R. Badugu, K. Ray, J.R. Lakowicz, Chem. Commun. 50 (2014) 9010.
[11] Z. Yang, S. Kang, R. Zhou, Nanoscale 6 (2014) 663.
[12] C.-F. Chan, M.-K. Tsang, H. Li, R. Lan, F.L. Chadbourne, W.-L. Chan, G.-L. Law, S. L. Cobb, J. Hao, W.-T. Wong, K.-L. Wong, J. Mater. Chem. B 2 (2014) 84.
[13] Y. Liang, Y. Li, H. Wang, J. Zhou, J. Wang, T. Regier, H. Dai, Nature Mater. 10 (2011) 780.
[14] L.U. Khan, H.F. Brito, J. Hölsä, K.R. Pirota, D. Muraca, M.C.F.C. Felinto, E.E. S. Teotonio, O.L. Malta, Inorg. Chem. 53 (2014) 12902.
[15] T. Grzyb, M. Runowski, K. Dąbrowska, M. Giersig, S. Lis, J. Nanopart. Res. 15 (2013) 1958.
[16] X. Zhang, H. Niu, W. Li, Y. Shi, Y. Cai, Chem. Commun. 47 (2011) 4454.
[17] J.P. Cheng, R. Ma, M. Li, J.S. Wu, F. Liu, X.B. Zhang, Chem. Eng. J. 210 (2012) 80.
[18] S.H. Joo, J.Y. Park, C.-K. Tsung, Y. Yamada, P. Yang, G.A. Somorjai, Nature Mater. 8 (2009) 126.
[19] J.-N. Park, P. Zhang, Y.-S. Hu, E.W. McFarland, Nanotechnology 21 (2010) 225708.
[20] M. Runowski, T. Grzyb, S. Lis, J. Rare Earths 29 (2011) 1117.
[21] T. Grzyb, M. Runowski, A. Szczeszak, S. Lis, J. Phys. Chem. C 116 (2012) 17188.
[22] S. Lis, J. Alloy. Comp. 341 (2002) 45.
[23] A. Dobrowolska, E.C. Karsu, A.J.J. Bos, P. Dorenbos, J. Lumin. 160 (2015) 321.
[24] K. Binnemans, Chem. Rev. 109 (2009) 4283.
[25] L.D. Carlos, R.A.S. Ferreira, V. de, Z. Bermudez, S.J.L. Ribeiro, Adv. Mater. 21 (2009) 509.
[26] G.S. Ofelt, J. Chem. Phys. 37 (1962) 511.
[27] P.A. Tanner, Chem. Soc. Rev. 42 (2013) 5090.
[28] A. D'Aléo, F. Pointillart, L. Ouahab, C. Andraud, O. Maury, Coord. Chem. Rev. 256 (2012) 1604.
[29] G. Blasse, Phys. Status Solidi A 73 (1982) 205.
[30] P. Dorenbos, J. Phys.: Condens. Matter 15 (2003) 8417.
[31] T. Grzyb, M. Runowski, S. Lis, J. Lumin. 154 (2014) 479.
[32] P. Qiu, N. Zhou, H. Chen, C. Zhang, G. Gao, D. Cui, Nanoscale 5 (2013) 11512.
[33] D.V. Sunitha, H. Nagabhushana, S.C. Sharma, B.M. Nagabhushana, R.P. S. Chakradhar, J. Alloy. Compd. 575 (2013) 434.
[34] D.T. Xueyuan Chen, Yongsheng Liu, Lanthanide-Doped Luminescent Nanomaterials, Springer, Berlin, 2014.
[35] M.L. Debasu, D. Ananias, I. Pastoriza-Santos, L.M. Liz-Marzán, J. Rocha, L. D. Carlos, Adv. Mater. 25 (2013) 4868.
[36] Z. Tang, N. a Kotov, M. Giersig, Science 297 (2002) 237.
[37] S. Hsu, Y.Y. Lin, S. Huang, K.W. Lem, D.H. Nguyen, D.S. Lee, Nanotechnology 24 (2013) 475102.
[38] C. Kirchner, T. Liedl, S. Kudera, T. Pellegrino, A. Muñoz Javier, H.E. Gaub, S. Stölzle, N. Fertig, W.J. Parak, Nano Lett. 5 (2005) 331.
[39] F. Gagné, D. Maysinger, C. André, C. Blaise, Nanotoxicology 2 (2008) 113.
[40] M. Runowski, S. Balabhadra, S. Lis, J. Rare Earths 32 (2014) 242.
[41] E. Antic-Fidancev, J. Hölsä, M. Lastusaari, A. Lupei, Phys. Rev. B 64 (2001) 195108.
[42] M. Runowski, K. Dąbrowska, T. Grzyb, P. Miernikiewicz, S. Lis, J. Nanopart. Res. 15 (2013) 2068.
[43] A. Szczeszak, T. Grzyb, B. Barszcz, V. Nagirnyi, A. Kotlov, S. Lis, Inorg. Chem. 52 (2013) 4934.
[44] R. Calderón-Villajos, C. Zaldo, C. Cascales, Nanotechnology 23 (2012) 505205.
[45] R.S. Yadav, V.K. Shukla, P. Mishra, S.K. Pandey, K. Kumar, V. Baranwal, M. Kumar, A.C. Pandey, J. Alloy. Compd. 547 (2013) 1.
[46] D. Zhang, C. Chen, F. Wang, D.M. Zhang, Appl. Phys. B 98 (2009) 791.
[47] P. Kulpinski, M. Namyslak, T. Grzyb, S. Lis, Cellulose 19 (2012) 1271.
[48] E. Hemmer, N. Venkatachalam, H. Hyodo, A. Hattori, Y. Ebina, H. Kishimoto, K. Soga, Nanoscale 5 (2013) 11339.
[49] A. Kar, A. Patra, Nanoscale 4 (2012) 3608.
[50] Q. Ma, J. Wang, X. Dong, W. Yu, G. Liu, J. Nanopart. Res. 16 (2014) 2239.
[51] C. Wang, D. Yin, J. Ouyang, K. Song, B. Liu, M. Wu, J. Nanosci. Nanotechnol. 14 (2014) 5232.
[52] Y. Ma, H. Li, L. Wang, J. Mater. Chem. 22 (2012) 18761.
[53] P. Yang, Z. Quan, Z. Hou, C. Li, X. Kang, Z. Cheng, J. Lin, Biomaterials 30 (2009) 4786.
[54] S.X.C. Mi, J. Zhang, H. Gao, X. Wu, M. Wang, Y. Wu, Y. Di, Z. Xu, C. Mao, Nanoscale 2 (2010) 1141.
[55] J. Drbohlavova, R. Hrdy, V. Adam, R. Kizek, O. Schneeweiss, J. Hubalek, Sensors 9 (2009) 2352.
[56] R. Massart, IEEE Trans. Magn. 17 (1981) 1247.
[57] W. Stöber, J. Colloid Interface Sci. 26 (1968) 62.
[58] M. Runowski, S. Lis, J. Alloy. Compd. 597 (2014) 63.
[59] B.R. Judd, J. Chem. Phys. 44 (1966) 839.
[60] K. Ostrikov, E.C. Neyts, M. Meyyappan, Adv. Phys. 62 (2013) 113.

Supplementary material for:

Synthesis, surface modification/decoration of luminescent-magnetic core/shell nanomaterials, based on the lanthanide doped fluorides (Fe_3O_4 /SiO_2/NH_2/PAA/LnF_3)

*Marcin Runowski, Stefan Lis**

Adam Mickiewicz University, Faculty of Chemistry, Department of Rare Earths, Umultowska 89b, 61-614 Poznań, Poland

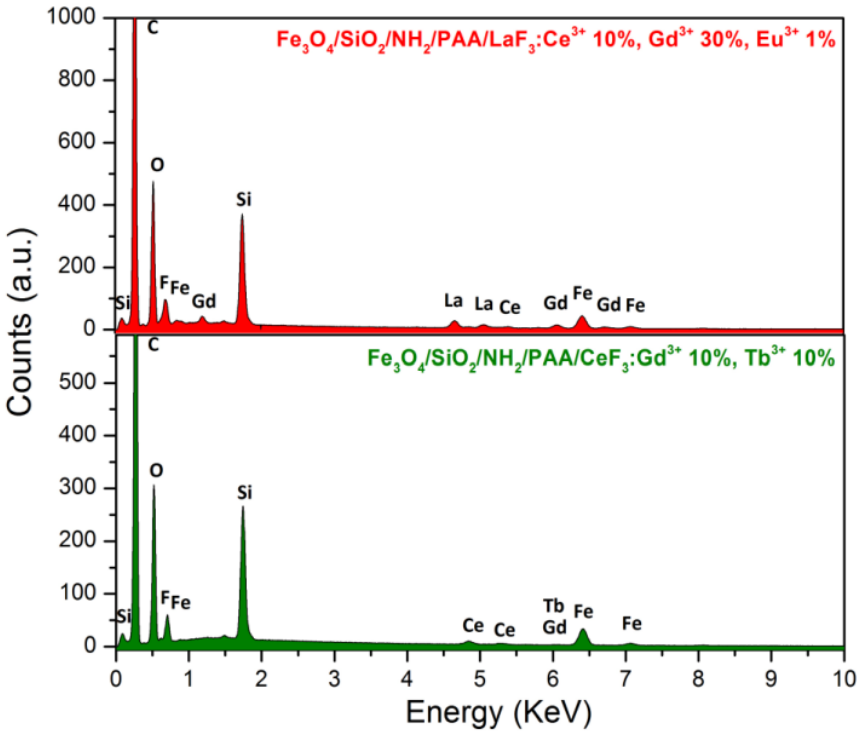

Fig. S1 EDX spectra of the synthesized Fe_3O_4 /SiO_2/NH_2/PAA/LnF_3 nanomaterials

Fig. S1 presents the recorded EDX spectra of the nanomaterials synthesized. The obtained elemental composition agrees with the expected one for the core/shell type products (presence of iron, silicon and lanthanides). However, in the case of the Tb^{3+} doped nanomaterial, the content of lanthanides is relatively smaller in comparison to the Eu^{3+} doped product (smaller amount of surface LnF_3 nanoparticles), which corresponds well to the XRD data.

The Table below presents the errors on the fitted parameters of the luminescence decay curves, corresponding to Fig. 7 in the manuscript.

Table S1 Fitting parameters: τ_1, τ_2, A_1, A_2, and the corresponding standard error values determined on the basis of the luminescence decay curves for the $Fe_3O_4/SiO_2/NH_2/PAA/LnF_3$ nanomaterials.

Compound name	τ_1 [ms]	standard error	A_1	standard error	τ_2 [ms]	standard error	A_2	standard error
$Fe_3O_4/SiO_2/NH_2/PAA/LaF_3$: 10% Ce^{3+}, 30% Gd^{3+}, 1% Eu^{3+}	**10,14217**	**0,04091**	**0,56279**	**0,0023**	**1,54007**	**0,03424**	**0,26509**	**0,00316**
$Fe_3O_4/SiO_2/NH_2/PAA/CeF_3$: 10% Gd^{3+}, 10% Tb^{3+}	**7,15511**	**0,02031**	**0,6668**	**0,00482**	**2,83922**	**0,03586**	**0,29828**	**0,00448**

τ_1 – decay constant 1 (first lifetime component)

τ_2 – decay constant 2 (second lifetime component)

A_1 – amplitude 1

A_2 – amplitude 2

Problemem badawczym jaki podjąłem w pracy pt. „*Synthesis, photophysical analysis, and in vitro cytotoxicity assessment of the multifunctional (magnetic and luminescent) core@shell nanomaterial based on lanthanide-doped orthovanadates*" było otrzymanie nowych biokompatybilnych nanomateriałów luminescencyjno-magnetycznych typu rdzeń/powłoka (core/shell), wykazujących jednocześnie intensywną luminescencję pod wpływem promieniowania UV oraz odpowiedź na przyłożone pole magnetyczne. Do tego celu wykorzystano nanocząstki oparte o domieszkowane jonami Eu^{3+} wanadany gadolinu wykazujące intensywną czerwoną luminescencję, które następnie zostały z powodzeniem przyłączone do powierzchni magnetycznych nanostruktur typu rdzeń/powłoka (core/shell). Wspomnianymi nanocząstkami magnetycznymi były ferryty żelaza, tj. Fe_3O_4 (magnetyt). Cząstki te następnie pokryto sfunkcjonalizowaną grupami karboksylowymi powłoka krzemionkową, przy użyciu TEOS-u i odpowiedniej pochodnej silanowej EDTA. Syntezę prowadzono w odwróconej mikroemulsji. W wyniku przeprowadzonej syntezy otrzymano sferyczne nanostruktury typu core/shell, mające na powierzchni kowalencyjnie związane grupy karboksylowe. Po wprowadzeniu odpowiednich jonów Ln^{3+} do roztworu koloidalnego otrzymanych nanostruktur, wytrącono bezpośrednio na ich powierzchni nanocząstki luminescencyjne. Było to możliwe dzięki uprzedniej modyfikacji powierzchni grupami karboksylowymi, kompleksującymi jony Ln^{3+}. Metodami XRD i FT-IR potwierdzono obecność pożądanej fazy magnetycznej (Fe_3O_4), krzemionki i struktur wanadanowych w strukturze otrzymanego nanomateriału. Morfologia cząstek została zobrazowana za pomocą zdjęć TEM pokazujących utworzenie się powłoki krzemionkowej na cząstkach magnetycznych oraz przyłączenie się nanokrystalicznych wanadanów lantanowców do powierzchni krzemionki. Powstałe nanomateriały wykazywały właściwości luminescencyjno-magnetyczne, czyli jednocześnie intensywną czerwoną emisję po naświetleniu światłem UV (254 nm) oraz odpowiedź na przyłożone pole magnetyczne. Właściwości te były obserwowane zarówno w ciele stałym jak i w roztworze (po przyłożeniu silnego magnesu stałego do roztworu koloidalnego nanocząstek, następowała migracja całej luminescencyjno-magnetycznej fazy rozproszonej). Otrzymane nanostruktury inkubowano *in-vitro* z komórkami erytrocytów ludzkich, w celu analizy ich właściwości biologicznych. Wykazano brak cytotoksyczności otrzymanych nanostruktur oraz ich biokompatybilność, co jest kluczowe w zastosowaniach biologicznych takich nanomateriałów.

Wkład własny w powstanie pracy: koncepcja badań, wykonanie syntezy i zbadanie części właściwości fizykochemicznych otrzymanych produktów. Analiza uzyskanych wyników.

J Nanopart Res (2015) 17:143
DOI 10.1007/s11051-015-2950-4

RESEARCH PAPER

Synthesis, photophysical analysis, and in vitro cytotoxicity assessment of the multifunctional (magnetic and luminescent) core@shell nanomaterial based on lanthanide-doped orthovanadates

Agata Szczeszak · Anna Ekner-Grzyb · Marcin Runowski · Lucyna Mrówczyńska · Tomasz Grzyb · Stefan Lis

Received: 16 November 2014 / Accepted: 6 March 2015 / Published online: 17 March 2015

Abstract Rare earths orthovanadates ($REVO_4$) doped with luminescent lanthanide ions (Ln^{3+}) play an important role as promising light-emitting materials. Gadolinium orthovanadate exhibits strong absorption of ultraviolet radiation and as a matrix doped with Eu^{3+} ions is well known for its efficient and intense red emission, induced by energy transfer from the VO_4^{3-} groups to Eu^{3+} ions. In the presented study, Fe_3O_4@SiO_2@$GdVO_4$:Eu^{3+} 5 % nanomaterial was investigated. The core@shell structures demonstrate attractive properties, such as higher thermal stability, enhanced water solubility, increased optical response, higher luminescence, longer decay times, and magnetic properties. Silica coating may protect nanocrystals from the surrounding environment. Therefore, such silica-covered nanoparticles (NPs) are successfully utilized in biomedical research. Multifunctional magnetic nanophosphors are very interesting due to their potential biomedical applications such as magnetic resonance imaging, hyperthermic treatment, and drug delivery. Therefore, the aim of our study was to investigate photophysical, chemical, and biological properties of multifunctional $REVO_4$ doped with Ln^{3+}. Moreover, the studied NPs did not affect erythrocyte sedimentation rate, cell membrane permeability, and morphology of human red blood cells.

Keywords Nanoparticles · Multifunctional nanostructures · Surface decoration · Erythrocytes · Hemolysis · Human red blood cells · Health effects

A. Szczeszak · M. Runowski · T. Grzyb · S. Lis (✉)
Department of Rare Earths, Faculty of Chemistry, Adam Mickiewicz University, Grunwaldzka 6, 60-780 Poznań, Poland
e-mail: blis@amu.edu.pl

A. Ekner-Grzyb
Department of Behavioural Ecology, Faculty of Biology, Adam Mickiewicz University, Umultowska 89, 61-614 Poznań, Poland

L. Mrówczyńska
Department of Cell Biology, Faculty of Biology, Adam Mickiewicz University, Umultowska 89, 61-614 Poznań, Poland

Introduction

The rapid development of functional nanomaterials has been observed over the last few years (Xue et al. 2011; Liu et al. 2011; Limaye et al. 2011; Yoo and Lee 2014). Nanomaterials are composed of particles having at least one dimension in the range of 1–100 nm (Henglein 1987). Due to the small size, such nanoparticles have large surface area-to-volume ratio and a possibility of the formation of stable aqueous colloids. What is more, they are smaller than living cells, which facilitates their interactions with the desired organic structures, investigated in vitro and in vivo (Selvan et al. 2009). This is the crucial feature of nanomaterials allowing their applications in

biology and medicine, e.g., drug carriers, contrast agents, or biomarkers.

Lanthanide (Ln^{3+})-doped compounds are well known as efficient phosphors (light emitters), applied in optoelectronics, forensics, documents protection, new light sources, solar cells, etc. (Dosev et al. 2008; Chander 2005). They exhibit bright multicolor luminescence, long radiative lifetimes (in the range of ms), large Stokes shifts, narrow emission bands, and tunable luminescence dependent on the coordination environment (Dosev et al. 2008; Chander 2005; Grzyb et al. 2014, 2012a). Because of the intensive and bright luminescence, Eu^{3+} and Tb^{3+} ions are commonly used as red and green light sources, respectively. The direct excitation of Ln^{3+} ions is usually inefficient, because of the forbidden character of the 4f-4f transitions, in these ions. That is why, the energy transfer (ET) and charge transfer (CT) phenomena are often used to increase the luminescence efficiency of such compounds (Grzyb et al. 2014, 2012b). Ce^{3+} and Gd^{3+} ions are well-known energy donors (light harvesting ions) in the case of UV-light excitation (energy down-conversion) (Grzyb et al. 2012a; Yang et al. 2011), and Yb^{3+} ions are used as energy donors during IR-light excitation (energy up-conversion) (Niu et al. 2011).

Gadolinium orthovanadate ($GdVO_4$) exhibits many advantages, e.g., high thermal conductivity, broad emission, and large absorption cross section. Moreover, Gd^{3+} ($4f^7$, ^8S)-based matrices have played an important role as phosphors due to relatively high energy of the lowest excited state in connection with stability of a half-filled of the ground state of gadolinium (Wu and Yan 2008). $GdVO_4$ shows strong absorption of ultraviolet (UV) radiation, and doping with Eu^{3+} ions enables the efficient and intense red emission, induced by ET from the VO_4^{3-} groups to Eu^{3+} ions (Li et al. 2011).

The luminescent nanomaterials based on the lanthanide-doped nanoparticles have large interest in the case of scientific, industrial, and biological applications. In comparison to the organic dyes and semiconducting quantum dots, they have all of the mentioned advantages characteristic of Ln^{3+} ions and also reveal photo- and thermo-stability, resistance to oxidation, and low cytotoxicity (Blasse and Grabmaier 1994; Binnemans 2009; Grzyb et al. 2013; Runowski et al. 2013).

Core@shell-type nanostructures are composed of at least two distinguished phases of the core and the shell. The nanosized core as well as nanoshell can be inert or active, i.e., exhibits selective affinity to the desired structures, luminescence, magnetism, catalytic activity, etc. (Grzyb et al. 2013; Haidar 2010; Chen et al. 2011; Runowski et al. 2012). What is more, the shell can be appropriately modified according to the expected requirements of such composite materials (Runowski et al. 2013; Lu et al. 2010; Hu et al. 2010). The external shell may also function as a protective barrier from the destructive impact of the environment, e.g., high temperature, oxidizing atmosphere, aggressive agents, and so on (Park et al. 2010). Currently, the fabrication of bifunctional and multifunctional nanomaterials attracts much interest of scientists because of the benefits resulting from their multimodal nature (Chen et al. 2011; Runowski et al. 2012; Lou et al. 2011; Kang et al. 2013b; Zhou et al. 2014; Deshmukh et al. 2014).

The nanomaterials exhibiting simultaneously luminescence and magnetism have been intensively studied over the last few years (Runowski et al. 2012; Lou et al. 2011; Gai et al. 2010; Wang et al. 2014; Tong et al. 2013; Ma et al. 2014). Such nanostructures can be used in luminescent tracing combined with magnetic separation, multimodal bioimaging (simultaneous luminescence and magnetic imaging), novel targeted treatment such as hyperthermia combined with photodynamic therapy, or highly specific drug delivery (Selvan et al. 2009; Lou et al. 2011; Gai et al. 2010; Corr et al. 2008). Except of the mentioned bioapplications, such multifunctional luminescent-magnetic nanomaterials can be applied in localized (thanks to the luminescence) magnetic enrichment of the diluted precious substances and organic structures (Hu et al. 2010). They can be also used as novel, hard to imitate protection materials, due to their magnetic properties and possible luminescence coding (unique combination of the spectral lines in the emission spectra) (Hölsä 2009; Cheng et al. 2008).

Core@shell-type nanoparticles seem to function perfectly as the mentioned luminescent-magnetic materials. The external shell can protect the magnetic core from a negative impact of the environment as well as increase the selectivity and affinity of such nanosystem. Moreover, if the shell of the given nanomaterial is decorated with luminescent nanoparticles, the final nanomaterial becomes multifunctional, which creates many new possibilities of its application in medical, biological, scientific, and industrial areas.

Despite the importance of vanadates doped with lanthanide ions, only a few studies concerned their

utilization in biology and medical science (Cheng et al. 2012; Shanta Singh et al. 2013; Wang et al. 2009), whereas some of the research showed that Ln:$GdVO_4$ nanoparticles (NPs) may have potential application in optical or MRI images (Huang et al. 2013; Nuñez et al. 2013; Kang et al. 2013a; Yin et al. 2012). In addition, combination of magnetic and luminescent properties of nanoparticles makes them particularly useful. Such multifunctional nanomaterials allow the simultaneous imaging using MRI techniques and phosphorescence (multimodal imaging) (Zhou et al. 2014). However, the first step toward utilization of chemical compounds in biological research is to determine their biocompatibility (Gnach et al. 2014). Therefore, one of the aims of our study was to investigate the cytotoxic effect of studied NPs on human cells. One of the most convenient systems for the study of cytotoxic properties of new chemical compounds are erythrocytes. To the best of our knowledge, there is no study on the influence of multifunctional, luminescent-magnetic nanocrystals doped with lanthanide ions on red blood cells.

Here we report the synthesis and characterization of the multifunctional core@shell-type nanomaterial exhibiting simultaneously luminescent and magnetic properties—Fe_3O_4@SiO_2@$GdVO_4$:Eu^{3+} 5 %. Our intention was to obtain an efficient, reproducible, and non-cytotoxic luminescent-magnetic nanomaterial based on the commonly used chemical compound, which can be used in various bioapplications as well as in science and industry. The desired product should also exhibit relatively long radiative lifetime (in the range of ms), in order to eliminate the potential background radiation, in the case of its bioapplications. Because of the potential bioapplications, we examined its biological properties, namely the in vitro cytotoxicity assays on human erythrocytes. Magnetite nanoparticles, Fe_3O_4, were used as nanocores because they can be synthesized in a simple and inexpensive way as nanocrystalline magnetic particles. There are many reports on their application as magnetic cores in core@shell-type nanostructures as well (Runowski et al. 2012; Lu et al. 2010; Hu et al. 2010; Park et al. 2010). The as-prepared magnetic cores were coated with silica shell by simple hydrolysis and subsequent co-condensation of silane derivatives. Silica shell provides cores separation from the environment, prevents their agglomeration, and simplifies the surface modification of the nanostructures synthesized (Runowski et al. 2013; Hu et al. 2010). The formed silica nanoshell facilitated subsequent surface decoration with $GdVO_4$:Eu^{3+} 5 % nanoparticles, exhibiting intensive red emission.

Materials and methods

Synthesis of Fe_3O_4

The magnetite nanoparticles were synthesized by a modified Massart method (Massart 1981). The water used in the whole experiment was purged with nitrogen, in order to remove dissolved oxygen. 0.3475 g of $FeSO_4$*7-H_2O was dissolved in 5 mL of water with the addition of 0.05 mL of 30 % HCl (to suppress oxidation of Fe^{2+} ions) and mixed with 0.675 g of $FeCl_3$*$6H_2O$, previously dissolved in 20 mL of water. The as-prepared solution of iron species was added dropwise (in 3 min) to the diluted solution of ammonia (100 mL of water and 10 mL of concentrated ammonia), which was magnetically stirred. After this, the black precipitate of magnetite nanoparticles (Fe_3O_4) appeared immediately. In order to improve the crystallinity of the product, the whole system was heated up to 353 K, for 30 min, with continuous magnetic stirring, under a protective layer of gasoline. Afterward, the obtained product was extracted with 20 mL of 1 % oleic acid in cyclohexane solution (0.2 mL of oleic acid dissolved in 20 mL of cyclohexane).

Synthesis of Fe_3O_4@SiO_2

In order to get non-agglomerated and monodispersive core@shell nanoparticles, a reverse microemulsion method was used to prepare Fe_3O_4@SiO_2 core@shell NPs (Ding et al. 2012). 2 g of Igepal CO-520 (nonionic surfactant) was dispersed in 40 mL of cyclohexane and sonicated for 10 min. Then 3.2 mL of Fe_3O_4 nanoparticles from cyclohexane solution (40 mg, 12.5 mg/mL) was added to the above solution. Subsequently, 0.4 mL of ammonium hydroxide (25 %) was added to the above mixture and sonicated for 15 min to get clear and homogeneous solution. Finally, 0.1 mL of TEOS (tetraethoxysilane) was added. After 1 h 0.1 mL of TEOS and 0.1 mL of 45 % aqueous solution of EDATAS (N-(trimethoxysilylpropyl)ethylenediamine triacetic acid, trisodium salt—silane derivative of EDTA) were added. The role of EDATAS was to facilitate the homogeneous silica decoration with

luminescent nanoparticles, by the chelating properties of EDTA molecules toward Ln^{3+} ions (precipitation of lanthanide nanoparticles on the silica surface). The whole reaction lasted 24 h using magnetic stirrer. The resulting Fe_3O_4@SiO_2 core@shell NPs were collected by precipitation with acetone and ethanol. Afterward, the product was magnetically purified by washing several times with ethanol and water. The final product was redispersed in ethanol, forming ultra-stable colloidal solution.

Synthesis of Fe_3O_4/SiO_2@$GdVO_4$:Eu^{3+} 5 %

The synthesis was performed to get 2.2 mg of the final product, composed of 2 mg magnetic core (Fe_3O_4@-SiO_2) and 0.2 mg of the luminescent shell ($GdVO_4$:Eu^{3+} 5 %). The aqueous solutions of $Gd(NO_3)_3$ (55 µL 0.0127 M) and $Eu(NO_3)_3$ (32 µL 0.00114 M) were mixed together and vigorously stirred at ambient conditions. Afterward, 0.53 mL of the colloidal Fe_3O_4/SiO_2 (C = 3.8 mg/mL − 2 mg) was added to the previous solution. The as-prepared colloid was intensively shaken and stirred. When the colloidal solution became homogeneous, 1 mL of NH_4VO_3 aqueous solution (C = 0.086 mg/mL − stoichiometric amount) was slowly added, drop by drop. When the synthesis was completed (even before purification of the product), the formed composite nanomaterial exhibited an intensive red luminescence and a response for the applied magnetic field (NdFeB magnet). Here it is worth noting that after magnet capture, the solution was fully transparent and did not illuminate under UV light (only the solid phase attracted by the magnet exhibited luminescence). After that, the whole product was thoroughly purified by the magnet capture and washing several times with ethanol and water.

Cytotoxicity assay and erythrocytes shape under the test compounds

Erythrocyte preparation

Fresh human erythrocyte suspensions were obtained from the blood bank. The erythrocytes were washed three times (3000 rpm, 10 min) in phosphate-buffered saline (PBS, pH 7.4) supplemented with 10 mM glucose. After washing, cells were suspended in the buffer at 1.65 × 10^9 cells/mL, stored at 277 K and used within 5 h.

Erythrocyte sedimentation under nanomaterials treatment

Erythrocytes (1.65 × 10^8 cells/mL) were incubated with nanoparticles in Eppendorf vials for 60 min, at 310 K, under gently mixing. Three different concentrations (1, 0.1, 0.01 mg/mL) of the nanoparticles were investigated. The cells incubated only in PBS (pH 7.4), and supplemented with 10 mM glucose, were taken as a control series. The erythrocyte sedimentation rate (ESR) was recorded by the use of a digital camera after 1 h. The morphologies of both treated and control erythrocytes were estimated using a light microscope. The erythrocyte shape was classified according to Bessis (Bessis et al. 1973). After observation, erythrocytes were fixed in 0.1 % glutaraldehyde for 1 h, at room temperature (RT). Each sample was repeated three times, and the experiments were repeated three times with erythrocytes from different donors.

Hemolysis assays

Erythrocytes (1.65 × 10^8 cells/mL, ~1.5 hematocrit) were incubated in PBS (pH 7.4) supplemented with 10 mM glucose and containing test compounds for 60 min at 310 K in a shaking water bath. Three different concentrations (1, 0.1, 0.01 mg/mL) for all of the nanoparticles were investigated. Erythrocytes incubated only in PBS were taken as the control. Following the incubation, the erythrocyte suspensions were centrifuged (3000 rpm, 10 min), and the degree of hemolysis was estimated by monitoring the hemoglobin in the supernatant as previously reported (Jasiewicz et al. 2014). The results were expressed as a percentage (%) of hemolysis. Hemolysis 0 % was taken as the absorbance of the supernatant of the erythrocyte suspensions in PBS only, while the total hemolysis (100 %) was determined when PBS was replaced by distilled water. Each sample was repeated three times and the experiments were repeated three times with erythrocytes from different donors.

Scanning electron microscope studies of erythrocytes shape alterations

Erythrocytes were fixed in 0.1 % glutaraldehyde for 1 h at room temperature. The fixed cells were washed by exchanging of the supernatant with PBS. The

samples were gently vortexed and the cells were fixed with 2 % glutaraldehyde for another hour. After washing as above, the cells were post-fixed with 1 % OsO_4 for 30 min at RT. The supernatant was exchanged with PBS, and samples were gently vortexed. Fixed cells were dehydrated in a series of ethanol solutions (50, 60, 70, 80, 90, 95, and 100 %), gold sputtered, and examined using an *EVO 40* (ZEISS, Germany) scanning electron microscope.

Characterization

X-ray diffraction pattern (XRD) was recorded using a Bruker AXS D8 Advance diffractometer in the Bragg–Brentano geometry, with $CuK_{\alpha 1}$ radiation (1.5406 Å) in the 2θ ranges from 6 to 60°. The XRD pattern was assigned to the Joint Committee on Powder Diffraction Standards (JCPDS) database. The transmission electron microscopy (TEM) images were recorded at FEI Tecnai G2 20 X-TWIN transmission electron microscope, by an accelerating voltage of 200 kV. The SEM images were done using *EVO 40* (ZEISS, Germany) scanning electron microscope. The IR absorption spectrum was recorded between 400 and 4000 cm^{-1} on the FT-IR spectrophotometer, JASCO 4200. The material was mixed with KBr and then pressed to disks. Luminescence properties of the synthesized samples were collected for the aqueous colloidal solution with concentration of 1 mg of the core@shell per 1 mL of colloid at a Hitachi F-7000 Fluorescence Spectrophotometer at RT (300 and 77 K) with the 150 W xenon lamp as the excitation source. Excitation and emission spectra were corrected for the instrumental response.

Results and disscussion

The multifunctional core@shell-type nanostructure of Fe_3O_4@SiO_2@$GdVO_4$:Eu^{3+} 5 % was synthesized using in sequence modified Massart method, reverse microemulsion method, and precipitation reaction (Fig. 1). For the synthesis of core@shell nanostructures and their surface modification, we used the modified methods reported in our previous papers (Runowski et al. 2011, 2014). Its structure and morphology was determined using XRD pattern, TEM images, and IR spectra.

In Fig. 2, the XRD pattern of the obtained nanomaterial is presented. It is well seen that all the diffraction peaks are well consistent with the diffraction lines of the reference patterns of the cubic *Fd-3 m* Fe_3O_4 and tetragonal $I4_1/amd$ $GdVO_4$. The presence of SiO_2 is not visible due to its amorphous character. All of the reflexes are broadened, which is related to the small size of crystallites. Additional reflexes are not visible, which confirmed lack of contamination in the nanomaterial obtained.

In Fig. 3, the FT-IR spectra of the Fe_3O_4, Fe_3O_4@SiO_2 and Fe_3O_4@SiO_2@$GdVO_4$:Eu^{3+} 5 % nanocrystals are presented. All the spectra show the most intense and broad band at 3444 cm^{-1} related to O–H stretching vibrations of hydrogen-bonded H_2O molecules (adsorbed on the nanoparticles surface). Additionally, at about 1633 cm^{-1}, the absorption peak associated also with water molecules was observed (deformation vibrations of the O–H groups). In the spectrum of Fe_3O_4, the peaks in the range of 2800–3000 cm^{-1} are related to νC-H vibration, and come from cyclohexane and oleic acid molecules (used during extraction) adsorbed on the nanoparticles surface (as other no described peaks at lower wavenumbers). The spectra of the Fe_3O_4@SiO_2 and Fe_3O_4@SiO_2@$GdVO_4$:Eu^{3+} 5 % nanostructures exhibit four peaks characteristic of silica: νSi–O–Si(asym) (1092 cm^{-1}), νSi–O$^-$(957 cm^{-1}), νSi–O–Si(sym) (799 cm^{-1}), and σSi–O–Si (464 cm^{-1}). The absorption bands denoted at 636 cm^{-1} as νFe–O and at 801 cm^{-1} as νVO_4^{3-} vibrations were recorded, which confirmed the presence of magnetic core and luminescent shell in the nanomaterials obtained. The performed FT-IR measurements proved the formation of the core@shell-type nanomaterials.

The size and morphology of the Fe_3O_4@SiO_2@$GdVO_4$:Eu^{3+} 5 % nanocrystals were analyzed by TEM. As shown in Fig. 4, the nanoparticles exhibit spherical shape, and the crystallites are rather agglomerated. An average core@shell nanoparticles size is about 40 nm. TEM images showed clearly formation of the core@shell-type structures, and the presence of vanadate nanoparticles decorated on the silica surface. What is more, there was no observed bare silica (core-free silica) during the product analysis.

The bifunctional magnetic-luminescent core@shell exhibited strong visible red emission under UV excitation due to doping of the Eu^{3+} ions. In Fig. 5 (left) there is an excitation spectrum monitored for the

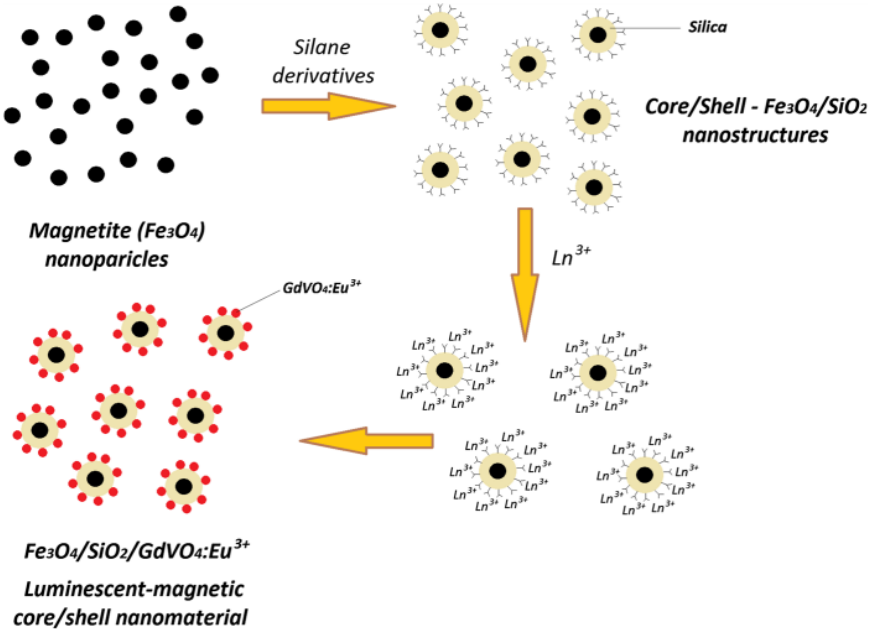

Fig. 1 Scheme of the synthesis of the Fe_3O_4@SiO_2@$GdVO_4$:Eu^{3+} 5 % nanostructures

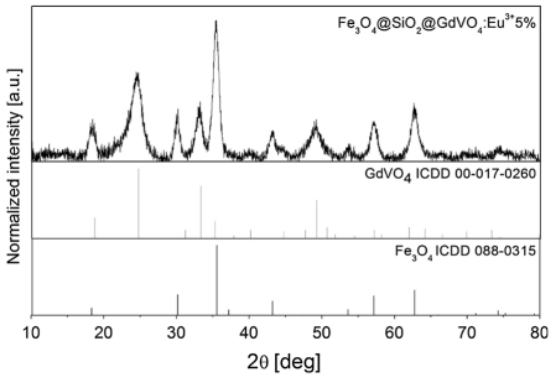

Fig. 2 XRD pattern of the synthesized Fe_3O_4 and Fe_3O_4@-SiO_2@$GdVO_4$:Eu^{3+} 5 % nanocrystals

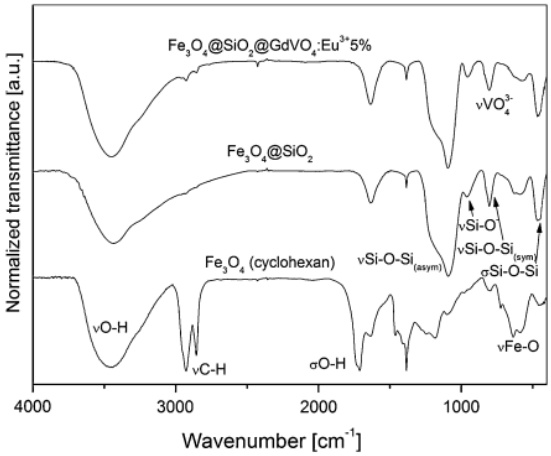

Fig. 3 IR spectra of the synthesized Fe_3O_4, Fe_3O_4@SiO_2 and Fe_3O_4@SiO_2@$GdVO_4$:Eu^{3+} 5 % nanomaterials

Eu^{3+} ions emission at 616 nm. The spectrum shows one intense and broad band peaking at $\lambda = 276$ nm, related to the CT bands $O^{2-} \rightarrow Eu^{3+}$. Figure 5 (right) presents the emission spectrum, which consists of five sharp bands, characteristic of the Eu^{3+} ions emission, connected with the transitions from the excited $^5D_0$ level to ^7F_J (J = 1–4) levels. A small band at $\lambda = 536$ nm assigned to $^5D_1 \rightarrow {}^7F_1$ is also visible. Moreover, red emission band at 616 nm is much more intense comparing to the orange emission band at 594 nm. The emission color is redder instead of orange-red emission and the chromaticity of the core@shell nanomaterial is improved. This is consistent with the Eu^{3+} ion site symmetry, D_{2d}, with no inversion center. Intensity of the emission lines related to f–f transitions is dependent on the local site symmetry of the Eu^{3+} ions. Based on the selection rules, the magnetic dipole transitions are allowed and the electric dipole transitions are forbidden. When the Eu^{3+} ions occupy site with lack of inversion

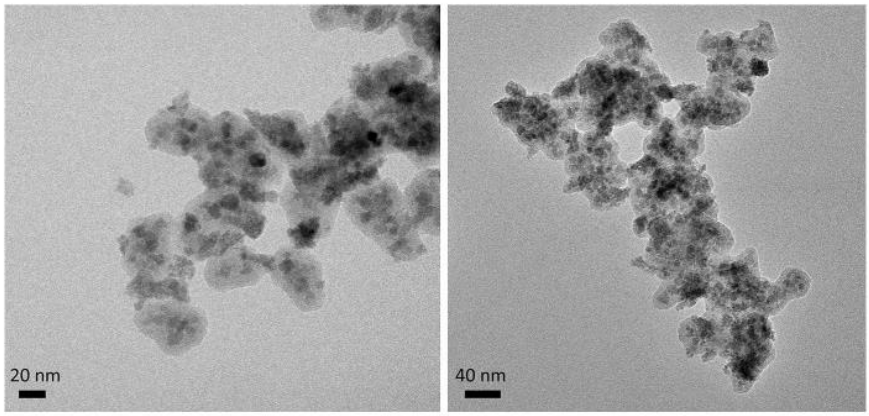

Fig. 4 TEM images of the synthesized $Fe_3O_4@SiO_2@GdVO_4:Eu^{3+}$ 5 % core@shell nanostructures

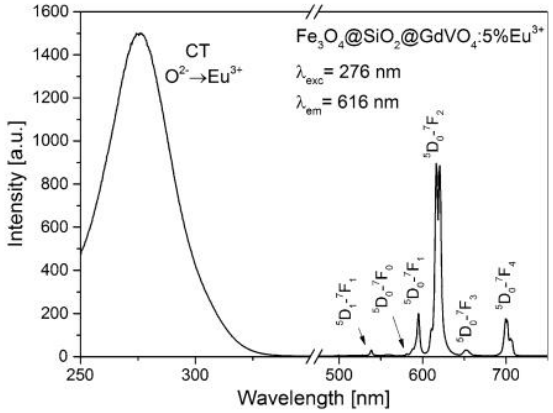

Fig. 5 Excitation (*left*) and emission (*right*) spectra of the $Fe_3O_4@SiO_2@GdVO_4:Eu^{3+}$ 5 % core@shell-type nanostructure

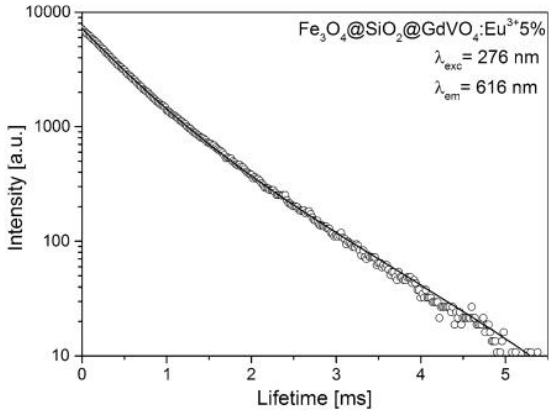

Fig. 6 Luminescence decay curves recorded for the $Fe_3O_4@SiO_2@GdVO_4:Eu^{3+}$ 5 % core@shell-type nanostructure

symmetry, the intensities ratio of the $^5D_0$–$^7F_2$ to $^5D_0$–$^7F_1$ transitions should be relatively high, as in the case of $Fe_3O_4@SiO_2@GdVO_4:Eu^{3+}$ 5 % core@-shell-type nanostructure.

The recorded emission decay curve can be well fitted by a biexponential function and luminescent lifetimes were calculated and are equal to $\tau_1 = 0{,}49$ and $\tau_2 = 1{,}05$ ms, respectively (Fig. 6). The shorter component is connected with the Eu^{3+} ions located at the surface of crystallites, where the external environment strongly influences on the luminescent lifetime and quench the excited states.

In Fig. 7, luminescent and magnetic properties of the $Fe_3O_4@SiO_2@GdVO_4:Eu^{3+}$ 5 % nanomaterial dispersed in water are presented. It is well seen that after magnet capture, all the nanoparticles were attracted to the magnet direction. Additionally, under UV light, the characteristic red luminescence of the Eu^{3+} ion was observed. The image showed confirms the formation of the bifunctional (magnetic–luminescent) $Fe_3O_4@SiO_2@GdVO_4:Eu^{3+}$ 5 % core@shell-type nanomaterial.

The $Fe_3O_4@SiO_2@GdVO_4:Eu^{3+}$ 5 % core@shell-type nanostructure did not influence the ESR (Fig. 8). Namely, the erythrocytes under nanoparticles treatment settled down with the same rate as the control cells.

The studied nanoparticles did not increase the erythrocyte membrane permeability and did not induce hemolysis up to concentration 1 mg/mL (results not shown). Moreover, nanoparticles treatment did not affect the discoid shape of erythrocytes

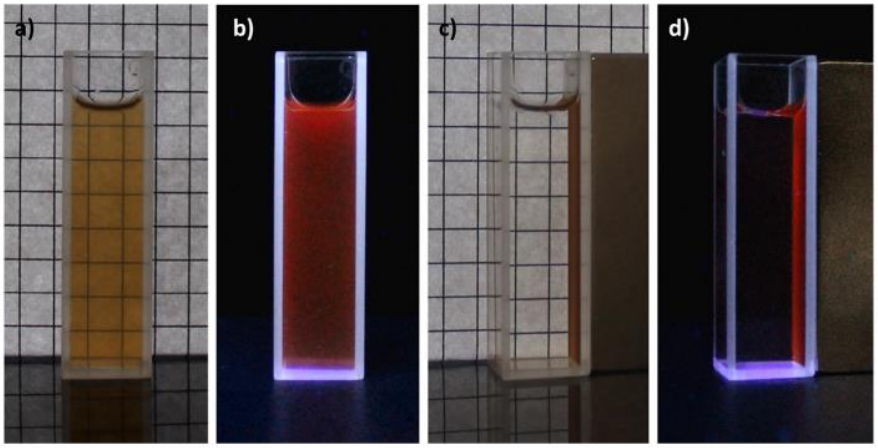

Fig. 7 Luminescent and magnetic properties of bifunctional Fe_3O_4@SiO_2@$GdVO_4$:Eu^{3+} 5 % core@shell-type nanostructure, before (**a**, **b**) and after (**c**, **d**) magnet capture. Presented sample was excited by UV lamp ($\lambda = 254$ nm)

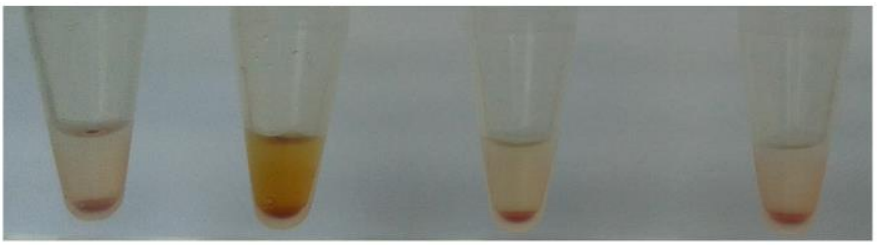

Fig. 8 The effect of the nanoparticles on the erythrocyte sedimentation rate. Nanoparticles concentration from the left: 0 mg/mL (control), 1, 0.1, 0.01 mg/mL

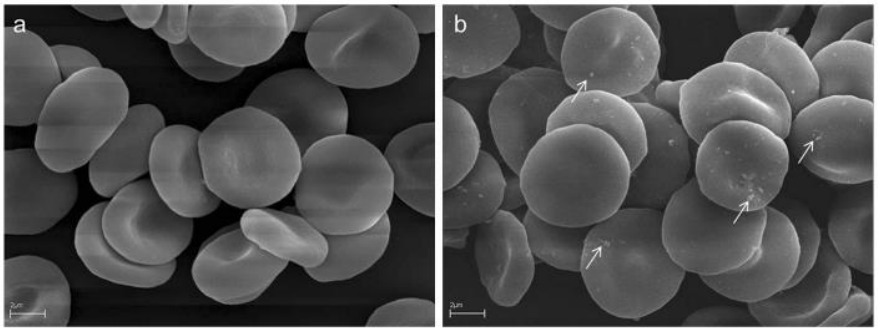

Fig. 9 The effect of Fe_3O_4@SiO_2@$GdVO_4$:Eu^{3+} 5 % core@-shell-type nanostructures, at the concentration 1 mg/mL on human erythrocytes morphology as observed by scanning electron microscope: **a** control cells, **b** cells incubated with core@shell nanostructures

(Fig. 9) although binding of nanoparticles to the erythrocyte membrane was detected (Fig. 9b). The white arrows indicate the core@shell-type nanostructures attached to the surface of erythrocytes.

Summing up, the studied nanostructures did not affect the ESR, neither morphology of red blood cells nor their membrane permeability. Therefore, we assume that the synthesized multifunctional nanomaterial

based on the doped rare earth orthovanadates is not toxic against human erythrocytes.

Conclusions

The luminescent-magnetic core@shell-type nanomaterial, Fe_3O_4@SiO_2@$GdVO_4$:Eu^{3+} 5 %, was successfully synthesized via a relatively simple and reproducible way. The obtained nanocomposite is composed of magnetic core, coated with a modified silica shell and surface decorated with red luminescent nanoparticles, having a long radiative lifetime. The nanocomposite synthesized has an average size about 40 nm and forms a stable aqueous colloid. When the magnetic field and UV light are applied the product reveals simultaneously bifunctional properties, namely intensive red luminescence and strong magnetism (the product follows by the applied magnet). What is more, the obtained luminescent-magnetic core@shell-type nanostructures do not exhibit toxicity against human erythrocytes, examined in vitro. All of the mentioned advantages of the nanomaterial synthesized allow its potential application in multimodal imaging, bio-labeling, drug delivery, targeted therapies, tracing techniques, forensics, and in other advanced applications.

Acknowledgments S.L., A. Sz., A.E.G, and T.G. kindly acknowledge the financial support from the National Science Centre (Grant DEC-2012/06/M/ST5/00325). M.R. gratefully acknowledges the financial support from the Polish Ministry of Science and Higher Education; scientific work was financed from the budget for science in 2012-2015 as a research project within the program called „Diamond Grant" Nr DI2011 011441. M.R. is a recipient of the scholarship from the Foundation of Adam Mickiewicz University in Poznań, for the 2014/2015 academic year. T.G. holds a scholarship from the Foundation for Polish Science for Young Scientists (FNP).

References

Bessis M, Weed RI, Leblond PF (1973) Red cell shape red cell shape; physiology, pathology, ultrastructure. Springer, Berlin, Heidelberg, pp 1–24. doi:10.1007/978-3-642-88062-9

Binnemans K (2009) Lanthanide-based luminescent hybrid materials. Chem Rev 109:4283–4374. doi:10.1021/cr8003983

Blasse G, Grabmaier BC (1994) Luminescent materials. Springer, Berlin

Chander H (2005) Development of nanophosphors—a review. Mater Sci Eng R Rep 49:113–155. doi:10.1016/j.mser.2005.06.001

Chen G, Desinan S, Nechache R, Rosei R, Rosei F, Ma D (2011) Bifunctional catalytic/magnetic Ni@Ru core-shell nanoparticles. Chem Comm 47:6308–6310. doi:10.1039/C1CC10619H

Cheng KH, Aijmo J, Ma L, Yao M, Zhang X, Como J, Hope-Weeks LJ, Huang J, Chen W (2008) Luminescence decay dynamics and trace biomaterials detection potential of surface-functionalized nanoparticles. J Phys Chem C 112:17931–17939. doi:10.1021/jp8065647

Cheng Z, Ma P, Hou Z, Wang W, Dai Y, Zhai X, Lin J (2012) YVO_4:Eu^{3+} functionalized porous silica submicrospheres as delivery carriers of doxorubicin. Dalton Trans 41:1481–1489. doi:10.1039/c1dt11399b

Corr SA, Rakovich YP, Gun'ko YK (2008) Multifunctional magnetic-fluorescent nanocomposites for biomedical applications. Nanoscale Res Lett 3:87–104. doi:10.1007/s11671-008-9122-8

Deshmukh AB, Devarapalli RR, Shelke MV (2014) Functional silicon nanostructures derived from drying-mediated self-assembly of gold nanoparticles. J Nanopart Res 16:2372. doi:10.1007/s11051-014-2372-8

Ding HL, Zhang YX, Wang S, Xu JM, Xu SC, Li GH (2012) Fe_3O_4@SiO_2 Core/Shell Nanoparticles: the silica coating regulations with a single core for different core sizes and shell thicknesses. Chem Mater 24:4572–4580. doi:10.1021/cm302828d

Dosev D, Nichkova M, Kennedy IM (2008) Inorganic lanthanide nanophosphors in biotechnology. J Nanosci Nanotechnol 8:1052–1067. doi:10.1166/jnn.2008.304

Gai S, Yang P, Li C, Wang W, Dai Y, Niu N, Lin J (2010) Synthesis of magnetic, up-conversion luminescent, and mesoporous core-shell-structured nanocomposites as drug carriers. Adv Funct Mater 20:1166–1172. doi:10.1002/adfm.200902274

Gnach A, Lipinski T, Bednarkiewicz A, Rybka J, Capobianco J (2014) Upconverting nanoparticles: assessing the toxicity. Soc. Rev, Chem. doi:10.1039/c4cs00177j

Grzyb T, Runowski M, Szczeszak A, Lis S (2012a) Influence of Matrix on the luminescent and structural properties of glycerine-capped, Tb^{3+}-doped fluoride nanocrystals. J Phys Chem C 116:17188–17196. doi:10.1021/jp3010579

Grzyb T, Szczeszak A, Rozowska J, Legendziewicz J, Lis S (2012b) Tunable luminescence of Sr_2CeO_4:M^{2+} (M = Ca, Mg, Ba, Zn) and Sr_2CeO_4:Ln^{3+} (Ln = Eu, Dy, Tm) nanophosphors. J Phys Chem C 116:3219–3226. doi:10.1021/jp208015z

Grzyb T, Runowski M, Dabrowska K, Giersig M, Lis S (2013) Structural, spectroscopic and cytotoxicity studies of TbF_3@CeF_3 and TbF_3@CeF_3@SiO_2 nanocrystals. J Nanopart Res 15:1958–1972. doi:10.1007/s11051-013-1958-x

Grzyb T, Runowski M, Lis S (2014) Facile synthesis, structural and spectroscopic properties of GdF_3:Ce^{3+}, Ln^{3+} (Ln^{3+}=Sm^{3+}, Eu^{3+}, Tb^{3+}, Dy^{3+}) nanocrystals with bright multicolor luminescence. J Lumin 154:479–486. doi:10.1016/j.jlumin.2014.05.020

Haidar ZS (2010) Bio-Inspired/-Functional colloidal core-shell polymeric-based nanosystems: technology promise in tissue engineering, bioimaging and nanomedicine. Polymers 2:323–352. doi:10.3390/polym2030323

Henglein A (1987) Q-particles: size quantization effects in colloidal semiconductors. Progr Colloid & Polymer Sci 73:1–4. doi:10.1007/3-798-50724-4_55

Holsa J (2009) Persistent luminescence beats the afterglow: 400 years of persistent luminescence. Electrochem Soc Interface Winter 18:42–45

Hu H, Wang Z, Pan L (2010) Synthesis of monodisperse Fe_3O_4@silica core–shell microspheres and their application for removal of heavy metal ions from water. J Alloys Compd 492:656–661. doi:10.1016/j.jallcom.2009.11.204

Huang S, Cheng Z, Ma P, Kang X, Dai Y, Lin J (2013) Luminescent $GdVO_4:Eu^{3+}$ functionalized mesoporous silica nanoparticles for magnetic resonance imaging and drug delivery. Dalton Trans 42:6523–6530. doi:10.1039/c3dt33114h

Jasiewicz B, Mrowczynska L, Malczewska-Jaskola K (2014) Synthesis and haemolytic activity of novel salts made of nicotine alkaloids and bile acids. Bioorg Med Chem Lett 24:1104–1107. doi:10.1016/j.bmcl.2014.01.005

Kang X, Yang D, Dai Y, Shang M, Cheng Z, Zhang X, Lian H, Ma P, Lin J (2013a) Poly(acrylic acid) modified lanthanide-doped $GdVO_4$ hollow spheres for up-conversion cell imaging, MRI and pH-dependent drug release. Nanoscale 5:253–261. doi:10.1039/c2nr33130f

Kang X, Yang D, Ma P, Dai Y, Shang M, Geng D, Cheng Z, Lin J (2013b) Fabrication of hollow and porous structured $GdVO_4:Dy^{3+}$ nanospheres as anticancer drug carrier and MRI contrast agent. Langmuir 29:1286–1294. doi:10.1021/la304551y

Li X, Yu M, Hou Z, Li G, Ma P, Wang W, Cheng Z, Lin J (2011) One-dimensional $GdVO_4:Ln^{3+}$ (Ln = Eu, Dy, Sm) nanofibers: Electrospinning preparation and luminescence properties. J Solid State Chem 184:141–148. doi:10.1016/j.jssc.2010.11.019

Limaye MV, Singh SB, Das R, Poddar P, Kulkarni SK (2011) Room temperature ferromagnetism in undoped and Fe doped ZnO nanorods: microwave-assisted synthesis. J Solid State Chem 184:391–400. doi:10.1016/j.jssc.2010.11.008

Liu J, Qiao SZ, Chen JS, Lou XW, Xing X, Lu GQ (2011) Yolk/shell nanoparticles: new platforms for nanoreactors, drug delivery and lithium-ion batteries. Chem. Comm. 47:12578–12591. doi:10.1039/c1cc13658e

Lou L, Yu K, Zhang Z, Li B, Zhu J, Wang Y, Huang R, Zhu Z (2011) Functionalized magnetic-fluorescent hybrid nanoparticles for cell labelling. Nanoscale 3:2315–2323. doi:10.1039/c1nr10066a

Lu P, Zhang J-L, Liu Y-L, Sun D-H, Liu G-X, Hong G-Y, Ni J-Z (2010) Synthesis and characteristic of the Fe_3O_4@SiO_2@$Eu(DBM)_3.2H_2O/SiO_2$ luminomagnetic microspheres with core-shell structure. Talanta 82:450–457. doi:10.1016/j.talanta.2010.04.052

Ma Q, Wang J, Dong X, Yu W, Liu G (2014) Electrospinning fabrication and characterization of magnetic-upconversion fluorescent bifunctional core–shell nanofibers. J Nanopart Res 16:2239. doi:10.1007/s11051-013-2239-4

Massart R (1981) Preparation of aqueous magnetic liquids in alkaline and acidic media. IEEE Trans Magn 17:1247–1248. doi:10.1109/TMAG.1981.1061188

Niu N, Yang P, Liu Y, Li C, Wang D, Gai S, He F (2011) Controllable synthesis and up-conversion properties of tetragonal $BaYF_5$:Yb/Ln (Ln = Er, Tm, and Ho) nanocrystals. J Colloid Interface Sci 362:389–396. doi:10.1016/j.jcis.2011.07.001

Nuñez NO, Rivera S, Alcantara D, de la Fuente JM, García-Sevillano J, Ocaña M (2013) Surface modified Eu:$GdVO_4$ nanocrystals for optical and MRI imaging. Dalton Trans 42:10725–10734. doi:10.1039/c3dt50676b

Park J-N, Zhang P, Hu Y-S, McFarland EW (2010) Synthesis and characterization of sintering-resistant silica-encapsulated Fe_3O_4 magnetic nanoparticles active for oxidation and chemical looping combustion. Nanotechnology 21:225708–225716. doi:10.1088/0957-4484/21/22/225708

Runowski M, Grzyb T, Lis S (2011) Bifunctional luminescent and magnetic core/shell type nanostructures Fe_3O_4@$CeF_3:Tb^{3+}/SiO_2$. J Rare Earths 29:1117–1122. doi:10.1016/S1002-0721(10)60609-6

Runowski M, Grzyb T, Lis S (2012) Magnetic and luminescent hybrid nanomaterial based on Fe_3O_4 nanocrystals and $GdPO_4:Eu^{3+}$ nanoneedles. J Nanopart Res 14:1188–1195. doi:10.1007/s11051-012-1188-7

Runowski M, Dabrowska K, Grzyb T, Miernikiewicz P, Lis S (2013) Core/shell-type nanorods of Tb^{3+}-doped $LaPO_4$, modified with amine groups, revealing reduced cytotoxicity. J Nanopart Res 15:2068–2083. doi:10.1007/s11051-013-2068-5

Runowski M, Ekner-Grzyb A, Mroczynska L, Balabhadra S, Grzyb T, Paczesny J, Zep A, Lis S (2014) Synthesis and organic surface modification of luminescent, lanthanide-doped core/shell nanomaterials (LnF_3@SiO_2@NH_2@Organic Acid) for potential bioapplications: spectroscopic, structural, and in vitro cytotoxicity evaluation. Langmuir 30:9533–9543. doi:10.1021/la501107a

Selvan ST, Tan TTY, Yi DK, Jana NR (2009) Functional and multifunctional nanoparticles for bioimaging and biosensing. Langmuir 26:11631–11641. doi:10.1021/la903512m

Shanta Singh N, Kulkarni H, Pradhan L, Bahadur D (2013) A multifunctional biphasic suspension of mesoporous silica encapsulated with $YVO_4:Eu^{3+}$ and Fe_3O_4 nanoparticles: synergistic effect towards cancer therapy and imaging. Nanotechnology 24:065101. doi:10.1088/0957-4484/24/6/065101

Tong L, Shi J, Ren X, Li Q, Ding H, Yang H (2013) Multifunctional nanocomposites with different coupling agents: synthesis, luminescent and magnetic properties. J Nanopart Res 15:1627. doi:10.1007/s11051-013-1627-0

Wang Y, Qin W, Zhang J, Cao C, LU S, Ren X (2009) Photoluminescence of colloidal YVO_4:Eu/SiO_2 core/shell nanocrystals. Opt Commun 282:1148–1153. doi:10.1016/j.optcom.2008.12.007

Wang C, Yin D, Ouyang J, Song K, Liu B, Wu M (2014) Synthesis of fluorescent and magnetic bi-functional $NaLuF_4$-based upconversion nanocrystals. J Nanosci Nanotechnol 14:5232–5237. doi:10.1166/jnn.2014.8672

Wu J, Yan B (2008) Photoluminescence intensity of $YxGd_{1-x}VO_4:Eu^{3+}$ dependence on hydrothermal synthesis time and variable ratio of Y/Gd. J Alloys Compd 455:485–488. doi:10.1016/j.jallcom.2007.01.162

Xue X, Wang F, Liu X (2011) Emerging functional nanomaterials for therapeutics. J Mater Chem 21:13107–13127. doi:10.1039/c1jm11401h

Yang D, Kang X, Shang M, Li G, Peng C, Li C, Lin J (2011) Size and shape controllable synthesis and luminescent properties of $BaGdF_5:Ce^{3+}/Ln^{3+}$ (Ln = Sm, Dy, Eu, Tb) nano/submicrocrystals by a facile hydrothermal process. Nanoscale 3:2589–2595. doi:10.1039/c1nr10203f

Yin W, Zhou L, Gu Z, Tian G, Jin S, Yan L, Liu X, Xing G, Ren W, Liu F, Pan Z, Zhao Y (2012) Lanthanide-doped $GdVO_4$ upconversion nanophosphors with tunable emissions and their applications for biomedical imaging. J Mater Chem 22:6974–6981. doi:10.1039/c2jm16152d

Yoo J-H, Lee S-W (2014) Fabrication and characterization of quantum dots-bound hydrogels with fluorescent and temperature-sensitive functionalities. J Nanosci Nanotechnol 14:7648–7653. doi:10.1166/jnn.2014.9411

Zhou J, Lu Z, Shan G, Wang S, Liao Y (2014) Gadolinium complex and phosphorescent probe-modified $NaDyF_4$ nanorods for T1- and T2-weighted MRI/CT/phosphorescence multimodality imaging. Biomaterials 35:368–377. doi:10.1016/j.biomaterials.2013.09.088

Podsumowanie

W nienijeszej pracy doktorskiej przedstawiono wyniki badań nad syntezą, modyfikacją powierzchni i badaniami właściwości fizykochemicznych wielofunkcyjnych nanomateriałów luminescencyjnych opartych o jony pierwiastków ziem rzadkich. W trakcie prowadzonych badań udało się uzyskać liczne nowe nanocząstki luminescencyjne, tj. nanoluminofory oparte o proste i złożone fluorki, fosforany oraz wanadany pierwiastków ziem rzadkich. Dzięki odpowiedniemu domieszkowaniu wybranymi jonami lantanowców (Ln^{3+}), powstałe produkty wykazywały po naświetleniu światłem UV intensywną wielobarwną luminescencję. Część otrzymanych produktów poddano obróbce hydrotermalnej lub organicznej modyfikacji powierzchni, co doprowadziło do otrzymania zaawansowanych materiałów wykazujących wielokolorową, przestrajalną luminescencję.

W dalszej kolejności wybrano optymalne struktury, odznaczające się znacznym stopniem jednorodności, stabilnością tworzonych koloidów wodnych oraz intensywną luminescencją. Tak wyselekcjonowane układy poddano modyfikacji powierzchni poprzez pokrycie otrzymanych nanocząstek powłoką krzemionkową sfunkcjonalizowaną grupami aminowymi lub karboksylowymi. W wyniku tego, otrzymano zaawansowane nanostruktury typu rdzeń/powłoka (*core/shell*). Nanomateriały takie wykazywały zmienione właściwości fizykochemiczne i biologiczne, w porównaniu do pokrywanych cząstek rdzeni. Zmianie uległy właściwości luminescencyjne, morfologiczne (rozmiar cząstek), powierzchniowe (ładunek powierzchniowy oraz wielkość powierzchni właściwej), jak również aktywność biologiczna otrzymanych nanomateriałów. W zależności od rozmiaru cząstek, ładunku powierzchniowego, porowatości i składu chemicznego powłoki obserwowano zwiększenie lub zmniejszenie cytotoksyczności otrzymanych nanostruktur w porównaniu do niemodyfikowanych cząstek. Wybrane krystaliczne nanocząstki oparte o domieszkowane fluorki lub wanadany lantanowców wykorzystano w syntezie wielofunkcyjnych nanomateriałów luminescencyjno-magnetycznych typu core/shell. Materiały te wykazywały jednocześnie intensywną zieloną lub czerwoną luminescencję pod wpływem promieniowania UV oraz odpowiedz na przyłożone pole magnetyczne.

Właściwości otrzymywanych nanomateriałów były badane metodami spektrofluorymetrii, XRD, mikroskopii elektronowej (TEM, HR-TEM, SEM, STEM),

spektroskopii FT-IR, analizy elementarnej, EDX, ICP-OES, DLS, ELS, TGA, analizy powierzchni właściwej i porowatości, testów SRB do oceny ich cytotoksyczności, etc.

Wyniki przeprowadzonych badań przedstawiono w formie ośmiu artykułów, opublikowanych w międzynarodowych czasopismach naukowych, z tzw. listy filadelfijskiej.

Otrzymane nanomateriały mogą być potencjalnie zastosowane w multimodalnym obrazowaniu, terapiach celowanych, kryminalistyce, jako nanosensory i bio-detektory, w śladowej analizie jakościowej i ilościowej jak również w przemyśle jako nowe źródła światła.